UNIVERSITEIT VAN PRETORIA
UNIVERSITY OF PRETORIA
YUNIBESITHI YA PRETORIA

HEAT TRANSFER AND PRESSURE DROP OF DEVELOPING FLOW IN SMOOTH TUBES IN THE TRANSITIONAL FLOW REGIME

by

Marilize Everts

Submitted in partial fulfilment of the requirements for the degree

MASTER OF ENGINEERING

In the Department of Mechanical and Aeronautical Engineering

University of Pretoria

December 2014

Supervisor: Prof J.P. Meyer

Abstract

Title: Heat Transfer and Pressure Drop of Developing Flow in Smooth Tubes in the Transitional Flow Regime

Supervisor: Prof J.P. Meyer

Department: Mechanical and Aeronautical Engineering

Degree: Master of Engineering (Mechanical Engineering)

Heat exchangers have a wide range of applications and engineers need accurate correlations to optimise the design of these heat exchangers. During the design process, the best compromise between high heat transfer coefficients and relatively low pressure drops is usually in the transitional flow regime. Limited research has been done on tube flow in the transitional flow regime. These studies considered either fully developed flow, or average measurements of developing flow across a tube length. No research has been done with the focus on developing flow in smooth tubes in the transitional flow regime. Therefore, the purpose of this study was to experimentally investigate the heat transfer and pressure drop characteristics of developing flow in the transitional flow regime. An experimental set-up was designed, built and validated against literature. Heat transfer and pressure drop measurements were taken at Reynolds numbers between 500 and 10 000 at three different heat fluxes (6.5, 8.0 and 9.5 kW/m^2). A total of 398 mass flow rate measurements, 19 158 temperature measurements and 370 pressure drop measurements were taken. Water was used as the test fluid and the Prandtl number ranged between 3 and 7. The test section was a smooth circular tube and had an inner diameter and length of 11.52 mm and 2.03 m, respectively. An uncertainty analysis showed that the uncertainties of the Nusselt numbers and Colburn *j*-factors varied between 4% and 5% while the friction factor uncertainties varied between 1% and 17%. Five different flow regimes (laminar, developing laminar, transitional, low-Reynolds-number-end and turbulent) were identified in the first part of the tube during the experiments and nomenclature was developed to more clearly identify the boundaries of the different flow regimes. The developing laminar regime was unique to developing flow and decreased along the tube length. Both the start and end of transition were delayed along the tube length and the width of the transition region decreased slightly. This is in contrast with the results obtained in literature where the effect of the non-dimensional distance from the inlet on fully developed flow in the transition region was investigated. Transition was also slightly delayed with increasing heat flux, but secondary flow effects had no significant influence on the width of the transition region. The relationship between heat transfer and pressure drop was investigated and correlations were developed to predict the Nusselt number as a function of friction factor, Reynolds number and Prandtl number in the laminar, transitional, low-Reynolds-number-end and turbulent flow regimes. Overall, it can be concluded that the heat transfer characteristics of developing and fully developed flow differ significantly and more work needs to be done to fully understand the fundamentals before the heat transfer and pressure drop characteristics are fully understood.

Conference Papers

The following conference papers were produced as part of the study and were or will be read:

1. Everts, M., Ayres, S.R., Mulock Houwer, F.A., Vanderwagen, C.P., Kotze, N.M. & Meyer, J.P.; The influence of surface roughness on transitional flow in a parabolic trough receiver tube, Second Southern African Solar Energy Conference (SASEC 2014), Port Elizabeth, 27-29 January 2014.
2. Everts, M., Ayres, S.R., Mulock Houwer, F.A., Vanderwagen, C.P., Kotze, N.M. & Meyer, J.P.; The influence of surface roughness on heat transfer in the transitional flow regime, 15th International Heat Transfer Conference (IHTC-15), Kyoto, 10-15 August 2015.
3. Everts, M. & Meyer, J.P.; Heat transfer characteristics of developing flow in the transitional flow regime of a solar receiver tube, Third Southern African Solar Energy Conference (SASEC 2015), Skukuza, Kruger National Park, 11-13 May 2015.
4. Everts, M. & Meyer, J.P.; Heat transfer of developing flow in the transitional flow regime, First Thermal and Fluid Engineering Summer Conference (TFESC), New York City, 9-12 August 2015.

Acknowledgements

I would like to acknowledge the following people for their help and support:

- Professor J.P. Meyer, for offering his support and guidance and placing his substantial knowledge at my disposal;
- Mr D. Gouws and Mr P. Kruger, for their technical advice and support with the experimental set-up and testing;
- Mr K.J. Mthombeni, for his assistance with the building of the experimental set-up;
- Mr J.C. Everts, Mrs M. Everts and Mr M. Kapp, for their continuous moral support.

I would also like to thank the following institutions for their financial support:

- NRF;
- TESP;
- Stellenbosch University/University of Pretoria;
- SANERI/SANEDI;
- CSIR;
- EEDSM Hub;
- NAC.

Table of Contents

List of Figures

List of Tables

Nomenclature

A	Area	m^2
c_p	Constant pressure specific heat	J/kg.K
D	Inner diameter[1]	m
EB	Energy balance	%
g	Gravitational acceleration	m/s^2
h	Heat transfer coefficient	W/m^2
I	Current	A
k	Thermal conductivity	W/m.K
L	Length	m
M	Measurement or calculated value	
$\dot{m}$	Mass flow rate	kg/s
ΔP	Pressure drop	Pa
$\dot{Q}$	Heat input	W
$\dot{q}$	Heat flux	W/m^2
R	Radius	m
R_{tube}	Thermal resistance	°C/W
r	Radial distance	m
T	Temperature	°C or K
V	Velocity	m/s
V	Voltage	V
x	Distance from inlet	m

Dimensionless parameters

a	Constant used in correlations
b	Constant used in correlations
c	Constant used in correlations
c_f	Skin-friction coefficient
d	Constant used in correlations
e	Constant used in correlations
f	Friction factor
ξ	Turbulent friction factor
Gr	Grashof number
Gz	Graetz number
j	Colburn *j*-factor
m	Flow parameter used in correlations
Nu	Nusselt number
Pr	Prandtl number
Ra	Rayleigh number
Re	Reynolds number
Re^*	Modified Reynolds number used in Equation 2.16
z^*	Dimensionless distance

---

[1] Except when defined differently with a subscript *o* to indicate outer diameter

Greek letters

α	Thermal diffusivity	m^2/s
β	Volume expansivity	1/K
ε	Roughness height	m
δ	Velocity boundary layer thickness	m
δ_t	Thermal boundary layer thickness	m
ρ	Density	kg/m^3
μ	Dynamic viscosity	kg/m.s
v	Kinematic viscosity	m^2/s
τ_w	Surface shear stress	N/m^2

Subscripts

app	Apparent
b	Bottom/Bulk
c	Cross-section
cor	Correlation
cr	Critical Reynolds number
cond	Conduction
conv	Convection
cp	Constant property
cv	Variable property
dl	Developing laminar flow regime
exp	Experimental
i	Inlet/Inner
l	Laminar
lre	Low-Reynolds-number-end
m	Mean
o	Outer/Outlet
p	Pressure
s	Heat transfer surface
t	Top/Turbulent
tr	Transition
w	Surface/Water

1. Introduction

1.1. Background

Heat exchangers have a wide range of applications in the generation and consumption of electrical energy. On the generation side, heat exchangers are indispensable components in the cycles of fossil fuel, nuclear and solar power plants. They are used to transfer heat in boilers from the energy source (fossils, nuclear reaction, solar, etc.) to the fluids (usually steam) used to drive turbines that generate electricity. Downstream of turbines, heat exchangers are used to condense steam and reject heat to the environment. On the consumption side, heat exchangers are again indispensable components and are found in process plants, petrochemical plants, petroleum refineries, natural gas processing, sewage treatment, manufacturing plants as well as in the heating, ventilation and air-conditioning (HVAC) industries. A classic example of heat exchangers is the radiator of an internal combustion engine. A circulating fluid flows through radiator coils while air flows past the coils. This cools the fluid and heats the incoming air, maintaining the engine at its operating temperature.

From a simple radiator to the generation of electrical energy, the efficiency of generating energy and consuming energy directly depends on the effectiveness of heat exchangers. It is therefore critical that sufficient design information is available so that heat exchanger effectiveness can be optimised. Designers usually have a choice to select between a flow regime that is either laminar or turbulent. The aim is to obtain high heat transfer coefficients and low pressure drops since the pressure drop is related to the pumping power and thus operational running cost. Laminar flow provides low pressure drops, but unfortunately, the heat transfer coefficients are low as well. Although turbulent flow provides high heat transfer coefficients, the pressure drops are significant. In many cases, the best compromise between high heat transfer coefficients and relatively low pressure drops is in or close to the transitional flow regime found between laminar and turbulent flow. Designers are, however, advised to avoid the transitional flow regime since the flow is believed to be unstable and chaotic. In this regime, the flow alternates between laminar and turbulent flow, while turbulent eddies will occur in flashes known as turbulent bursts. This might cause the pressure drop to increase with an order of magnitude (Meyer, 2014).

To improve the efficiency of heat exchangers, the heat transfer coefficients can be increased by making use of enhanced tubes, such as finned tubes, twisted tape inserts or helical microfin tubes. As these tubes became more effective, designers decreased the mass flow rate to reduce the pressure drop and thus the pumping power. With time, many of these tubes started operating close to or in the transitional flow regime. Changes in operating conditions, design constraints, additional equipment, scaling and corrosion can also cause the flow to move into the transitional flow regime (Meyer, 2014).

Flow regimes in tubes have been extensively investigated from as early as 1883, especially focusing on laminar and turbulent flow, while research has been done on the transitional flow regime since the 1990s. Transition occurs at a Reynolds number of 2 300 for uniform steady flow in a horizontal smooth tube with a rounded entrance (ASHRAE, 2009). However, this Reynolds number is significantly affected when the geometry and inside surface are changed, which is typically the case in heat exchangers.

According to a recent review paper by Meyer (2014), flow in the transitional flow regime has mainly been investigated by Professor Afshin Ghajar from Oklahoma State University and his co-workers, as well as by Professor Josua Meyer from the University of Pretoria and his co-workers. Ghajar and his co-workers were the first to investigate the influence of the inlet geometry on heat transfer and pressure drop in the transitional flow regime and their work can mainly be found in the following citations: Ghajar and Tam (1991, 1994, 1995), Ghajar and Madon (1992), Ghajar *et al*. (2010), Tam and Ghajar (1997, 1998) and Tam *et al.* (2009, 2010, 2012, 2013).

A constant heat flux boundary condition was used focusing on fully developed flow. Both isothermal and diabatic friction factor results revealed that transition was significantly influenced by the inlet geometry and was delayed for smoother inlet geometries. Furthermore, the diabatic friction factors increased in the laminar and transition regions due to the effect of secondary flow. In the turbulent flow regime, the friction factors were independent of the inlet geometry and secondary flow. Heating also influenced the start and end of the transition region and transition was delayed for increasing heat fluxes.

The heat transfer coefficients were also influenced by the inlet geometry and, similar to the pressure drop results, transition occurred first for the inlet with the greatest disturbance. The laminar heat transfer coefficients were strongly influenced by the secondary flow effects and increased with increasing heat flux. Similar to the friction factors, the heat transfer coefficients in the turbulent flow regime were independent of the inlet geometry and secondary flow.

Tam *et al.* (2012) conducted an extensive study on the available entrance and fully developed isothermal and diabatic friction factor correlations. The authors concluded that there were no correlations available to predict the isothermal and diabatic friction factors in the transitional flow regime. Pressure drop measurements were therefore taken at different locations along the test section under isothermal and diabatic conditions to investigate developing flow. Based on their experimental data, correlations to predict isothermal and diabatic friction factors for both developing and fully developed flow in the laminar and transitional flow regimes were developed.

Meyer and Olivier (Olivier and Meyer, 2010; Meyer and Olivier, 2011a, 2011b, 2014; Meyer, 2014) also investigated flow in the transitional flow regime, but using a constant surface temperature boundary condition. Water was used as the test fluid, leading to a significantly lower Prandtl number (approximately 7) than in the studies conducted by Ghajar (between 40 and 160). While Ghajar and his co-workers focused on fully developed flow, Meyer and Olivier considered the average measurements across a tube length. Their data were therefore mainly valid for developing flow (laminar and transitional regimes), but contained fully developed flow (turbulent flow regime) as well. Although their results were similar to the results obtained by Ghajar and co-workers, it was found that transition was independent of the inlet geometry when heating was applied. According to Nagendra (1973), the inlet disturbances have no effect on transition when the product of the Reynolds, Rayleigh and diameter-to-length ratio is greater than approximately 10^6.

Ghajar and his co-workers focused on fully developed flow only, except for Tam *et al.* (2012), who investigated pressure drop in both developing and fully developed flow. Meyer and Olivier

(2011a, 2011b, 2014) and Olivier and Meyer (2010) investigated developing flow, but the focus of their studies was on the effect of inlet geometries and enhanced tubes and not on developing flow. Furthermore, the average measurements across the tube length were used. Although Tam *et al.* (2012) investigated developing flow, different mixtures of ethylene glycol and distilled water were used, which resulted in very high Prandtl numbers.

1.2. Importance of developing flow

The thermal entrance length is a function of the tube diameter, Reynolds number and Prandtl number and therefore increases with increasing Reynolds number. An example of the importance of developing flow is the construction of chillers. A typical chiller tube diameter is approximately 15 mm. At a Reynolds number of 2 000, fully developed flow for water (with an average Prandtl number of 6) flowing through a 15 mm tube will be obtained after 9 m. When a glycol mixture (with an average Prandtl number of 20) is used as the test fluid, the flow will take up to 30 m to become fully developed. However, the length of most industrial chillers with capacities of 3 500 kW (1 000 tons) is less than approximately 4 m. It can therefore be concluded that the flow in these chillers will in general be developing, rather than fully developed.

Another example of the importance of developing flow is commercial concentrated solar power plants operating with parabolic troughs. In the parabolic trough is a receiver tube on which the incoming radiation is focused. The inner diameter of the receiver tube is approximately 66 mm and the fluid being heated on the inside of the tube is typically a thermal oil with a Prandtl number of 5. At a Reynolds number of 2 000, the thermal entrance length will be approximately 33 m. However, the parabolic plants usually consist of several 4 m receiver tubes. Up to 10 receiver tubes are connected to each other before a bend in the tube occurs. As the total heated length would then be 40 m, it implies that more than 80% (33 m) of the receiver tube will have developing flow and only the last 7 m will have fully developed flow. This implies that most of the heat transfer phenomena will be dominated by developing flow rather than fully developed flow. Therefore, it is important that the fundamentals of developing flow in the transitional flow regime should be well understood and that design data are made available to engineers.

1.3. Problem statement

As indicated in Section 1.1, previous work has been done on flow in the transitional flow regime, but these studies focused primarily on fully developed flow (Ghajar and co-workers) or the average measurements of developing flow across a tube length (Meyer and Olivier). Therefore, the heat transfer and pressure drop characteristics of developing flow in the transitional flow regime have not yet received the required attention.

1.4. Aim

The purpose of this study was to investigate the heat transfer and pressure drop characteristics of developing flow in the transitional flow regime in a smooth horizontal tube.

1.5. Objectives

The main objectives of this study were:

- to obtain the local and average heat transfer coefficients as a function of Nusselt number and Colburn *j*-factor for different Reynolds numbers under both forced and mixed convection conditions;

- to obtain the average friction factor data across a tube length as a function of Reynolds number at different heat fluxes;
- to obtain the local heat transfer coefficients and temperature differences between the surface and fluid to investigate the thermal entrance length;
- to obtain the ratio of the local heat transfer coefficients at the top and bottom of the tube to investigate the effects of secondary flow;
- to determine the start and end Reynolds numbers of the transitional flow regime for different values of x/D;
- to investigate the relationship between heat transfer and pressure drop by comparing the Colburn j-factors and friction factors.

These objectives were met by means of physical measurements of temperatures, pressure drops and mass flow rates in a smooth horizontal tube.

1.6. Scope of work

As the aim of this study was to investigate developing flow in the transitional flow regime, the Reynolds number was varied between approximately 500 and 10 000 to ensure that the whole transitional flow regime, as well as sufficient parts of the laminar and turbulent flow regimes, was covered. One smooth circular horizontal tube with an inner diameter and length of 11.52 mm and 2.03 m, respectively, was used. Therefore, the study considered developing flow in macro-tubes. A square-edged inlet was used and the tube was heated at different constant heat fluxes. Water was used as the test fluid. This study thus focused on the heat transfer and pressure drop characteristics of relatively low (approximately 6) Prandtl number fluids. A test section was built and installed into an existing experimental set-up, containing the necessary instrumentation used for similar research studies.

1.7. Overview of dissertation

In Chapter 2, a literature survey is presented compiled on the work done by Professor Ghajar from Oklahoma State University and his co-workers and by Professor Meyer from the University of Pretoria and his co-workers on flow in the transitional flow regime. In Chapter 3, details are provided of the experimental set-up, the data reduction, as well as the results of the uncertainty analysis. Nomenclature to define the boundaries of the different flow regimes was also developed. Chapter 4 contains the validation of the experimental set-up and data reduction method. Chapters 5 and 6 cover the experimental heat transfer and pressure drop results for local and average data, respectively. Chapter 7 concludes the study and provides some recommendations for further work.

Appendix A contains the calibration procedure of the thermocouples and pressure transducers. Heating wire was coiled around the test section to obtain a constant heat flux boundary condition. However, to ensure that the heating wire did not influence the thermocouple readings, a separate test section was built and tested to determine the appropriate distance between the heating wire and thermocouple junction. Four different techniques were investigated and the results are summarised in Appendix B. Appendix C contains the uncertainty analysis of all the relevant variables. During the experiments, it was found that the surface temperatures fluctuated in the transitional flow regime. These temperature fluctuations are summarised in Appendix D. The local surface temperatures across the test section are investigated in Appendix E. Appendix F contains a CD with all the experimental data as well as the journal articles and conference papers that were consulted during the study. The experimental data are also available on UPSpace (Institutional research repository of the University of Pretoria), http://repository.up.ac.za, which is an open access digital institutional repository hosted by the University of Pretoria, or more specifically at http://hdl.handle.net/2263/44245.

2. Literature Survey

2.1. Introduction

This chapter summarises a few fundamental concepts which are key to many equations and concepts relevant to heat transfer and transitional flow in smooth tubes. The chapter also briefly discusses the different flow regimes as well as developing and fully developed flow. Up to now, flow in the transitional flow regime has mainly been investigated by Professor Afshin Ghajar from Oklahoma State University and Professor Josua Meyer from the University of Pretoria, along with their co-workers. Their work will be briefly discussed and compared.

2.2. Non-dimensional parameters

2.2.1. Reynolds number

Reynolds showed as early as 1883 that transition depends on the surrounding disturbances. Therefore, the surface geometry, surface roughness, flow velocity, surface temperature and type of fluid are all factors which affect the transition from laminar to turbulent flow. Although Stokes identified the ratio of the inertia ($\rho V^2/D$) to viscous ($\mu V/D^2$) forces, the Reynolds number was named after Osborne Reynolds in recognition of his work (Meyer, 2014) and can be defined as follows for tube flow (White, 2009):

$$Re = \frac{Inertia\ forces}{Viscous\ forces} = \frac{\rho V D}{\mu} \tag{2.1}$$

When the Reynolds numbers are small (laminar flow), the viscous forces are able to suppress the random fluctuations (inertia forces) of the fluid. However, at large Reynolds numbers (turbulent flow), the inertia forces are large compared with the viscous forces and therefore the viscous forces are unable to prevent these fluctuations of the fluid.

2.2.2. Friction factor

Pressure drop is an important quantity in the analysis of tube flow since it is directly related to the power requirements of the pump. The pressure drop due to viscous effects can be expressed as follows (Cengel and Cimbala, 2006):

$$\Delta P = f \frac{L}{D} \frac{\rho V^2}{2} \tag{2.2}$$

The friction factor (*f*) also known as the Darcy friction factor is named after Henry Darcy and can be defined as follows (Cengel and Cimbala, 2006):

$$f = \frac{8\,\tau_w}{\rho V^2} \tag{2.3}$$

The friction factor should not be confused with the skin friction coefficient (also known as Fanning friction factor), since it is four times greater (Cengel and Cimbala, 2006). To prevent confusion, only the friction factor will be used in this study.

$$C_f = \frac{2\,\tau_w}{\rho V^2} = \frac{f}{4} \tag{2.4}$$

2.2.3. Nusselt number

When the fluid involves some motion, heat transfer through the fluid layer is by convection, while heat transfer is by conduction when the fluid layer is motionless. The Nusselt number is the ratio of the convection heat transfer to conduction heat transfer and therefore represents the enhancement of heat transfer through a fluid due to the fluid motion. Hence, pure conduction heat transfer is represented by a Nusselt number of 1. The Nusselt number is a dimensionless heat transfer coefficient and is named after Wilhelm Nusselt, who made significant contributions to convective heat transfer (Cengel, 2006). The Nusselt number for a circular tube is defined as follows:

$$Nu = \frac{\dot{q}_{conv}}{\dot{q}_{cond}} = \frac{hD}{k} \tag{2.5}$$

2.2.4. Prandtl number

The relative thickness and growth of the velocity boundary layer (δ) and thermal boundary layer (δ_t) are described by the Prandtl number. It is named after Ludwig Prandtl, who introduced the concept of boundary layer in 1904 and made significant contributions to boundary layer theory (Holman, 1986). The Prandtl number is defined as follows:

$$Pr = \frac{Molecular\ diffusivity\ of\ momentum}{Molecular\ diffusivity\ of\ heat} = \frac{\nu}{\alpha} = \frac{\mu\, C_p}{k} \approx \left(\frac{1}{1.026}\frac{\delta}{\delta_t}\right)^3 \tag{2.6}$$

When the Prandtl number is unity, heat and momentum dissipate through the fluid at the same rate and thus the thickness of the thermal and velocity boundary layers is the same. The Prandtl number of liquid metals is very small ($Pr \ll 1$), which indicates that heat diffuses very quickly and the thermal boundary layer is greater than the velocity boundary layer. On the other hand, the Prandtl number of oils is very large ($Pr \gg 1$) and therefore heat dissipates very slowly relative to momentum. One of the most important fluids used by engineers is water, which has a Prandtl number of approximately 7 at a temperature of 20 °C. This means that heat diffuses approximately two times (using Equation 2.6) slower than momentum through the boundary layer.

2.2.5. Grashof and Rayleigh numbers

The effect of natural convection can be quantified with the Grashof number. It represents the ratio of the buoyancy forces to the viscous forces and is defined as follows for flow inside a tube (Ghiaasiaan, 2011):

$$Gr = \frac{g\beta(T_w - T_b)D^3}{\nu^2} \tag{2.7}$$

When heat is applied to a tube, buoyancy effects often become significant and the flow is then dominated by mixed convection rather than forced convection. The Rayleigh number is the product of the Grashof number and Prandtl number (Ghiaasiaan, 2011):

$$Ra = Gr\ Pr \tag{2.8}$$

The Rayleigh numbers can be plotted on a flow regime map (Section 2.7.4) and is used as a guideline to determine whether the flow in a tube is dominated by forced or mixed convection. This is a valuable tool because it is used to determine whether or not secondary flow effects can be neglected.

2.2.6. Graetz number

The Graetz number can be used as a guideline to determine whether the flow is fully developed and is defined as follows:

$$Gz = RePr\frac{D}{x} \tag{2.9}$$

It represents the ratio of the time taken by heat to diffuse radially into the fluid by conduction to the time taken by the fluid to reach an axial distance *x* from the tube inlet. When the Graetz number is smaller than 20, the local Nusselt numbers for both a constant heat flux boundary condition and a constant surface temperature boundary condition become a straight horizontal line. The flow can then be assumed to be fully developed (Cengel and Ghajar, 2011).

2.3. Thermal entrance length

When a fluid at a uniform temperature enters a tube with a different surface temperature (for example, a tube heated at a constant heat flux), the fluid particles adjacent to the surface assume the surface temperature. The result is that the temperature of the fluid near the surface is different from the fluid near the centre line of the tube. This temperature difference inside the fluid leads to convection heat transfer in the radial direction, as well as the development of a thermal boundary layer. The thickness of the thermal boundary layer increases along the tube length and once the boundary layer thickness is the same as the radius of the tube, the flow is thermally fully developed. Downstream from this point, the axial temperature distribution in a radial direction will be constant (Section 2.4). The thermal entrance length in laminar (L_l) and turbulent (L_t) flow can be theoretically estimated using the following equations (Cengel, 2006):

$$L_l = 0.05\, Re\, Pr\, D \tag{2.10}$$

$$L_t = 10D \tag{2.11}$$

2.4. Fully developed flow

The region after the thermal entrance region is the thermally fully developed flow region and the dimensionless temperature profile, $(T_w - T)/(T_w - T_m)$, remains constant. Water is used as the test fluid in this study and since the Prandtl number of water is greater than 1, the thermal entrance length is greater than the hydrodynamic entrance length. Once the flow is thermally fully developed, it will be hydrodynamically fully developed as well and therefore it can be said that the flow is fully developed.

In the fully developed region, the dimensionless temperature profile, $(T_w - T)/(T_w - T_m)$, is independent of *x* since the derivative of $(T_w - T)/(T_w - T_m)$ with respect to *x* is zero. The derivative of $(T_w - T)/(T_w - T_m)$ with respect to *r* should also be independent of *x*, since the dimensionless temperature profile remains constant in the fully developed region. This can be mathematically expressed as follows (Cengel, 2006):

$$\frac{\partial}{\partial r}\left(\frac{T_w - T}{T_w - T_m}\right)\bigg|_{r=R} = \frac{-(\partial T/\partial r)|_{r=R}}{T_w - T_m} \neq f(x) \tag{2.12}$$

The heat flux to the tube surface can be expressed as follows (Cengel, 2006):

$$\dot{q}_w = h_x(T_w - T_m) = k\frac{\partial T}{\partial r}\bigg|_{r=R} \rightarrow h_x = \frac{k(\partial T/\partial r)|_{r=R}}{T_w - T_m} \tag{2.13}$$

From Equation 2.12, it can be concluded that the local heat transfer coefficient (Equation 2.13) remains constant (independent of *x*) when the flow is fully developed. However, it is important to note that although the dimensionless temperature profile is independent of *x* in the fully developed region, the temperature profile is not. Therefore, the temperature profile may vary along the tube length, which is usually the case.

2.5. Flow regimes

Flow inside tubes are traditionally divided into three regimes, namely the laminar, transitional and turbulent flow regimes. These three regimes are briefly discussed in Sections 2.5.1 to 2.5.3.

2.5.1. Laminar flow

Osborne Reynolds investigated laminar flow in 1883 by injecting dye into the flow in a glass tube. Reynolds concluded that the dye streak formed a straight line when the velocities were sufficiently low (Reynolds, 1883). Secondary flow effects play a significant role in the laminar flow regime and it is therefore important to distinguish between forced and mixed convection.

2.5.1.1. Forced convection

Forced convection exists when, for example, the fluid motion is forced through a heated or cooled tube by means of a pump. However, the velocity of the fluid should be sufficiently high to suppress the buoyancy-induced secondary flow, for example, turbulent flow with a constant heat flux boundary condition.

2.5.1.2. Mixed convection

Natural convection occurs when the fluid motion is created by buoyancy forces, which are caused by the difference in temperature inside the fluid. The flow is dominated by mixed convection when a pump is used to create the fluid motion, but the secondary flow effects remain significant. Laminar and transitional flows are usually dominated by mixed convection when heating is applied to the tube since the velocity of the fluid is not high enough to suppress the secondary flow effects.

2.5.1.3. Heat transfer correlations

In order to validate the experimental set-up and data reduction method in this study, the data should be compared with existing correlations. Table 2.1 contains some of the laminar Nusselt number correlations. The purpose of this table is not to summarise all the laminar Nusselt number correlations, but rather to summarise the most important ones, which will be used for the validation of the experimental set-up and data reduction method of this study (presented in Chapter 4).

2.5.1.4. Pressure drop correlations

Table 2.2 provides the correlations which can be used to predict the friction factors in the laminar flow regime. Equations 2.20 and 2.22 were developed for isothermal flow conditions and will be used for the validation of the friction factors in Chapter 4. Equations 2.21 and 2.23 will not be used in this study, but were also included since they were developed by Ghajar and his co-workers.

2.5.2. Turbulent flow

Osborne Reynolds also investigated turbulent flow with his dye experiments and found that when the velocity of the fluid was high, the fluid motion was highly disordered. Random and rapid zigzag formations were observed, which indicated the velocity fluctuations inside the tube (White, 2006). Turbulent flow is dominated by forced convection since the fluid motion suppresses the secondary flow effects inside the tube. The heat transfer coefficients are also high in this flow regime due to the rapid mixing of the fluid particles inside the tube.

2.5.2.1. Heat transfer correlations

Table 2.3 contains some of the available correlations which can be used to calculate the Nusselt numbers in the turbulent flow regime. Some of these equations will also be used to validate the experimental set-up and data reduction method in Chapter 4. The heat transfer coefficients in the turbulent flow regime are insensitive to different types of boundary conditions and secondary flow effects are negligible. It is therefore not necessary to distinguish between forced and mixed convection, or between a constant heat flux and constant surface temperature boundary condition.

2.5.2.2. Pressure drop correlations

Table 2.4 contains the two correlations which will be used to validate the friction factors in the turbulent flow regime. The Blasius (1913) equation was developed for isothermal flow, while Allen and Eckert (1964) introduced the viscosity correction term to account for the effect of heating.

Table 2.1: Laminar Nusselt number correlations

Oliver (1962)

$$Nu = 1.75(Gz + 5.6x10^{-4}(GrPrL/D)^{0.7})^{1/3} \qquad (2.14)$$

$7 \le Gz \le 187$; $1.9 \le Pr \le 326$; $29 \le Gr \le 1.6\text{x}10^5$

Percentage deviation: ±20%

Shah and London (1978)

$$\frac{Nu + 1}{5.364[1 + (220\ z^*/\pi)^{-10/9}]^{3/10}} = \left[1 + \left(\frac{\pi/(115.2\, z^*)}{\{1 + (Pr/0.0207)^{2/3}\}^{1/2}\,\{1 + (220\ z^*/\pi)^{-10/9}\}^{3/5}}\right)^{5/3}\right]^{3/10} \qquad (2.15)$$

Percentage deviation: uncertain

Palen and Taborek (1985)

$$Nu = 2.5 + 4.55(Re^* D/L)^{0.37} Pr^{0.17} (\mu/\mu_w)^{0.14} \qquad (2.16)$$

$$Re^* = Re + 0.8 Gr^{0.5} exp(-42/Gr^2)$$

$0 \le L/D \le \infty$; $0.1 \le Re \le 2\,000$; $20 \le Pr \le 10^4$; $0 \le Gr \le 10^7$; $10^{-3} \le \mu/\mu_w \le 55$

Percentage deviation: ±30%

Ghajar and Tam (1991)

$$Nu = 1.44[(Re\ Pr\ D/x) + 0.0083(GrPr)^{0.75}]^{1/3}(\mu/\mu_w)^{0.14} \qquad (2.17)$$

$3.2 \le x/D \le 192.3$; $281 \le Re \le 2\,524$; $30 \le Pr \le 158$; $1\,031 \le Gr \le 5\text{x}10^4$

Percentage deviation: ±10%

Ghajar and Tam (1994)

$$Nu = 1.24[(Re\ Pr\ D/x) + 0.025(GrPr)^{0.75}]^{1/3}(\mu/\mu_w)^{0.14} \qquad (2.18)$$

$3 \le x/D \le 192$; $280 \le Re \le 3\,800$; $40 \le Pr \le 160$; $1\,000 \le Gr \le 2.8\text{x}10^4$; $1.2 \le \mu/\mu_w \le 3.8$

Percentage deviation: -16.9% to +15.4%

Gnielinski (2010)

$$Nu = (Nu_1^3 + 0.6^3 + (Nu_2 - 0.6)^3 + Nu_3^3)^{1/3} \qquad (2.19)$$

$$Nu_1 = 4.354$$

$$Nu_2 = 1.953\sqrt[3]{Re\ Pr\ D/L}$$

$$Nu_3 = 0.924\sqrt[3]{Pr}\ \sqrt{Re\ D/L}$$

Percentage deviation: uncertain

Table 2.2: Laminar friction factor correlations

Classical relation by Poiseuille (1840)

$$f = \frac{64}{Re} \tag{2.20}$$

$Re \leq 2\,100$

Tam and Ghajar (1997)

$$f = \frac{64}{Re}\left(\frac{\mu_b}{\mu_w}\right)^m \tag{2.21}$$

$m = 1.65 - 0.013\, Pr^{0.84} Gr^{0.17}$

$1\,100 \leq Re \leq 7\,400$; $17\,100 \leq Gr \leq 95\,600$; $1.25 \leq \mu_b/\mu_w \leq 2.4$; $6 \leq Pr \leq 36$

Percentage deviation: -12.6% to +12.1%

Tam *et al.* (2013)

$$f_{app} = \frac{4}{Re}\left(16 + \frac{0.00314}{0.00004836 + 0.0609\left(\frac{x/D}{Re}\right)^{1.28}}\right) \tag{2.22}$$

$799 \leq Re \leq 2\,240$; $3 \leq x/D \leq 200$

Percentage deviation: -26.1% to +28.1%

Tam *et al.* (2013)

$$f_{app} = \frac{4}{Re}\left(16 + \frac{0.00314}{0.00004836 + 0.0609\left(\frac{x/D}{Re}\right)^{1.28}}\right)\left(\frac{\mu_b}{\mu_w}\right)^m \tag{2.23}$$

$m = -5.06 + 0.84\, Pr^{0.23} Gr^{0.09}$

$897 \leq Re \leq 2\,189$; $7\,141 \leq Gr \leq 18\,224$; $1.27 \leq \mu_b/\mu_w \leq 1.56$; $39 \leq Pr \leq 47$

Percentage deviation: -29% to +25.2%

Table 2.3: Turbulent Nusselt number correlations

Second Pethukhov equation (Cengel, 2006)

$$Nu = \frac{(f/8) Re\, Pr}{1.07 + 12.7 (f/8)^{0.5} (Pr^{2/3} - 1)} \tag{2.24}$$

$$\xi = (0.79\, ln\, Re - 1.64)^{-2}$$

$10^4 \leq Re \leq 5\text{x}10^6$; $0.5 \leq Pr \leq 2\,000$

Percentage deviation: uncertain

Gnielinski (1976)

$$Nu = \frac{(\xi/8)(Re - 1000) Pr}{1 + 12.7\sqrt{(\xi/8)}(Pr^{2/3} - 1)}\left[1 + \left(\frac{D}{L}\right)^{2/3}\right]\left(\frac{Pr}{Pr_w}\right)^{0.11} \tag{2.25}$$

$\xi = (1.8 \log_{10} Re - 1.5)^{-2}$ (Filonenko, 1954)

$3\text{x}10^3 \leq Re \leq 5\text{x}10^6$; $0.5 \leq Pr \leq 2\,000$

Percentage deviation: uncertain

Ghajar and Tam (1991)

$$Nu = 0.023\, Re^{0.8}\, Pr^{0.385}\, (\mu/\mu_w)^{0.14} \tag{2.26}$$

$x/D \geq 12.8$; $8\,475 \leq Re \leq 48\,337$; $4.4 \leq Pr \leq 29$

Percentage deviation: ±5%

Ghajar and Tam (1994)

$$Nu = 0.023\, Re^{0.8}\, Pr^{0.385}\, (x/D)^{-0.0054} (\mu/\mu_w)^{0.14} \tag{2.27}$$

$3 \leq x/D \leq 192$; $7\,000 \leq Re \leq 49\,000$; $4 \leq Pr \leq 34$; $1.1 \leq \mu/\mu_w \leq 1.7$

Percentage deviation: -10.3% to +10.5%

Table 2.4: Turbulent friction factor correlations

Blasius (1913)	$f = 0.316Re^{-0.25}$ 3 000 ≤ Re ≤ 100 000 Percentage deviation: uncertain	(2.28)
Allen and Eckert (1964)	$f = 0.316Re^{-0.25}\left(\frac{\mu_b}{\mu_w}\right)^{-0.25}$ Percentage deviation: uncertain	(2.29)

2.5.3. Transitional flow

The transition between laminar and turbulent flow does not occur instantaneously, but over a Reynolds number region. In this region, the flow alternates between laminar and turbulent while it is fully laminar at the start of the transition region and fully turbulent at the end. Random velocity and pressure fluctuations also occur throughout this region (Meyer, 2014). The state of the art on transition heat transfer at present is that the transition region can be divided into two regions, namely the transition region and the low-Reynolds-number-end region. In the low-Reynolds-number-end region, the flow approaches turbulent flow, but is not fully turbulent yet. Figure 2.1 summarises the different flow regimes in terms of the Nusselt numbers. The low-Reynolds-number-end regime (between Re_{lre} and Re_t in Figure 2.1) is where the extension of the straight line (on a log-log scale) of the turbulent Nusselt number as a function of Reynolds number overpredicts the actual Nusselt numbers.

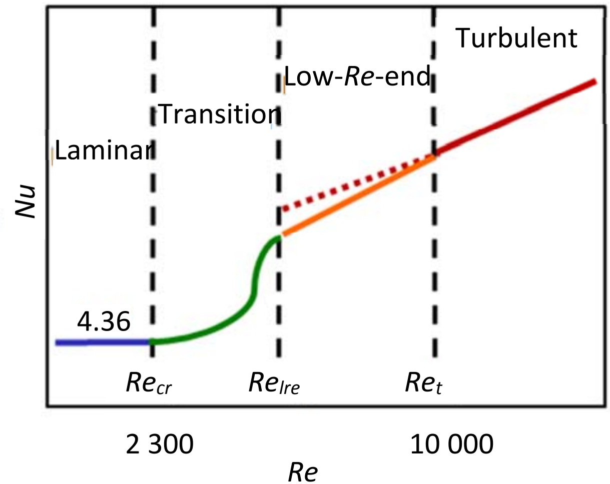

Figure 2.1: The four different flow regimes in terms of the Nusselt number against Reynolds number

Extensive research has been done in the laminar and turbulent flow regimes and several correlations exist to calculate the heat transfer coefficients and friction factors in these two regimes. However, the transitional and low-Reynolds-number-end regimes have not yet been properly understood and the available correlations to predict the heat transfer coefficients and friction factors are still very limited (Meyer, 2014). Correlations for heat transfer and pressure drop in the transitional flow regime include the low-Reynolds-number-end region as well, since no clear distinction was made between these two regimes. The available heat transfer and pressure drop correlations in the transitional flow regime (including the low-Reynolds-number-end regime) are revised in this sub-section as well as the factors that influence transition. Although separate correlations are available for a square-edged, re-entrant and bellmouth inlet, only the square-edged inlet correlations are presented since this type of inlet geometry was used in this study.

2.5.3.1. Heat transfer correlations

Table 2.5 contains equations which can be used to predict Nusselt numbers and thus heat transfer in the transitional flow regime. However, these equations cannot be used for validation purposes as they were developed for fully developed flow while this study focuses on developing flow.

Table 2.5: Transitional Nusselt number correlations for a square-edged inlet

Ghajar and Tam (1991)

$$Nu = Nu_l + \{[exp((a - Re)/b)/Nu_l^c] + Nu_t^d\}^e \tag{2.30}$$

$$Nu_l = 14.5$$

$$Nu_t = 1.44[(Re\ Pr\ D/x) + 0.0083(GrPr)^{0.75}]^{1/3}(\mu/\mu_w)^{0.14}$$

a = 3 129; b = 277.85; c = 1.0442; d = -0.9594; e = -0.9577

1 718 ≤ Re ≤ 11 350; 4.7 ≤ Pr ≤ 52

Percentage deviation: ±20%

Ghajar and Tam (1994)

$$Nu = Nu_l + \{exp((a - Re)/b) + Nu_t^c\}^c \tag{2.31}$$

$$Nu = 1.24[(Re\ Pr\ D/x) + 0.025(GrPr)^{0.75}]^{1/3}(\mu/\mu_w)^{0.14}$$

$$Nu = 0.023\ Re^{0.8}\ Pr^{0.385}\ (\ x/D)^{-0.0054}(\mu/\mu_w)^{0.14}$$

a = 2 617; b = 207; c = -0.95

3 ≤ x/D ≤ 192; 1 600 ≤ Re ≤ 10 700; 5 ≤ Pr ≤ 55

Percentage deviation: -23.9% to +24.3%

Table 2.6: Transitional friction factor correlations for a square-edged inlet

Ghajar and Madon (1992) (2.32)

$$c_f = -2.56x10^{-2} + 2.49x10^{-5}Re - 4.25x10^{-9}Re^2$$

2 055 ≤ Re ≤ 3 140

Percentage deviation: ±1.9%

Tam and Ghajar (1997) (2.33)

$$c_f = \left[1 + \left(\frac{Re}{a}\right)^b\right]^c \left(\frac{\mu_b}{\mu_w}\right)^m$$

a = 4 230; b = -0.16; c = -6.57; m = -1.13 – 0.396 $Pr^{5.1}Gr^{-0.16}$

3 500 ≤ Re ≤ 6 900; 6 800 ≤ Gr ≤ 104 500; 1.11 ≤ $\mu_b/\ \mu_w$ ≤ 1.89; 12 ≤ Pr ≤ 29

Percentage deviation: -11.8% to +20%

Tam *et al.* (2013) (2.34)

$$c_f = \left(\frac{16}{Re}\right)\{[1 + (0.0049Re^{0.75})^a]^{1/a} + b\}$$

a = 0.5; b = -4

2 111 ≤ Re ≤ 4 141; 3 ≤ x/D ≤ 200

Percentage deviation: -8.6% to +7.9%

Tam *et al.* (2013) (2.35)

$$f_{app} = c_f\left[1 + \left(\frac{c}{x/D}\right)\right]$$

c = 3

2 109 ≤ Re ≤ 4 148; 3 ≤ x/D ≤ 200

Percentage deviation: -25.9% to +21.9%

Tam *et al.* (2013) (2.36)

$$f_{app} = f_{app}\left(\frac{\mu_b}{\mu_w}\right)^m$$

m = -1.13 +0.48 $Pr^{0.55}Gr^{-0.15}$

2 084 ≤ Re ≤ 3 980; 6 169 ≤ Gr ≤ 35 892; 1.1 ≤ $\mu_b/\ \mu_w$ ≤ 1.54; 19.6 ≤ Pr ≤ 47.3

Percentage deviation: -28% to +27.6%

2.5.3.2. Pressure drop correlations

Table 2.6 contains the available correlations which can be used to predict skin friction coefficients and thus friction factors and pressure drop in the transitional flow regime. The friction factors can be obtained by multiplying the skin friction coefficient by four. These equations were developed for fully developed flow and will therefore not be used for the validation, since the focus of this study is on developing flow.

2.5.3.3. Factors influencing transition

According to Meyer (2014), who revised all the literature on transition, transition is influenced by upstream turbulence levels, upstream fluctuations, upstream conditions and inlet geometries. The only effect that has been researched so far is the effect of inlet geometries, which is discussed in detail in Sections 2.6 and 2.7.

2.6. Inlet geometries

The local heat transfer coefficient and thus the transition from laminar to turbulent flow along the tube length are affected, among others, by the type of inlet geometry (as summarised in Section 2.5.3.3). There are typically four different inlet geometries that were used in previous work and these are shown schematically in Figure 2.2. The figure shows that there are in general two categories of inlet geometries. In the first type (Figures 2.2(a) and (b)), an abrupt geometry change occurs between the inlet distributor and the tube inlet and therefore additional disturbance is generated as the flow enters the tube. In the second category, the diameter changes gradually (Figures 2.2(c) and (d)) from the inlet distributor to the tube inlet and no additional turbulence is created at the tube inlet.

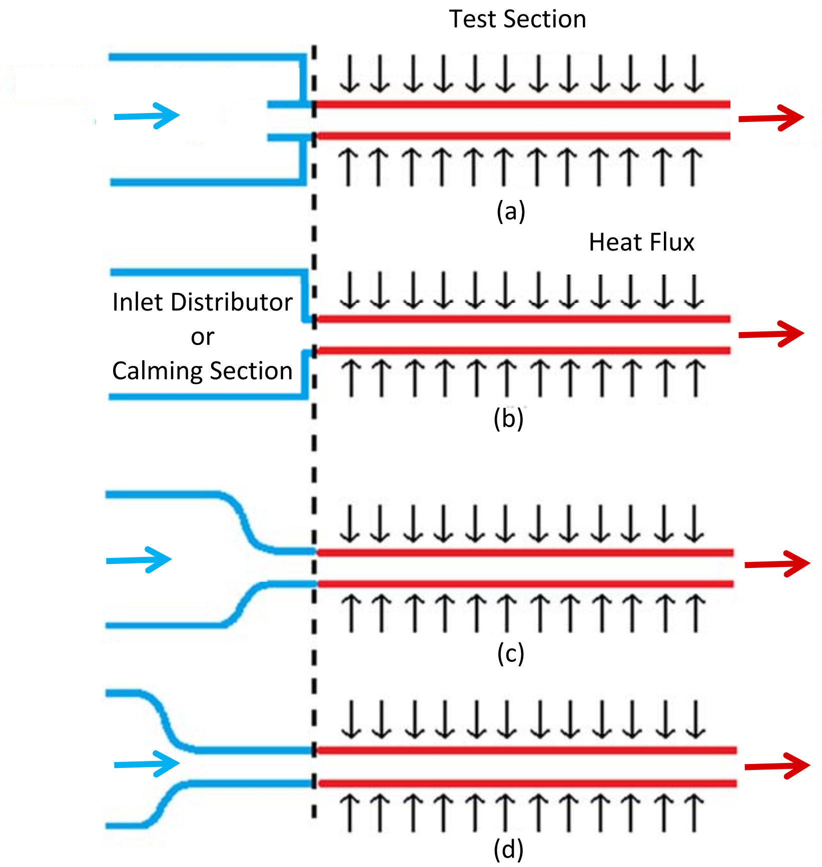

Figure 2.2: Schematic representation of the different inlet geometries: (a) re-entrant, (b) square-edged, (c) bellmouth and (d) hydrodynamically fully developed. Heating occurs in the red part and blue indicates the unheated part.

In previous work, the different inlet geometries were connected to a calming section that represents different types of inlet distributors. The first three inlet geometries were investigated by Ghajar and his co-workers (Ghajar and Tam, 1991, 1994, 1995; Ghajar and Madon, 1992; Ghajar *et al.*, 2010; Tam and Ghajar, 1997, 1998; Tam *et al.*, 2009, 2010, 2012, 2013) and the fourth by Meyer and Olivier (Olivier and Meyer, 2010; Meyer and Olivier, 2011a, 2011b):

- Re-entrant (Figure 2.2(a))
  This entrant contains a square-edged inlet with the tube installed one diameter into the head of the inlet distributor. No other studies were conducted with the inlet more than one or less than one diameter into the head of the inlet distributor.
- Square-edged (Figure 2.2(b))
  This type of inlet is characterised by a sudden contraction of flow and simulates the header of a shell-and-tube heat exchanger.
- Bellmouth (Figure 2.2(c))
  This inlet contains a smooth and gradual contraction and is used in some heat exchangers to avoid eddies that cause erosion near the tube inlet.
- Hydrodynamically fully developed (Figure 2.2(d))
  The diameter of this inlet section is the same as that of the test section. This inlet is used to obtain a fully developed velocity profile, since the velocity profile of the other three inlet geometries is developing.

2.7. Work of Ghajar and co-workers

Professor Afshin Ghajar from Oklahoma State University and his co-workers did extensive research on the effect of different inlet geometries on flow in the transitional flow regime. They also investigated the boundary between forced and mixed convection and developed a flow regime map for a constant heat flux boundary condition.

2.7.1. Diabatic investigation: Heat transfer coefficients

Ghajar and Tam (1991, 1994) investigated laminar, transitional and turbulent fully developed flow using different inlet geometries. When the heat transfer results were plotted in terms of the Colburn *j*-factor, the laminar heat transfer results had an almost parallel shift above the line for laminar forced convection results. This was due to the strong buoyancy forces, which led to mixed convection. A Nusselt number of approximately 14.5 was obtained instead of the theoretical fully developed laminar forced convection Nusselt number of 4.36. The authors also concluded that transition depended on the inlet geometry and occurred first for the inlet with the greatest disturbance.

An interesting observation was that although the authors investigated fully developed flow only, the transition region, in terms of Nusselt number, still varied when different locations on the tube were considered. The lower bound of the transition region (Re_{cr} in Figure 2.1) increased with 3.4% with increasing x/D, while the upper bound (Re_t in Figure 2.1) increased as much as 11%. This increase was due to the variation of the physical properties. The wall and bulk temperatures increased along the length of the tube, thus the kinematic viscosity decreased. This, in turn, led to increased Reynolds numbers. The authors explained that the increase in the bulk fluid temperature was more at high Reynolds numbers, thus the upper bound of the transition region was more affected than the lower bound.

Tam and Ghajar (1998) investigated the effect of different inlet geometries on the local heat transfer coefficients and paid special attention to the bellmouth inlet since the behaviour of this inlet was unusual. Although extra turbulence was caused by the re-entrant and square-edged inlets as the fluid entered the test section, these inlets had no significant influence on the local heat transfer coefficients in the laminar and turbulent flow regimes. The heat transfer coefficients of the re-entrant and square-edged inlets decreased asymptotically along the tube length. This trend was also observed with the bellmouth inlet in the laminar flow regime, but not in the turbulent flow regime. In the turbulent flow regime, the local heat transfer coefficients experienced a sharp decline after the inlet before it started to behave similar to the other inlets. A possible reason for this unusual behaviour is the low turbulence levels created by the bellmouth inlet. The temperature and velocities at the inlet of the test section were uniform. Therefore, as the fluid entered the test section, the boundary layer was first laminar, then transitional and then turbulent. This change in boundary layer did not occur in the other two inlets since the extra turbulence caused by the inlet disturbances led to a turbulent boundary layer at the inlet of the test section.

The behaviour of the re-entrant and square-edged inlets was similar in the transitional flow regime. The local heat transfer coefficients reached a minimum at approximately $x/D = 25$ and then increased linearly along the tube length. The authors used Newton's law of cooling to explain the increasing heat transfer coefficient along the tube length (Tam and Ghajar, 1998). Once the fluid was fully developed, the surface temperature and fluid temperature increased linearly along the tube length. However, the rate of increase of the fluid temperature was larger than the rate of increase of the surface temperature and therefore the temperature difference between the surface and fluid decreased along the tube length. This decreasing temperature difference then led to the increasing heat transfer coefficient. The reason needs to be investigated as fully developed flow will imply that the temperature difference is constant (Section 2.4). It is also not clear why the rate of heat transfer to the surface and the rate of heat transfer to the fluid are not the same when the flow is fully developed, since a constant heat flux boundary condition was used.

Tam and Ghajar (1998) also found that the dip in the local heat transfer coefficients of the bell-mouth inlet was approximately 25 diameters in the turbulent flow regime, but up to 140 diameters in the transitional flow regime. Therefore, the length of the dip decreased as the Reynolds number increased. For the bellmouth inlet, the local Nusselt numbers in the transitional flow regime varied between 30 and 80. This dip had a significant influence on both the local and average heat transfer characteristics. The authors also investigated the effect of an inlet disturbance on the bellmouth inlet by adding three different mesh screens just before the inlet. It was concluded that the Reynolds number at which this unusual behaviour began, depended on the inlet disturbance. When the inlet turbulence level was high (coarsest screen), transition occurred at a Reynolds number of 3 470 and when the inlet turbulence level was decreased (finest screen), transition was delayed to 9 640.

2.7.2. Isothermal investigation: Friction factors

The effect of different inlet geometries on pressure drop for fully developed flow in the transitional flow regime was investigated in several studies (Ghajar and Madon, 1992; Tam and Ghajar, 1997; Tam *et al.*, 2013). The Reynolds number for the start of transition (Re_{cr} in Figure 2.1) was taken as the Reynolds number corresponding to the point where the first abrupt change in the friction factor occurred. The end of transition (Re_t in Figure 2.1 since the low-Reynolds-number-end region was treated as part of the transitional flow regime) was indicated by the point where the friction factor reached the fully developed turbulent friction factor line. Similar to the heat transfer coefficient results, transition was delayed for smoother inlet geometries. Therefore, it can be concluded that the Reynolds number range in which transition occurs can be manipulated by changing the inlet geometry.

Ghajar *et al.* (2010) investigated isothermal friction factors in the transitional flow regime using mini- and macro-tubes. Twelve different tube diameters ranging from 337 µm to 2 083 µm were investigated. The authors found that the friction factors in the transition region were not influenced by the tube diameter when the diameter was greater than 1 372 µm. However, once the diameter was decreased further, transition was not only affected by the diameter, but the surface roughness became significant relative to the diameter of the tube. The greater relative roughness inside the tube increased the friction factors (even in the laminar flow regime) and transition occurred earlier. Furthermore, as the tube diameter was decreased, the Reynolds number range for the transition region became narrower.

Tam *et al.* (2014) investigated the effect of tube diameter and surface roughness in mini-tubes. Seven stainless steel tubes with inner diameters between 2 000 µm and 508 µm were investigated and the surface roughness was varied between 1.94 µm and 5.3 µm. The authors found that when the diameter was decreased from 2 000 µm to 750 µm, the start of transition was delayed from a Reynolds number of 1 410 to 2 310. However, when the diameter was decreased further from 750 µm to 508 µm, the start of transition was delayed to a Reynolds number of 2 240, while the end of transition shifted from a Reynolds number of 3 410 to 3 160. Therefore, similar to the results obtained by Ghajar *et al.* (2010), the transition region became narrower as the diameter was decreased. However, Tam *et al.* (2014) found that surface roughness had no significant influence on the laminar and turbulent friction factors, as well as the transitional friction factors of tubes with a diameter greater than 838 µm. When the diameter was decreased below 750 µm, both Reynolds numbers corresponding to the start and end of transition decreased, thus transition occurred earlier.

Tam *et al.* (2013) investigated the effect of inlet geometries on the friction factors in the entrance as well as fully developed regions. The apparent friction factor refers to the friction factor in the entrance region of the tube and therefore includes the pressure drop due to the momentum flux during the development of the velocity profile, as well as shear stresses at the wall. Thus the apparent friction factor is greater than the skin friction coefficient in the entrance region, but equal to the skin friction coefficient in the fully developed region (Ghajar and Madon, 1992). Tam *et al.* (2013) found that a longer entrance length was required for the apparent friction factors of the re-entrant inlet to reach the fully developed friction factors than for the square-edged inlet. Therefore, the additional disturbance caused by the inlet geometry led to a longer entrance flow region.

2.7.3. Diabatic investigation: Friction factors

When heat is applied to a tube, the temperature of the fluid increases between the inlet and outlet, as well as between the surface and centre of the tube, thus the fluid properties vary in both radial and axial directions. The property ratio method can be used to account for the variable property effect (Tam and Ghajar, 1997). In this method, the properties are evaluated at the bulk fluid temperature. The variable property effect is accounted for by multiplying the ratio of one of the properties evaluated at the bulk to the same property evaluated at the surface. The variation of viscosity is responsible for most of the variable property effects in liquids. Therefore, the variable property friction factor can be obtained as follows (Tam and Ghajar, 1997):

$$c_f = c_{vp} = c_{cp}\left(\frac{\mu_b}{\mu_w}\right)^m \tag{2.35}$$

where c_{vp} refers to the variable property solution (diabatic investigation) and c_{cp} refers to the constant property solution (isothermal investigation) and the exponent m is a flow parameter. This viscosity correction term is commonly used in heat transfer and diabatic pressure drop correlations.

Heating has a significant influence on the friction factors in the laminar flow regime. This effect is less in the transitional flow regime and negligible in the turbulent flow regime. The strong influence in the laminar and transitional regions is due to the effect of secondary flow. Tam and Ghajar (1997) explain that the velocity profile changes when mixed convection occurs. The shear stress and density of the fluid is changed, which leads to a change in the friction factor. When the heat flux is increased, the density decreases and the shear stress due to the change in the velocity profile increase, which then leads to increased friction factors. In the transitional flow regime, the effect of heating was a more stable flow and delayed transition. Similar to the heat transfer coefficients and isothermal friction factors, transition occurred first for the re-entrant inlet and last for the bell-mouth inlet. Tam *et al.* (2013, 2014) found that the friction factors in the laminar and transitional regimes decreased when heating was applied. The authors explained that this decrease was due to the temperature increase of the fluid near the surface, which decreased the viscosity of the fluid.

2.7.4. Forced and mixed convection heat transfer boundary and flow regime map

When heat is applied to the surface of a tube, a temperature difference occurs in the fluid. The fluid near the surface has a higher temperature and lower density and circulates in an upward direction (against gravity), while the fluid near the centre line of the tube has a lower temperature and higher density and therefore circulates downwards. These counter-rotating vortices, also known as secondary flow, are superimposed on the stream-wise main flow and increase the forced convection heat transfer significantly (Tam *et al.*, 2009). Although these buoyancy effects are always present (even in forced convection flow), it is important to know when these effects can be neglected. Ghajar and Tam (1991) used the local heat transfer data to determine the boundary between forced and mixed convection. When the ratio of the local heat transfer coefficient at the top of the tube to the local heat transfer coefficient at the bottom of the tube (h_t/h_b) was close to unity, the flow was dominated by forced convection, while mixed convection dominated when this ratio was much less than unity (< 0.8).

It was found that at higher Reynolds numbers ($Re > 3\,000$), the flow was dominated by forced convection since the heat transfer coefficient ratio did not fall below 0.9. At lower Reynolds numbers, when the flow was dominated by mixed convection, the heat transfer coefficient was close to unity at the tube inlet, but decreased significantly with increasing *x/D*. After approximately 125 diameters, the heat transfer coefficient ratio stabilised at 0.3. It was therefore concluded that the secondary flow effects needed a considerable starting length to become dominant. Ghajar and Tam (1994) found that when the Reynolds number was greater than 2 500 for the re-entrant inlet, 3 000 for the square-edged inlet and 8 000 for the bellmouth inlet, the flow was dominated by forced convection since the heat transfer coefficient ratio did not fall below 0.9. The authors concluded that the buoyancy effects depended on the Reynolds number, Prandtl number, Grashof number, inlet geometry, boundary conditions as well as length-to-diameter ratio of the tube.

Tam and Ghajar (1997) found in their investigation that the ratio of the local heat transfer coefficients decreased with increasing heat flux in the laminar flow regime, as expected, because the effects of secondary flow increase with increasing heat flux. In the transition region, secondary flow effects were significant at lower Reynolds numbers. However, as the Reynolds number was increased, the heat transfer coefficient ratio increased and approached unity in the upper part. In the turbulent flow regime, the secondary flow effects were suppressed by the turbulent motion of the fluid and the flow was dominated by forced convection. Thus, there was no significant difference between the results of the different heat fluxes in the turbulent flow regime.

A flow regime map can be used to determine whether heat transfer in internal flow is in the mixed or forced convection regime for a given boundary condition and values of *Re*, *Pr*, *Gr* and *D/x*. Metais and Eckert (1964) developed two flow regime maps for a constant surface temperature boundary condition, one for vertical flow and another for horizontal flow. The boundary between forced and mixed convection was arbitrarily defined as the location where the difference between forced and mixed convection heat transfer did not exceed 10%. Ghajar and Tam (1991) plotted their results on the flow regime map of Metais and Eckert (1964). Although the turbulent forced convection data were predicted accurately, the laminar and transition data were not predicted correctly. This was due to the constant heat flux boundary condition which was used, while the flow regime map was developed for a constant surface temperature. In the laminar and transitional flow regimes, the boundary condition has a significant influence on the heat transfer characteristics of the flow, while turbulent flow is insensitive to different boundary conditions. Furthermore, the influence of the buoyancy effects is also stronger with a constant heat flux boundary condition than with a constant surface temperature boundary condition.

Ghajar and Tam (1995) developed a flow regime map for a constant heat flux boundary condition based on the ratio of the local peripheral heat transfer coefficients at the top and bottom of the tube. However, Tam *et al*. (2009) improved this flow regime map by making use of the multi-class support vector machines (SVM) method. Three flow regime maps (re-entrant, square-edged and bellmouth inlets) were developed and the five flow regimes (forced turbulent, forced transition, mixed transition, forced laminar and mixed laminar) were identified using the Rayleigh and Reynolds numbers. The SVM-based flow regime maps were able to classify 88% of the data points of Ghajar and Tam (1994) correctly and the overall accuracy of these flow regime maps was better than that of Ghajar and Tam (1995).

Tam *et al*. (2010) developed a unified SVM-based flow regime map, which can be used for the re-entrant, square-edged and bellmouth inlets. The overall accuracy of this flow regime map was also better than the three individual SVM-based flow regime maps. Figure 2.3 contains the unified flow regime map of Tam *et al*. (2010). The boundary between forced and mixed convection was independent of the inlet geometry, while separate upper and lower bounds of the transitional flow regime were included for the different inlet geometries. However, for clarity purposes, only the upper and lower transitional regime boundaries of the square-edged inlet are included in Figure 2.3 since this inlet geometry will be used in the present study.

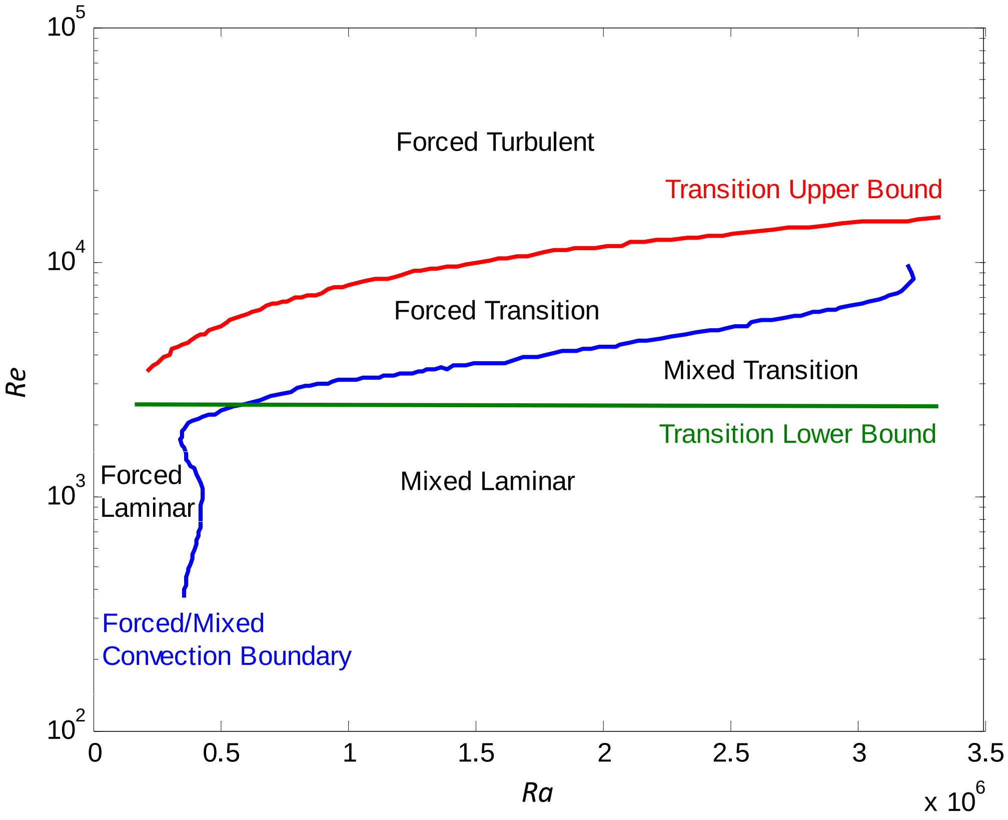

Figure 2.3: Unified SVM-based flow regime map for a constant heat flux boundary condition (Tam *et al.*, 2010)

2.7.5. Microfin tubes

Tam *et al.* (2012) investigated the influence of internal microfin tubes on heat transfer coefficients and friction factors. The isothermal results showed an upward parallel shift in the laminar friction factors to the classical laminar relation due to the increased roughness caused by the microfins. The transition region of the microfin tubes was also significantly wider than for smooth tubes. Furthermore, the friction factors in the transitional and turbulent flow regimes increased with increasing spiral angle. As the spiral angle was increased, the drag on the surface of the tube increased, which led to the increased friction factors. Furthermore, the transition region became narrower with increasing spiral angle. The start of transition was delayed, while the end of transition was advanced.

From the diabatic friction factor results, Tam *et al.* (2012) concluded that the start of transition was both inlet and spiral angle dependent, while the end of transition only depended on the spiral angle. Once again, heating delayed the start of transition, but had a negligible effect on the end of transition. The heat transfer coefficients in the upper part of the transition region, as well as the turbulent region, were significantly higher than for the smooth tube. These increased heat transfer coefficients were due to the swirling motion induced by the fins. As expected, the heat transfer coefficients increased with increasing spiral angle due to the enhanced mixing of the bulk fluid and the fluid near the surface, which led to increased heat transfer.

2.7.6. Simultaneous heat transfer and friction factor analysis

Tam *et al.* (2013) investigated heat transfer and friction factor data simultaneously by plotting the friction factors and heat transfer coefficients on a single graph. The laminar heat transfer and friction factor data had the same trend and decreased linearly with increasing Reynolds number.

The transition region started slightly earlier for the heat transfer coefficients (*Re* = 2 298) than for the diabatic friction factors (*Re* = 2 316). However, the transition region ended significantly earlier for the diabatic friction factors (*Re* = 3 941) than for heat transfer coefficients (*Re* = 8 357). Therefore, the authors concluded that heat transfer had a much wider transition region than pressure drop. In the turbulent region, both heat transfer coefficients and friction factors decreased linearly with increasing Reynolds number. The slope of the friction factors was, however, greater than the slope of the heat transfer coefficients.

2.8. Work of Meyer and co-workers

Professor Josua Meyer, from the University of Pretoria, and his PhD student, Olivier, also investigated flow in the transitional flow regime, but followed a different experimental approach from Ghajar. Meyer pointed out four main differences of their work compared with the work of Ghajar in a recent keynote paper (Meyer, 2014). Firstly, in their studies, the fluid was cooled, while Ghajar and his co-workers investigated heating. When a fluid is being cooled, the characteristics are different from when it is heated. For example, the viscosity near the surface is lower than the bulk, which leads to higher shear stress at the surface of the tube and therefore higher pressure drops (Olivier and Meyer, 2010). Secondly, Meyer and Olivier considered a constant surface temperature boundary condition while the work of Ghajar and co-workers was done with a constant heat flux boundary condition. The constant surface temperature boundary condition is of significant practical importance in applications where condensation and evaporation occur. Thirdly, an additional inlet geometry, the hydrodynamically fully developed inlet, was investigated. Fourthly, Ghajar and his co-workers focused mainly on local measurements, while Meyer and Olivier used the average measurements of developing flow over a finned tube length. Thus, their data contained both developing and fully developed flow. Another difference is that Ghajar used different ethylene glycol-water mixtures as the test fluid, while Meyer and Olivier used mainly water with a limited number of experiments with ethylene glycol-water mixtures. The Prandtl number of water remained fairly constant, unlike the high Prandtl number fluids such as ethylene glycol-water mixtures.

2.8.1. Smooth tubes

Olivier and Meyer (2010) investigated the influence of different inlet geometries on heat transfer and pressure drop in the transitional flow regime. Four inlet geometries (hydrodynamically fully developed, square-edged, re-entrant and bellmouth), as shown in Figure 2.2, were investigated. From the isothermal friction factor results, it was concluded that transition strongly depended on the inlet geometry. Similar to the results of the work done by Ghajar, transition occurred first for the inlet geometry which created the most turbulence. The laminar friction factors were slightly higher than the friction factors predicted by the Poiseuille (1840) equation. The authors explained that the higher friction factors were due to the growing hydrodynamic boundary layer along the surface of the tube from the inlet of the tube. The retardation of the fluid near the surface caused the fluid in the centre of the tube to accelerate, which led to an increase in shear and therefore higher friction factors.

Olivier and Meyer (2010) found that the diabatic friction factors were significantly higher than the isothermal friction factors. According to Meyer and Olivier (2014), there are two factors that lead to increased diabatic friction factors. The first factor is the viscosity difference between the fluid near the surface and the fluid near the centre line of the tube, which influences the shear stress at the surface. The second factor is the secondary flow, which is caused by the temperature (and thus density) difference between the fluid near the surface and the fluid near the centre line of the tube. Secondary flow distorts the velocity profile in such a way that the velocity gradient is steeper near the surface and therefore leads to higher friction factors. Olivier and Meyer (2010) also found that transition for the diabatic friction factors was independent of the inlet geometry. Furthermore, the transition region was narrower compared with the isothermal case.

Olivier and Meyer (2010) investigated the heat transfer coefficients in terms of the Colburn *j*-factor using water as well as a 50% v/v water-propylene glycol mixture. It was concluded that, similar to the friction coefficient results, transition was independent of the inlet geometry when water was used as the test fluid. Meyer and Olivier (2014) observed the same trend when the heat transfer coefficients were investigated in terms of the Nusselt numbers. According to Nagendra (1973), the inlet disturbances have no effect on transition when the product of the Reynolds number, Rayleigh number and diameter-to-length ratio is greater than approximately 10^6. Meyer and Olivier (2014) also found that the laminar heat transfer coefficients increased due to the secondary flow effects that enhanced mixing inside the tube.

2.8.2. Enhanced tubes

The efficiency of heat exchangers can be improved by increasing the heat transfer surface area. Due to the higher efficiency, the flow rates inside the tubes can be reduced to lower the pressure drop and pumping power. For this reason, more heat exchangers started to operate in or close to the transitional flow regime. Meyer and Olivier published two papers on transitional flow inside enhanced tubes with different inlet geometries (Meyer and Olivier, 2011a, 2011b). Four different types of enhanced tubes were investigated and the outer diameters varied between 15.9 mm and 19.1 mm. The tubes had either 25 or 35 fins, which corresponded to helix angles of 18° and 27°, respectively. The fin heights were 0.4 mm for the 15.9 mm tubes and 0.5 mm for the 19.1 mm tubes. Two smooth tubes with approximately the same diameters were used for comparison purposes.

In their first study, Meyer and Olivier (2011a) investigated the isothermal pressure drops. The authors concluded that the friction factors of enhanced tubes were higher than for smooth tubes in both laminar and turbulent flow regimes, with transition also occurring earlier. This was due to the increased roughness and increased resistance to flow, caused by the fins. A secondary transition occurred between Reynolds numbers of 3 000 and 10 000 where there was a smooth second increase in friction factors. This trend was not visible in the results of previous studies where different types of rough tubes were compared with each other.

Furthermore, the authors concluded that the fins were ineffective to rotate the fluid at low Reynolds numbers, but as the velocity increased, the fins became effective in rotating the fluid. An interesting conclusion made by the authors was that the only geometrical aspect of enhanced tubes that influenced transition was the fin height-to-diameter-ratio. Meyer and Olivier (2011a) also performed experiments using a hydrodynamically fully developed inlet. Similar to the smooth tube results, transition was delayed for smoother inlets, while the inlet geometry had no effect on the secondary transition. The end of transition was influenced by the helix angle and occurred earlier with increasing helix angle due to the extra turbulence that was created. There was no significant difference between the friction factors of the different inlet geometries in the laminar and turbulent flow regimes.

Meyer and Olivier (2011b) also investigated the effect of heating on friction factors. The diabatic friction factors of the enhanced tubes were higher than the isothermal friction factors of the smooth and enhanced tubes, especially in the laminar and transitional flow regimes. This increase was not only due to the secondary flow effects, but also due to the improved mixing caused by the fins. The authors also found that the friction factors increased with increasing helix angle and concluded that this was once again due to the improved mixing. However, the fins had a negative influence in the laminar flow regime since it acted as a barrier for secondary flow and prevented the bulk of the fluid to mix with the fluid near the surface of the tube. The tubes were cooled from the outside, thus the relatively unmixed fluid between the fins was at a lower temperature than that of the bulk of the fluid. This led to a higher viscosity and greater shear stress and thus increased friction factors. The main difference between the results of the isothermal and diabatic friction factors was that, similar to the smooth tube results, transition was independent of the inlet geometry and occurred at a Reynolds number of approximately 2 000 (Meyer, 2014).

Meyer and Olivier (2011b) also investigated the heat transfer coefficients in terms of the Colburn *j*-factor. The authors found that the heat transfer coefficients increased with increasing Reynolds numbers between 3 000 and 8 000. Shah and Seculic (2003) explain that this increase is due to the laminar viscous sublayer (which can account for up to 60% of the fluid's temperature drop in the turbulent flow regime) which is disrupted by the fins. Furthermore, it was noticed that heat transfer was higher in the tubes with a greater helix angle. Fins with a greater helix angle have the ability to spin the fluid more effectively, which leads to better mixing and increased heat transfer. However, from the laminar diabatic results, it was concluded that the fins had a negative influence on heat transfer, as the results of the enhanced tubes were slightly lower than those of the smooth tubes. Similar to the diabatic pressure drop results, transition was independent of the inlet geometry.

2.8.3. Nanofluids

With the continuous growth in communication, computing technologies and electronics, the size of equipment decreases while the thermal management load increases. The conventional approach to improving heat transfer is to increase the heat transfer area, but it is not possible in modern devices. The general approach is therefore modified to obtain greater cooling capacities and a decreased size of the thermal management system. By adding nanometre-sized solid particles, the thermal conductivity of the fluid can be approximately 5 000 times larger than that of water. The efficiency of a heat exchanger can thus be significantly improved by increasing the thermal conductivity of the fluid. Meyer *et al.* (2013) investigated the influence of multi-walled carbon nanotubes (MWCNT) on heat transfer and pressure drop characteristics in the transitional flow regime. Three different volume concentrations of MWCNT (0.33%, 0.75% and 1%) were investigated at a constant heat flux of 13 kW/m^2.

All three concentrations of nanofluids showed enhancement when the heat transfer results were presented as a function of Reynolds number, with transition occurring earlier as the nanofluid concentration increased. However, when the heat transfer results were presented as a function of average velocity, it was concluded that transition was delayed and the heat transfer coefficient decreased with increasing concentration. The increased Nusselt numbers were due to the high thermal conductivity of the base fluid (3 000 W/m.K) compared with water (0.61 W/m.K). The Reynolds number is a function of viscosity and since the viscosity of the nanofluids increased, the Reynolds numbers decreased. It was therefore difficult to make a simple comparison regarding the Reynolds numbers at which transition occurred.

From the diabatic friction factor results, it was concluded that the nanofluids did not have a significant influence in the turbulent flow regime, since the friction factors were similar to that of water. In the laminar flow regime, the friction factors decreased with increasing nanofluid concentration and transition occurred earlier. This was due to the viscosity of the fluid that changed when the nanoparticles were added. However, when the pressure drops and fluid velocities were compared, the authors found that the pressure drop increased when the nanofluids were added. Furthermore, transition occurred earlier with increasing concentration.

2.8.4. Micro-channels

In order to design thermally effective and energy-efficient cooling systems, it is important to understand the performance of micro-channels in the laminar, transitional and turbulent flow regimes. Dirker *et al.* (2014) investigated the effect of inlet flow conditions on heat transfer and pressure drop in small-scale rectangular channels. Three different hydraulic diameters (0.57, 0.85 and 1.05 mm) were investigated using a sudden contraction, bellmouth and swirl-inlet sections. All three inlet geometries had a significant influence on the transitional flow regime; however, for the swirl inlet, the laminar, transition and turbulent flow regimes were influenced. The Nusselt numbers and friction factors were also higher when the swirl inlet was used. The swirl effect, together with the altered flow pattern, led to better mixing and therefore increased heat transfer coefficients. As mentioned earlier in this chapter, the work done by Ghajar and co-workers, as well as by Meyer and Olivier, showed that transition was delayed for the bellmouth inlet. However, the results of this study were different since the authors found that transition occurred first for the bellmouth inlet and the transition region was wider as well. A possible reason for this might be the fact that the previous investigations considered circular macro-tubes, while rectangular mini-channels were used in this investigation. Therefore, a geometric size relationship between the critical Reynolds number and the channel diameter might exist. The authors also found that the friction factor transition was delayed when increasing heat fluxes were applied, with the friction factors decreasing in this case.

2.9. Summary and conclusions

This chapter revised a few fundamental concepts, the different flow regimes as well as developing and fully developed flow. A brief overview of previous work done on flow in the transitional flow regime was also given. Ghajar and co-workers focused on fully developed flow with a constant heat flux boundary condition using different ethylene glycol mixtures (high Prandtl numbers). On the other hand, Meyer and co-workers considered the average measurements over a tube length; thus the data included developing flow (laminar and transitional regimes) and fully developed flow (turbulent flow regime). Furthermore, Meyer and his co-workers used a constant surface temperature boundary condition and water as the test fluid (significantly lower Prandtl numbers).

Overall, transition was delayed not only for smoother inlet geometries, but also for increasing heat fluxes. Thus, the Reynolds number range in which transition occurs can be manipulated by changing the inlet geometry and heat flux. The transition region also varied when different locations on the tube were considered even though the flow was fully developed.

Isothermal friction factors in mini-tubes were also investigated and the transition region became narrower as the tube diameter was decreased. Although it was initially concluded that the earlier and narrower transition was due to the increased relative roughness of the tube, a later study showed that surface roughness had no significant influence on the transitional friction factors of tubes with an inner diameter greater than 838 µm. Once the inner diameter was decreased below 750 µm, transition occurred earlier as a result of the surface roughness of the tube.

The apparent friction factor was greater than the fully developed skin friction coefficient and it was found that the additional disturbance caused by the re-entrant and square-edged inlets led to a longer entrance flow region. When the average measurements across a tube length were used, the isothermal friction factors in the laminar flow regime were slightly higher than the friction factors predicted by the Poiseuille (1840) equation due to the growing hydrodynamic boundary layer along the surface of the tube from the inlet. The retardation of the fluid near the surface caused the fluid in the centre of the tube to accelerate, which led to an increase in shear and therefore increased friction factors. Heating increased the friction factors in the laminar and transitional flow regimes due to the effect of secondary flow. When the heat transfer and friction factor results were plotted on a single graph, it was concluded that heat transfer had a much wider transition region than pressure drop.

The influence of internal microfin tubes on heat transfer coefficients and friction factors was also investigated. The increased surface roughness and increased resistance to flow caused by the fins led to increased friction factors in the laminar and transitional flow regimes and transition occurred earlier. However, the fins had a negative influence on heat transfer in the laminar regime since it prevented the bulk of the fluid to mix with the fluid near the surface of the tube and thus acted as a barrier for secondary flow. As the spiral angle was increased, the drag on the surface of the tube increased, which led to increased friction factors. The heat transfer coefficients in the upper part of the transition region and turbulent region also increased with increasing spiral angle due to the improved mixing of the bulk fluid and the fluid near the surface. Furthermore, the start of transition was delayed while the end of transition occurred earlier. This caused the transition region to become narrower with increasing spiral angles.

Overall, it can be concluded that Ghajar and his co-workers focused on fully developed flow only while Meyer and Olivier investigated developing flow, although the average measurements across a tube length were used. The pressure drop of developing flow was investigated briefly using different mixtures of ethylene glycol and distilled water, which led to higher Prandtl numbers. The heat transfer and pressure drop characteristics of developing flow in the transitional flow regime of low Prandtl number fluids have not yet been investigated.

3. Experimental Set-up and Data Reduction

3.1. Introduction

The purpose of this chapter is to describe the experimental set-up that was used to conduct heat transfer and pressure drop experiments in a smooth horizontal tube at different heat fluxes as a function of different mass flow rates. It also gives an overview of the components of the experimental set-up, the test section, as well as the material, equipment and instrumentation used. The experimental procedure and data reduction method are also discussed and an overview of the results of an uncertainty analysis is given. In order to investigate the heat transfer and pressure drop characteristics of transitional flow in this study, new nomenclature to identify the boundaries of the different flow regimes as well as terminology to define the transition characteristics, are also presented.

3.2. Experimental set-up

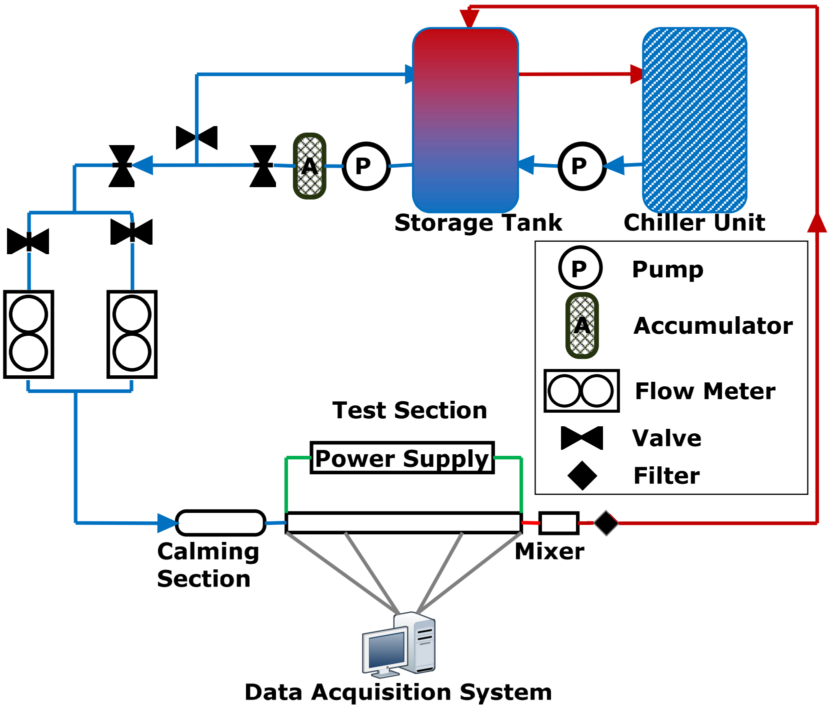

Figure 3.1: Schematic representation of experimental set-up used to conduct heat transfer and pressure drop measurements. Water was circulated from the storage tank through the test section and back using a pump. An accumulator was used to dampen the flow pulsations and the mass flow rate was measured using Coriolis flow meters. The temperatures, pressures and mass flow rates were recorded using a data acquisition system.

The basic layout of the experimental set-up is shown in Figure 3.1. The experimental set-up consisted of a closed-loop system, which circulated the test fluid from the storage tank, through the test section and back to the storage tank, using an electronically controlled positive displacement pump with a maximum flow rate of 2 000 ℓ/h. The test fluid was chosen as water and the capacity of the storage tank filled with water (which was circulated through the test section) was 1 000 ℓ which was maintained at approximately 20 °C, as it was externally connected to a chiller that cooled the heated water.

A 4 litre bladder accumulator was installed prior to the flow meters and the test section to dampen possible pulsations from the pump that might have an effect on transition. This ensured a constant pressure and mass flow rate at the inlet of the test section.

A bypass valve was inserted between the accumulator and the mass flow meters to allow the water to flow back to the tank. The bypass valve was also used to increase the backpressure on the pump, since the pulsations decreased with increasing pump speed. During experiments, the supply valve was partially closed and the bypass valve partially opened, so that the speed of the pump had to be as high as possible in order to supply the correct mass flow rate of water to the test section. The valve positions were continuously adjusted to minimise the flow pulsations for all the measurements. Figure 3.2 contains the mass flow rate measurements as a function of time with and without back pressure. Figure 3.2(a) contains the data in the laminar flow regime at a Reynolds number of 2 000. The blue data were taken at 150 rpm and 0 kPa (gauge) back pressure, while the red data were taken at 411 rpm with 120 kPa (gauge) back pressure. From this graph, it follows that the flow pulsations decreased significantly with increasing pump speed and back pressure and the standard deviation of the mass flow rate decreased with 61.6% from 2.41x10^{-5} kg/s to 9.25x10^{-6} kg/s.

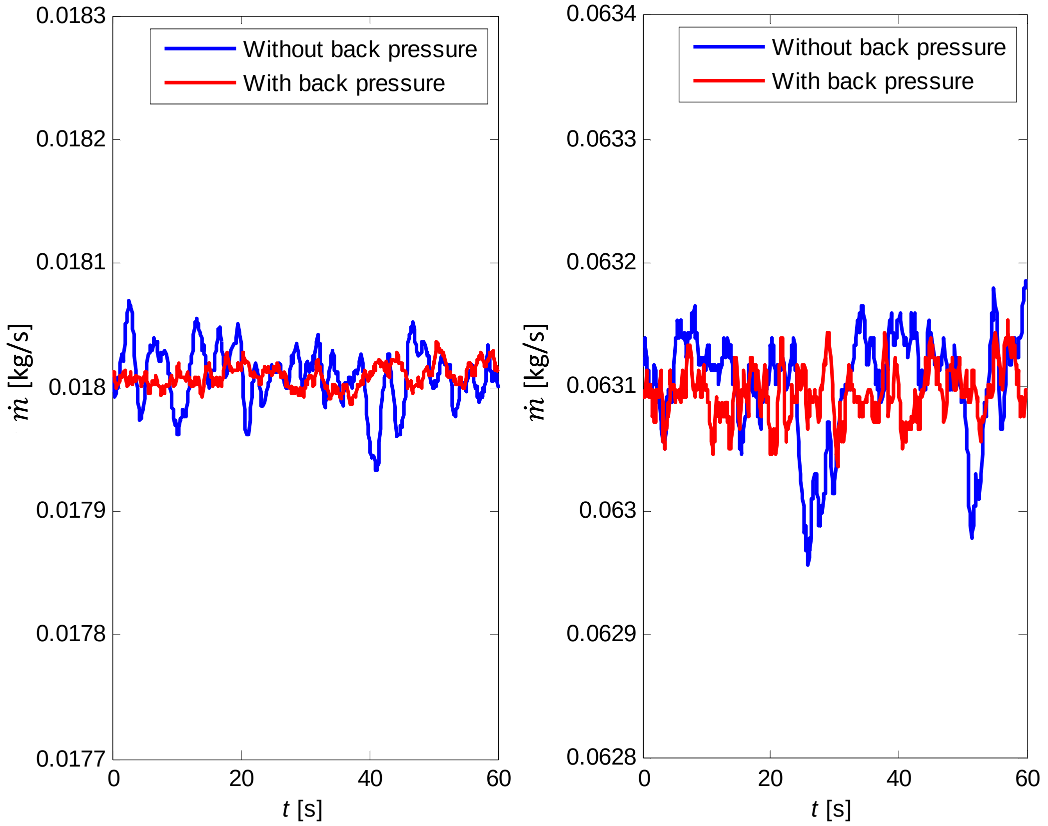

(a) (b)

Figure 3.2: Comparison of mass flow rate as a function of time with and without back pressure at a Reynolds number of (a) 2 000 (laminar flow) and (b) 7 000 (turbulent flow). The mass flow rate measurements were taken at a frequency of 10 Hz.

Figure 3.2(b) contains the data in the turbulent flow regime at a Reynolds number of 7 000. The blue data were taken at 219 rpm and 0 kPa (gauge) back pressure while the red data were taken at

593 rpm and 200 kPa (gauge) back pressure. Although there is a difference between the data with and without back pressure, the standard deviation of the mass flow rate only decreased with 51.6% from 4.44x10^{-5} kg/s to 2.15x10^{-5} kg/s, thus this difference was significantly smaller than the laminar flow case in Figure 3.2(a). The flow pulsations that occurred in the turbulent flow regime were probably not due to the pump, but rather due to the inherent velocity fluctuations of turbulent flow.

As the mass flow rates varied over a wide range, two Coriolis mass flow meters with different capacities were installed in parallel. The mass flow meter with the appropriate range was selected during the experiments. All measurements that were conducted were within the prescribed ranges of the mass flow meters. The mass flow rates were controlled by frequency drives that were connected to the pump and therefore the required mass flow rate was obtained by increasing or decreasing the pump speed. After the mass flow meters, the fluid flowed through the calming section to the test section and back into the storage tank.

3.3. Calming section

A calming section (Figure 3.3), similar to the one used by Ghajar (Ghajar and Tam, 1991, 1994, 1995; Ghajar and Madon, 1992; Ghajar *et al.*, 2010; Tam and Ghajar, 1997, 1998; Tam *et al.*, 2009, 2010, 2012, 2013) and Meyer (Olivier and Meyer, 2010; Meyer and Olivier, 2011a, 2011b, 2014), was installed prior to the test section to straighten the flow, as well as to detect any air bubbles that might have entered the system. The calming section was made form clear acrylic plastic with an inner diameter and length of 90 mm and 500 mm, respectively. A wire mesh with an open-area ratio (OAR[1]) of 0.6 and wire diameter of 0.3 mm was installed 100 mm after the inlet of the calming section. Two honeycomb sections with an OAR of 0.93 and length of 50 mm were also used to straighten the flow. One honeycomb was located adjacent to the wire mesh and the other 150 mm prior to the outlet of the calming section.

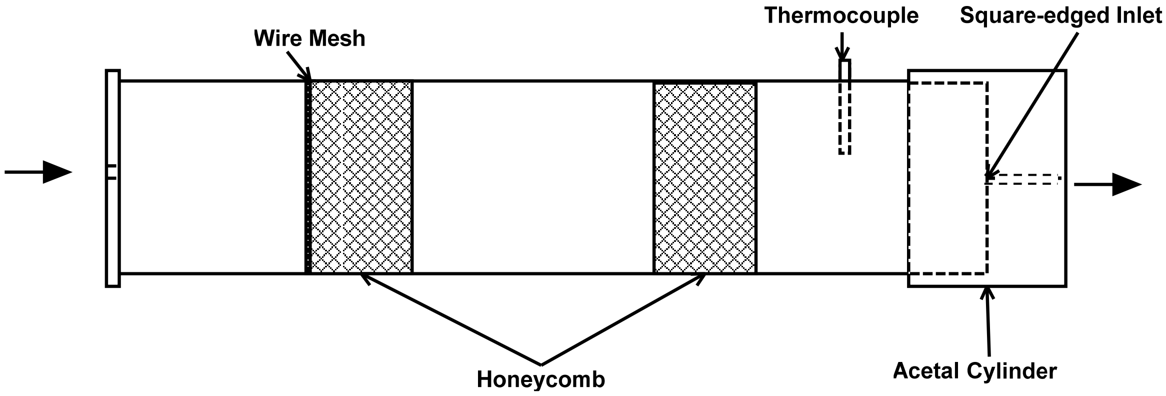

Figure 3.3: Schematic representation of calming section with a wire mesh, honeycomb sections and a thermocouple probe to measure the inlet water temperature. The calming section ends with a square-edged inlet, which is the inlet of the test section in Figure 3.4.

One thermocouple was placed inside the calming section to measure the inlet water temperature. The thermocouple was soldered inside a capillary tube to form a little thermocouple probe and the capillary tube was fixed to the calming section by means of a compression fitting. The purpose of the compression fitting was twofold: first, to house the thermocouple inside the calming section, and second, to bleed the air that might have entered the section. The calming section was properly insulated against heat loss using 50 mm thick insulation with a thermal conductivity of 0.034 W/m.K.

---

[1] The OAR is the ratio of the area occupied by the holes of the wire mesh to the total area of the wire mesh.

However, peeping holes and lids were incorporated into the insulation to be able to detect any air bubbles.

3.4. Test section

An acetal cylinder with a diameter and length of 120 mm and 100 mm, respectively, was used to connect the calming section (Figure 3.3) and test section (Figure 3.4) and to obtain a square-edged inlet. The thermal conductivity of acetal is 0.31 W/m.K, which is very low in comparison to the thermal conductivity of the test section, and thus the acetal cylinder was also used to prevent axial heat conduction from the test section to the calming section. To ensure a proper square-edged inlet, care was taken to ensure that the start of the test section was flush with the start of the acetal cylinder.

The test section was manufactured from a hard-drawn copper tube with a measured (with a split-ball unit and a vernier calliper) inside diameter of 11.52 mm, outside diameter of 12.7 mm and a length of 2.03 m. The tube roughness (ε) was measured using a hand-held roughness tester TR200 to be approximately 0.455 µm to 0.508 µm. The relative surface roughness (ε/D) was thus approximately 0.00004 and for all practical purposes, the tube was considered as being smooth. The test section was insulated with 150 mm thick insulation with a thermal conductivity of 0.034 W/m.K. The maximum heat loss was estimated with one-dimensional conduction heat transfer calculations to be less than 1% as a worst-case condition. Figure 3.4 is a schematic layout of the test section.

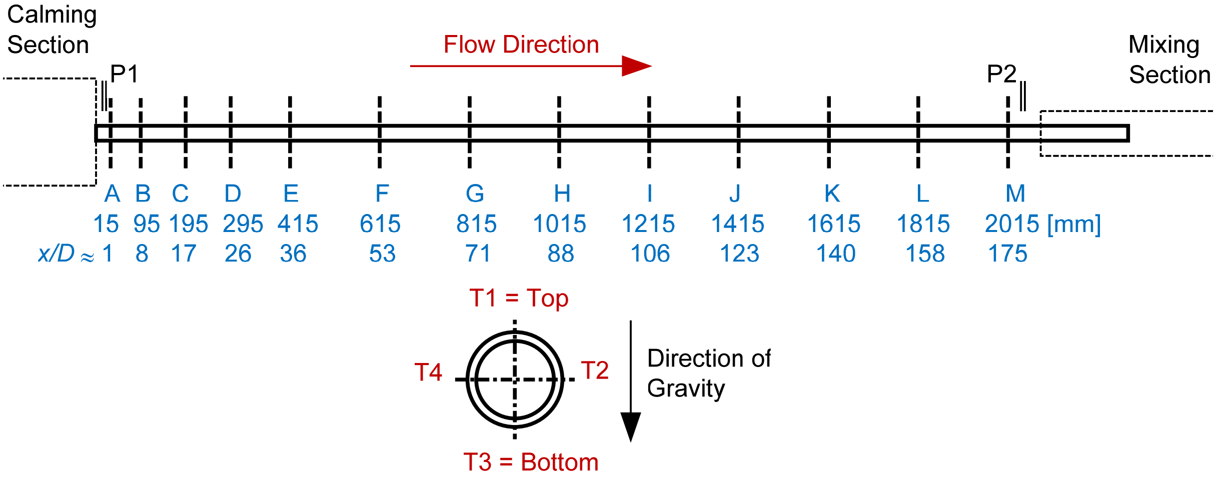

Figure 3.4: Schematic representation of the test section indicating the two pressure taps, P1 and P2, as well as the 13 thermocouple stations, A-M. A cross-sectional view of the test section is also included to indicate the four thermocouples spaced around the periphery of the tube.

T-type thermocouples with a wire diameter of 0.25 mm and accuracy of 0.1 °C were used to measure the surface temperatures at 13 selected axial locations, shown as A to M in Figure 3.4. The thermocouple stations were spaced closer to each other near the inlet of the test section to accurately obtain the temperatures of the developing flow, while the thermocouple stations in the remaining 1.6 m of the tube were spaced 200 mm apart. Four thermocouples were used at each thermocouple station to investigate possible circumferential temperature distributions caused by secondary flow along the tube length.

The thermocouples were attached to the tube by first drilling a 1.8 mm depression into the tube. Solder was inserted into the depression and heated up to the melting point. The thermocouple was then inserted into the depression and the heat was removed allowing the solder to cool down. The thermocouples were checked to ensure good contact with the tube. The thermocouples were calibrated by pumping water from the thermal bath through the calming section, test section mixing section, and back into the thermal bath. Reference temperatures were obtained using PT-100 probes at the inlet of the calming section, at the outlet of the mixing section and in the thermostat bath. The temperature of the thermostat bath was varied between 20 °C and 60 °C. The thermocouple calibration is discussed in Appendix A.

To obtain a constant heat flux boundary condition, two constantan wires (which have a high electrical resistance) with a diameter of 0.38 mm were coiled around the test section. Two heating wires were connected in parallel to obtain the desired resistance while limiting the current flowing through each wire.

When coiling the heating wire, it was important to consider how close the heating wire could be to the thermocouple junction before affecting the temperature measurements. The thermocouple can be supported by coiling the heating wire once or twice over the thermocouple wire, but it is important to ensure that the heating wire over the thermocouple wire does not affect the temperature measurements. A schematic representation of the heating wire coiled around the tube and the thermocouple wire is shown in Figure 3.5. Extra experiments were conducted to determine which coiling technique will give the best results. The details of these experiments are given in Appendix B. It was concluded that a gap of approximately 1 mm between the heating wire and the thermocouple junction was sufficient. Furthermore, when the heating wire was coiled twice over the thermocouple wire, the thermocouple was secured while the temperature measurements remained unaffected.

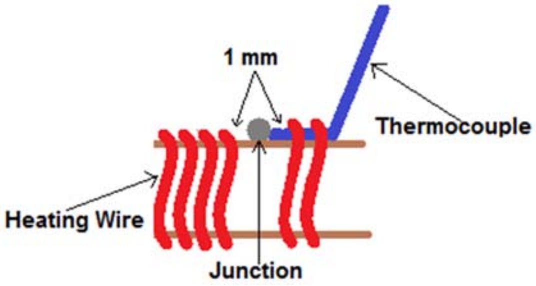

Figure 3.5: Schematic representation of the heating wire coiled at a thermocouple junction

Two pressure taps were fixed to the tube by silver soldering a 30 mm long capillary tube on each end of the test section. A 1 mm hole was then drilled through the capillary tube and the copper tube. This small diameter was chosen to ensure that the pressure taps did not cause flow obstructions in the test section and that the diameter was less than 10% of the test section's inner diameter (Rayle, 1959). Care was taken to remove all the burrs from the inside of the test section to prevent incorrect pressure drop measurements. A boroscope was pulled through the test section to visually inspect and ensure that all the burrs were properly removed. A bush tap with a quick release coupling was inserted over the capillary tubes. Nylon tubing was used to connect the pressure taps to the differential pressure transducer. The last pressure tap was placed 300 mm from the outlet of the test section to prevent any upstream flow effects, created by the mixer, from influencing the pressure measurements.

3.5. Mixing section

To ensure a uniform outlet temperature, a mixer was inserted after the test section to mix the water exiting the test section. The mixer design was based on work done by Bakker *et al.* (2000), who investigated laminar flow in static mixers with helical elements. The mixer consisted of a copper tube with the same diameter as the test section and five copper splitter plates. The length-to-diameter ratio of the splitter plates was 1.5; therefore each splitter plate had a length of 16.8 mm. The elements were positioned and soldered such that the leading edge of an element was perpendicular to the trailing edge of the next element. Every splitter plate repeatedly split the thermal boundary layers to ensure a uniform temperature gradient in the radial direction. Four thermocouples were placed after the splitter plates to measure the average outlet temperature of the fluid (mixer position indicated in Figure 3.1).

3.6. Instrumentation

3.6.1. Power supply

Two direct current (DC) power supplies were used in the experimental set-up. Both power supplies had a maximum power output of 3 kW, maximum voltage of 360 V and maximum current of 15 A. The accuracy of both voltage and current was 0.2% of the nominal value. The maximum supplied power and voltage from each power supply were 345 W and 260 V, respectively. The heat flux of the study was limited to 9.5 kW/m^2. This ensured that the outlet temperature of the test fluid did not exceed 60 °C, which was the upper limit of some of the tube fittings downstream of the test section.

In an effort to reduce the effect of electromagnetic interference (EMI) caused by the current regulation of the DC power supplies, the two heating wires were connected to different power supplies and arranged with opposing polarities. According to Lenz's law, the opposing directions of current flow should induce both positive and negative voltages, which will, in turn, largely cancel each other out (Ulaby *et al*., 2010).

3.6.2. Pressure transducers

Differential pressure transducers with interchangeable diaphragms were used to measure the pressure drop across the test section. In order to minimise the uncertainties of the pressure drop measurements, two different diaphragms were used. A small diaphragm with a full scale of 0.86 kPa was used for Reynolds number measurements between 500 and 1 700, while a larger diaphragm with a full scale of 5.5 kPa was used for Reynolds numbers greater than 1 700. The accuracy of both diaphragms was 0.25% of the full scale, therefore, the resolutions of the 0.86 kPa and 5.5 kPa diaphragms were 2.15 Pa and 13.75 Pa, respectively.

The 0.86 kPa diaphragm was calibrated using a Betz manometer with an accuracy of 2.5 Pa and the 5.5 kPa diaphragm was calibrated using a low pressure controlled air manometer with an accuracy of 10 Pa. The details of the pressure transducer calibration are also given in Appendix A.

3.6.3. Flow meters

Two Coriolis flow meters with different capacities were used to measure the mass flow rate. For low mass flow rates, the small flow meter with a maximum flow rate capacity of 108 ℓ/h was used, while the large flow meter with a maximum capacity of 2 180 ℓ/h was used for the high flow rates. The accuracy of both flow meters was 0.05% of the full scale; thus the resolutions of the small and large flow meter were 0.054 ℓ/h and 1.09 ℓ/h, respectively.

3.6.4. Control and data logging

The mass flow rate of the pump was controlled by frequency drives that were connected to the pump. The frequency drives were also connected to a personal computer via a data acquisition system. The data acquisition system was used to record the data from the thermocouples (temperatures), pressure transducers (pressure drops) and flow meters (mass flow rates). The data acquisition system consisted of a personal computer using National Instruments Labview software which was used to log the data. The data acquisition system also consisted of SCXI (Signal Conditioning eXtensions for Instrumentation) products which included terminal blocks, analogue-to-digital converters and multiplexers. A Mathworks MATLAB script was used for the data processing.

3.7. Data reduction

The Reynolds number in the test section was calculated as:

$$Re = \frac{\dot{m}D}{\mu A_c} \tag{3.1}$$

where $\dot{m}$ is the measured mass flow rate inside the tube, D is the inner-tube diameter, μ is the dynamic viscosity and A_c is the cross-sectional area of the test section.

The properties of water were determined using the thermophysical correlations for liquid water (Popiel and Wojtkowiak, 1998) at the bulk fluid temperature for the average properties and at the mean fluid temperature for the local properties. A constant heat flux boundary condition was applied to the test section and thus the average axial temperature of the water increased linearly. The bulk fluid temperature was the average of the inlet (obtained from the thermocouple inside the calming section) and outlet (obtained from the four thermocouples inside the mixing section) temperatures of the fluid:

$$T_b = \frac{T_i + T_o}{2} \tag{3.2}$$

The cross-sectional area of the test section was calculated as follows:

$$A_c = \frac{\pi}{4} D^2 \tag{3.3}$$

The electrical energy input remained constant, resulting in a constant heat flux. The total power input was obtained by measuring the current and voltage. Three different heat fluxes were applied to the test section by adjusting the voltage (V) across the heating wire, which was coiled around the tube. The heat flux was determined from the following equation:

$$\dot{q} = \frac{\dot{Q}_{electric}}{A_s} = \frac{VI}{\pi DL} \tag{3.4}$$

The average surface temperature of the test section was calculated using the trapezoidal rule:

$$T_w = \frac{1}{L}\int_0^L T_w(x)\, dx \tag{3.5}$$

The thermal resistance across the tube wall was calculated using the following equation:

$$R_{tube} = \frac{ln\left(\frac{D_o}{D}\right)}{2\pi Lk} \tag{3.6}$$

The thermal conductivity of copper is 401 W/m.K, which is high. The temperature difference across the tube wall can then be calculated using Equation 3.6, since the thermal resistance and heat input are known:

$$\Delta T = \dot{Q}R_{tube} \tag{3.7}$$

The thermal resistance was calculated to be 7.9x10^{-6} °C/W. Therefore, the temperature difference across the tube wall was approximately 0.005 °C when the maximum heat input of this study (688 W) was applied to the test section. The negligible temperature difference led to the assumption that the temperature on the inside surface of the test section was equal to the temperature measurement on the outside surface of the test section, since the temperatures in general could only be measured to an accuracy of 0.1 °C. Therefore, it was assumed that the average surface temperature, determined from Equation 3.5, was the average surface temperature on the inside of the tube.

The average heat transfer coefficient was then determined from the following equations, since the heat flux, surface temperature, and bulk fluid temperature were available:

$$h = \frac{\dot{q}}{(T_w - T_b)} \tag{3.8}$$

The local heat transfer coefficients were calculated using the following equation:

$$h(x) = \frac{\dot{q}}{(T_w(x) - T_m(x))} \tag{3.9}$$

The average of the four temperature measurements on the outer surface at a station was used as the inner-surface temperature at a specific thermocouple station, $T_w(x)$, where the local heat transfer coefficient was determined. Again this assumption is valid because of the very small temperature difference over the tube wall, as indicated in Equation 3.7. The mean fluid temperature, $T_m(x)$, was the average temperature of the water at a thermocouple station and was found by using the gradient of the line joining the inlet and outlet temperatures of the fluid:

$$T_m(x) = \left(\frac{T_o - T_i}{L}\right)x + T_i \tag{3.10}$$

Finally, the average and local Nusselt numbers were determined as follows:

$$Nu = \frac{hD}{k} \tag{3.11}$$

$$Nu(x) = \frac{h(x)D}{k} \tag{3.12}$$

where k is the thermal conductivity of the fluid obtained using the thermophysical equations of liquid water at the bulk fluid temperature for the average Nusselt number and at the mean fluid temperature for the local Nusselt number.

The heat transfer rate to the water ($\dot{Q}_w = \dot{m}C_p(T_o - T_i)$) was compared with the electrical power ($\dot{Q}_{electric} = VI$) of the power supply by using the following energy balance:

$$EB = \left|\frac{\dot{Q}_{electric}-\dot{Q}_w}{\dot{Q}_{electric}}\right| * 100 = \left|\frac{VI-\dot{m}C_p(T_o-T_i)}{VI}\right| * 100 \quad (3.13)$$

The energy balance at the maximum Reynolds number (*Re* = 10 000) was approximately 6% due to the small temperature differences between the inlet and outlet temperatures. However, an energy balance of less than 1.5% was obtained when the Reynolds number was reduced below 4 000. The average energy balance of all the experiments that were conducted was less than 2%.

The heat transfer results were also investigated in terms of the Colburn *j*-factor to account for the variation in the Prandtl number. The Prandtl number is a function of C_p, μ and k. It was found that during experiments, the viscosity changed significantly and the Prandtl number varied between 3 and 7, depending on the conditions and location on the test section. The Colburn *j*-factor is:

$$j = \frac{Nu}{RePr^{\frac{1}{3}}} \quad (3.14)$$

The friction factor was also determined from the mass flow and pressure drop measurements between the two pressure taps, which were positioned 2.03 m from each other. The fluid properties were determined at the bulk temperature.

$$f = \frac{2\,\Delta P\,D}{L_p\,\rho V^2} = \frac{\Delta P \rho D^5 \pi^2}{8\dot{m}^2 L_p} \quad (3.15)$$

In general in this study, the percentage error of a measurement or calculated value (*M*) was determined as follows:

$$\%error = \frac{|M_{measured}-M_{predicted}|}{M_{measured}} * 100 \quad (3.16)$$

The average percentage error was taken as the average of the absolute errors of the data points.

3.8. Experimental procedure

Steady-state conditions were reached approximately 30 minutes after the start. After the initial steady state was achieved, the mass flow rate was decreased in relatively large increments in the laminar and turbulent regions and in smaller increments in the regions where transition was expected. The time required to reach steady state depended on the mass flow rate inside the test section and the heat flux applied. In the turbulent flow regime, approximately 10 minutes was required for steady state. As the mass flow rate was decreased, the time required for steady state increased and at a Reynolds number of 500, up to 30 minutes was required. Although the mass flow rates in the transitional flow regime were greater than in the laminar flow regime, approximately 30 minutes was required to reach steady state due to the temperature fluctuations inside the tube. Steady-state conditions were obtained once there was no significant increase or decrease in temperatures, pressure drops and mass flow rates. Data were only captured once steady-state conditions were obtained.

According to Olivier and Meyer (2010) and Meyer (2014), the effects of hysteresis are negligible in the transitional flow regime; therefore, the experiments were only conducted for decreasing Reynolds numbers. The experiments started at a maximum flow rate (*Re* = 10 000) and ended at the minimum flow rate (*Re* = 500). The Reynolds number was decreased by reducing the mass flow rate using the frequency drives connected to the pump. The supply and bypass valves were adjusted after each flow rate increment to ensure that there was sufficient backpressure to reduce the flow pulsations. Three different heat fluxes were applied to the test section by adjusting the applied voltage of the power supply. After steady state had been reached, 200 measuring points (temperature, pressure and mass flow rate) were captured at a frequency of 10 Hz. The average of the 200 measuring points was then used to obtain a single data point, which was used in the calculations.

3.9. Uncertainties

The method suggested by Dunn (2010) was used to calculate the uncertainties of the parameters obtained in the data reduction. All uncertainties were calculated within the 95% confidence interval and the uncertainty analysis method is given in Appendix C. Table 3.1 summarises the instruments with their range, bias, precision and accuracy. The range and bias were obtained from the manufacturer's specifications while the precision was obtained by multiplying the standard deviation of 200 measuring points with Student's *t*-variable (Dunn, 2010). The accuracy was obtained from the bias and precision.

Table 3.1: Ranges and accuracies of measuring instruments

Instrument	Range	Accuracy
Thermocouple	< 150 °C	0.1 °C
Flow Meters		
CMF010	0 – 108 ℓ/h	0.054 ℓ/h
CMF025	0 – 2 180 ℓ/h	1.09 ℓ/h
Pressure Transducer		
0.86 kPa diaphragm	0 – 0.86 kPa	2.15 Pa
5.5 kPa diaphragm	0 – 5.5 kPa	13.75 Pa
Power Supply		
Voltage	0 – 360 V	0.2% of nominal value
Current	0 – 150 A	0.2% of nominal value

The uncertainties for the Reynolds numbers, friction factors, Nusselt numbers and Colburn *j*-factors of the different heat fluxes are summarised in Figure 3.6. The Reynolds number uncertainty remained approximately constant at 1% for all Reynolds numbers and heat fluxes. Two different flow meters were used during the experiments to minimise the uncertainty of the mass flow rate measurements. The small flow meter was used for flow rates less than 100 ℓ/h (Reynolds number of approximately 3 000), while the large flow meter was used for flow rates greater than 100 ℓ/h. The Reynolds number uncertainty is a function of the density, diameter, velocity and viscosity, which explains why there was no significant difference between the Reynolds number uncertainties below and above a Reynolds number of 3 000. The Reynolds number uncertainty remained approximately constant for all heat fluxes, thus it can be concluded that temperature difference had a negligible influence on the uncertainties of the fluid properties.

From Figure 3.6(a), it follows that the friction factor uncertainty was approximately 7% at a Reynolds number of 500. As the Reynolds number increased, the friction factor uncertainty decreased to 0.5% at a Reynolds number of 4 200. However, a sharp discontinuity occurred just after this Reynolds number and the friction factor uncertainty at a Reynolds number of 4 600 was 2%. This discontinuity occurred in the region where the two pressure transducers were switched to ensure small pressure drop uncertainties. The 0.86 kPa diaphragm was used for Reynolds numbers between 500 and 4 200, while the 5.5 kPa diaphragm was used for Reynolds numbers between 4 200 and 15 000. As the Reynolds number was increased further, the friction factor uncertainty decreased to 1%. The pressure drop, and therefore friction factor, increased with increasing Reynolds number, which led to the decreasing uncertainties. When comparing Figures 3.6(a) to (d), it also follows that the friction factor uncertainty increased with increasing heat flux. This was due to the pressure drop that slightly decreased with increasing heat flux since the density of the water decreased with increasing temperature. Furthermore, the oxygen solubility decreased with increasing temperature, which implied that more oxygen was released. Thus the compressibility of the test fluid was increased due to very small air bubbles inside the test fluid. Overall, it can be concluded that the friction factor uncertainties varied between 1% and 17% depending on the heat flux, mass flow rate, as well as the pressure transducer used. However, at Reynolds numbers greater than 2 000, the friction factor uncertainties were less than 2.2%.

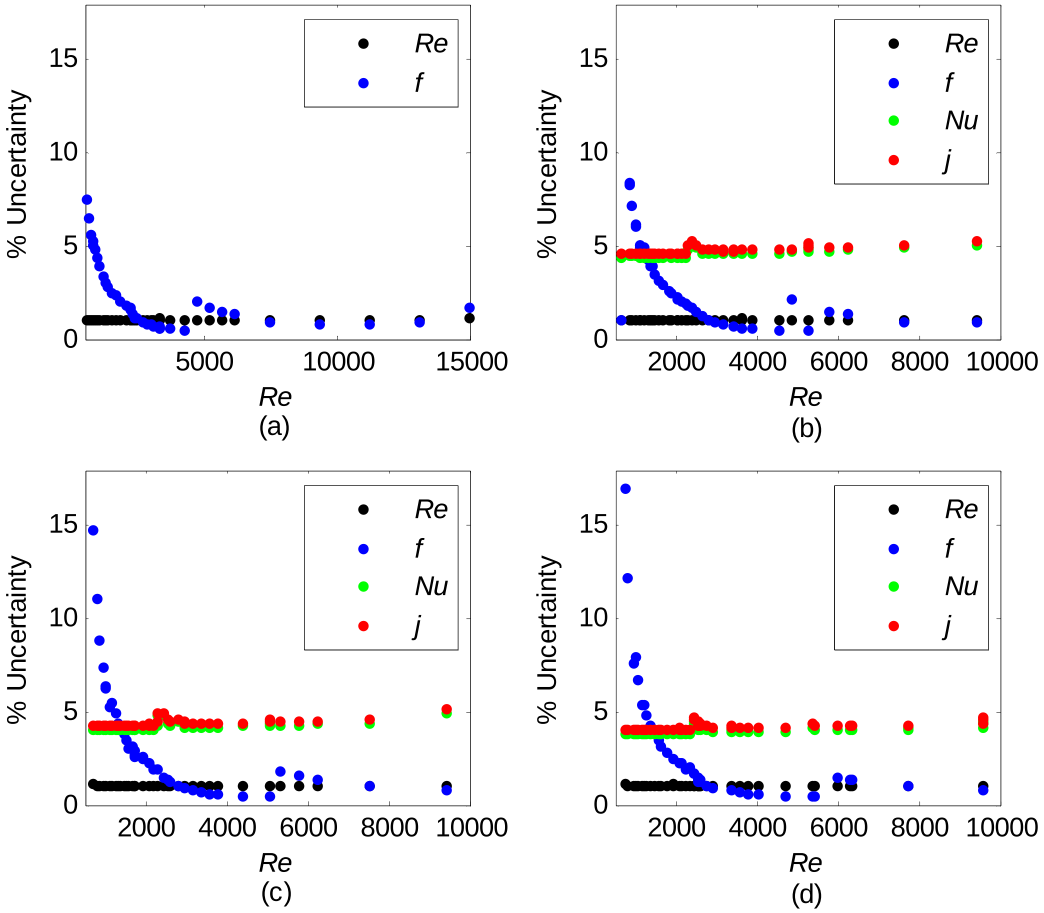

(a) (b) (c) (d)

Figure 3.6: Uncertainty for Reynolds numbers, friction factors, Nusselt numbers and Colburn *j*-factors as a function of Reynolds number for (a) isothermal, (b) heat flux of 6.5 kW/m², (c) heat flux of 8.0 kW/m² and (d) heat flux of 9.5 kW/m²

From Figure 3.6(b), it follows that the Nusselt number and Colburn *j*-factor uncertainties remained approximately constant at 4.6% between Reynolds numbers of 500 and 2 000 and increased gradually to 5% between Reynolds numbers of 3 000 and 10 000. The temperature differences between the inlet and outlet, as well as between the surface and fluid, decreased with increasing Reynolds number and thus the uncertainty increased. The Nusselt number uncertainty is a function of the heat transfer coefficient uncertainty, which is, in turn, a function of the temperature uncertainty. Therefore, the Nusselt number uncertainty increased with increasing temperature uncertainty. When comparing Figure 3.5(b) with (d), it follows that both Nusselt number and Colburn *j*-factor uncertainties decreased with increasing heat flux. The temperature differences increased with increasing heat flux and thus the temperature and Nusselt number uncertainties decreased.

The Nusselt number and Colburn *j*-factor uncertainties were also higher (approximately 5%) during transition ($Re \approx 2\,300$). During transition, the temperature fluctuations were much greater than during laminar and turbulent flow, as shown in Figure 3.7. The temperature uncertainty consists of two components, namely the bias and precision. The bias of each thermocouple was obtained from the calibration data and was approximately 0.1 °C. The precision consists of the standard deviation multiplied with Student's *t* variable (Dunn, 2010).

During transition, the temperatures across the test section fluctuated severely, which led to greater standard deviations and therefore greater precision errors and temperature uncertainties. Since both Nusselt number and Colburn *j*-factor uncertainties depended on the temperature uncertainty, these uncertainties increased as well. The standard deviation during transition was approximately 0.5 °C, while the standard deviation in laminar and turbulent flow was approximately 0.02 °C. The overall temperature uncertainty increased in the transition region due to the temperature fluctuations. These temperature fluctuations are discussed in more detail in Appendix D.

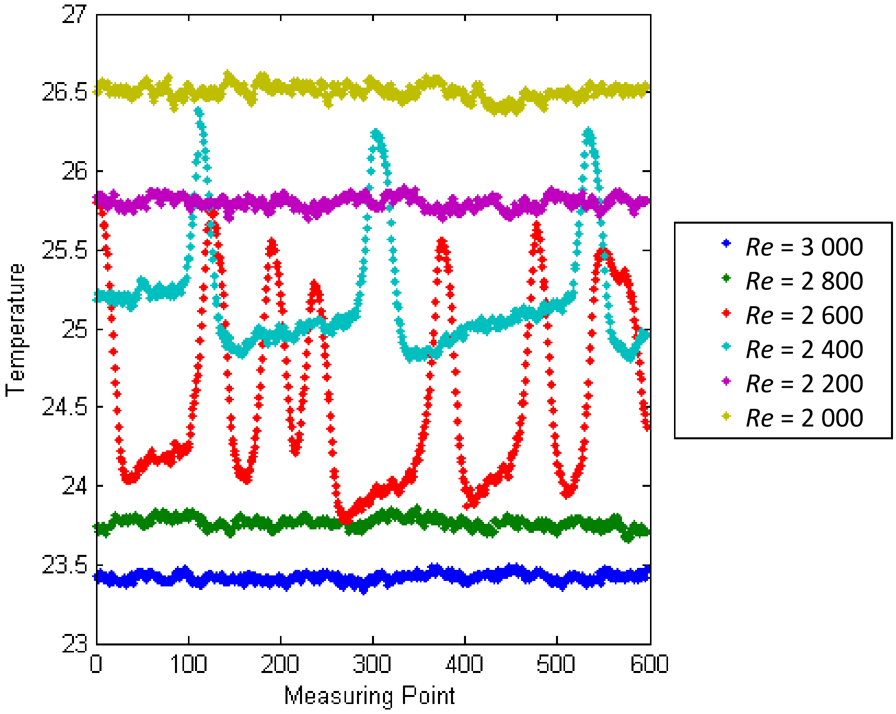

Figure 3.7: Temperature fluctuations measured in the mixing section at a frequency of 10 Hz for different Reynolds numbers and a heat flux of 8.0 kW/m^2

3.10. Flow regime nomenclature and terminology

Up to now, the boundary between the laminar and transitional flow regime as well as between the transitional and turbulent flow regime has not been clearly defined. Furthermore, in most of the cases, no distinction between the transitional and low-Reynolds-number-end regimes is made. In order to investigate the heat transfer and pressure drop characteristics of transitional flow, new nomenclature to identify the boundaries of the different flow regimes as well as terminology to define the transition characteristics, are presented in this section.

Figure 3.8 is a schematic representation of the different flow regimes in terms of the Nusselt numbers (Figure 3.8(a)), Colburn *j*-factors (Figure 3.8(b)) and fiction factors (Figure 3.8(c)), as a function of Reynolds number. The boundaries of the different flow regimes (Re_{cr}, Re_{lre} and Re_t) are also included. The laminar Nusselt numbers (Figure 3.8(a)) form a horizontal line and should be approximately 4.36 for fully developed forced convection laminar flow. The trend of the laminar Colburn *j*-factors (Figure 3.8(b)) and friction factors (Figure 3.8(c)) is similar since it decreases with increasing Reynolds number and forms a straight diagonal line. However, the gradient of the friction factors is greater than for the Colburn *j*-factors.

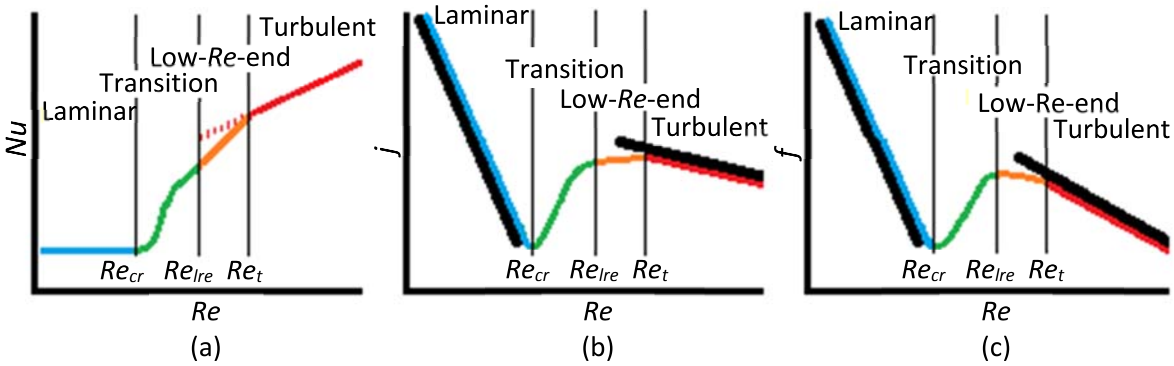

Figure 3.8: Schematic representation of the different flow regimes for forced convection in terms of (a) Nusselt number, (b) Colburn *j*-factor and (c) friction factor as a function of Reynolds number

The critical Reynolds number (Re_{cr}) defines the start of the transitional flow regime. When the heat transfer coefficients are investigated in terms of the Nusselt number, Re_{cr} is where the Nusselt numbers start to deviate (increase) from the horizontal line. When the heat transfer coefficients are investigated in terms of the Colburn *j*-factors (Figure 3.8(b)), transition starts at the point where the gradient is zero (before the Colburn *j*-factors start to increase). Similar to the Colburn *j*-factors, the start of transition when the pressure drop is investigated in terms of the friction factors (Figure 3.8(c)), is at the zero gradient (before the friction factors start to increase).

The end of transition cannot be easily defined using the Nusselt numbers (Figure 3.8(a)). However, it can be identified from the Colburn *j*-factor (Figure 3.8(b)) and friction factor (Figure 3.8(c)) graphs. The end of the transition region and thus the start of the low-Reynolds-number-end region (Re_{lre}), is at the point where the gradient of the Colburn *j*-factors and friction factors changes. As mentioned in Section 2.5.3, when the heat transfer coefficients are investigated in terms of the Nusselt numbers, the low-Reynolds-number-end region is where the extension of the straight line (on a log-log plot) of the turbulent Nusselt numbers, as a function of Reynolds number, overpredicts the actual Nusselt numbers. In the low-Reynolds-number-end region, the Colburn *j*-factors continue to increase with increasing Reynolds number, however, the gradient is less than in the transitional flow regime. The end of transition (Re_{lre}) can be easily identified from the friction factors since it occurs at the point where the gradient is zero. The friction factors in the low-Reynolds-number-end region decrease with increasing Reynolds number. Not much research has been devoted to the heat transfer and pressure drop characteristics of flow in the low-Reynolds-number-end region and this region is often regarded as part of the transitional flow region because the flow is not fully turbulent yet.

The end of the low-Reynolds-number-end region and thus the start of the turbulent flow regime (Re_t), is also better defined when the Colburn *j*-factors (Figure 3.8(b)) and friction factors (Figure 3.8(c)) are used. The flow is fully turbulent once the Colburn *j*-factors and friction factors are on or parallel to the Colburn *j*-factors and friction factors predicted using fully developed turbulent flow correlations. The Nusselt numbers (Figure 3.8(a)) in the turbulent flow regime increase with increasing Reynolds number, while the Colburn *j*-factors (Figure 3.8(b)) and friction factors (Figure 3.8(c)) decrease with increasing Reynolds number.

From Chapter 2, it was concluded that the transition region can be manipulated by changing the inlet geometry and heat flux and that the transition region varied when different locations on the tube were considered. In order to quantify the changes in the transition region, two gradients are defined and will be used in this study. Figure 3.9 is a schematic representation of the friction factors as a function of Reynolds number. The transition gradient (indicated by the purple TG line) represents a trend line through the straight diagonal friction factors in the transitional flow regime. The transition region gradient (indicated by the blue TRG line) represents the line between the start (Re_{cr}) and end (Re_{lre}) of the transition region. The transition region gradient seems to be smaller than the transition gradient and will not give a true representation of the transitional friction factors. However, it gives a good indication of the width of the transition region, while the transition gradient gives a good indication of the rate of change of the friction factors in the transitional flow regime.

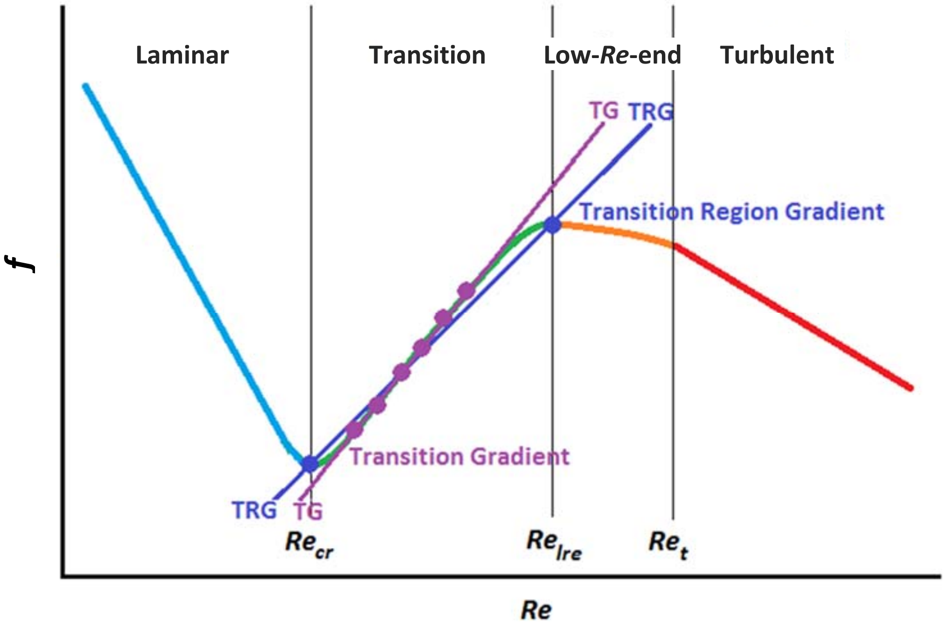

Figure 3.9: Schematic representation of the transition gradient and transition region gradient in terms of the friction factor as a function of Reynolds number

The laminar and turbulent flow regimes have been extensively investigated, while the transitional and low-Reynolds-number-end regimes have not yet been fully understood. For this reason, the results in this study will be discussed by starting with the laminar and turbulent flow regimes since these are well-known. The low-Reynolds-number-end region will be discussed next and the transitional flow regime will be discussed last because it is the main focus of this study.

3.11. Summary and conclusions

The experimental set-up, data reduction method and experimental procedure were described in this chapter. The test section consisted of a smooth circular tube with an inner diameter and length of 11.52 mm and 2.03 m, respectively, and a square-edged inlet. The Reynolds number was varied between 500 and 10 000 and water was used as the test fluid. A constant heat flux boundary condition was used and three different heat fluxes were applied to the test section. The test section was properly insulated and the maximum heat loss was estimated to be less than 1%. Thirteen thermocouple stations, each with four thermocouples, were spaced across the test section to measure the surface temperature. The inlet temperature of the fluid was obtained from a thermocouple inside the calming section, while the outlet temperature was obtained from the thermocouples in the mixing section. The pressure drop measurements were taken across the whole tube length; thus the measurements included developing (laminar and transitional flow regimes) and fully developed (turbulent flow regime) flow.

Adequate time after the start, as well as between increments, was allowed to ensure that steady-state conditions were always obtained. The measurements were only taken once the temperature variation was less than 0.1 °C and the mass flow rate and pressure drop were constant. Care was also taken during the experiments to ensure that there was always sufficient back pressure and a high enough pump speed to reduce the effect of flow pulsations.

An uncertainty analysis was conducted and the Reynolds number uncertainty remained approximately constant at 1% for all Reynolds numbers and heat fluxes. The Nusselt number and Colburn *j*-factor uncertainties were less than 5% for the entire Reynolds number range and increased slightly at Reynolds numbers greater than 3 000. The slight increase was due to the temperature differences between the inlet and outlet, as well as between the surface and fluid, which decreased with increasing Reynolds number. Both Nusselt number and Colburn *j*-factor uncertainties were higher (approximately 5%) during transition ($Re \approx 2\ 300$) due to the temperature fluctuations inside the tube. The friction factor uncertainties varied between 1% and 17% depending on the heat flux and mass flow rate. However, at Reynolds numbers greater than 2 000, the friction factor uncertainties were less than 2.2%.

Literature shows that the boundary between the laminar and transitional flow regime as well as between the transitional and turbulent flow regime has not been clearly defined yet. Therefore, new nomenclature to identify the boundaries of the different flow regimes as well as terminology to define the transition characteristics, were presented in order to investigate the heat transfer and pressure drop characteristics of transitional flow.

4. Validation

4.1. Introduction

This chapter validates the experimental set-up and data reduction method by comparing the heat transfer and pressure drop data with existing correlations as well as experimental data from previous studies. This validation ensures that the results presented in Chapters 5 and 6 can be used with confidence. For heat transfer, the local laminar Nusselt numbers are validated for forced convection conditions in Section 4.2 and for mixed convection conditions in Section 4.3. The average laminar Nusselt numbers are validated in Section 4.4 and the average turbulent Nusselt numbers are validated in Section 4.5. For pressure drop, Section 4.6 compares the isothermal friction factors with existing correlations as well as experimental data from previous studies.

4.2. Local laminar Nusselt numbers (forced convection)

For fully developed flow in a circular smooth tube with a constant heat flux boundary condition, the theoretical Nusselt number should be approximately 4.36 (Cengel, 2006). A flow regime map was used as a guideline to determine whether the flow conditions inside the test section of a specific experiment would be dominated by forced or mixed convection. The unified SVM-based flow regime map of Tam *et al*. (2010) was used as a guideline to ensure that forced convection experimental conditions were obtained.

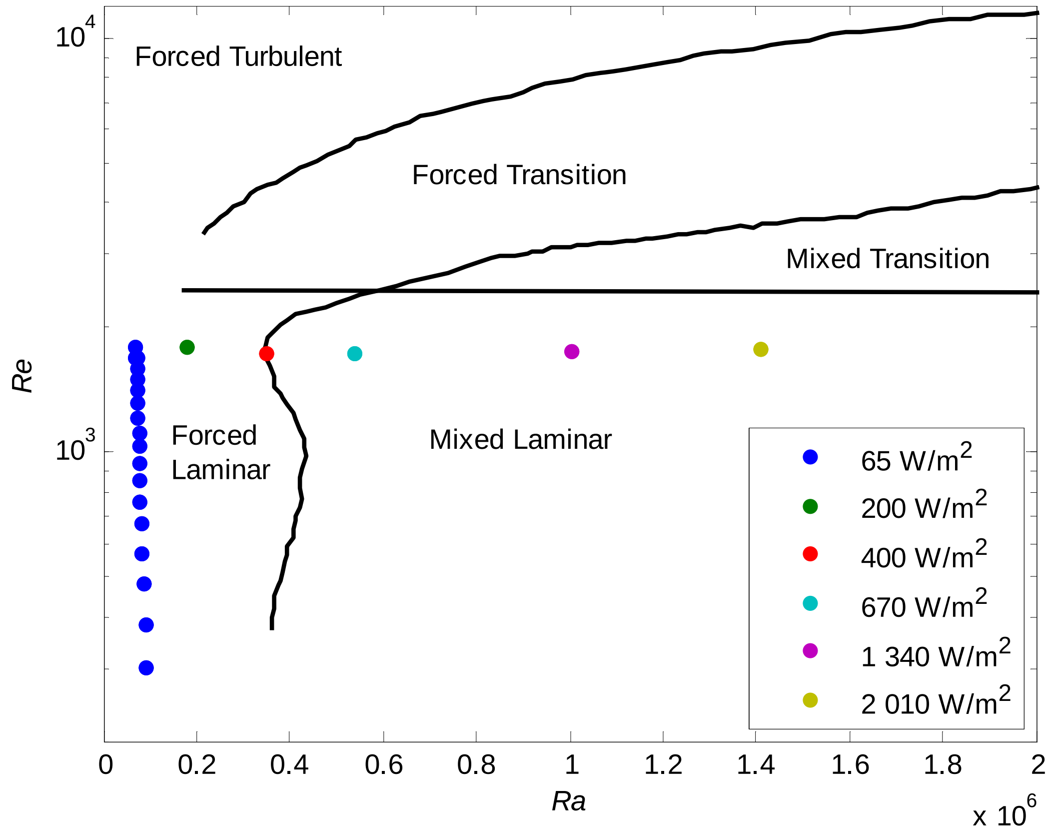

Figure 4.1: Unified SVM-based flow regime map for a constant heat flux boundary condition (Tam *et al*., 2010)

An experiment was conducted at a Reynolds number of 1 900 and a heat flux of 2 010 W/m^2, but from the flow regime map in Figure 4.1 (yellow data point), it was concluded that the flow was dominated by mixed convection. The Reynolds number was kept constant, but the heat flux was then gradually reduced from 2 010 W/m^2 to 65 W/m^2, as shown in Figure 4.1. In this process, the Rayleigh number was decreased from 1.4x10^6 to 0.1x10^6. At a Reynolds number of 1 900 and a heat flux of 65 W/m^2, the theoretical thermal entrance length was calculated to be approximately 7.6 m. Thus, although forced convection conditions were obtained, the flow in the test section was developing and not fully developed. The Reynolds number was then gradually reduced form 1 900 to 300 and the theoretical thermal entrance length reduced from 7.6 m to 1.2 m. At a Reynolds number of 300, fully developed forced convection conditions were obtained in the last 0.8 m of the test section.

The local Nusselt numbers at a Reynolds number of 300 and heat flux of 65 W/m^2 were compared with existing correlations in Figure 4.2. The correlations of Oliver (1962), Shah and London (1978), Palen and Taborek (1985), Ghajar and Tam (1991, 1994) and Gnielinski (2010), summarised in Table 2.1, were used for the validation. The average fully developed Nusselt number (the average of the last four thermocouple stations in Figure 4.2, which were all within the theoretical fully developed region) was found to be 4.57. This was within 4.6% of the theoretical value of 4.36 and confirmed that fully developed forced convection conditions were obtained.

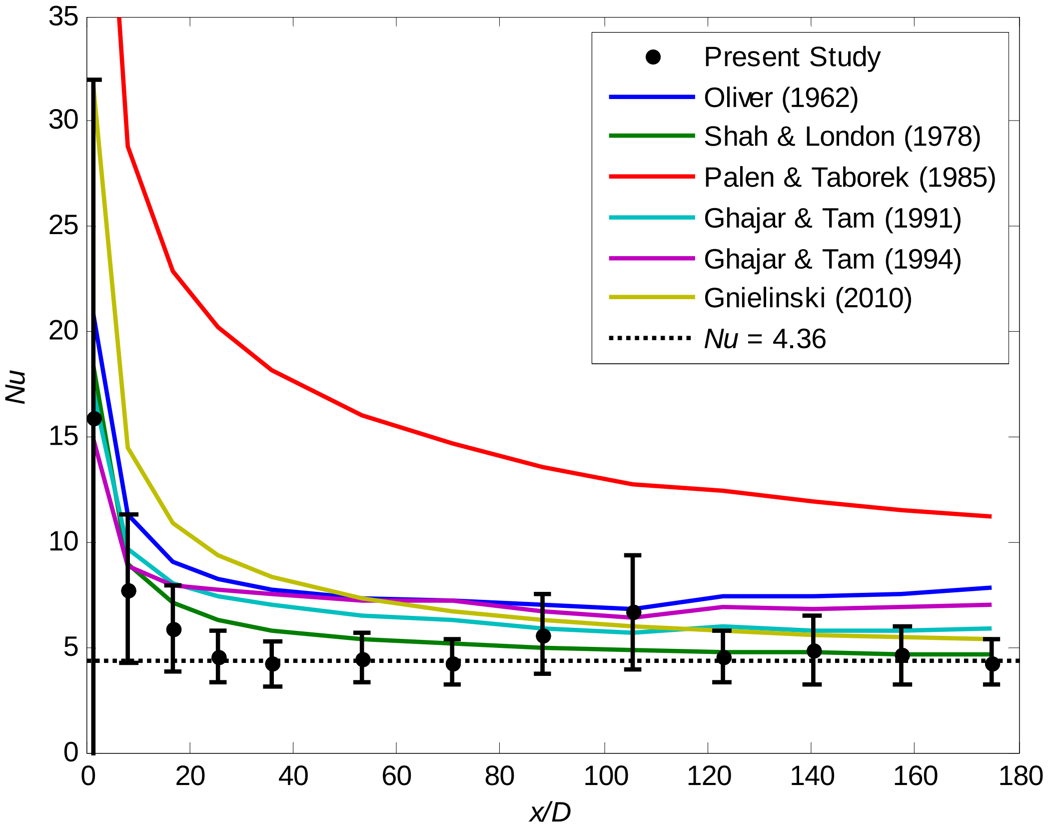

Figure 4.2: Local laminar forced convection Nusselt numbers as a function of axial position at an average Reynolds number of 300, average Grashof number of 1.4x10^4, average Prandtl number of 7.16 and a Graetz number of up to 184

From Figure 4.2, it follows that fully developed forced convection laminar flow was obtained between approximately *x/D* = 26 and *x/D* = 175. To verify this, the local surface and fluid temperatures as well as the temperature differences between the surface and fluid were calculated and are presented in Figure 4.3. The temperature profile in Figure 4.3(a) became an approximate straight diagonal line after *x/D* = 36 and temperature difference between the surface and fluid in Figure 4.3(b) showed no distinct increase or decrease. There seems to be scatter in the data in Figure 4.3(b), however, all the temperature differences were within the uncertainty of the temperature measurements. The uncertainty of the temperature measurements was 0.1 °C. Therefore, the uncertainty of the temperature difference between the fluid and surface can be up to 0.2 °C, which is indicated by the error bars in Figure 4.3(b). Although the theoretical thermal entrance length was calculated to be 1.2 m (*x/D* = 107.4) using Equation 2.10, it seems from Figure 4.3 that the flow might already be fully developed after *x/D* = 36. However, the temperature differences were too small compared with the uncertainties to make a definitive conclusion regarding the exact thermal entrance length.

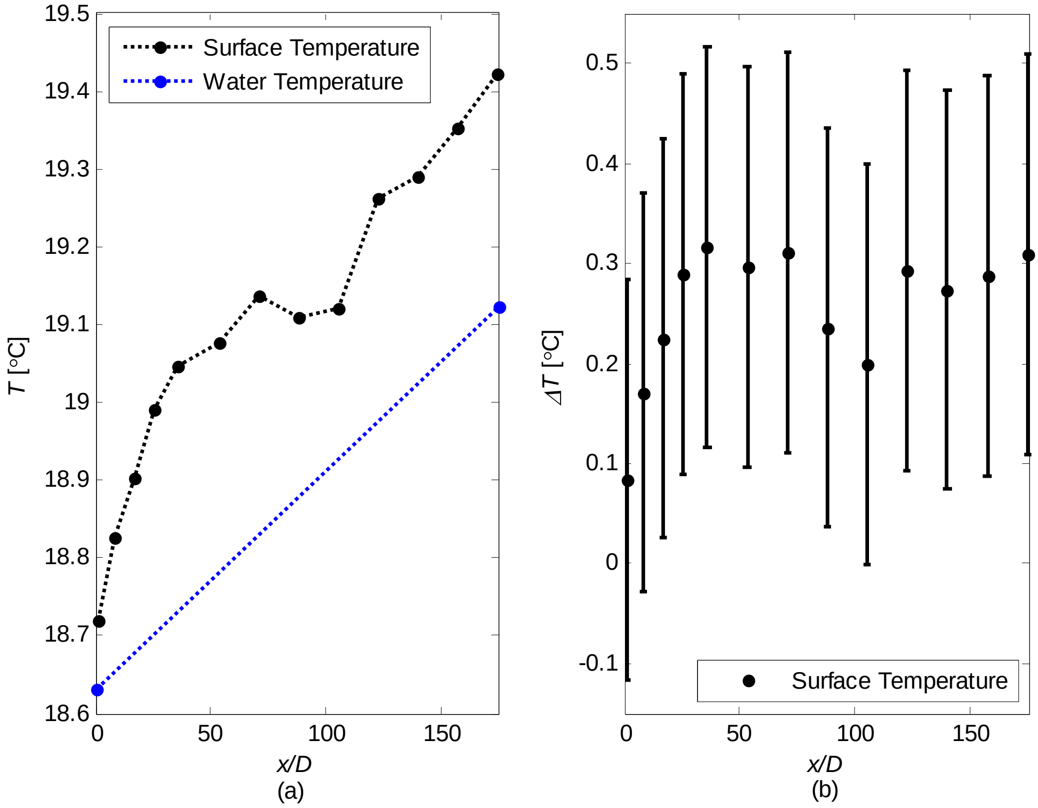

Figure 4.3: (a) Temperature profile and (b) local temperature differences as a function of axial position at a Reynolds number of 300, a Grashof number of 1.4x10^4, a Prandtl number of 7.16 and a Graetz number of 184. The local Nusselt numbers for this case are given in Figure 4.2.

The Nusselt number uncertainties are also included in Figure 4.2 and although the uncertainty was very high (100%) at the first thermocouple station, it decreased along the test section to a minimum of 28%. The main reason for the high uncertainties of the forced convection heat transfer experiments conducted in this study is the small temperature difference between the surface and the fluid. The average thermocouple uncertainty was 0.1 °C and at the first thermocouple station, the temperature difference between the surface and fluid was only 0.1 °C. This led to a high temperature uncertainty. The temperature difference between the surface and fluid increased along the test section to 0.2 °C at the last thermocouple station. Therefore, the temperature uncertainty decreased, and thus the Nusselt number uncertainty decreased as well.

However, from Figure 4.2, it follows that the Nusselt number uncertainty was significantly higher at *x/D* = 88 and *x/D* = 105. This might be due to the higher precision error of the thermocouples at these two stations as it was found that the standard deviation at these stations was larger than at the other stations. While the standard deviation of the other thermocouples was approximately 0.01 °C, the average standard deviation of the thermocouples at these two stations was 0.011 °C. Although this difference might seem negligible, it does become significant when very small temperature differences, as in this case, have to be measured. The local Nusselt numbers at *x/D* = 88 and *x/D* = 105 were greater than 4.36 due to the lower surface temperatures in Figure 4.3(a) and thus smaller temperature differences between the surface and fluid in Figure 4.3(b).

The average Nusselt number between *x/D* = 26 and *x/D* = 175 (excluding *x/D* = 88 and *x/D* = 105) was 4.476. This was within 2.6% of the theoretical value of 4.36. Even with the two thermocouple stations at *x/D* = 88 and *x/D* = 105 included, the average Nusselt number was found to be 4.836, which was within 10% of the theoretical value. This was within the uncertainties of the measurements and it can therefore be concluded that forced convection measurements were successfully obtained in the laminar flow regime.

Comparing the different correlations with each other in Figure 4.2, the equation of Shah and London (1978) came the closest to the theoretical Nusselt number of 4.36, with an average deviation of 15%. A maximum deviation of 27% was obtained at *x/D* = 25 and *x/D* = 36 because the flow started to become fully developed earlier than theoretically predicted. A minimum deviation of less than 2% was obtained at *x/D* = 140 and *x/D* = 157. The correlations of Ghajar and Tam (1991) and Gnielinski (2010) came close to a Nusselt number of 5. The Nusselt numbers predicted with the correlations of Oliver (1962) and Palen and Taborek (1985) were significantly higher than 4.36, since these equations were mainly developed for mixed convection.

4.3. Local laminar Nusselt numbers (mixed convection)

To validate the local laminar Nusselt numbers when the flow was dominated by mixed convection, experiments were conducted at a heat flux of 6.5 kW/m^2 and a Reynolds number of 700. At this condition, the heat flux was 100 times higher and the Reynolds number was 2.3 times higher than the forced convection condition considered in the flow regime map in Figure 4.1. According to the flow regime map in Figure 4.1, the flow regime should be mixed laminar flow.

The results of the local Nusselt numbers are presented in Figure 4.4 and were compared with existing correlations from literature. The heat transfer coefficients in the laminar flow regime are very sensitive to the heating or cooling methodology, Prandtl number, forced and mixed convection, as well as developing and fully developed flow. Furthermore, the conditions for which the correlations were developed are not always known. It was therefore difficult to find correlations which were suitable for the conditions (developing mixed convection laminar flow with low Prandtl numbers) of this study.

From Figure 4.4, it follows that the Nusselt number at the inlet of the test section was 18, but decreased to 10 at *x/D* = 8.2. Between *x/D* = 8.2 and *x/D* = 175, the Nusselt number gradually increased to 15. The trend of the experimental data was similar to the Nusselt numbers predicted by the correlation of Oliver (1962) and the average deviation was 17%. However, after *x/D* = 120, this correlation overpredicted the local Nusselt numbers between 10% and 17%. Although the trend of the experimental data was different from the Nusselt numbers predicted by the correlation of Ghajar and Tam (1991) between *x/D* = 8.2 and *x/D* = 70, the average deviation was 15%. Furthermore, the average deviation between *x/D* = 70 and *x/D* = 175 was less than 7% and it can therefore be concluded that the data correlated well with this correlation.

The correlation of Ghajar and Tam (1994) overpredicted the local Nusselt numbers by an average of 25%. This might have been caused by the Prandtl number, as the correlation of Ghajar and Tam (1994) was developed for Prandtl numbers greater than 40, while the Prandtl numbers during this validation were between 4 and 6. The Nusselt number is a function of the Reynolds number and Prandtl number, which explains why the Nusselt numbers predicted by this correlation were significantly higher. From Figure 4.4, it follows that the correlations of Shah and London (1978) and Gnielinski (2010) are better suited for laminar forced convection flow, since the local Nusselt number decreased towards the theoretical Nusselt number of 4.36 for fully developed forced convection laminar flow.

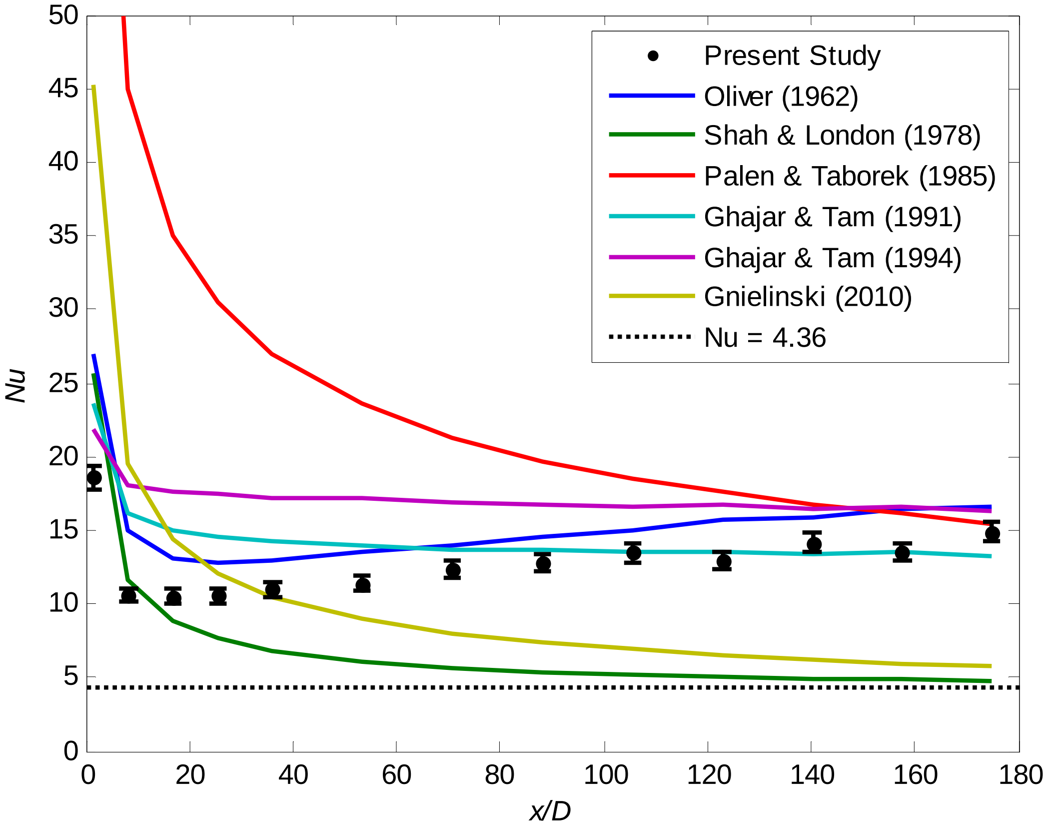

Figure 4.4: Local laminar mixed convection Nusselt numbers as a function of axial position at a Reynolds number of 700, a Grashof number of 1.1x10^6, a Prandtl number of 5.18 and a Graetz number of 382

Figure 4.5 contains the local surface and fluid temperatures as well as the temperature differences between the surface and fluid. A Reynolds number of 700 was used for this validation, therefore the theoretical thermal entrance length should be approximately 2 m (the length of the test section used in this study was 2.03 m), which implies that the flow inside the tube was still developing. From the temperature profile in Figure 4.5(a), it seems as if the flow became fully developed after approximately *x/D* = 88, where the temperature profile became a straight diagonal line. However, from Figure 4.5(b), it can be concluded that the flow inside the entire tube was still developing since the temperature gradient continued to decrease with increasing *x/D*.

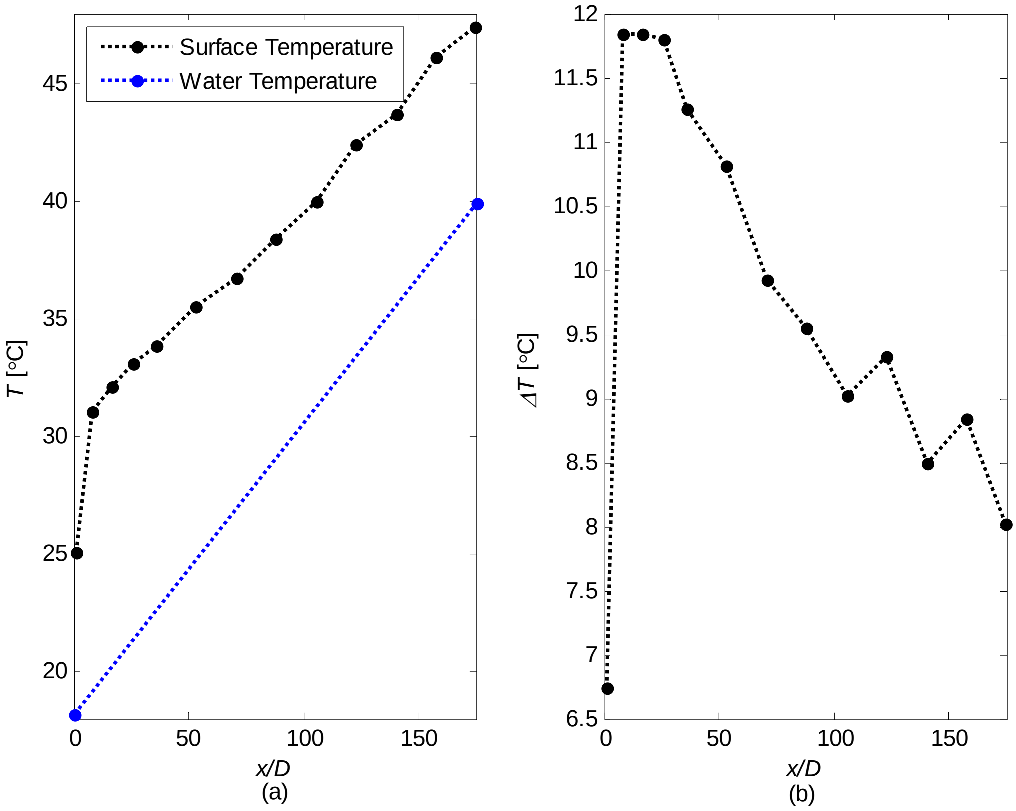

Figure 4.5: (a) Temperature profile and (b) local temperature differences as a function of axial position at an average Reynolds number of 700, an average Grashof number of 1.1x10^6, an average Prandtl number of 5.18 and a Graetz number of up to 382. The local Nusselt numbers for this case are given in Figure 4.4.

4.4. Average laminar Nusselt numbers

The average Nusselt numbers were obtained by using the bulk fluid temperature between the inlet and outlet and the average surface temperature across the test section. The average laminar Nusselt numbers obtained between Reynolds numbers of 600 and 1 900 at a heat flux of 6.5 kW/m^2 were used for the validation. The results were compared with existing correlations in Figure 4.6. For this Reynolds number range ($600 \leq Re \leq 1\,900$), the theoretical thermal entrance length varied between 2.4 m and 7.6 m while the length of the test section was only 2.03 m, thus the flow was still developing and not fully developed.

As expected, the laminar Nusselt numbers were significantly higher than the theoretical Nusselt number of 4.36 due to the effects of secondary flow and the fact that the flow was still developing. The experimental data correlated fairly well with the correlation of Ghajar and Tam (1991) and the average deviation between Reynolds numbers of 600 and 1 900 was 17%. Exact correlation was not expected since this correlation was developed for Prandtl numbers between 30 and 158 while the Prandtl numbers during the validation experiments varied between 4 and 6.

The Nusselt numbers predicted by the correlation of Shah and London (1978) and Gnielinski (2010) were significantly lower than those of the experimental results. A possible reason for this might be that the correlations were developed for fully developed flow. The average heat transfer coefficients of developing flow are higher than for fully developed flow (due to the higher heat transfer coefficients near the inlet of the test section), which explains why the experimental results were significantly higher than the Nusselt numbers predicted using fully developed flow correlations. The Nusselt numbers predicted by the correlation of Oliver (1962) and Ghajar and Tam (1994) were significantly higher than the experimental data. This might once again be due to the smaller Prandtl numbers of this validation ($4 \leq Pr \leq 6$) compared with the Prandtl numbers used by Ghajar and Tam (1994) to develop this correlation.

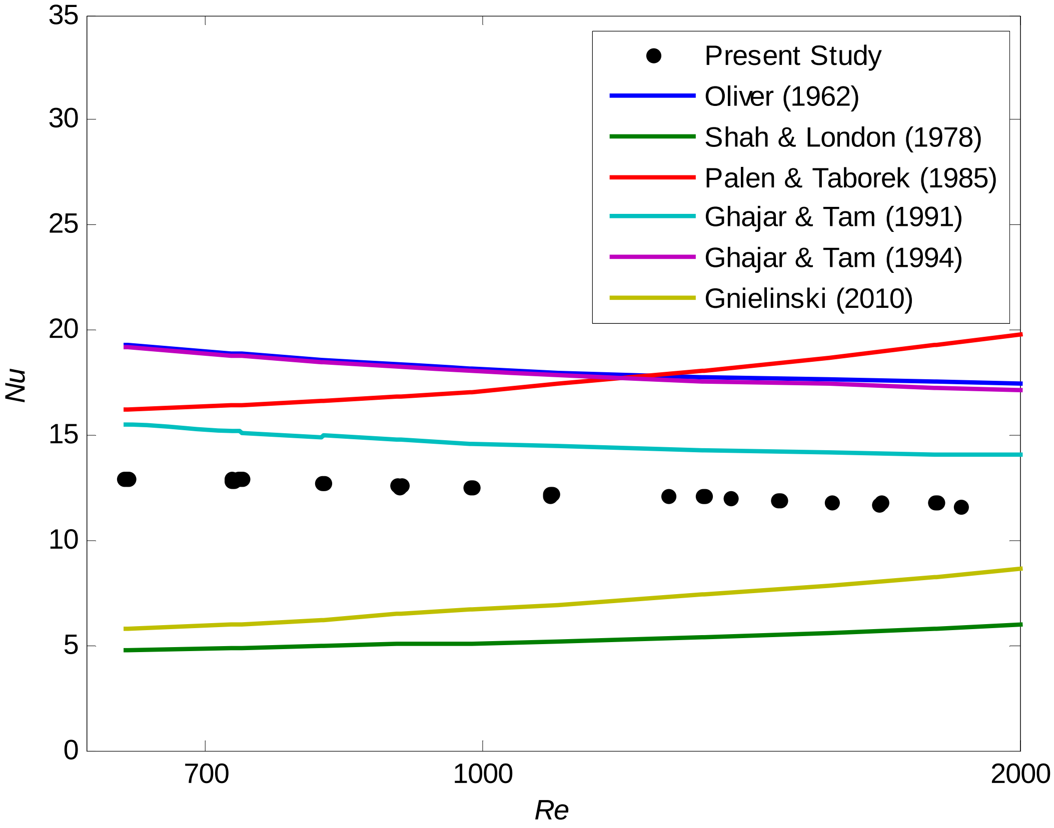

Figure 4.6: Average laminar Nusselt numbers as a function of Reynolds number between Reynolds numbers of 600 and 1 900 at a 6.5 kW/m^2 heat flux

4.5. Average turbulent Nusselt numbers

To validate the turbulent Nusselt numbers, the Reynolds number was varied between 4 000 and 10 000 and a heat flux of 14 kW/m^2 was used. The average Nusselt numbers were compared with the Gnielinski (1976) correlation, the turbulent forced convection heat transfer correlation of Ghajar and Tam (1994), as well as the experimental data of Meyer *et al*. (2013) in Figure 4.7. These two correlations, as well as their ranges, were summarised in Table 2.3. Meyer *et al*. (2013) also used a constant heat flux boundary condition and applied a heat flux of 13 kW/m^2 to the test section.

The Nusselt numbers correlated very well with the experimental data of Meyer *et al*. (2013) and the maximum deviation of 3% was found at a Reynolds number of 8 000. The average deviation between Reynolds numbers of 4 000 and 8 000 was 2% while a minimum deviation of 0.82% was found at a Reynolds number of 5 872. The data also correlated fairly well with the equation of Ghajar and Tam (1994) and the average deviation was 7.4%. Although this equation was developed for Reynolds numbers between 7 000 and 49 000, the maximum deviation at a Reynolds number of 4 000 was 9.4%. The data correlated better with the Nusselt numbers predicted with the correlation of Ghajar and Tam (1994) between Reynolds numbers of 7 000 and 10 000, however, the average deviation between the experimental data and the Nusselt numbers predicted with the correlation of Gnielinski (1976) was also 7.4%. A maximum deviation of 15% was obtained at a Reynolds number of 10 000 while the deviation between Reynolds numbers of 4 000 and 6 000 was only 2.4%.

It is shown that the uncertainties of the Nusselt numbers in Figure 4.7 increased with increasing Reynolds numbers. This is due to higher temperature uncertainties caused by the decreasing temperature differences between the surface and fluid, as well as between the inlet and outlet of the test section, as the Reynolds number increased.

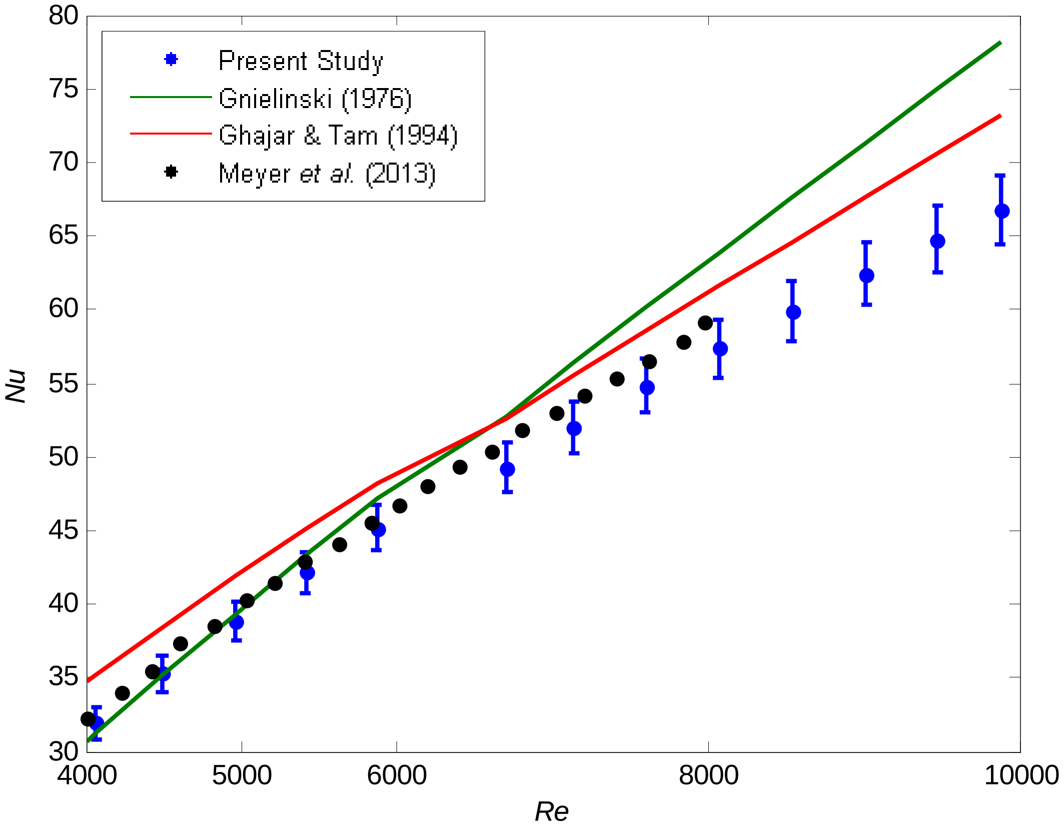

Figure 4.7: Average turbulent Nusselt numbers as a function of Reynolds number between Reynolds numbers of 4 000 and 10 000 at a 14 kW/m^2 heat flux

4.6. Isothermal friction factors

Pressure drop experiments were conducted across the entire test section length (2.03 m), therefore the friction factors contained both developing (laminar and transitional flow regimes) and fully developed (turbulent flow regime) flow. The isothermal friction factors were validated by considering 57 data points. The Reynolds number was decreased from 15 000 to 500 to ensure that both laminar and turbulent flow regimes were covered. The measurements were made without any heat transfer to eliminate the effect of varying viscosity and density. The isothermal friction factors are summarised in Figure 4.8 and compared with the Poiseuille (1840) equation, the correlation of Tam *et al.* (2013) for laminar developing flow and the Blasius (1913) equation for fully developed turbulent flow. These equations are summarised in Tables 2.2 and 2.4.

The laminar results were compared with the Poiseuille (1840) equation, which is valid for fully developed laminar flow, as well as with the correlation of Tam *et al.* (2013), which is valid for developing laminar flow. When comparing the friction factors predicted by the Poiseuille (1840) equation with those predicted by the correlation of Tam *et al.* (2013), it follows that the friction factors of Tam *et al.* (2013) were slightly larger and the difference increased with increasing Reynolds number. At a Reynolds number of 2 300, the friction factors predicted by the correlation of Tam *et al.* (2013) were 8.3% larger than those predicted with the Poiseuille (1840) equation. The correlation of Tam *et al.* (2013) is for developing flow, while the Poiseuille (1840) equation is for fully developed flow. The maximum wall shear stress is found at the inlet of the test section, where the boundary layer is the thinnest. Therefore, the pressure drop and friction factors are the highest at the inlet. This explains why the friction factors for developing flow were higher than for fully developed flow. Since the developing flow was investigated in this study, the laminar friction factors correlated well with the friction factors predicted by the correlation of Tam *et al.* (2013). The average deviation between Reynolds numbers of 500 and 2 000 was 2.2% and a maximum deviation of 5% occurred at a Reynolds number of 2 200 where transition started.

The turbulent results were compared with the Blasius (1913) equation, which is valid for fully developed turbulent flow. The experimental data correlated very well with this equation and the average deviation was 1% between Reynolds numbers of 3 500 and 15 000. A maximum deviation of 2% occurred at a Reynolds number of 4 200.

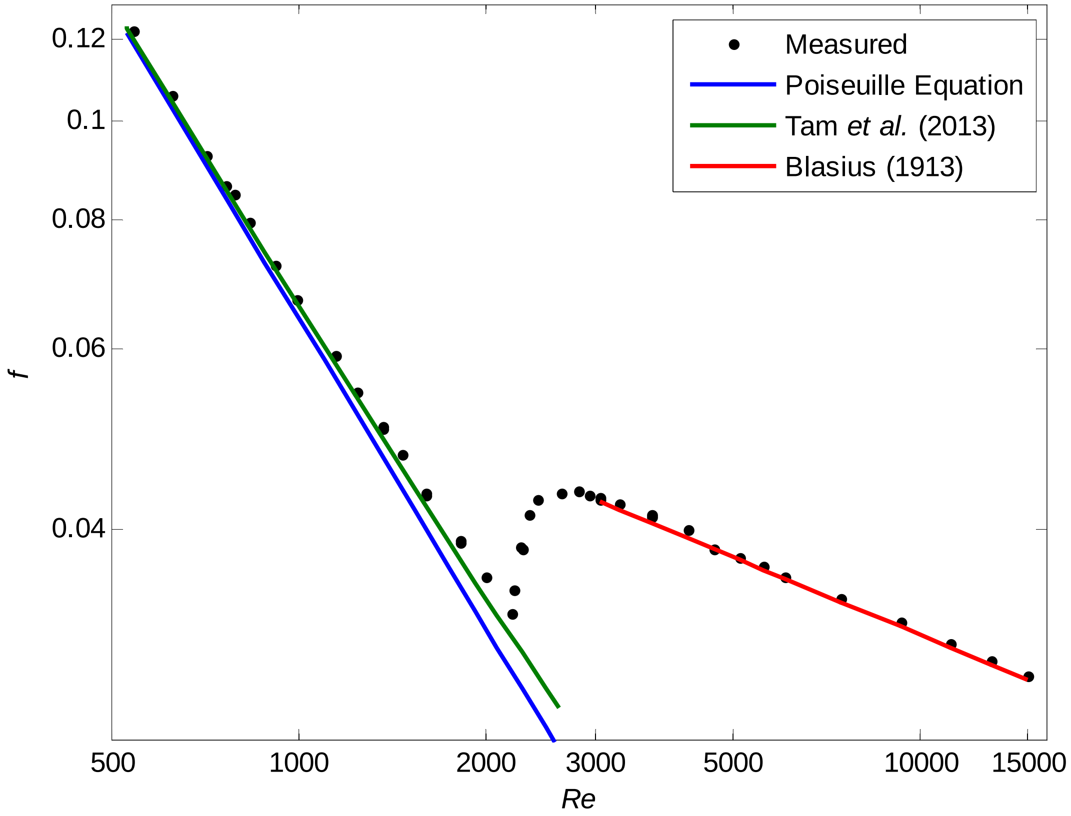

Figure 4.8: Isothermal friction factors as a function of Reynolds number between Reynolds numbers of 500 and 15 000

4.7.Conclusion

The experimental set-up and data reduction method for heat transfer and pressure drop were validated in this chapter. The conclusions were presented in the order of local forced convection laminar Nusselt numbers, local mixed convection laminar Nusselt numbers, average mixed convection laminar Nusselt numbers, average forced convection turbulent Nusselt numbers and average friction factors.

The heat transfer coefficients were first validated using forced convection data. The average fully developed Nusselt numbers (the average of the last four thermocouple stations, which were all within the theoretical fully developed region) were found to be 4.57. This was within 4.6% of the theoretical value of 4.36, thus it was concluded that forced convection measurements were successfully measured in the laminar flow regime. The local forced convection laminar Nusselt numbers also correlated well with literature and the average deviation was 15%. A maximum deviation of 27% was obtained at x/D = 25 and x/D = 36 because the flow began to develop earlier than theoretically expected. A minimum deviation of less than 2% was obtained at x/D = 140 and x/D = 157.

The local Nusselt numbers were also validated for mixed convection conditions to account for the effects of secondary flow. Once again the data correlated well with literature and the average deviation over the whole test section was 15% while the average deviation between x/D = 70 and x/D = 175 was less than 7%. The average laminar Nusselt numbers were validated using the data at a heat flux of 6.5 kW/m^2 and the flow was dominated by mixed convection. The Nusselt numbers were significantly higher than the theoretical Nusselt number of 4.36 for fully developed laminar forced convection flow, as it should be, due to the buoyancy-induced secondary flow. The experimental data correlated fairly well with literature and the average deviation between Reynolds numbers of 600 and 1 900 was 17%.

The average turbulent Nusselt numbers were validated between Reynolds numbers of 4 000 and 10 000 at a heat flux of 14 kW/m^2. The data correlated very well with experimental data of a previous study and the average deviation was 2%. The data also correlated well with existing correlations and the average deviation was less than 7.4%. A maximum deviation of 10% was obtained at a Reynolds number of 10 000.

The pressure drop was measured across the entire test section and therefore the friction factors contained both developing and fully developed flow. The laminar friction factors correlated well with developing flow correlations and the average deviation between Reynolds numbers of 500 and 2 000 was 2.2%, while a maximum deviation of 5% occurred at a Reynolds number of 2 200 where transition started. The turbulent results were also compared with literature and the average deviation between Reynolds numbers of 3 500 and 15 000 was 1%. A maximum deviation of 2% occurred at a Reynolds number of 4 200.

It can be concluded that the heat transfer coefficients and friction factors correlated well with existing correlations. The experimental set-up and data reduction method could therefore be considered as validated and reliable results can be expected for other heat fluxes and mass flow rates of experiments that were conducted.

5. Results: Local Heat Transfer Data

5.1. Introduction

The purpose of this chapter is to present the local heat transfer data for different heat flux measurements. The raw data can be found in the Excel file on the data and publications repository CD at the end of Appendix F. From Chapter 2, it was concluded that previous work focused mainly on fully developed flow, therefore the focus of this chapter is on developing flow. To ensure that the flow inside the tube is developing, the thermal entrance length is first investigated. The effect of secondary flow is then investigated, and finally, the local heat transfer coefficients are presented in terms of the Nusselt number and Colburn *j*-factor.

5.2. Experimental test matrix

Experiments were conducted (summarised in Table 5.1) at different mass flow rates and heat fluxes of 0 kW/m^2 (isothermal), 0.065 kW/m^2, 6.5 kW/m^2, 8.0 kW/m^2 and 9.5 kW/m^2. A total of 398 tests were conducted, which consisted of 370 mass flow rate measurements, 19 158 temperature measurements and 370 pressure drop measurements. The isothermal and diabatic pressure drop results are presented in Chapter 6.

Table 5.1: Experimental test matrix

Heat flux	Reynolds number range	Mass flow rate measurements	Temperature measurements	Pressure drop measurements
0 W/m^2	$538 \leq Re \leq 14\,968$	47	2 256	47
65 W/m^2	$303 \leq Re \leq 1\,793$	28	1 344	-
6.5 kW/m^2	$460 \leq Re \leq 9\,630$	111	5 382	111
8.0 kW/m^2	$470 \leq Re \leq 9\,600$	103	4 944	103
9.5 kW/m^2	$470 \leq Re \leq 9\,800$	109	5 232	109
Total		398	19 158	370

5.3. Theoretically calculated thermal entrance lengths

According to literature (Cengel, 2006), the thermal entrance length ($L_l = 0.05RePrD$) in the laminar flow regime is a function of Reynolds number, Prandtl number and tube diameter. In the turbulent flow regime, the thermal entrance length ($L_t = 10D$) is independent of Reynolds and Prandtl numbers and is significantly shorter. Figure 5.1 summarises the theoretically calculated thermal entrance lengths for all Reynolds numbers and heat fluxes.

From Figure 5.1, it follows that the thermal entrance length in the laminar flow regime increased with increasing Reynolds number, as expected, because the thermal entrance length is a function of Reynolds number. When the Reynolds number was greater than 2 300 (transition is assumed to start at a Reynolds number of 2 300), the thermal entrance length remained constant at 0.1152 m. This is due to the thermal entrance length in the turbulent flow regime being only a function of the tube diameter. Furthermore, it can be concluded that the thermal entrance length decreased slightly with increasing heat flux. This is caused by the average Prandtl number decreasing with increasing temperature.

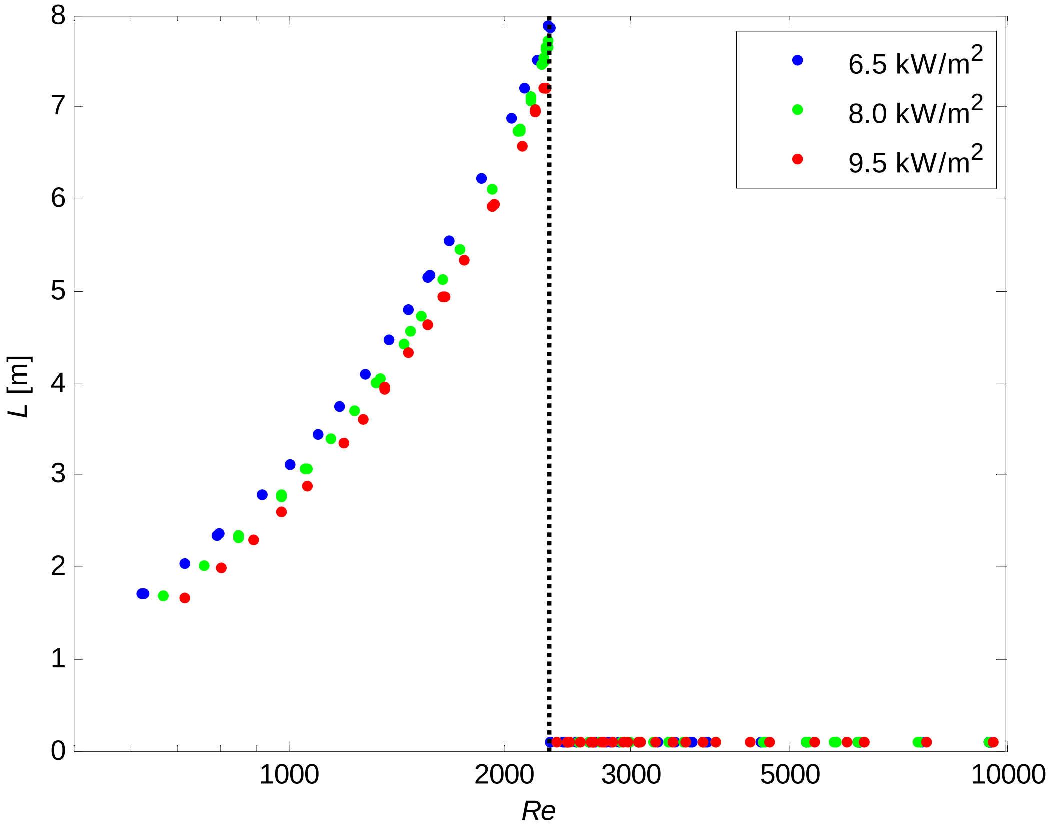

Figure 5.1: Theoretical thermal entrance lengths as a function of Reynolds number at different heat fluxes using the Prandtl numbers calculated at the bulk temperature, which was obtained from measurements

5.3.1. Forced convection

The flow regime map in Figure 4.1 was used as a guideline to ensure that the flow is dominated by forced convection. The Reynolds number was varied between 300 and 1 900 in order to cover a sufficient part of the laminar flow regime. The local surface temperatures along the test section, as well as the temperature difference between the fluid and the surface, for different Reynolds numbers and a heat flux of 65 W/m^2 are summarised in Figure 5.2.

The flow is assumed to be fully developed once the temperature difference between the surface and fluid is approximately constant. From the temperature profiles in Figure 5.2(a), it follows that the temperature profile was approximately the same for all Reynolds numbers and the temperature increased linearly between $x/D = 36$ and $x/D = 176$. From Figure 5.2(b), it follows that the temperature difference between the surface and fluid increased significantly between $x/D = 0$ and $x/D = 36$ for all the different Reynolds numbers, which implies that the flow is still developing. At Reynolds numbers of 300 and 500, the temperature differences fluctuated slightly between $x/D = 36$ and $x/D = 176$, but there was no distinct increase or decrease. Therefore, the flow might be fully developed.

The average uncertainty of the temperature measurements was approximately 0.1 °C. Therefore, the uncertainty of the temperature difference between the surface and fluid could be up to 0.2 °C. This uncertainty is indicated by the blue error bars in Figure 5.2(b) for a Reynolds number of 300. The temperature differences in Figure 5.2(b) were very small compared with the uncertainty of the temperature measurements. It was thus not possible to make accurate conclusions regarding the thermal entrance length from this graph. The two thermocouple stations at $x/D = 88$ and $x/D = 105$

appeared to be inaccurate, as was already observed during calibration experiments. As mentioned in Section 4.2, this might be due to the higher precision component of the uncertainty of the temperature measurements at these two stations.

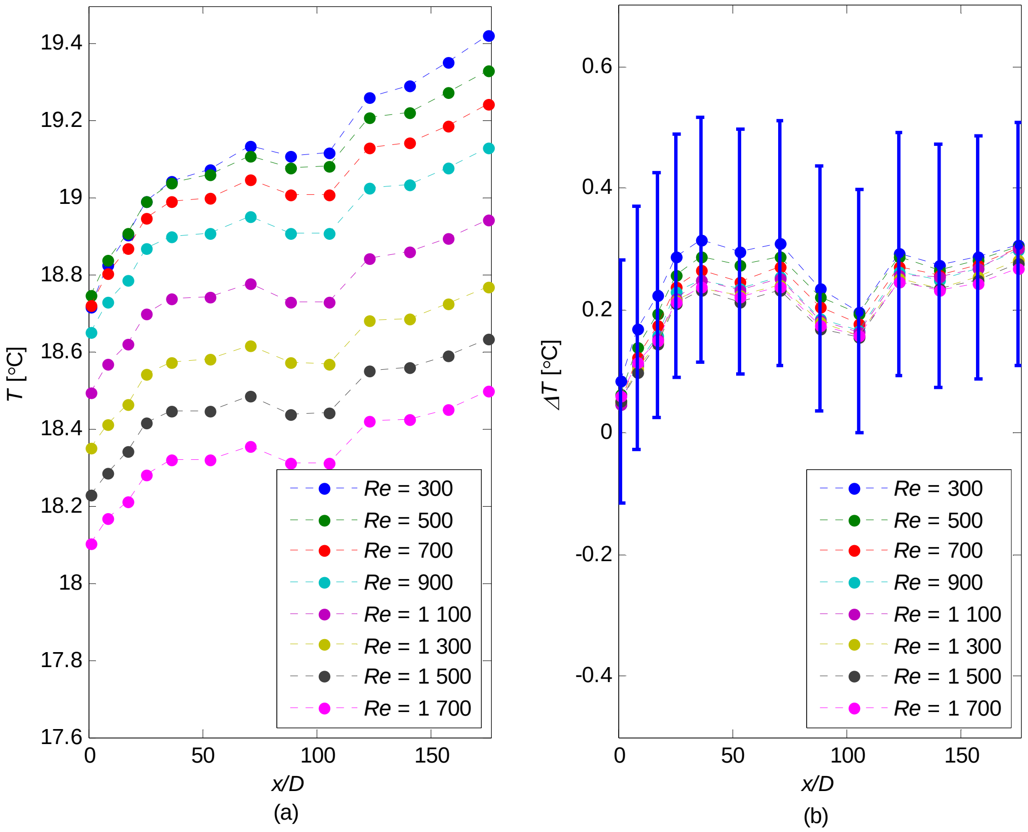

(a) (b)

Figure 5.2: Comparison of (a) surface temperatures and (b) temperature difference between the surface and fluid as a function of *x/D* for different Reynolds numbers at a heat flux of 65 W/m^2

The thermal entrance length can also be investigated by plotting the local heat transfer coefficients and Nusselt numbers across the test section in Figure 5.3. The local heat transfer coefficients and Nusselt numbers were calculated using Equations 3.9 and 3.11. From Section 2.4, it was concluded that for fully developed flow, the heat transfer coefficient should be constant since both the heat input and temperature difference are constant.

Figure 5.3(a) summarises the local heat transfer coefficients as a function of *x/D* for different Reynolds numbers at a heat flux of 65 W/m^2. The local heat transfer coefficients for all Reynolds numbers decreased significantly between *x/D* = 0 and *x/D* = 36, which confirmed that the flow was still developing. For a Reynolds number of 300, the local heat transfer coefficients were approximately constant between *x/D* = 36 and *x/D* = 175, indicating that the flow was fully developed. Furthermore, for laminar fully developed forced convection flow, the local Nusselt number should be 4.36 (indicated by the dotted black line in Figure 5.3(b)). It can therefore be concluded that fully developed forced convection laminar flow was obtained at a Reynolds number of 300, since the local Nusselt numbers were approximately 4.36 between *x/D* = 36 and *x/D* = 175. For the other Reynolds numbers (500 ≤ *Re* ≤ 1 700), the heat transfer coefficients decreased slightly between *x/D* = 36 and *x/D* = 175. Therefore, although the flow appeared to be fully developed in Figure 5.2(a), it was not, as the temperature differences were not yet constant.

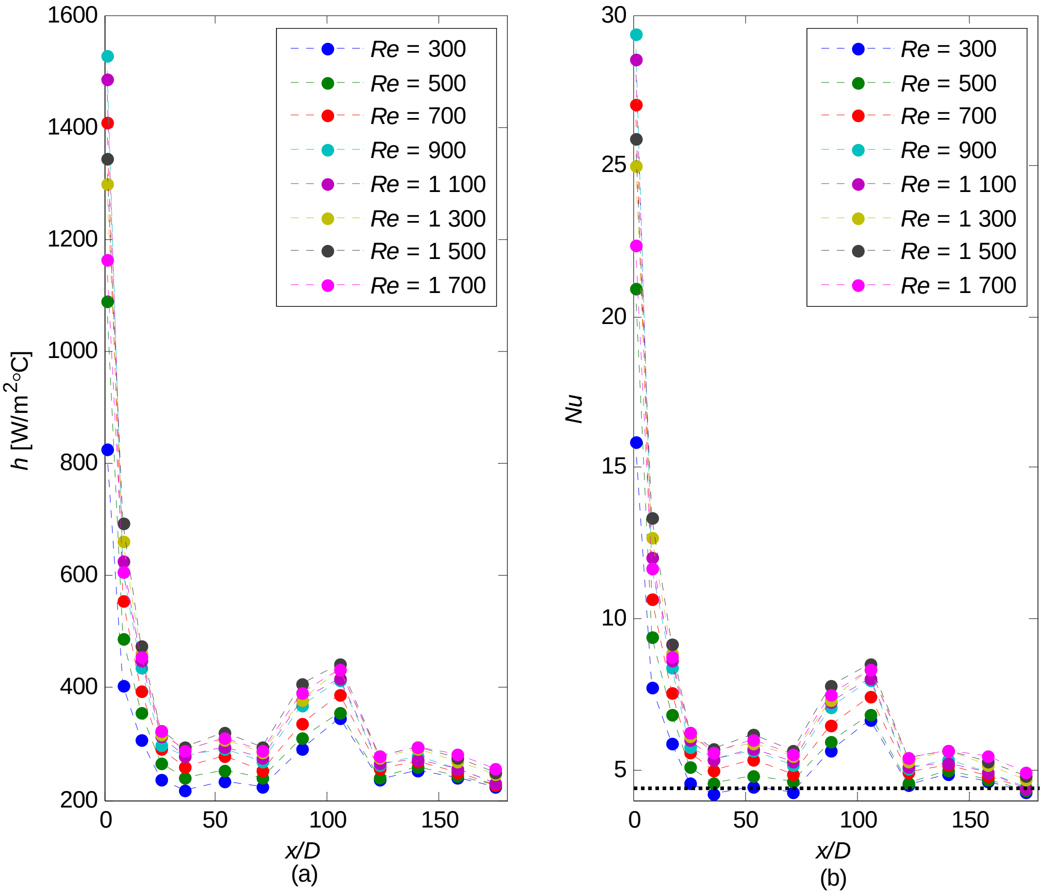

Figure 5.3: Comparison of local (a) heat transfer coefficients and (b) Nusselt numbers as a function of *x/D* for different Reynolds numbers and a heat flux of 65 W/m^2. The horizontal dotted black line in (b) identifies *Nu* = 4.36.

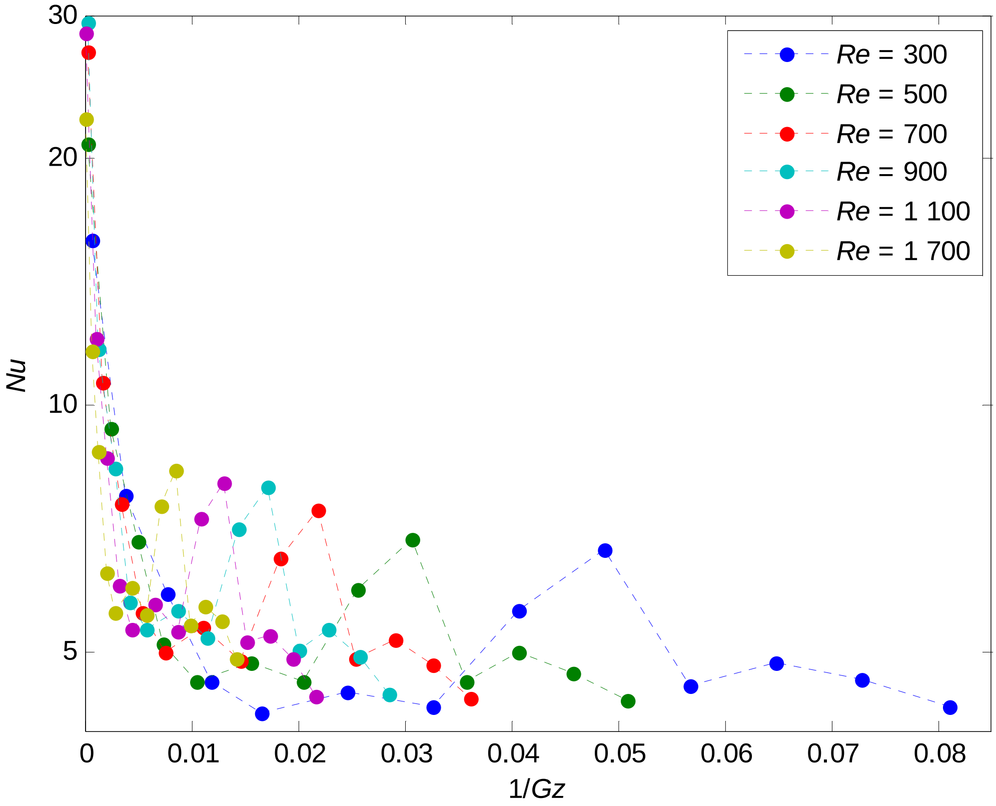

Figure 5.4: Comparison of local Nusselt numbers against the inverse of the Graetz numbers for different Reynolds numbers at a heat flux of 65 W/m^2

The local Nusselt numbers are also plotted against the inverse of the Graetz number in Figure 5.4 for different Reynolds numbers at a heat flux of 65 W/m^2. Fully developed flow conditions exist when the inverse of the Graetz number is greater than 0.05 (Cengel and Ghajar, 2011). From Figure 5.4, it follows that at Reynolds numbers of 300 and 500, the local Nusselt numbers were approximately constant and the inverse of the Graetz number was greater than 0.05. It can therefore be concluded that the flow was fully developed at these two Reynolds numbers. As mentioned in Section 4.2, the average Nusselt number between *x/D* = 26 and *x/D* = 175 (excluding *x/D* = 88.1 and *x/D* = 105.5) at a Reynolds number of 300 was 4.476.

The Nusselt number is a function of the heat transfer coefficient, tube diameter and thermal conductivity of the fluid. The thermal conductivity of the fluid is a function of temperature and will therefore increase slightly across the test section due to the increasing fluid temperature. The local thermal conductivities of the fluid as a function of *x/D* for different Reynolds numbers at a heat flux of 65 W/m^2 are summarised in Figure 5.5(a). From this graph, it follows that the increase in thermal conductivity between the inlet and outlet of the test section was less than 1%. This explains why there was no significant difference in the shape of the local heat transfer coefficients in Figure 5.3(a) and the local Nusselt numbers in Figure 5.3(b).

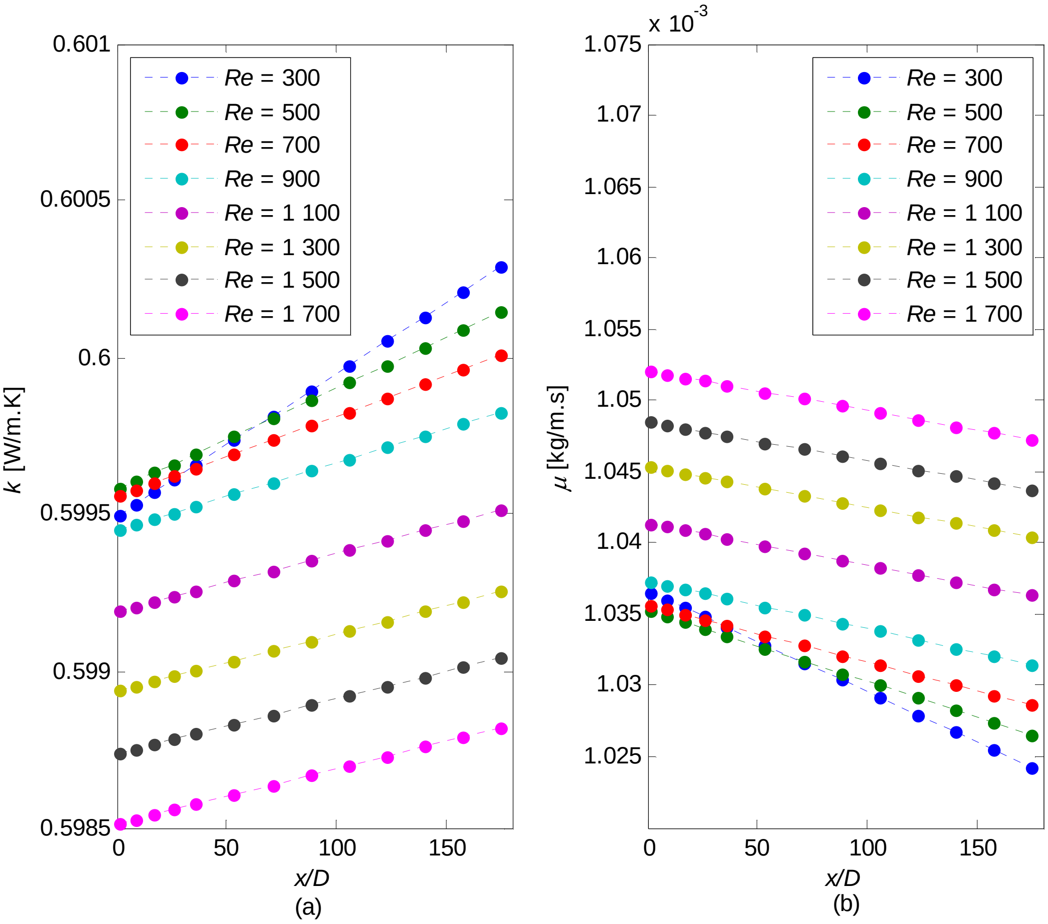

Figure 5.5: Comparison of local (a) thermal conductivity and (b) dynamic viscosity as a function of *x/D* for different Reynolds numbers at a heat flux of 65 W/m^2

The Reynolds number is a function of the dynamic viscosity of the fluid, thus for a fixed mass flow rate, the Reynolds number may increase slightly with increasing fluid temperature due to the decreasing dynamic viscosity. Figure 5.5(b) summarises the local dynamic viscosities of the fluid as a function of *x/D* for different Reynolds numbers at a heat flux of 65 W/m^2. Similar to the thermal conductivities, the difference in the viscosities at the inlet and outlet of the test section was less than 1% due to the small temperature increase.

5.3.2. Mixed convection

The mixed convection data were taken at heat fluxes of 6.5 kW/m^2 (100 times more than the forced convection data in Section 5.3.1), 8.0 kW/m^2 and 9.5 kW/m^2. The Reynolds numbers in the previous section on forced convection varied between 300 and 1 700, while in this part of the work, it varied between 600 and 10 000. The Rayleigh numbers of the experimental data of all three heat fluxes are plotted on the flow regime map of Tam *et al*. (2010) in Figure 5.6 to determine whether the flow was dominated by forced or mixed convection. However, only the laminar data of the 6.5 kW/m^2 heat flux (blue data points) were used in this section. Although the flow regime map was developed for Rayleigh numbers up to 3.5x10^6, it can still be used as a guideline to determine whether the flow in the experiments of this study was dominated by forced or mixed convection.

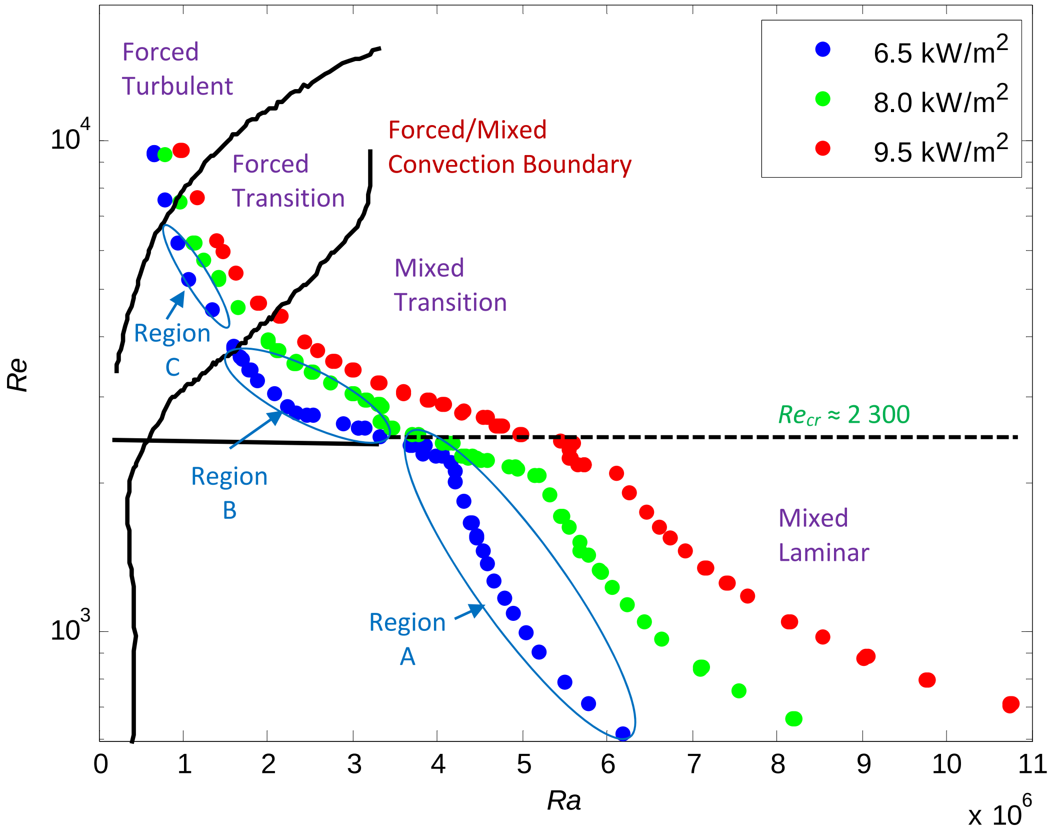

Figure 5.6: Unified SVM-based flow regime map for a constant heat flux boundary condition (Tam *et al.*, 2010) with experimental data for different Reynolds numbers and heat fluxes. Regions A, B and C are discussed in Section 5.3.2.

From Figure 5.6, it follows that the experiments conducted in the entire laminar flow regime (Region A) and lower part of the transitional flow regime (Region B) were dominated by mixed convection since it was to the right-hand side of the forced/mixed convection boundary. The upper part of the transitional flow regime (Region C) and turbulent flow regime were dominated by forced convection since it was to the left-hand side of the forced/mixed convection boundary.

The local surface temperatures, as well as the temperature difference between the surface and fluid for different Reynolds numbers, are summarised in Figures 5.7 to 5.9 for heat fluxes of 6.5 kW/m^2, 8.0 kW/m^2 and 9.5 kW/m^2. The Reynolds number was varied between 600 and 10 000 to ensure that the whole transitional flow regime, as well as sufficient parts of the laminar and turbulent flow regimes, was covered. From Figures 5.7(a), 5.8(a) and 5.9(a), it appears that fully developed flow was obtained between $x/D = 122$ and $x/D = 175$ since the temperature profiles became an approximate straight diagonal line. However, this was not the case and from Figures 5.7(b), 5.8(b) and 5.9(b), it follows that the temperature difference continued to decrease along the test section for all Reynolds numbers smaller than 3 000. Thus the flow was still developing.

Furthermore, from Figures 5.7(b), 5.8(b) and 5.9(b), it follows that at Reynolds numbers of 4 500 and 6 200, the temperature difference across the test section remained approximately constant after x/D = 17 and thus the flow was fully developed between x/D = 17 and $x/D = 175$. At a Reynolds number of 4 500, the flow was in the low-Reynolds-number-end flow regime, while at a Reynolds number of 6 200, the flow was turbulent. The thermal entrance length was therefore 10 diameters (Equation 2.11). This explains why the thermal entrance length was significantly shorter at these two Reynolds numbers.

When comparing Figures 5.7(b), 5.8(b) and 5.9(b), no significant difference between the profiles of the temperature differences of the different heat fluxes was observed. However, the magnitude of the temperature differences increased with increasing heat flux, which led to increasing secondary flow effects. The different flow regimes were identified from the temperature difference graphs in Figures 5.7(b), 5.8(b) and 5.9(b).

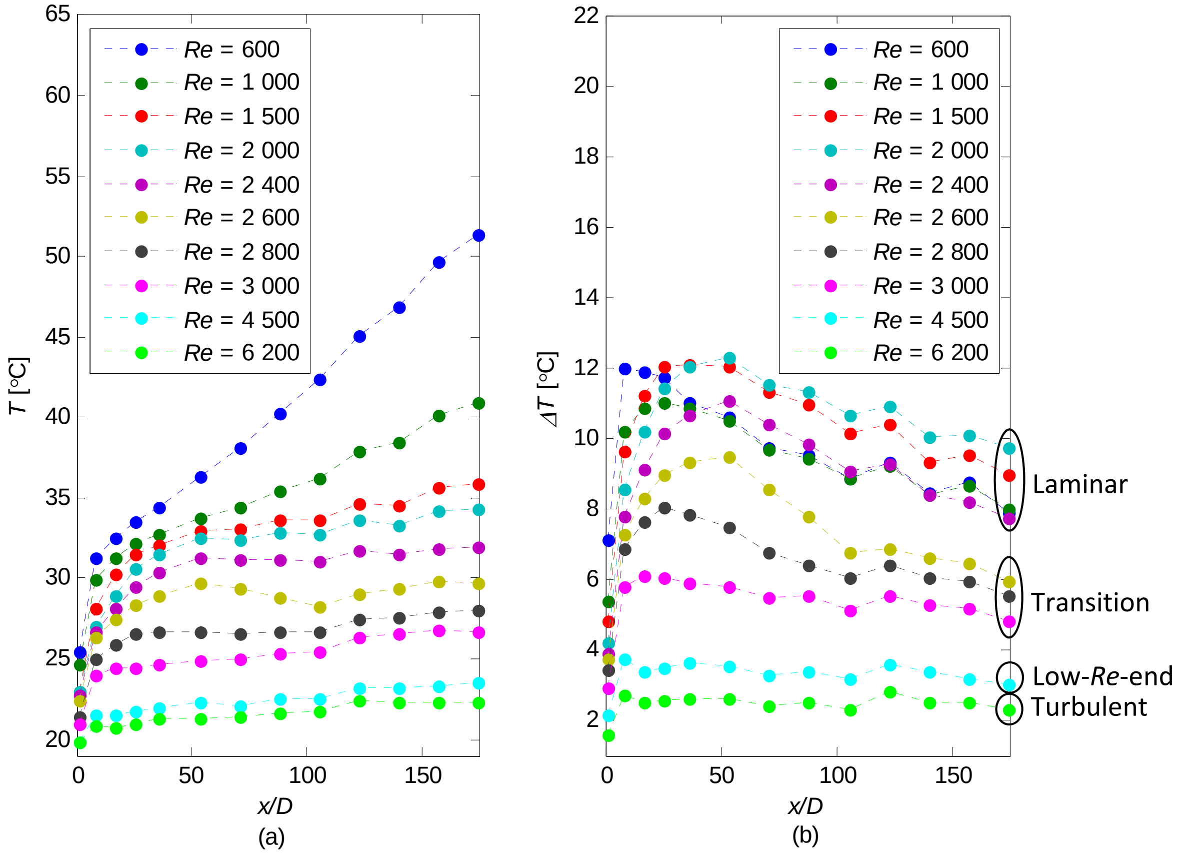

(a)

(b)

Figure 5.7: Comparison of (a) temperature profiles and (b) local temperature differences as a function of axial position for different Reynolds numbers at a heat flux of 6.5 kW/m^2

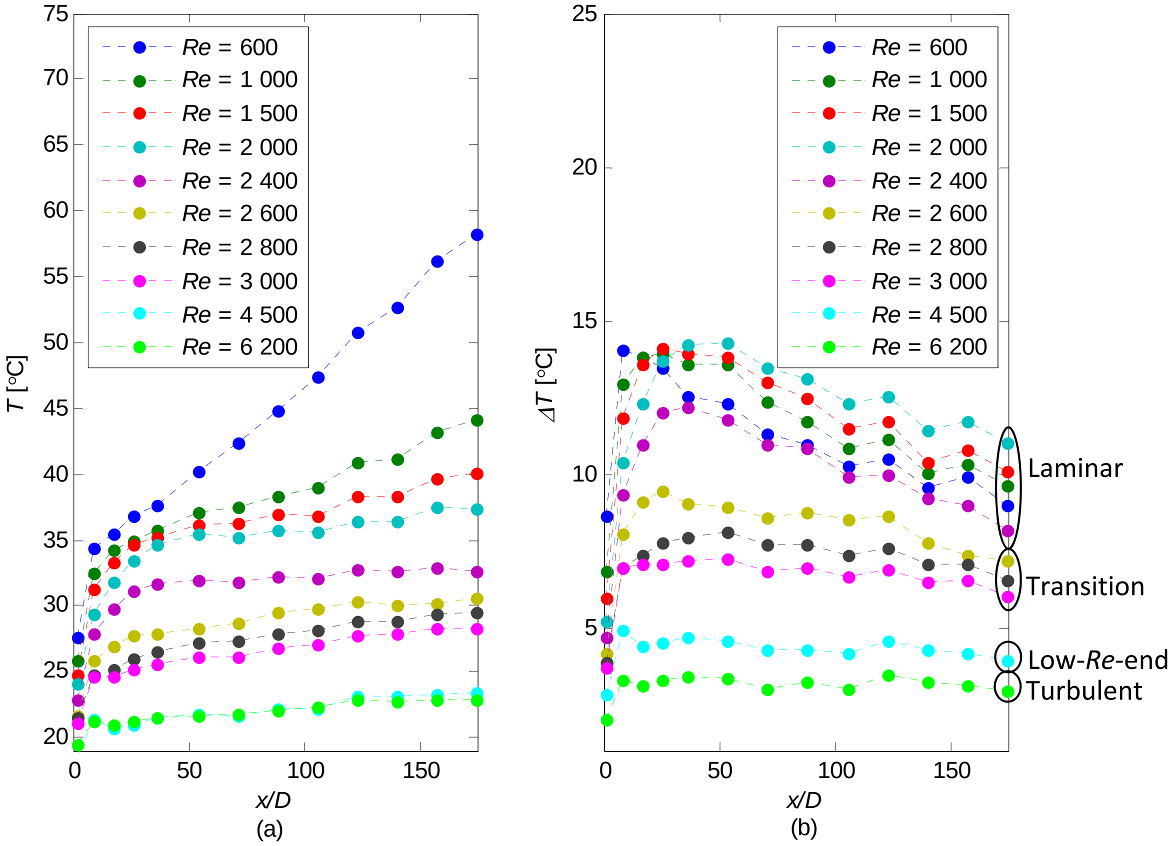

Figure 5.8: Comparison of (a) temperature profiles and (b) local temperature differences as a function of axial position for different Reynolds numbers at a heat flux of 8.0 kW/m^2

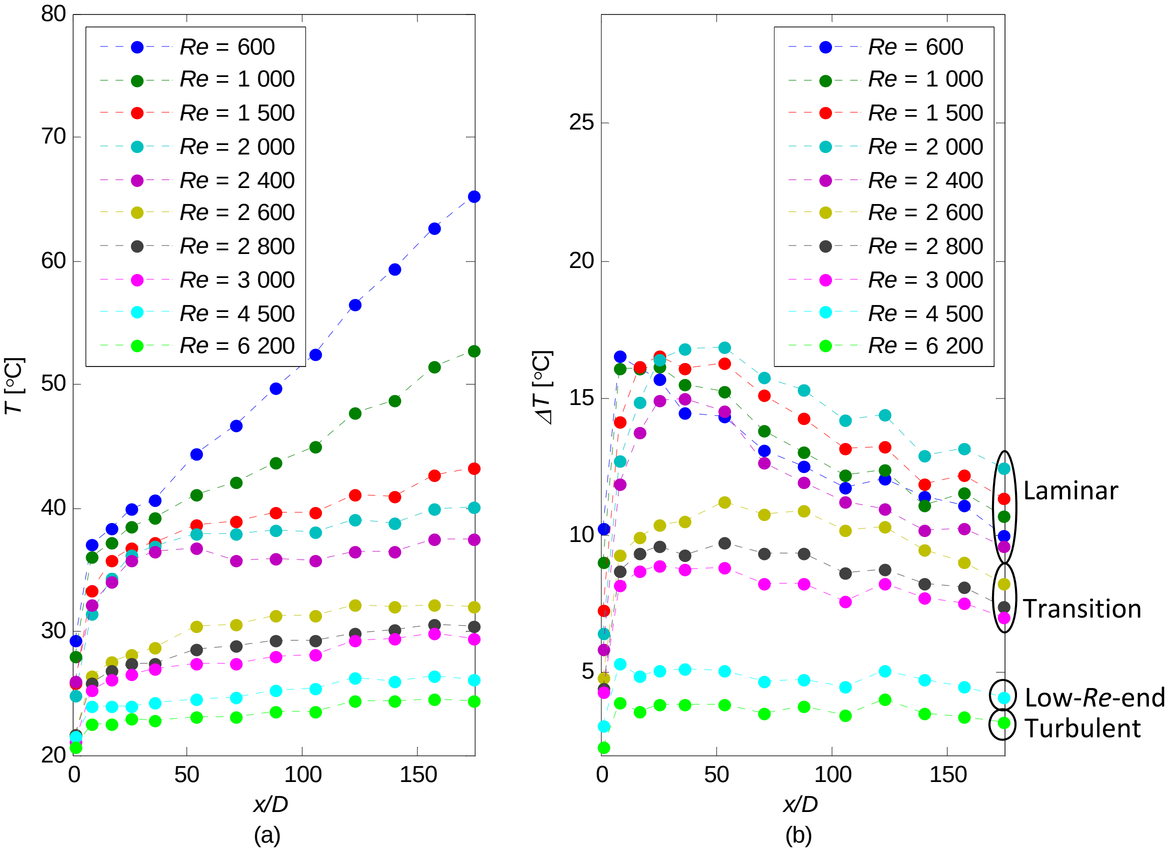

Figure 5.9: Comparison of (a) temperature profiles and (b) local temperature differences as a function of axial position for different Reynolds numbers at a heat flux of 9.5 kW/m^2

The flow was laminar between Reynolds numbers of 600 and 2 400 and the temperature difference between the fluid and surface was large, thus secondary flow effects were significant. Between Reynolds numbers of 2 600 and 3 000, the flow was in the transitional flow regime. The temperature differences were lower than in the laminar flow regime since the fluid motion slightly suppressed the buoyancy effects. At Reynolds numbers of 4 400 and 6 200, the flow was in the low-Reynolds-number-end regime and turbulent flow regime, respectively. The temperature differences in these regimes were small compared with the laminar flow regime and the flow was dominated by forced convection since the secondary flow effects were suppressed.

The gradient ($\Delta T/\Delta x$) of the temperature difference between the surface and fluid might give a better indication of whether the flow is developing or fully developed. For fully developed flow, this gradient should be zero as the temperature difference between the surface and fluid should be constant (Section 2.4). Laminar temperature gradients across the tube for Reynolds numbers between 700 and 2 000 at a heat flux of 6.5 kW/m^2 are summarised in Figure 5.10.

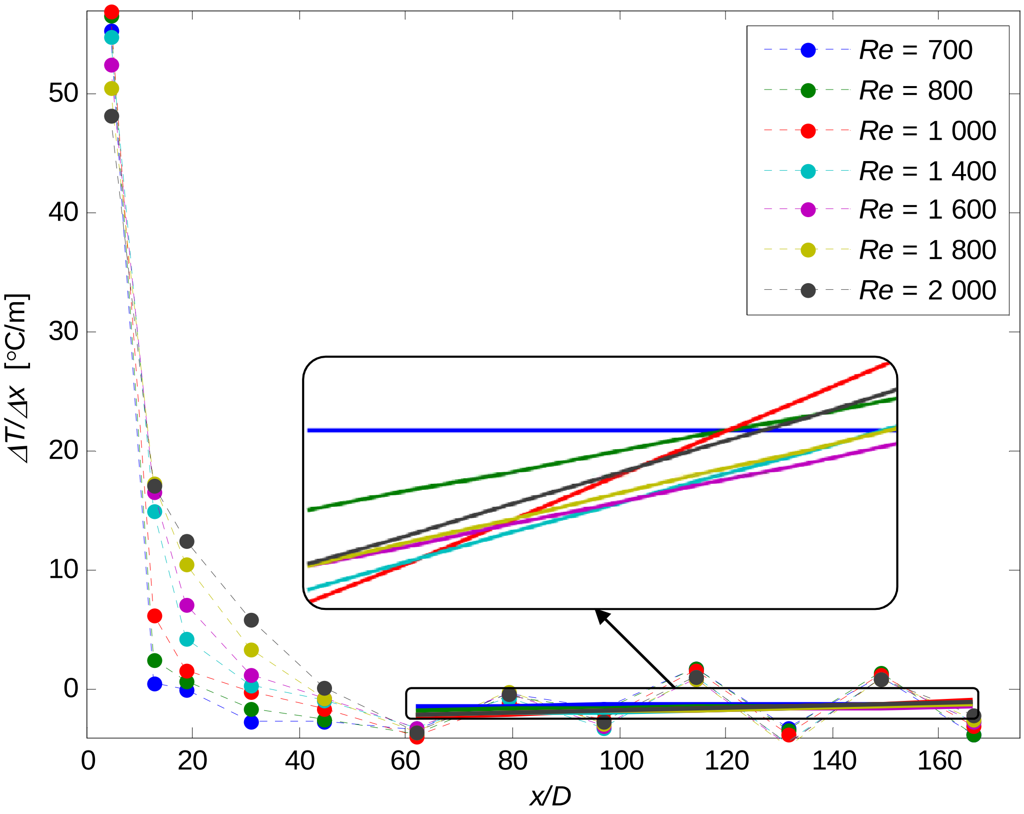

Figure 5.10: Temperature gradients as a function of axial position for laminar Reynolds numbers between 700 and 2 000 at a heat flux of 6.5 kW/m^2. Trend lines fitted through the last seven data points indicate the average gradients.

From Figure 5.10, it follows that the temperature gradient was a maximum at the inlet of the test section and decreased with increasing *x/D* as the flow approached fully developed flow. Furthermore, the temperature gradient increased with increasing Reynolds number between *x/D* = 0 and *x/D* = 50. The thermal entrance length also increased with increasing Reynolds number, which implies that at, for example, *x/D* = 16.9, the flow was "closer" to fully developed flow at a Reynolds number of 700, than at a Reynolds number of 2 000. This explains the increase in temperature gradients with increasing Reynolds number in the laminar flow regime. There seems to be some scatter in the data between *x/D* = 60 and *x/D* = 175 and thus an accurate conclusion regarding the thermal entrance length could not be made.

Trend lines were fitted through the last seven data points between *x/D* = 60 and *x/D* = 175 to gain a better understanding of the temperature gradients in this region. From this detailed view, it follows that the temperature gradient was approximately zero between *x/D* = 60 and *x/D* = 175 when the Reynolds number was 700 (indicated by the blue line) and thus the flow seems to be close to fully developed flow (trend lines were also generated between the last three data points and the results were similar). However, as the Reynolds number was increased, the gradient increased as well, which confirms that the flow was still developing.

The temperature gradients in the transitional flow regime (2 200 ≤ *Re* ≤ 4 300) at a heat flux of 6.5 kW/m^2 are summarised in Figure 5.11. Similar to the laminar flow regime, the temperature gradients were a maximum at the inlet of the test section and decreased with increasing *x/D*. However, at a fixed *x/D*, for example, *x/D* = 1.3, the temperature gradient decreased with increasing Reynolds number. Thus, the thermal entrance length decreased with increasing Reynolds number in the transitional flow regime, as the flow approached turbulent (and thus fully developed) flow. A trend line was added through the data points between *x/D* = 60 and *x/D* = 175. Similar to the detailed view in Figure 5.10, the gradient increased with increasing Reynolds number for Reynolds numbers of 2 200 and 2 600, as the flow was still developing. However, for Reynolds numbers greater than 3 000, the gradient decreased with increasing Reynolds number since the flow approached fully developed flow.

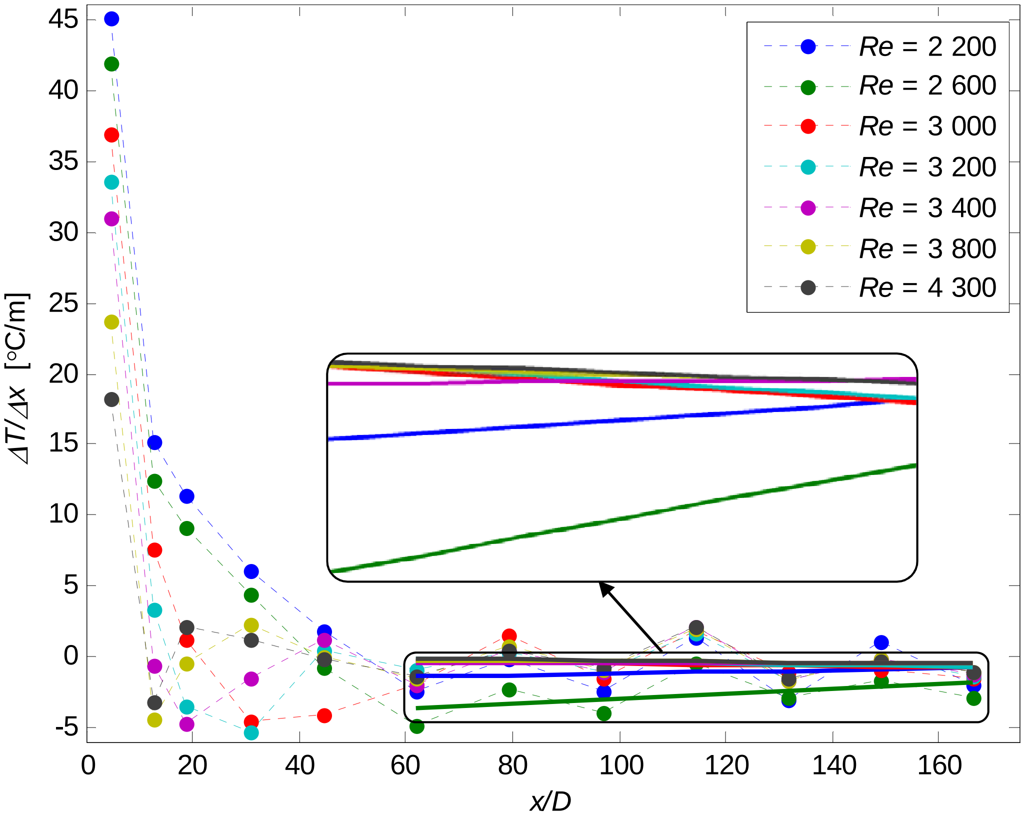

Figure 5.11: Temperature gradients as a function of axial position for transitional Reynolds numbers between 2 200 and 4 300 at a heat flux of 6.5 kW/m^2. Trend lines fitted through the last seven data points indicate the average gradients.

The temperature gradients across the test section for different turbulent Reynolds numbers (5 200 ≤ *Re* ≤ 9 500) at a heat flux of 6.5 kW/m^2 are summarised in Figure 5.12. It can be concluded that the temperature gradient in the turbulent flow regime was independent of Reynolds number since the temperature gradient profiles of all four Reynolds numbers were approximately the same.

A trend line was fitted through the data points between *x/D* = 20 and *x/D* = 175 and from Figure 5.12, it follows that it was close to zero (indicated by the dotted black line). The average slope of the trend lines was 1.509x10^{-3}, while the average slope in Figure 5.11 was 5.868x10^{-3}. This confirms that the flow in the turbulent flow regime was fully developed.

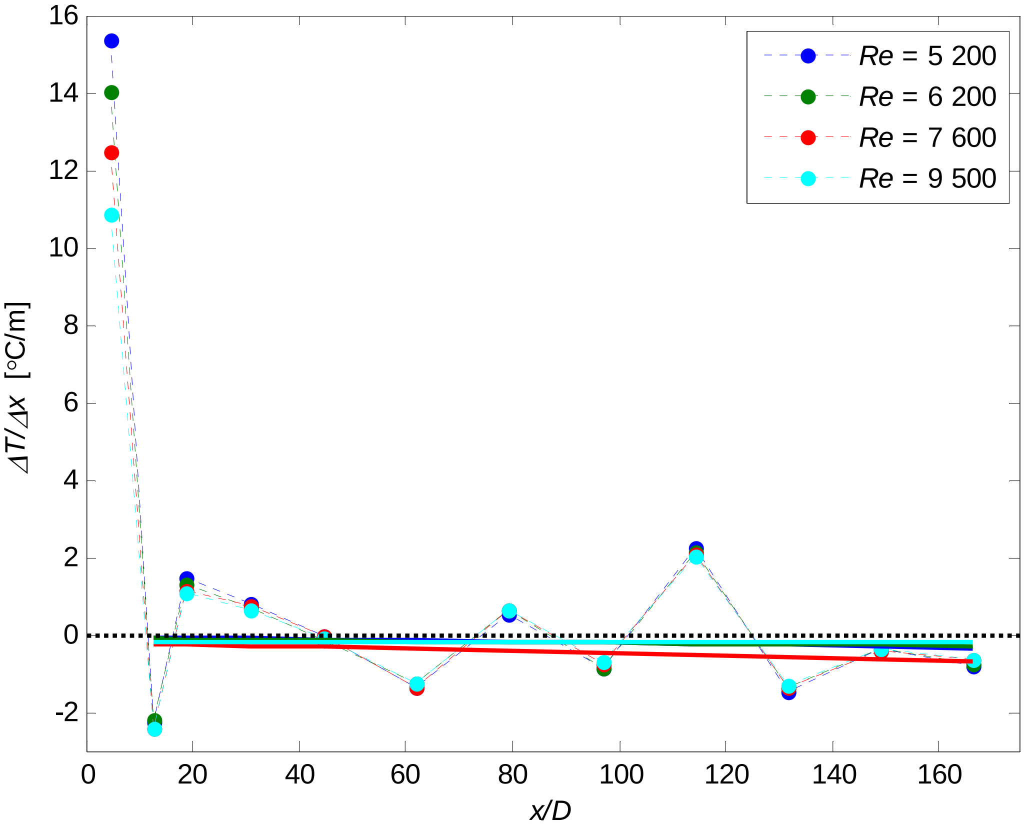

Figure 5.12: Temperature gradients as a function of axial position for turbulent Reynolds numbers between 5 200 and 9 500 at a heat flux of 6.5 kW/m^2. Trend lines fitted through the last 10 data points indicate the average gradients.

To further investigate the thermal entrance lengths, the local heat transfer coefficients and Nusselt numbers are summarised in Figures 5.13 to 5.15 for a heat flux of 6.5 kW/m^2, 8.0 kW/m^2 and 9.5 kW/m^2, respectively. From Figure 5.13, it follows that the local heat transfer coefficients and Nusselt numbers decreased significantly between the inlet of the test section and *x/D* = 8 and then increased gradually along the test section between *x/D* = 17 and *x/D* = 175. This increase was due to the decreasing temperature difference (Figure 5.7(b)) between the surface and fluid, which implies that the flow was still developing.

In the laminar flow regime (600 ≤ *Re* ≤ 2 000), the gradient of the increasing heat transfer coefficients and Nusselt numbers decreased with increasing Reynolds number. However, this gradient increased slightly with increasing Reynolds number in the transitional flow regime (2 400 ≤ *Re* ≤ 2 800). As the Reynolds number was increased further to the low-Reynolds-number-end and turbulent flow regimes, the gradients of the heat transfer coefficients and Nusselt numbers along the tube decreased and approached zero. This confirms that the flow in the turbulent flow regime was fully developed.

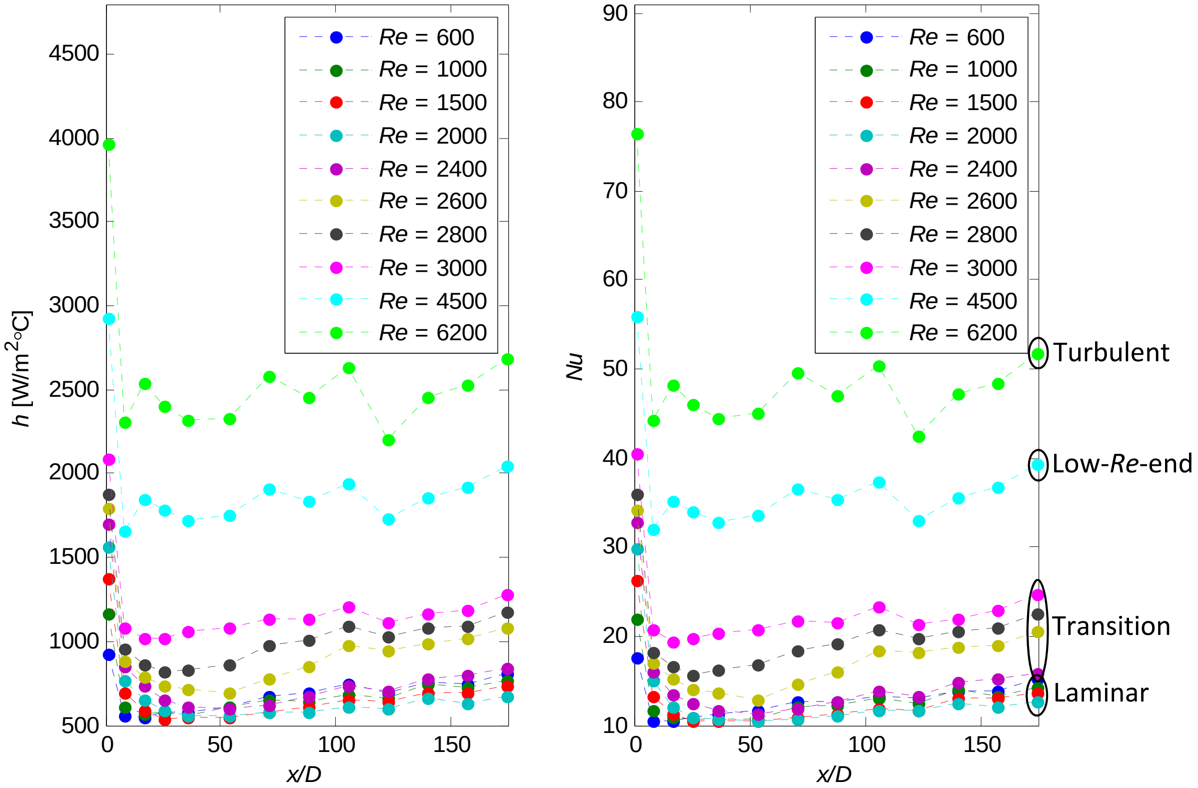

(a) (b)

Figure 5.13: Comparison of local (a) heat transfer coefficients and (b) Nusselt numbers as a function of axial position for different Reynolds numbers at a heat flux of 6.5 kW/m^2

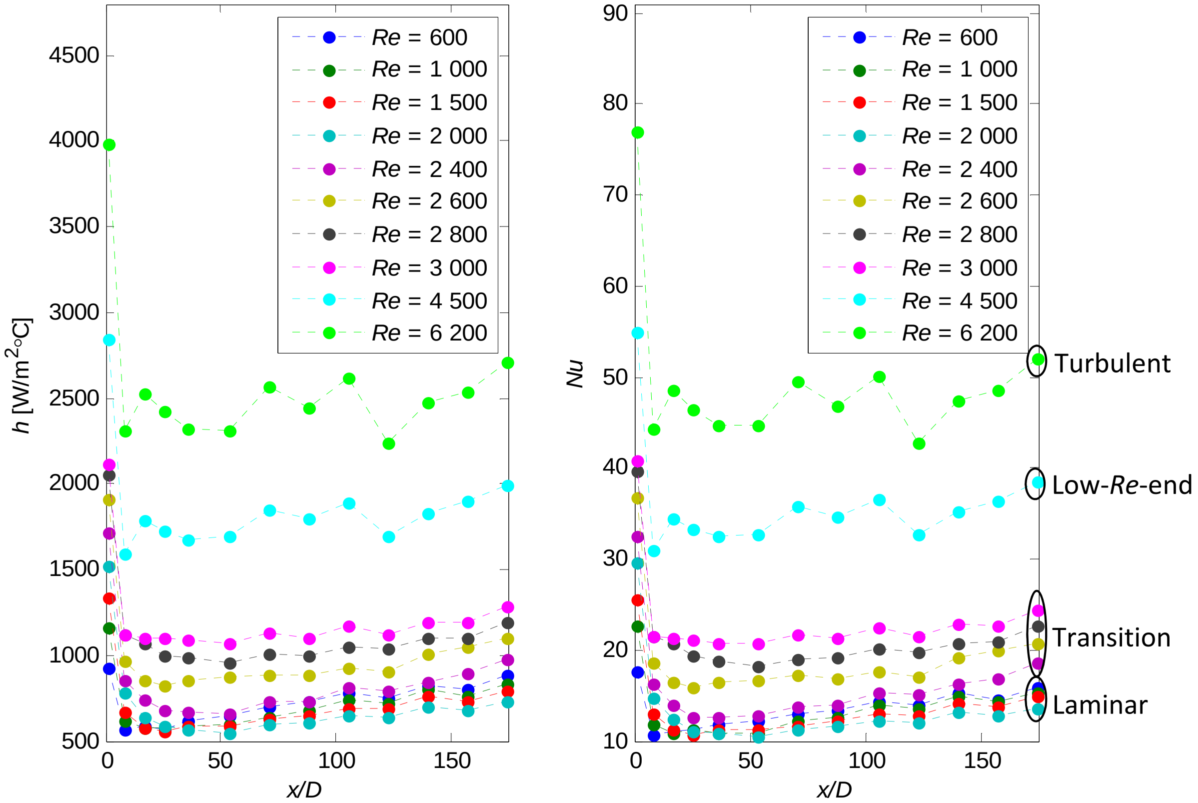

(a) (b)

Figure 5.14: Comparison of local (a) heat transfer coefficients and (b) Nusselt numbers as a function of axial position for different Reynolds numbers at a heat flux of 8.0 kW/m^2

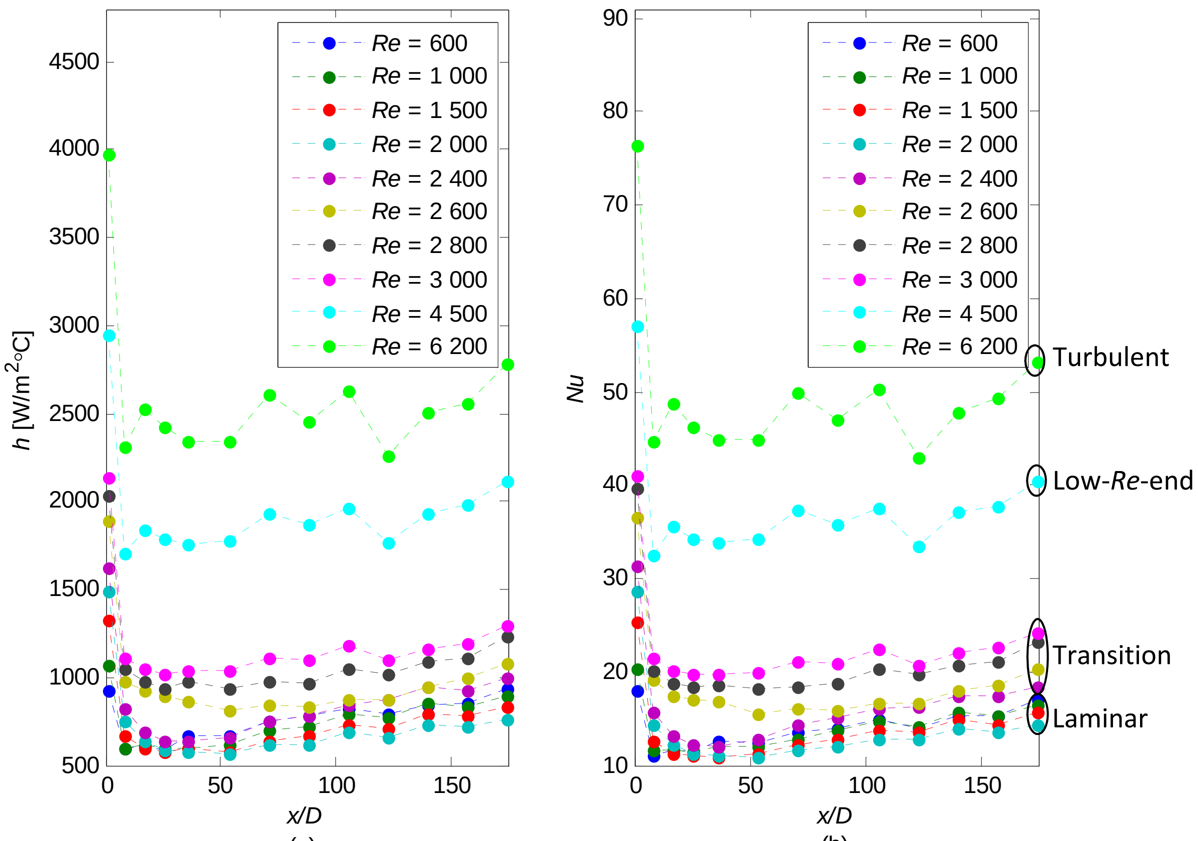

(a) (b)

Figure 5.15: Comparison of local (a) heat transfer coefficients and (b) Nusselt numbers as a function of axial position for different Reynolds numbers at a heat flux of 9.5 kW/m^2

The same trend is observed in the local heat transfer coefficients and Nusselt numbers in Figures 5.14 and 5.15 for the 8.0 kW/m^2 and 9.5kW/m^2 heat fluxes, respectively. As expected, the gradients of the local heat transfer coefficients and Nusselt numbers increased slightly with increasing heat flux. Since the Nusselt number is a function of the Reynolds number and Prandtl number, this increase could either be due to the Prandtl number and/or the effect of secondary flow.

From Figures 5.13 to 5.15, it can be concluded that for Reynolds numbers below 3 000, both heat transfer coefficients and Nusselt numbers increased gradually between *x/D* = 25 and *x/D* = 175. The flow was fully developed between *x/D* = 17 and *x/D* = 175 for Reynolds numbers of 4 400 and 6 200, since the local heat transfer coefficients and Nusselt numbers were approximately constant.

From both forced convection and mixed convection heat transfer theory, it is known that the Nusselt number is a function of not only the Reynolds number, and Rayleigh number for mixed convection, but also the Prandtl number, which is a function of the fluid temperature. To investigate the effect of the Prandtl number, the local Prandtl numbers for different Reynolds numbers at a heat flux of 9.5 kW/m^2 are summarised in Figures 5.16 to 5.18 for laminar, transitional and low-Reynolds-number-end and turbulent flow, respectively.

From Figure 5.16, it follows that the Prandtl number in the laminar flow regime, decreased with increasing *x/D*. A constant heat flux was applied to the test section and thus the temperature of the fluid increased linearly between the inlet and outlet of the test section. This led to decreasing Prandtl numbers as the Prandtl number decreased with increasing temperature.

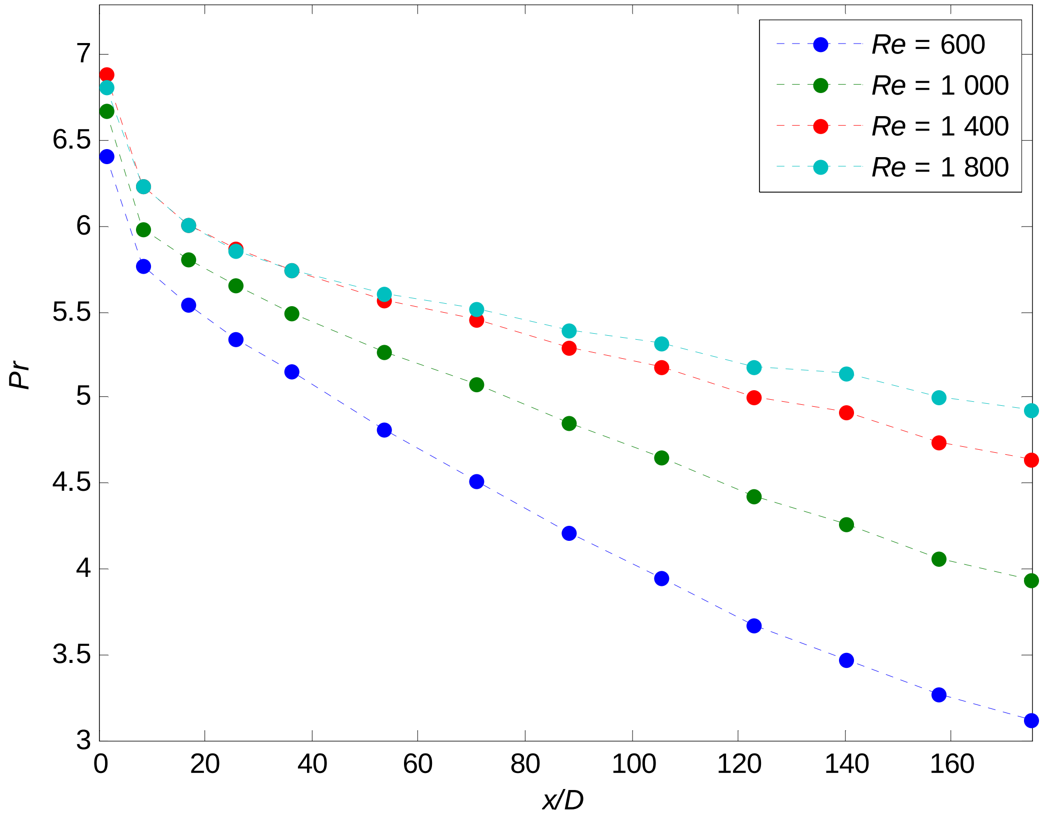

Figure 5.16: Comparison of local Prandtl numbers as a function of axial position for laminar Reynolds numbers between 600 and 1 800 at a heat flux of 9.5 kW/m^2

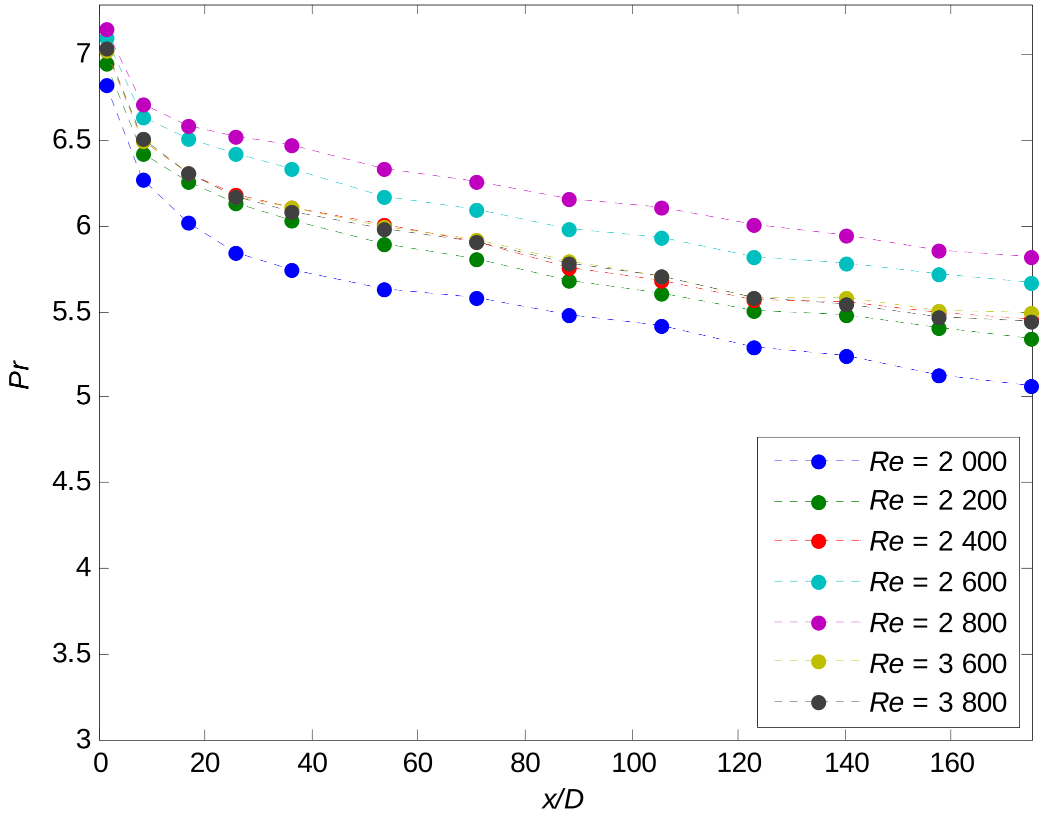

Figure 5.17: Comparison of local Prandtl numbers as a function of axial position for transitional Reynolds numbers between 2 000 and 3 800 at a heat flux of 9.5 kW/m^2

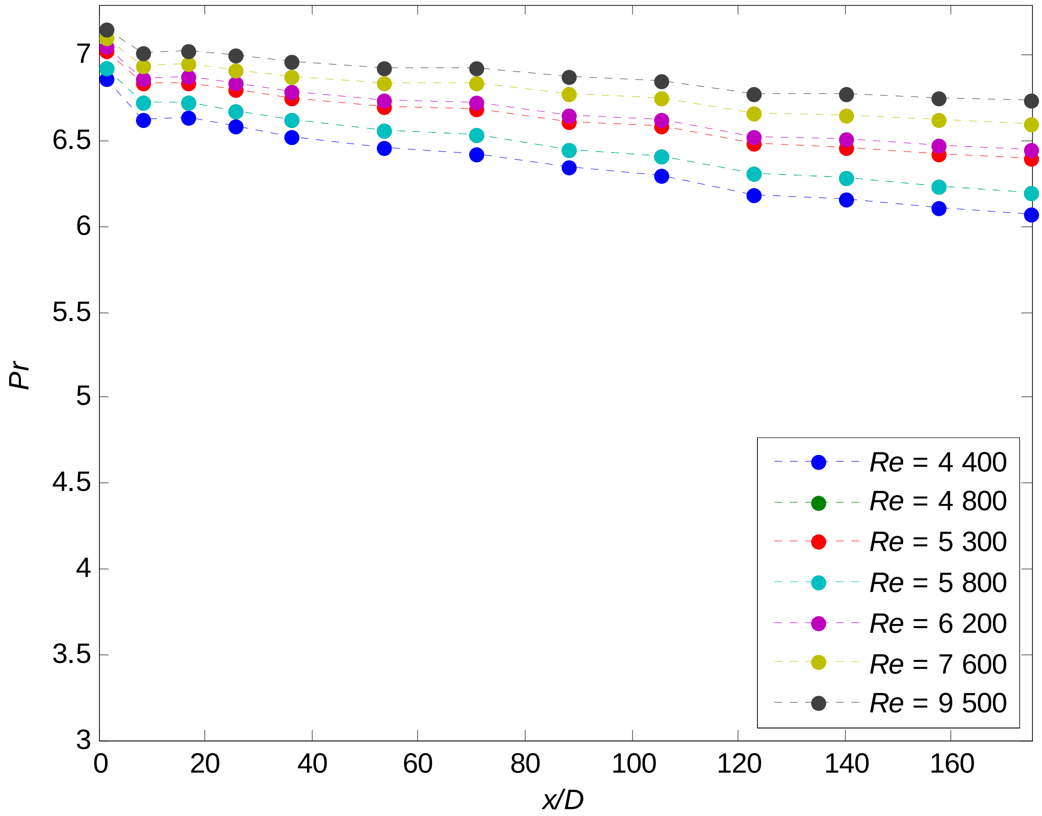

Figure 5.18: Comparison of local Prandtl numbers as a function of axial position for low-Reynolds-number-end and turbulent Reynolds numbers between 4 400 and 9 500 at a heat flux of 9.5 kW/m^2

The same trend was found in Figures 5.17 and 5.18. Furthermore, the magnitude of the drop in Prandtl number decreased with increasing Reynolds number due to the decreasing temperature difference between the inlet and outlet of the test section. The increase in local Nusselt numbers along the tube length was thus not due to the contribution of the Prandtl number, but rather due to the effect of secondary flow. This will be investigated further in Section 5.4.

The local Nusselt numbers against the inverse of the Graetz number (Equation 2.6) for different Reynolds numbers are compared in Figure 5.19. Figure 5.19(a) contains the laminar Reynolds numbers between 600 and 1 800 and Figure 5.19(b) contains the transitional Reynolds numbers between 2 000 and 3 800. Unlike in Figure 5.4 when the flow was dominated by forced convection, the local Nusselt numbers in Figure 5.19(a) increased along the test section ($1/Gz \geq 0.004$) when the flow was dominated by mixed convection. The increasing Nusselt numbers along the test section were therefore due to the effects of secondary flow. The same trend was observed in Figure 5.19(b) in the transitional flow regime between Reynolds numbers of 2 000 and 2 800. However, as the Reynolds number was increased to 3 600 and 3 800, the flow was in the low-Reynolds-number-end regime and the secondary flow effects were suppressed by the turbulent motion of the fluid, thus the Nusselt numbers remained approximately constant.

From Figure 5.19(a) and (b), it can also be concluded that the gradient of the Nusselt numbers along the test section increased with increasing Reynolds number when the Reynolds number varied between 600 and 2 800. This was due to the fact that the flow was still developing. The thermal entrance length increased with increasing Reynolds number and therefore the flow near the outlet of the test section was “closer” to fully developed flow at a Reynolds number of 600 than at 2 800.

Thus, the increasing Nusselt numbers along the test section were also due to the decreasing temperature differences between the surface and fluid since the flow was still developing.

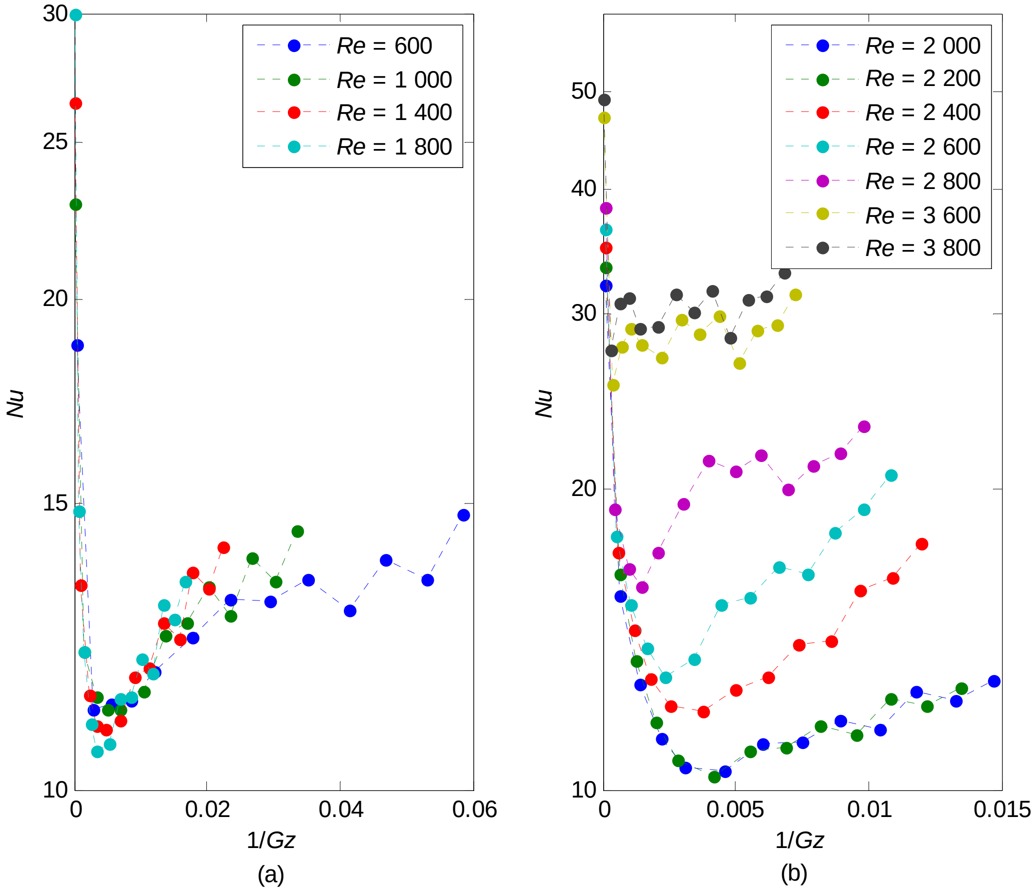

Figure 5.19: Local Nusselt number against the inverse of the Graetz number for (a) laminar and (b) transitional Reynolds numbers at a heat flux of 6.5 kW/m^2

5.4. Secondary flow

When a constant heat flux is applied, the surface and fluid temperatures increase between the inlet and outlet of the test section. Since the properties of the fluid are temperature dependent, the fluid properties vary across the test section. The property-ratio method can be used to account for the variation in fluid properties across the test section (Tam and Ghajar, 1997). The variation in viscosity is responsible for most of the variable property effects. Therefore, to investigate the effects of secondary flow, the ratio of the local heat transfer coefficients at the top and bottom of the test section as well as the ratio of the local dynamic viscosities at the top and bottom of the test section are plotted against *x/D*.

Figure 5.20 compares the heat transfer coefficient ratios and dynamic viscosity ratios for laminar Reynolds numbers, while Figures 5.22 and 5.23 compare the ratios for transitional and turbulent Reynolds numbers at a heat flux of 6.5 kW/m^2. According to Ghajar and Tam (1991), the flow is dominated by forced convection when the heat transfer coefficient ratio is close to unity, while the flow is dominated by mixed convection when the heat transfer coefficient is much less than unity (≤ 0.8).

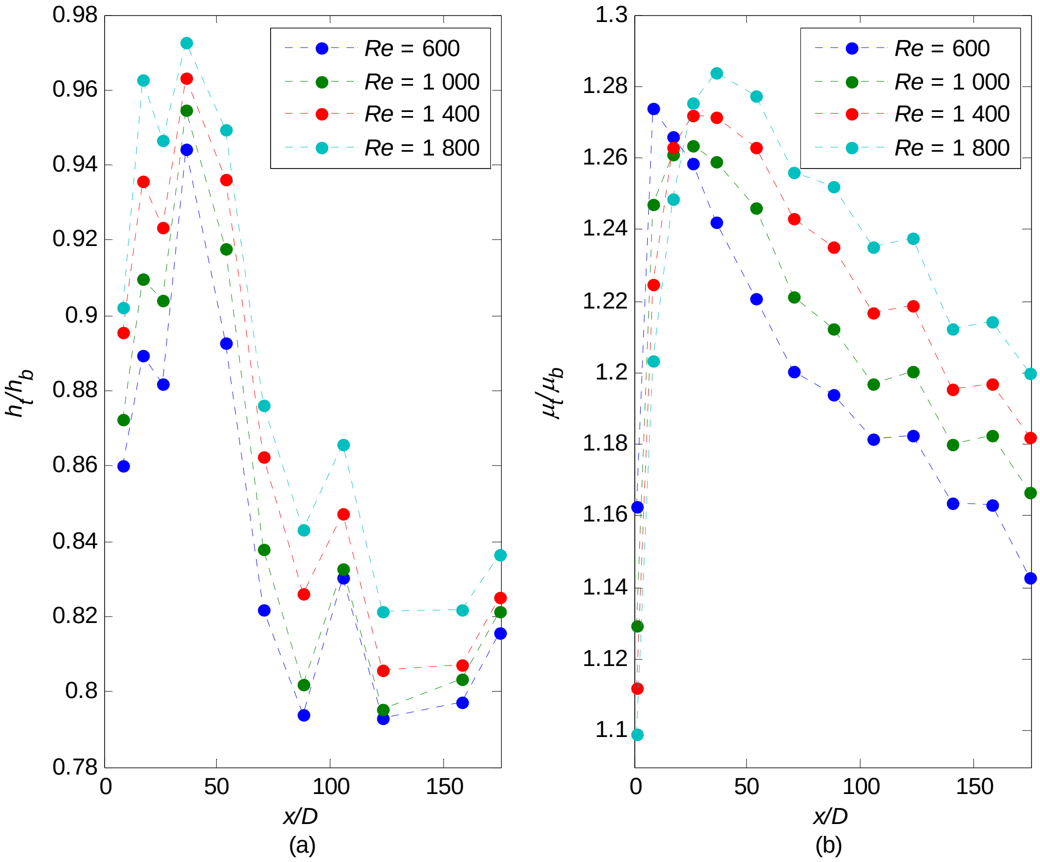

(a) (b)

Figure 5.20: Comparison of (a) local heat transfer coefficient ratio and (b) local dynamic viscosity ratio as a function of axial position for Reynolds numbers between 600 and 1 800 and a heat flux of 6.5 kW/m^2

From Figure 5.20(a), it follows that the secondary flow effects were small in the first part of the test section (*x/D* ≤ 88) where the heat transfer coefficient ratio was close to unity. As *x/D* increased beyond 88, the heat transfer coefficient ratio decreased to below 0.8 and secondary flow effects became significant. Similar to the results obtained by Ghajar and his co-workers, secondary flow effects required a certain tube length to develop and become dominant. The thickness of the thermal boundary layer might be a reason for this as it increased with increasing *x/D*. Figure 5.21 is a schematic representation of the secondary flow effects inside a horizontal tube with a developing thermal boundary layer. Secondary flow exists due to the temperature difference (and density difference) between the fluid near the surface and the fluid outside the thermal boundary layer. When the thermal boundary layer is very thin, the secondary flow effects are suppressed. As the thickness of the thermal boundary layer increases, there is more “room” for secondary flow and mixed convection dominates.

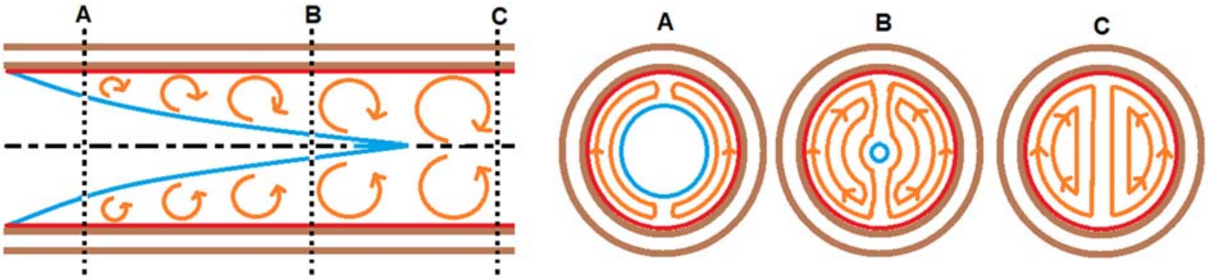

Figure 5.21: Schematic representation of secondary flow inside a heated tube with an increasing thermal boundary layer

From Figure 5.20(a), it also follows that the heat transfer coefficient ratio increased with increasing Reynolds number. As the Reynolds number was increased, the thermal entrance length increased and the thickness of the thermal boundary layer decreased. Thus, at a specific location on the test section, the thickness of the thermal boundary layer decreased with increasing Reynolds number, which led to decreasing secondary flow effects. Furthermore, from Figure 5.20(b), it follows that the viscosity ratio decreased with increasing Reynolds number due to the decreasing temperature between the surface and fluid (as shown in Figure 5.7).

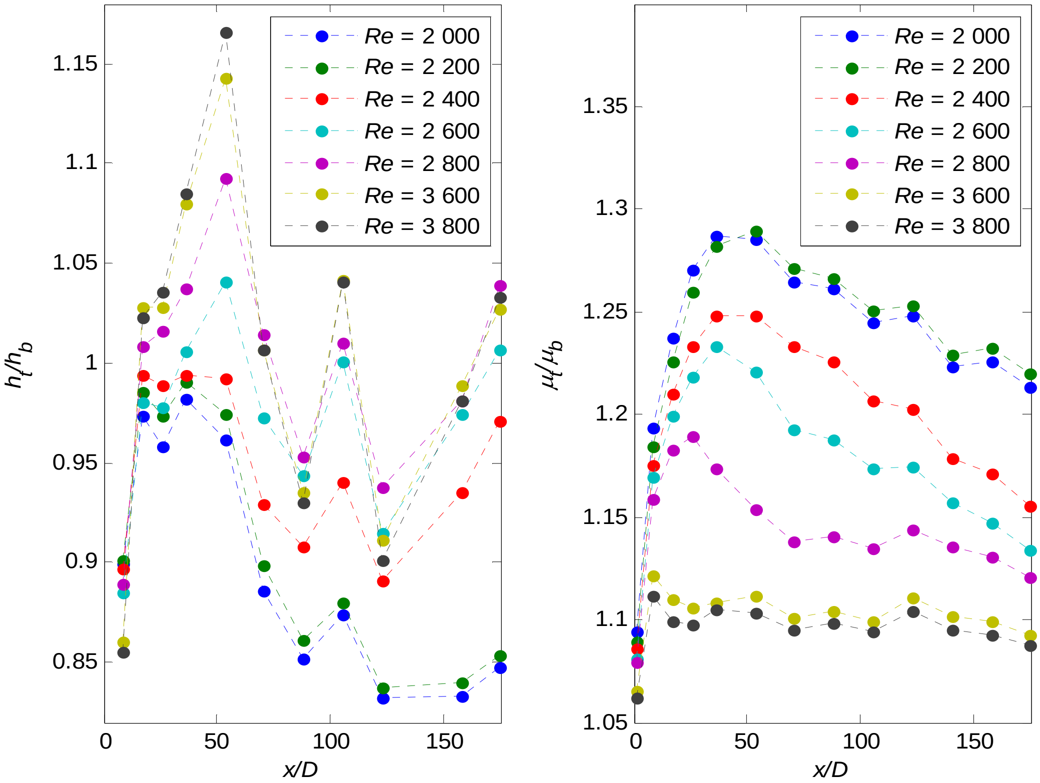

(a) (b)

Figure 5.22: Comparison of (a) local heat transfer coefficient ratio and (b) local dynamic viscosity ratio as a function of axial position for transitional Reynolds numbers between 2 000 and 3 800 at a heat flux of 6.5 kW/m^2

In the transitional flow regime, the measurements show that the heat transfer coefficient ratio decreased significantly with decreasing Reynolds numbers between *x/D* = 122 and *x/D* = 175 (Figure 5.22(a)). At the beginning of the transitional flow regime (*Re* = 2 000 and *Re* = 2 200), the trend was similar to that of laminar flow since the heat transfer coefficient ratio increased between *x/D* = 1.3 and *x/D* = 53.4 and then decreased as *x/D* was increased further. At a Reynolds number of 2 400, the secondary flow effects decreased and the viscosity ratio varied between 0.9 and 1. As the Reynolds number was increased further and the flow approached the end of the transitional flow regime, the velocity of the fluid suppressed the secondary flow effects and the heat transfer coefficient ratio was close to unity. Similar to Figure 5.20(b), the dynamic viscosity ratios in Figure 5.22(b) also decreased with increasing Reynolds number due to the decreasing temperature difference between the surface and the fluid. When the Reynolds number was greater than 3 600, the dynamic viscosity ratios along the test section were close to unity due to the small temperature difference between the fluid near the surface and the centre line of the tube.

The experiments in the low-Reynolds-number-end and turbulent flow regimes (Figure 5.23(a)) showed that the heat transfer coefficient ratio was close to unity for all Reynolds numbers. Thus, the turbulent motion of the fluid suppressed the secondary flow effects and the flow was dominated by forced convection. However, a significant peak was found at $x/D = 53.4$ and the magnitude of this peak increased with increasing Reynolds number. To investigate the reason for this peak, the surface temperatures along the test section were analysed and the details can be found in Appendix E. It was concluded that the thermocouples at the bottom of the test section at $x/D = 36$ and $x/D = 53.4$ measured slightly higher temperatures. As the temperature differences in the low-Reynolds-number-end and turbulent flow regimes were very small, these "higher temperatures" only became significant at Reynolds numbers greater than 4 400.

Similar to Figures 5.20(b) and 5.22(b), the dynamic viscosity ratios in Figure 5.23(b) continued to decrease with increasing Reynolds number. This seemed unexpected at first, but from Figure 5.7, it follows that the temperature difference between the surface and the fluid decreased with increasing Reynolds number in the low-Reynolds-number-end and turbulent flow regimes. This explains why the viscosity ratio approached unity as the Reynolds number was increased.

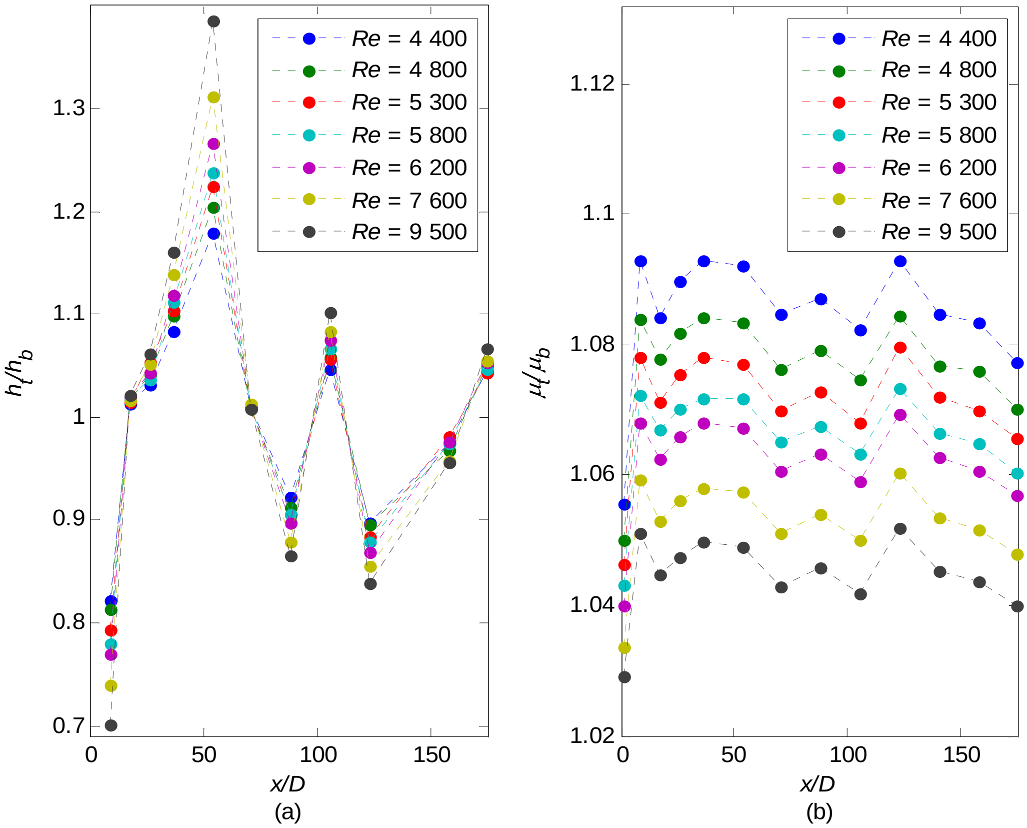

(a)

(b)

Figure 5.23: Comparison of (a) local heat transfer coefficient ratio and (b) local dynamic viscosity ratio as a function of axial position for Reynolds numbers between 4 400 and 9 500 at a heat flux of 6.5 kW/m^2

Figure 5.24 compares the heat transfer coefficient ratios and dynamic viscosity ratios for laminar Reynolds numbers between 600 and 1 800 at a heat flux of 9.5 kW/m^2. When comparing Figures 5.20 and 5.24, it can be concluded that the secondary flow effects increased with increasing heat flux. As the heat flux was increased, the temperature difference between the surface and fluid increased (as shown in Figures 5.7 and 5.9), which not only led to increased heat transfer coefficients, but also increased the Grashof and Rayleigh numbers, thus increased secondary flow effects.

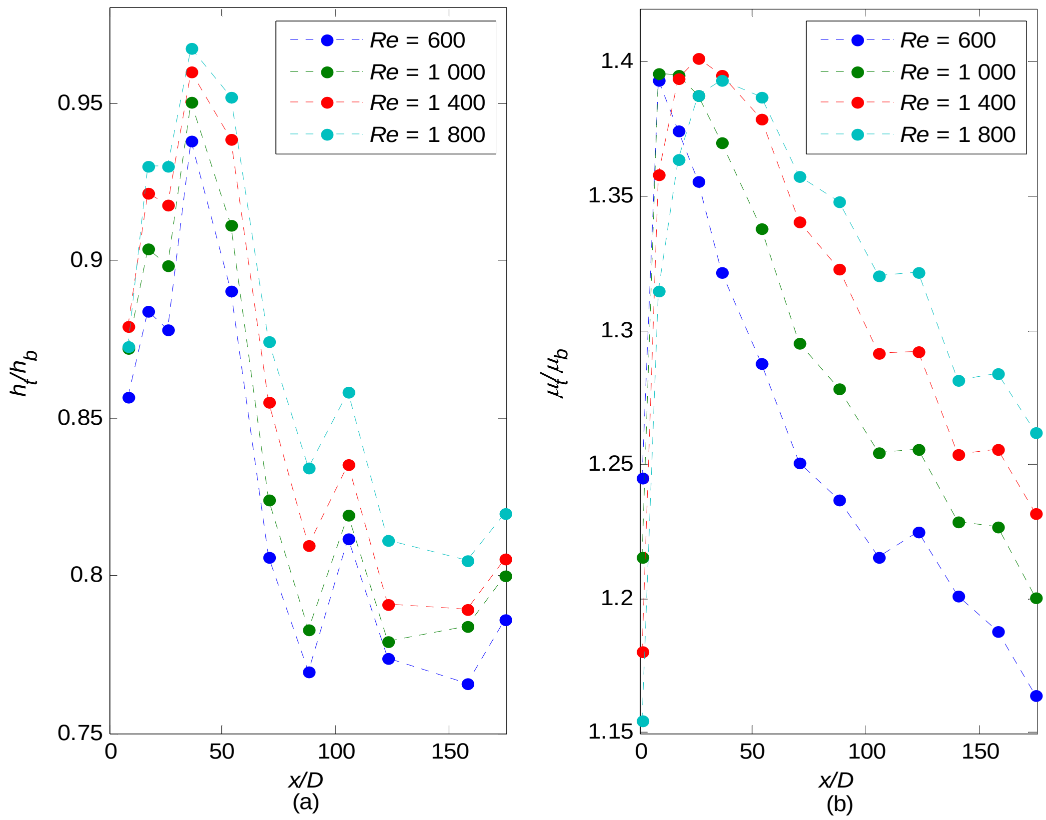

Figure 5.24: Comparison of (a) local heat transfer coefficient ratio and (b) local dynamic viscosity ratio as a function of axial position for laminar Reynolds numbers between 600 and 1 800 at a heat flux of 9.5 kW/m²

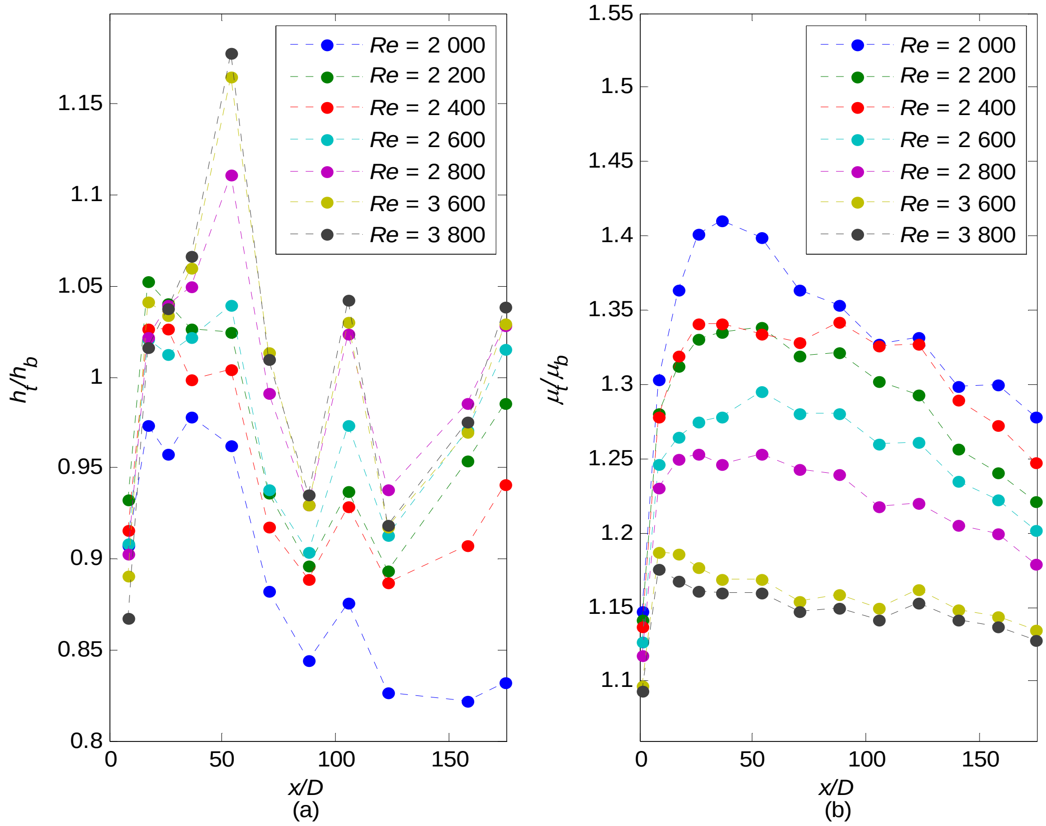

Figure 5.25: Comparison of (a) local heat transfer coefficient ratio and (b) local dynamic viscosity ratio as a function of axial position for Reynolds numbers between 2 000 and 3 800 at a heat flux of 9.5 kW/m²

Figure 5.25 compares the heat transfer coefficient ratios and dynamic viscosity ratios for transitional Reynolds numbers between 2 000 and 3 800 at a heat flux of 9.5 kW/m^2. When comparing Figures 5.22(a) and 5.25(a), it is found that, similar to the laminar flow regime, the secondary flow effects increased with increasing heat flux when the Reynolds number was below 2 800. Once the Reynolds number was increased further, the velocity of the fluid suppressed the secondary flow effects and the difference between the two heat fluxes became negligible. From Figures 5.22(b) and 5.25(b), it follows that the magnitude of the dynamic viscosity ratio increased with increasing heat flux due to the increasing temperature differences between the surface and the fluid.

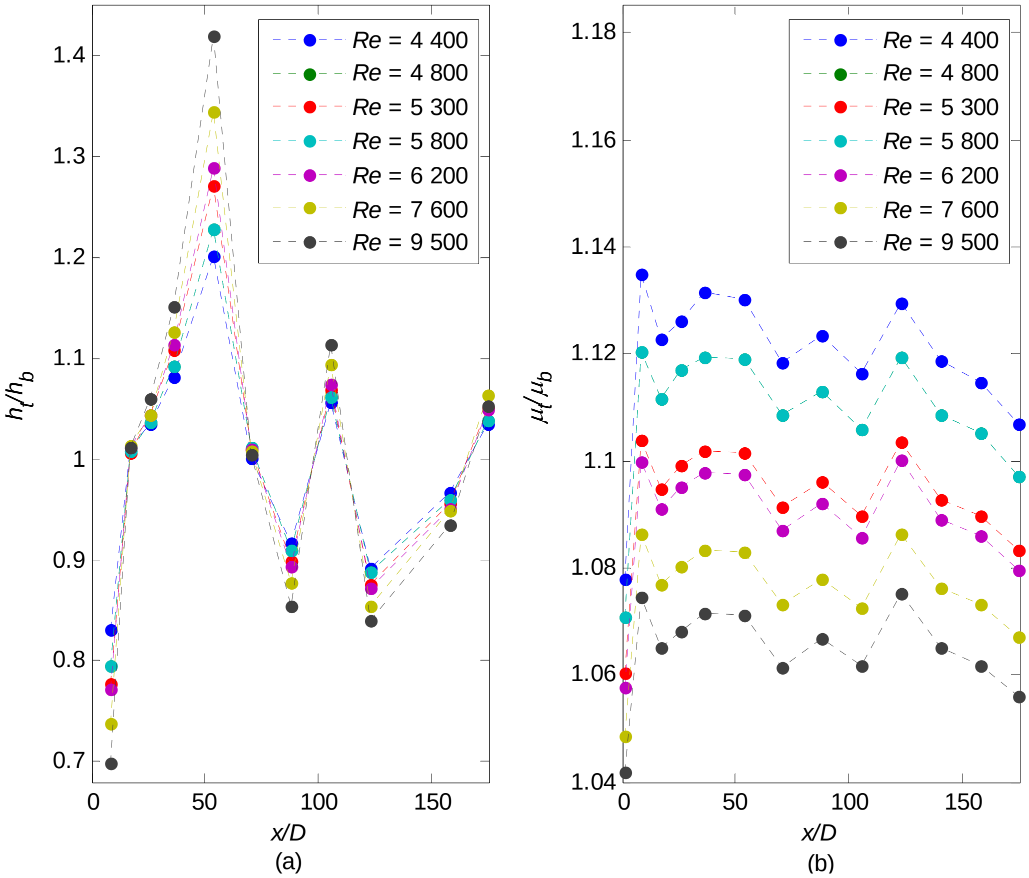

Figure 5.26: Comparison of (a) local heat transfer coefficient ratio and (b) local dynamic viscosity ratio as a function of axial position for Reynolds numbers between 4 400 and 9 500 at a heat flux of 9.5 kW/m^2

The heat transfer coefficient ratios and dynamic viscosities for low-Reynolds-number-end and turbulent Reynolds numbers between 4 400 and 9 500 when a heat flux of 9.5 kW/m^2 was applied are summarised in Figure 5.26. Similar to Figure 5.23(a), the heat transfer coefficient ratio increased between x/D = 1.3 and x/D = 53.4 and then decreased as x/D was increased further. The heat transfer coefficient ratio also increased at x/D = 53.4, due to the thermocouple at the bottom of the test section which measured a slightly higher temperature. Although the dynamic viscosity ratios in Figure 5.26(b) were close to unity, they were slightly higher than the dynamic viscosity ratios in Figure 5.23(b). This is due to the increased heat flux and therefore greater temperature difference between the surface and fluid.

5.5. Heat transfer coefficients

As highlighted in Chapters 1 and 2, previous studies focused primarily on the heat transfer characteristics of fully developed flow. Therefore, this section is devoted to the heat transfer characteristics of developing flow. As shown in Figure 3.4, 13 thermocouple stations were spaced along the test section. The Nusselt numbers and Colburn *j*-factors were calculated at each thermocouple station and were compared with each other in this section. The advantage of the Colburn *j*-factor results is that it considers the variation of the Prandtl number (or variation in fluid properties), which is not constant during experiments.

Figure 5.27 contains the Nusselt numbers and Colburn *j*-factors as a function of Reynolds number at $x/D = 1.3$ to $x/D = 36$ at a heat flux of 6.5 kW/m^2. The Reynolds number was varied between 500 and 10 000 to ensure that the whole transitional flow regime, as well as sufficient parts of the laminar and turbulent flow regimes, was covered. From Figure 5.27(a), it follows that Nusselt numbers at the thermocouple station close to the inlet of the test section ($x/D = 1.3$) were significantly higher than at the other thermocouple stations, as expected, because the thermal boundary layer at this station was the thinnest. The local heat transfer coefficients were significantly higher at the inlet of the test section and then decreased as the flow developed. This explains why the Nusselt numbers in Figure 5.27(a) decreased with increasing x/D.

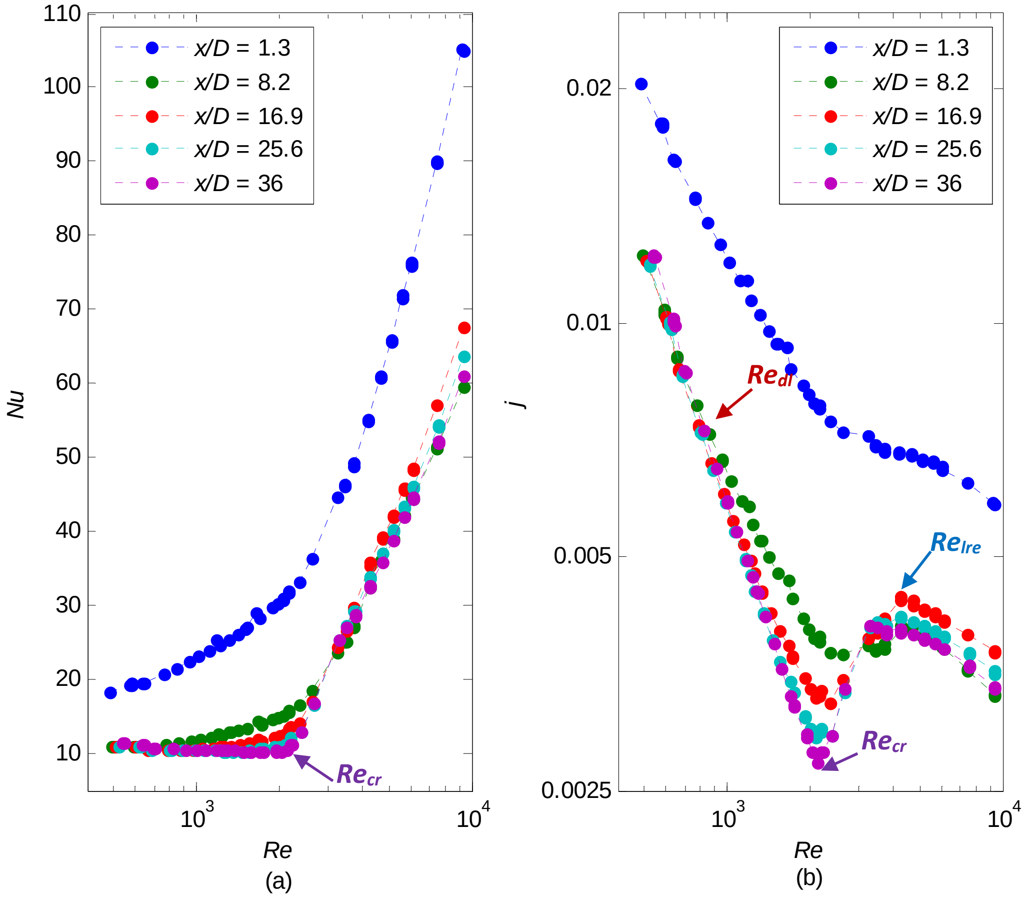

Figure 5.27: Comparison of (a) Nusselt numbers and (b) Colburn *j*-factors as a function of Reynolds number for $x/D = 1.3$ to $x/D = 36$ at a heat flux of 6.5 kW/m^2

At $x/D = 1.3$, the Nusselt numbers increased gradually with increasing Reynolds number and a clear distinction between the different flow regimes could not be made. A similar trend is observed at $x/D = 8.2$, however, the Nusselt numbers were significantly lower than at $x/D = 1.3$ as the flow started to develop. At $x/D = 16.9$, the laminar and turbulent flow regimes were more pronounced. The laminar flow regime is where the Nusselt numbers formed an approximate horizontal line between Reynolds numbers of 400 and 1 000, while the turbulent flow regime is where the Nusselt numbers formed a diagonal line between Reynolds numbers of 5 000 and 10 000.

The same trend is observed in the Colburn *j*-factors in Figure 5.27(b). The Colburn *j*-factors were significantly higher at $x/D = 1.3$, due to the high heat transfer coefficients at the inlet of the test section. As x/D increased, the Colburn *j*-factors decreased due to the decreasing heat transfer coefficients along the tube length. From Figure 5.27, it also follows that the Reynolds number at which transition started (Re_{cr}) and ended (Re_{lre}) decreased with increasing x/D.

Although four flow regimes were defined in Figure 3.8, five different flow regions were identified from the Colburn *j*-factors in Figure 5.27(b) and these regions are summarised in Figure 5.28. The transitional (Region C), low-Reynolds-number-end (Region D) and turbulent (Region E) flow regimes remained the same. However, the laminar flow regime was split into the laminar (Region A) and developing laminar (Region B) flow regimes.

Between Reynolds numbers of 500 and 800 (depending on the value of x/D), the Colburn *j*-factors formed a straight diagonal line, which indicated that the flow was laminar (Region A). As x/D was increased, the Reynolds number (Re_{dl}) at which the Colburn *j*-factors began to deviate from this line increased, which implied that the width of the laminar flow regime ($Re < Re_{dl}$) was increased. However, between the end of the laminar region (Re_{dl}) and the start of the transitional region (Re_{cr}), the Colburn *j*-factors deviated from the straight diagonal line. This developing laminar region (Region B) seems to be unique to developing flow, since the width of the developing laminar region ($Re_{dl} \leq Re \leq Re_{cr}$) decreased with increasing x/D and occurred only between $x/D = 1.3$ and $x/D = 36$.

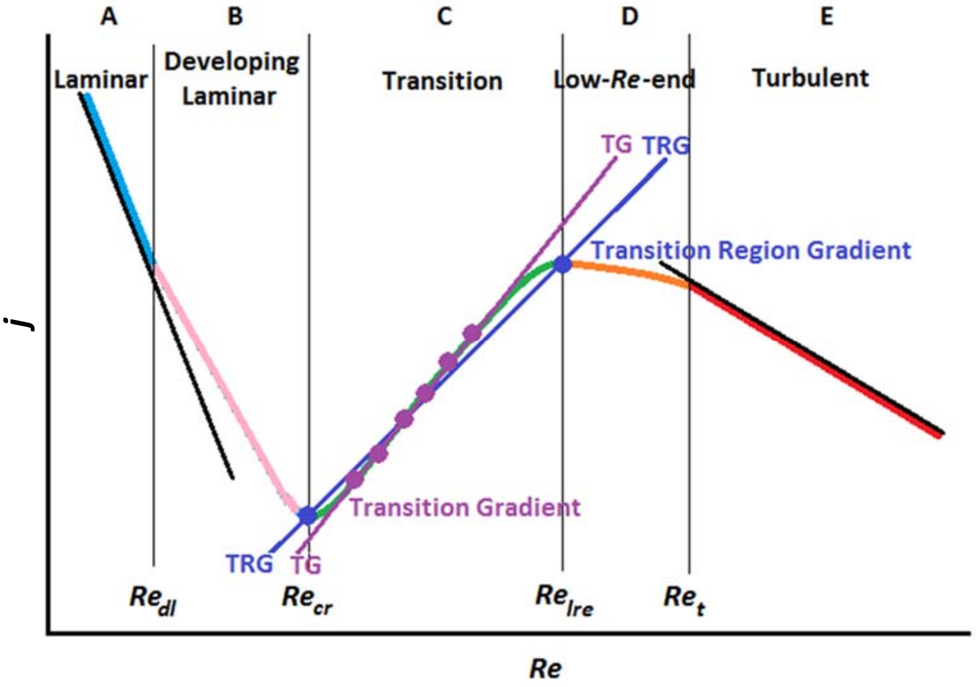

Figure 5.28: Schematic representation of the laminar, developing laminar, transitional, low-Reynolds-number-end and turbulent flow regimes

Figure 5.29 contains the Nusselt numbers and Colburn *j*-factors for $x/D = 53.4$ to $x/D = 174.9$ at a heat flux of 6.5 kW/m^2 and the Reynolds number was varied between 500 and 10 000. From Figure 5.29(a), it follows that the Nusselt numbers increased with increasing x/D in the laminar flow regime.

As shown in Figure 5.20, secondary flow only became significant after approximately *x/D* = 53. This explains why the laminar Nusselt numbers ($Re \leq 1\,000$) in Figure 5.27 were independent of *x/D*, while the laminar Nusselt numbers in Figure 5.29 increased with increasing *x/D*. Furthermore, the Nusselt numbers increased slightly with increasing *x/D* in the transitional, low-Reynolds-number-end and turbulent flow regimes.

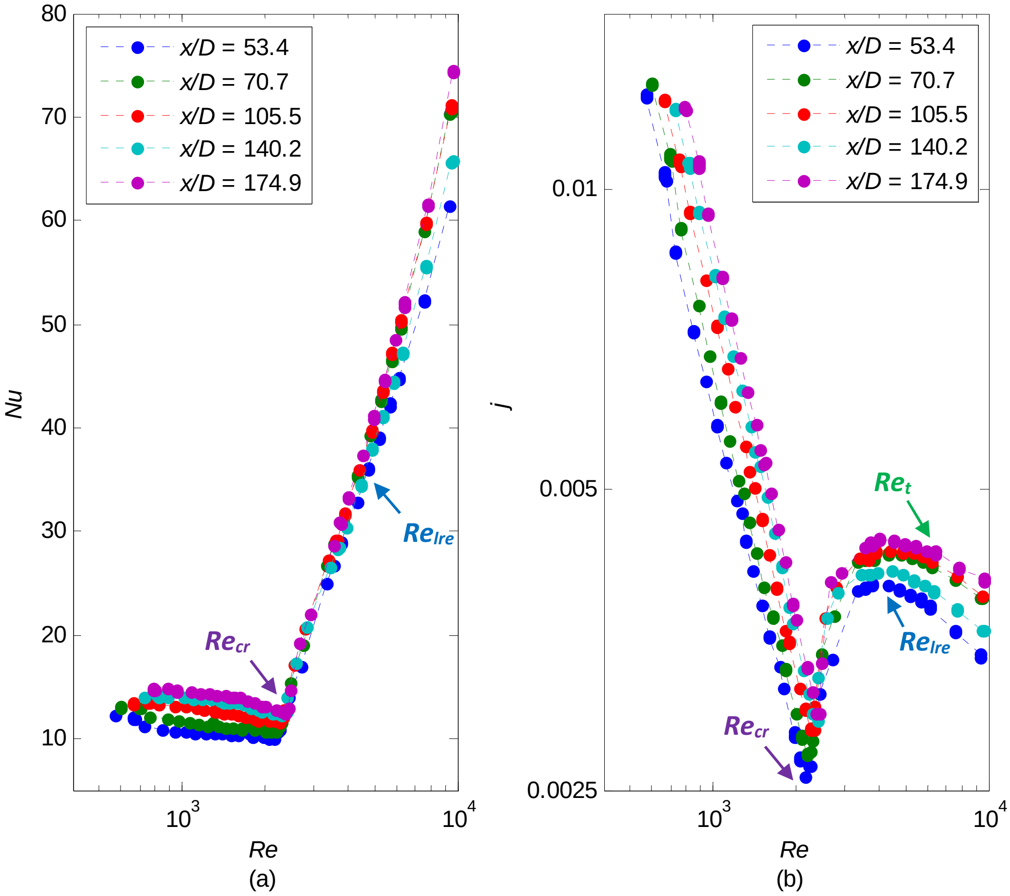

Figure 5.29: Comparison of (a) Nusselt numbers and (b) Colburn *j*-factors as a function of Reynolds number for *x/D* = 53.4 to *x/D* = 174.9 at a heat flux of 6.5 kW/m^2

The different flow regimes can be identified from the Nusselt numbers in Figure 5.29(a). Between Reynolds numbers of approximately 500 and 2 300 (depending on the value of *x/D*), the flow was laminar and the Nusselt numbers formed a straight line, but decreased slightly with increasing Reynolds number. At a Reynolds number of approximately 2 300, the Nusselt numbers began to increase, which indicated the start of the transitional flow regime (Re_{cr}). The low-Reynolds-number-end and turbulent flow regimes followed at a Reynolds number of approximately 4 000. However, no clear distinction between these two flow regimes could be made from the Nusselt number results.

From Figure 5.29(b), it follows that the Colburn *j*-factors in the laminar, transitional, low-Reynolds-number-end and turbulent flow regimes increased with increasing *x/D*. This increase was the greatest in the laminar flow regime, less in the turbulent and low-Reynolds-number-end regimes and very little in the transitional flow regime. In the laminar flow regime, secondary flow effects dominated. However, as the velocity of the fluid was increased, the secondary flow effects were suppressed by the velocity of the fluid. In the turbulent flow regime, the flow was dominated by forced convection, therefore the increasing Colburn *j*-factors could not be due to secondary flow effects.

When the turbulent heat transfer coefficients were investigated in terms of the Nusselt number in Figure 5.29(a), there was a slight difference between the different values of *x/D*, however, this difference was less than when the heat transfer coefficients were investigated in terms of the Colburn *j*-factors in Figure 5.29(b). From Equation 3.14 it follows that the Colburn *j*-factor is a function of the Nusselt number, Reynolds number and Prandtl number. It was concluded from Figure 5.18, that the Prandtl numbers in the turbulent flow regime decreased along the tube length. Since the Colburn *j*-factors were inversely proportional to the Prandtl number, the decreasing Prandtl numbers led to increasing Colburn *j*-factors along the tube length.

Transition started (Re_{cr}) at a Reynolds number of 2 148 at *x/D* = 53.4 and was delayed to 2 368 at *x/D* = 174.9. The end of transition (Re_{lre}) was also delayed from a Reynolds number of 4 302 at *x/D* = 53.4 to 4 507 at *x/D* = 174.9. The low-Reynolds-number-end region occurred between Reynolds numbers of approximately 4 300 and 6 200 (depending on the value of *x/D*). From Figure 5.29(b), it also follows that the turbulent region (Re_t) started at approximately 6 200 for all values of *x/D*, as expected, because the flow in the turbulent flow regime was fully developed and was therefore independent of *x/D*.

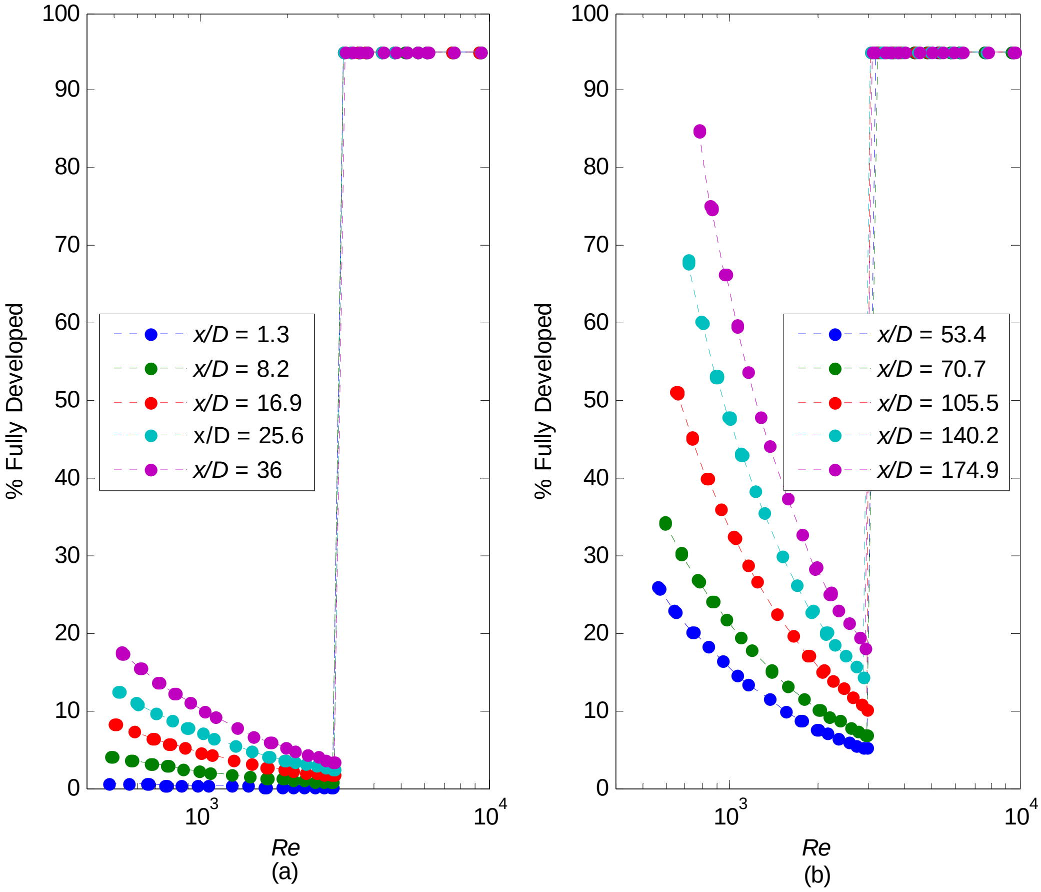

(a)

(b)

Figure 5.30: Comparison of percentage fully developed flow tube length as a function of Reynolds number for (a) *x/D* = 1.3 to *x/D* = 36 and (b) *x/D* = 53.4 to *x/D* = 174.9 at a heat flux of 6.5 kW/m²

Figure 5.30 compares the percentage fully developed regions for different values of *x/D* at a heat flux of 6.5 kW/m². The percentage fully developed flow was determined by dividing the tube length at the specific thermocouple station with the theoretical thermal entrance length. From Figure 5.30, it follows that the percentage fully developed flow at a fixed *x/D* in the laminar flow regime decreased with increasing Reynolds number, as expected, because the thermal entrance length increased with increasing Reynolds number. In the low-Reynolds-number-end and turbulent flow regimes, it can be assumed that the flow in the entire test section was fully developed since the thermal entrance length was only 5% of the length of the test section. When comparing Figures 5.30(a) and (b), it follows that the percentage fully developed regions of the tube in the laminar flow regime increased with increasing *x/D*, as expected.

Figures 5.31 and 5.32 contain the Nusselt numbers and Colburn *j*-factors for different values of *x/D*. The Reynolds number was varied between 500 and 10 000 and a heat flux of 8.0 kW/m^2 was applied in Figure 5.31 while a heat flux of 9.5 kW/m^2 was applied in Figure 5.32. The same trends that were observed in the results of the 6.5 kW/m^2 heat flux were observed in the results of the 8.0 kW/m^2 and 9.5 kW/m^2 heat fluxes. The laminar Nusselt numbers of all three heat fluxes were independent of *x/D* when *x/D* was smaller than 53.4 and thus confirmed that the secondary flow effects required a certain length to become significant. Furthermore, both start and end of transition occurred earlier with increasing *x/D.*

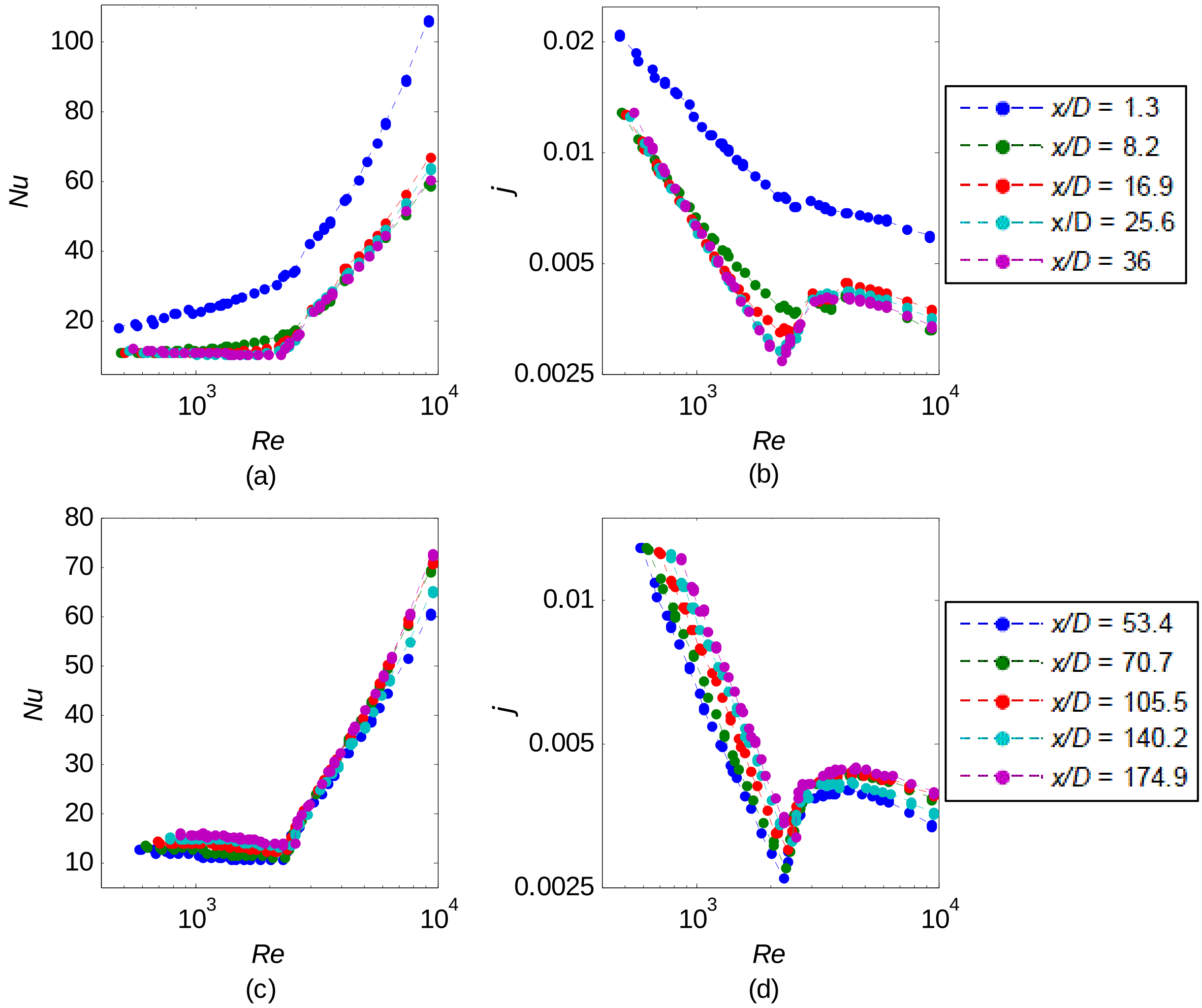

Figure 5.31: Comparison of (a) Nusselt numbers and (b) Colburn *j*-factors for *x/D* = 1.3 to *x/D* = 36 and (c) Nusselt numbers and (d) Colburn *j*-factors for *x/D* = 53.4 to *x/D* = 174.9 as a function of Reynolds number at a heat flux of 8.0 kW/m^2

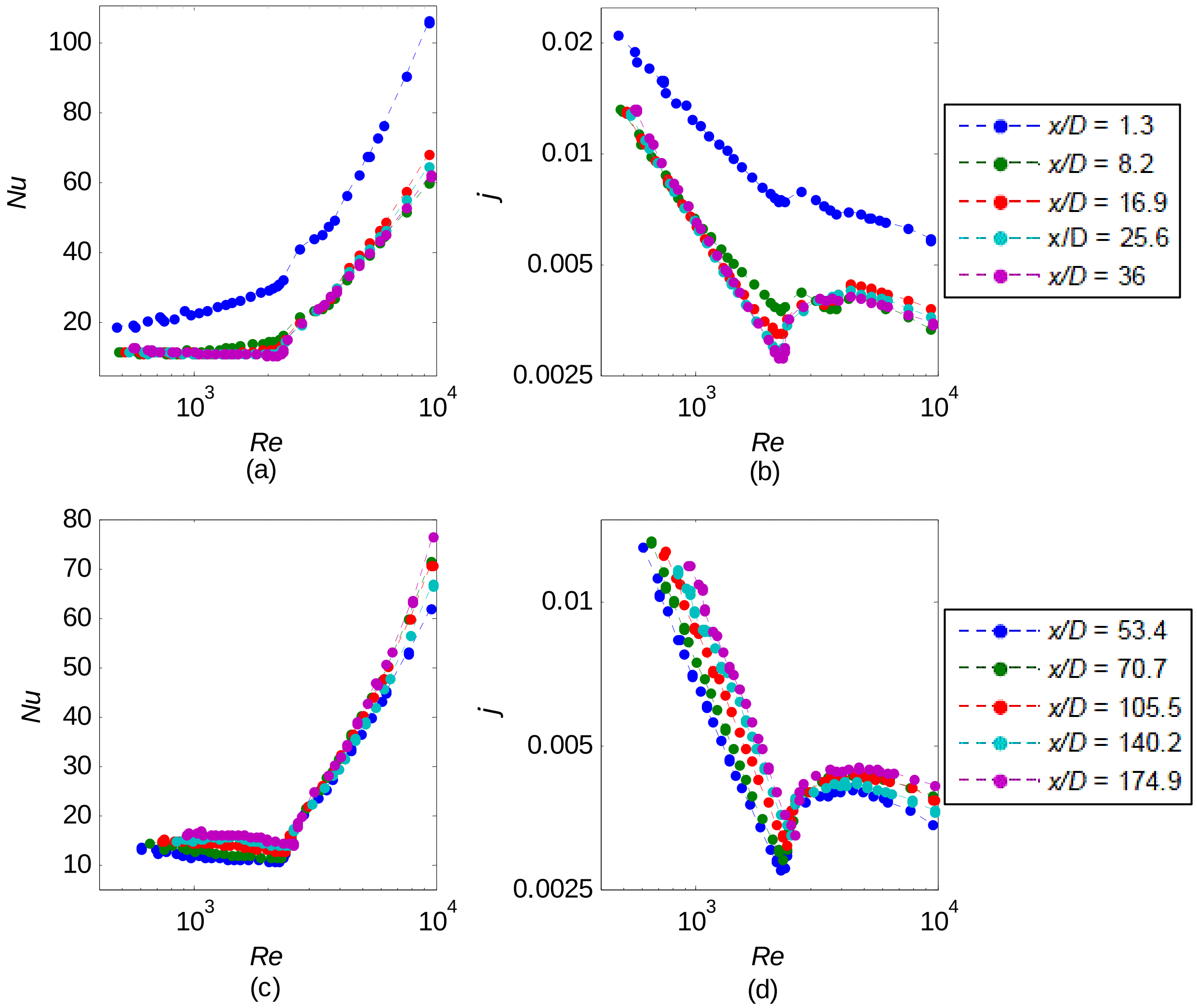

Figure 5.32: Comparison of (a) Nusselt numbers and (b) Colburn *j*-factors for *x/D* = 1.3 to *x/D* = 36 and (c) Nusselt numbers and (d) Colburn *j*-factors for *x/D* = 53.4 to *x/D* = 174.9 as a function of Reynolds number at a heat flux of 9.5 kW/m²

To gain a better understanding of the influence of heat flux on developing flow, the Colburn *j*-factors of the 6.5 kW/m² and 9.5 kW/m² heat fluxes were compared in Figure 5.33. When considering Figure 5.33(a) and (b), it follows that a slightly shorter thermal entrance length was required when the heat flux was increased since the shape of the laminar and transitional Colburn *j*-factors at *x/D* = 25.6 and *x/D* = 36 in Figure 5.33(b) was closer to the shape of fully developed flow Colburn *j*-factors. The shape of fully developed Colburn *j*-factors is similar to that of the Colburn *j*-factors at *x/D* = 174.9 in Figure 5.33(c). There was no significant difference in the magnitude of the Colburn *j*-factors of the two different heat fluxes in Figures 5.33(a) and (b), which confirmed that secondary flow required a certain length to develop. However, when comparing Figures 5.33(c) and (d), it follows that the laminar Colburn *j*-factors of the 9.5 kW/m² heat flux were greater than for the 6.5 kW/m² heat flux due to the effects of secondary flow. However, there was no significant difference between the magnitudes of the turbulent Colburn *j*-factors. When comparing Figures 5.33(c) and (d), it also follows that transition *(Re_{cr})* was slightly delayed for increasing heat flux.

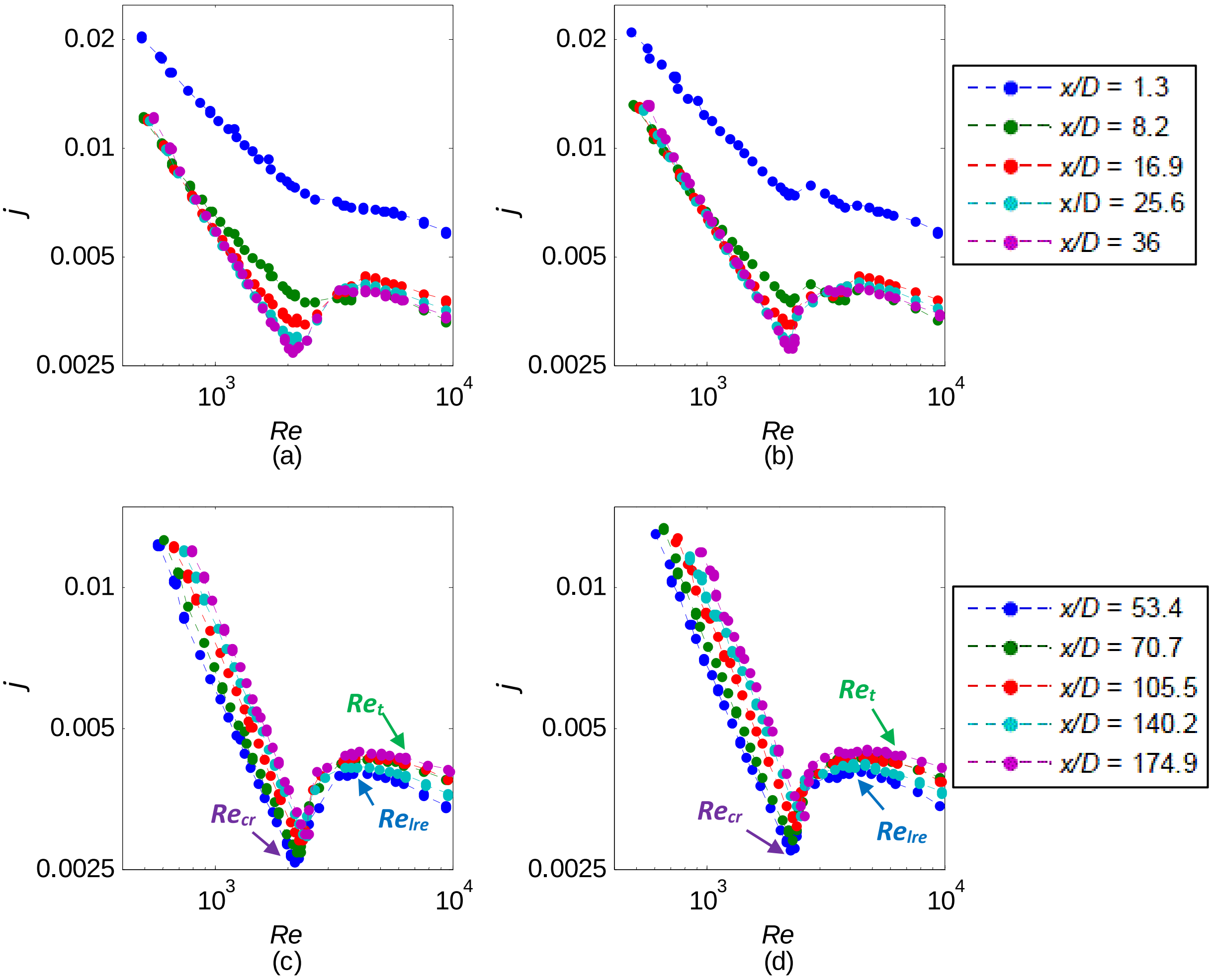

Figure 5.33: Comparison of Colburn *j*-factors as a function of Reynolds number at *x/D* = 1.3 to *x/D* = 36 at a heat flux of (a) 6.5 kW/m² and (b) 9.5 kW/m² and at *x/D* = 53.4 to *x/D* = 174.9 at a heat flux of (c) 6.5 kW/m² and (d) 9.5 kW/m²

An overall trend in Figure 5.33 was that the transition gradient (as defined in Figure 3.9) increased along the tube length. To investigate this, the transition gradients and the transition region gradients are summarised in Table 5.2 and Figure 5.34. From Table 5.2, it follows that the average transition gradient of the 6.5 kW/m² heat flux was significantly lower than for the other two heat fluxes. This was confirmed when a trend line was fitted through the transition gradients along the tube length in Figure 5.34(a). Therefore, as the heat flux was increased, a small change in velocity (or Reynolds number) led to a greater change in heat transfer (or Colburn *j*-factor).

From Figure 5.34(b), it follows that the transition region gradient remains approximately constant along the tube length and from Table 5.2, it follows that the average transition region gradient of all three heat fluxes was 5.8805×10^{-7}. Slight deviations did occur between *x/D* = 53.4 and *x/D* = 140.2, however, there was no significant increase or decrease. Figure 5.33(c) can be used to explain this trend. Both the start (Re_{cr}) and end (Re_{lre}) of transition were delayed along the tube length and the Colburn *j*-factors increased as well. However, the relative distance between the start (Re_{cr}) and end (Re_{lre}) of transition remained approximately constant and therefore the transition region gradient remained approximately constant.

Table 5.2: Transition gradients (TG) and transition region gradients (TRG) for different locations on the tube at different heat fluxes

x/D	6.5 kW/m^2		8.0 kW/m^2		9.5 kW/m^2	
	TG	TRG	TG	TRG	TG	TRG
8.2	1.8386x10^{-7}	2.0548x10^{-7}	-	2.6490x10^{-7}	-	1.3088x10^{-7}
16.9	6.5012x10^{-7}	6.4309x10^{-7}	1.9545x10^{-6}	6.1580x10^{-7}	4.0214x10^{-7}	5.6283x10^{-7}
25.6	8.1431x10^{-7}	5.8878x10^{-7}	1.5686x10^{-6}	6.5940x10^{-7}	7.2840x10^{-7}	6.4873x10^{-7}
36	9.4512x10^{-7}	5.9369x10^{-7}	1.4706x10^{-6}	6.5509x10^{-7}	6.3041x10^{-7}	6.2530x10^{-7}
53.4	1.2236x10^{-6}	6.6852x10^{-7}	2.7131x10^{-6}	7.0458x10^{-7}	6.1209x10^{-6}	6.1290x10^{-7}
70.7	2.0796x10^{-6}	7.4349x10^{-7}	4.5000x10^{-6}	7.9681x10^{-7}	3.8462x10^{-6}	6.7836x10^{-7}
88.1	3.2292x10^{-6}	6.5086x10^{-7}	3.6517x10^{-6}	6.6367x10^{-7}	3.0476x10^{-6}	5.6351x10^{-7}
105.5	2.3871x10^{-6}	6.7505x10^{-7}	2.5787x10^{-6}	6.5967x10^{-7}	5.1786x10^{-6}	5.7790x10^{-7}
122.8	2.5685x10^{-6}	4.9837x10^{-7}	1.9847x10^{-6}	4.7136x10^{-7}	4.8246x10^{-6}	4.1280x10^{-7}
140.2	1.7701x10^{-6}	5.8224x10^{-7}	3.8953x10^{-6}	5.0652x10^{-7}	3.0582x10^{-6}	4.3741x10^{-7}
157.6	3.4364x10^{-6}	6.1625x10^{-7}	5.3294x10^{-6}	5.8494x10^{-7}	6.2727x10^{-6}	5.2631x10^{-7}
174.9	5.0000x10^{-6}	6.8256x10^{-7}	9.8750x10^{-6}	6.4484x10^{-7}	7.1963x10^{-6}	5.8879x10^{-7}
Average	2.0400x10^{-6}	5.9570x10^{-7}	3.5929x10^{-6}	6.0230x10^{-7}	3.7551x10^{-6}	5.3048x10^{-7}

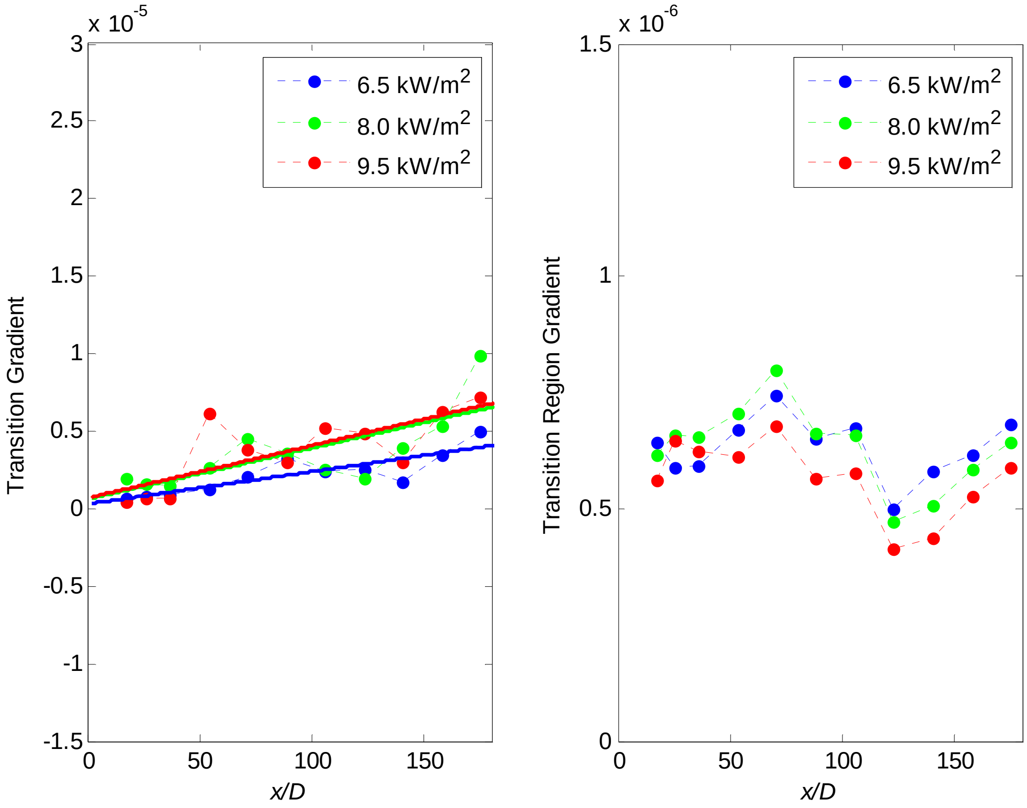

(a) (b)

Figure 5.34: Comparison of (a) transition gradients (TG) and (b) transition region gradients (TRG) as a function of axial position for different heat fluxes

The Reynolds numbers at which transition started and ended in Figures 5.27, 5.29, 5.31 and 5.32 are summarised in Figure 5.35 and Table 5.3. From Figure 5.35, it follows that the start of transition occurred earlier with increasing values of *x/D* between *x/D* = 1.3 and approximately *x/D* = 25.6, but was delayed as *x/D* was increased further. The end of transition was delayed for increasing values of *x/D* along the whole tube length. Furthermore, from Figure 5.35 and Table 5.3, it seems as if the width of the transition region ($Re_{cr} \leq Re \leq Re_{lre}$) remained approximately constant (Reynolds number range of 2 100) between $x/D = 25.6$ and $x/D = 174.9$, however from Table 5.3, it follows that it decreased slightly.

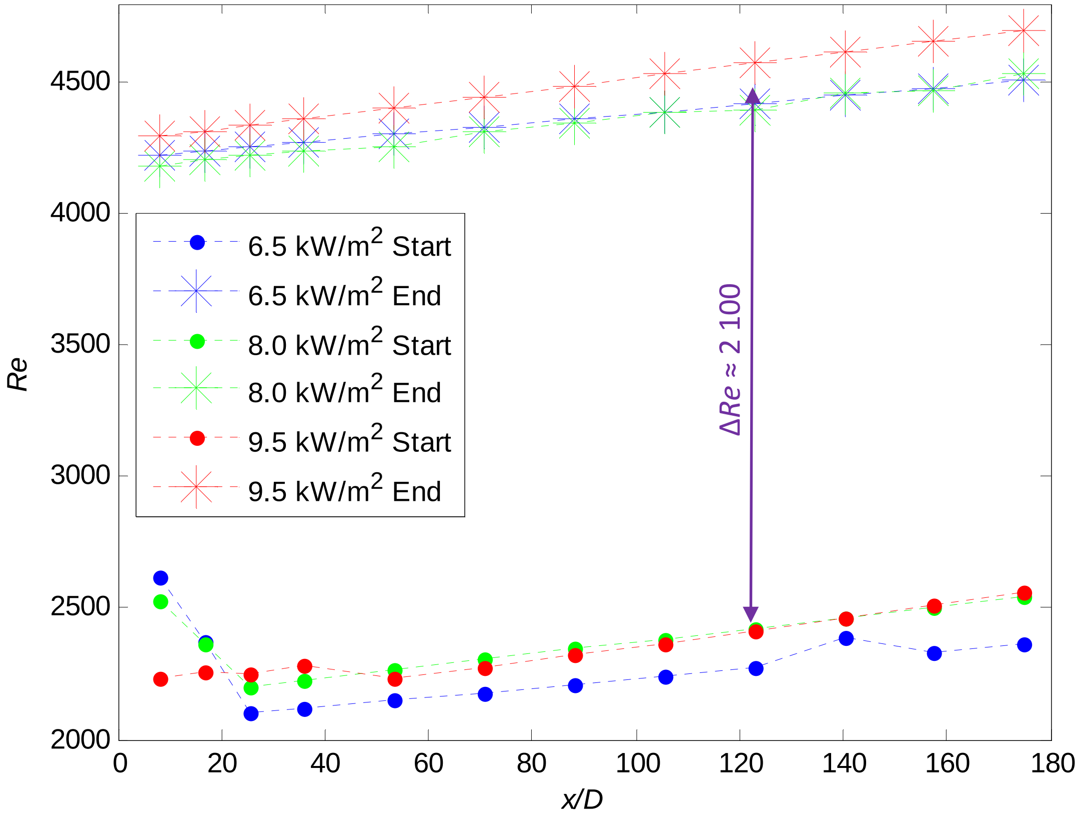

Figure 5.35: Reynolds numbers at which transition started and ended as a function of axial position at different heat fluxes

Table 5.3: Reynolds numbers at which transition started (Re_{cr}) and ended (Re_{lre}) for different locations on the tube at different heat fluxes

x/D	6.5 kW/m²			8.0 kW/m²			9.5 kW/m²		
	Re_{cr}	Re_{lre}	ΔRe	Re_{cr}	Re_{lre}	ΔRe	Re_{cr}	Re_{lre}	ΔRe
8.2	2 620	4 226	1 606	2 524	4 185	1 661	2 232	4 295	2 063
16.9	2 375	4 241	1 866	2 368	4 203	1 835	2 254	4 315	2 061
25.6	2 099	4 256	2 157	2 204	4 221	2 017	2 253	4 334	2 081
36	2 117	4 273	2 156	2 227	4 242	2 015	2 280	4 359	2 079
53.4	2 148	4 302	2 154	2 266	4 253	1 987	2 231	4 401	2 170
70.7	2 179	4 331	2 152	2 305	4 313	2 008	2 277	4 444	2 167
88.1	2 209	4 360	2 151	2 345	4 349	2 004	2 321	4 486	2 165
105.5	2 241	4 389	2 148	2 384	4 385	2 001	2 368	4 531	2 163
122.8	2 271	4 418	2 147	2 424	4 397	1 973	2 415	4 571	2 156
140.2	2 387	4 448	2 061	2 464	4 458	1 994	2 465	4 614	2 149
157.6	2 335	4 477	2 142	2 504	4 470	1 966	2 510	4 657	2 147
174.9	2 374	4 507	2 139	2 545	4 530	1 985	2 560	4 700	2 140
Average (25.6 ≤ *x/D* ≤ 174.9)			2 073			1 954			2 128

From Table 5.3 it seems as if the average width of the transition region ($\Delta Re \approx$ 2 051) was within 12% of the average Reynolds number at which transition started ($Re_{cr} \approx$ 2 323). This implies that the width of the laminar flow regime and transitional flow regime might be similar. However, it is recommended that this be investigated in more detail in another study.

When comparing the transition regions of the three heat fluxes, it follows that transition occurred earlier with increasing heat flux between x/D = 1.3 and x/D = 25.6. However, both the start and end of transition were slightly delayed with increasing heat fluxes for x/D between x/D = 25.6 and x/D = 174.9. The width of the transition region of the 6.5 kW/m^2 and 9.5 kW/m^2 heat fluxes was approximately the same, while the transition region of the 8.0 kW/m^2 heat flux was slightly narrower. Thus, it seems as if secondary flow does not have a significant influence on the width of the transition region of developing flow.

Although Ghajar and Tam (1994) investigated fully developed flow, they found in their investigation that the transition region became wider with increasing x/D. In order to make an accurate conclusion regarding the width of the transition region of developing flow, experiments need to be conducted using a longer test section. It will only be possible to make valid and accurate conclusions once the entire entrance region as well as a sufficient part of the fully developed region is covered. This will ensure a better understanding of how developing flow affects the width of the transition region compared with fully developed flow. However, it can already be concluded that the heat transfer characteristics of developing and fully developed flow are significantly different, although this could have been anticipated.

5.6. Summary, conclusions and recommendations

This chapter presented the local heat transfer results for developing flow. To ensure that the flow was developing, the thermal entrance length was first investigated for both forced and mixed convection conditions. In the laminar flow regime, the thermal entrance length was a strong function of the Reynolds number, Prandtl number and tube diameter. The thermal entrance length increased significantly with increasing Reynolds number, but decreased slightly with increasing heat flux due to the change in fluid properties presented by the Prandtl number. The thermal entrance length in the low-Reynolds-number-end and turbulent flow regimes was independent of Reynolds number and Prandtl number, since it is only a function of the tube diameter. When comparing forced and mixed convection, the thermal entrance length during forced convection seemed to be shorter, however, due to the small temperature differences compared with the uncertainty of the temperature measurements, no accurate conclusions could be made regarding the thermal entrance length during forced convection conditions.

Secondary flow was investigated by plotting the ratios of the heat transfer coefficients and dynamic viscosities at the top and bottom of the test section. The secondary flow effects were suppressed near the inlet of the test section but became significant along the tube length as the thickness of the thermal boundary layer increased. As expected, secondary flow effects increased with increasing heat flux due to the increased temperature difference between the surface and the fluid. However, the effects of secondary flow at a specific location on the test section decreased with increasing Reynolds number in the laminar flow regime, since the thickness of the thermal boundary layer decreased.

To investigate the heat transfer characteristics of developing flow, the Nusselt numbers and Colburn *j*-factors were calculated at each of the 13 thermocouple stations and compared. The maximum heat transfer coefficients were found at the inlet of the test section where the thickness of the thermal boundary layer was a minimum. Thus the Nusselt numbers and Colburn *j*-factors at the first thermocouple station were significantly higher than at all the other stations. Furthermore, the Nusselt numbers increased gradually with increasing Reynolds number and there were no distinct boundaries between the laminar, transitional and turbulent flow regimes. As the non-dimensional distance from the inlet of the test section (*x/D*) increased, the laminar and turbulent regimes could be identified. Between *x/D* = 1.3 and *x/D* = 36, there was no significant difference between the heat transfer coefficients in the laminar flow regime. However, as *x/D* was increased beyond 53, secondary effects became significant and the laminar heat transfer coefficient increased with increasing *x/D*. This confirmed that the secondary flow effects required a certain length to become significant.

Between *x/D* = 1.3 and *x/D* = 36, five different flow regions (laminar, developing laminar, transitional, low-Reynolds-number-end and turbulent) were identified from the Colburn *j*-factors. The developing laminar region was unique to *x/D* between 1.3 and 36 and became narrower with increasing *x/D* as the laminar region was extended. The start of transition occurred earlier with increasing values of *x/D* between *x/D* = 1.3 and approximately *x/D* = 25.6, but was delayed as *x/D* was increased further. The end of transition was delayed for increasing values of *x/D* along the whole tube length. Although the width of the transition region seemed to be approximately constant (Reynolds number range of approximately 2 100) between *x/D* = 25.6 and *x/D* = 174.9, it decreased slightly. Transition occurred earlier with increasing heat flux between *x/D* = 1.3 and *x/D* = 25.6. However, both the start and end of transition was slightly delayed with increasing heat fluxes for *x/D* between *x/D* = 25.6 and *x/D* = 174.9. Secondary flow effects also had no significant influence on the width of the transition region.

A previous investigation on fully developed flow found that the transition region became wider along the tube length, which is different from the developing flow results obtained during this study. However, in order to make accurate conclusions regarding the transition region of developing flow, the entire entrance region as well as a sufficient part of the fully developed region should be covered. A longer test section will give better insights regarding the influence of the transition from developing to fully developed flow on the start and end of the transitional flow regime.

It was concluded that the heat transfer characteristics of developing and fully developed flow are different. Engineers therefore need more insight into the heat transfer characteristics of developing flow in order to optimise the design of heat exchangers.

6. Results: Average Heat Transfer and Pressure Drop Data

6.1. Introduction

The average heat transfer and pressure drop results are presented in this chapter and the raw data can be found in the Excel file on the data and publications repository CD at the end of Appendix F. Experiments were conducted at different mass flow rates at three constant heat fluxes of 6.5 kW/m^2, 8.0 kW/m^2 and 9.5 kW/m^2. For each heat flux, the Reynolds number was varied between approximately 500 and 10 000 and a total of 398 tests were run.

The heat transfer results are divided into two parts, namely the Nusselt numbers and Colburn *j*-factor results, while the pressure drop results are divided into the isothermal friction factor results and diabatic friction factor results. The heat transfer and pressure drop results are also investigated simultaneously at the end of the chapter to determine the relationship between heat transfer and pressure drop. Correlations to determine the Nusselt numbers as a function of friction factor, Reynolds number and Prandtl number, in the laminar, transitional, low-Reynolds-number-end and turbulent flow regimes are also developed. Throughout this chapter, Figure 5.28 was used as a reference to identify the boundaries of the different flow regimes.

6.2. Nusselt numbers

Figure 6.1 contains the heat transfer results in terms of the average Nusselt numbers as a function of Reynolds number. The results in the low-Reynolds-number-end and turbulent flow regimes are also compared with recent experimental results of Meyer *et al*. (2013).

It should be noted that the flow in the laminar and transitional flow regimes was not fully developed. The graph consists of 111 data points for the 6.5 kW/m^2 heat flux, 103 data points for the 8.0 kW/m^2 heat flux and 104 data points for the 9.5 kW/m^2 heat flux. The Reynolds number was varied between 600 and 10 000 to ensure that the whole transitional flow regime, as well as sufficient parts of the laminar and turbulent flow regimes, was covered. The Reynolds number could not be decreased below 600, as the outlet temperature of the water became too high (>60 °C) for the material limitations of the experimental set-up. The Reynolds number was also limited to a maximum of 10 000, since the temperature difference between the inlet and outlet, as well as between the surface and fluid, became too small and the uncertainty too high to take accurate heat transfer measurements. The results are discussed in four separate parts: laminar (Section 6.2.1), turbulent (Section 6.2.2), low-Reynolds-number-end (Section 6.2.3) and transitional (Section 6.2.4).

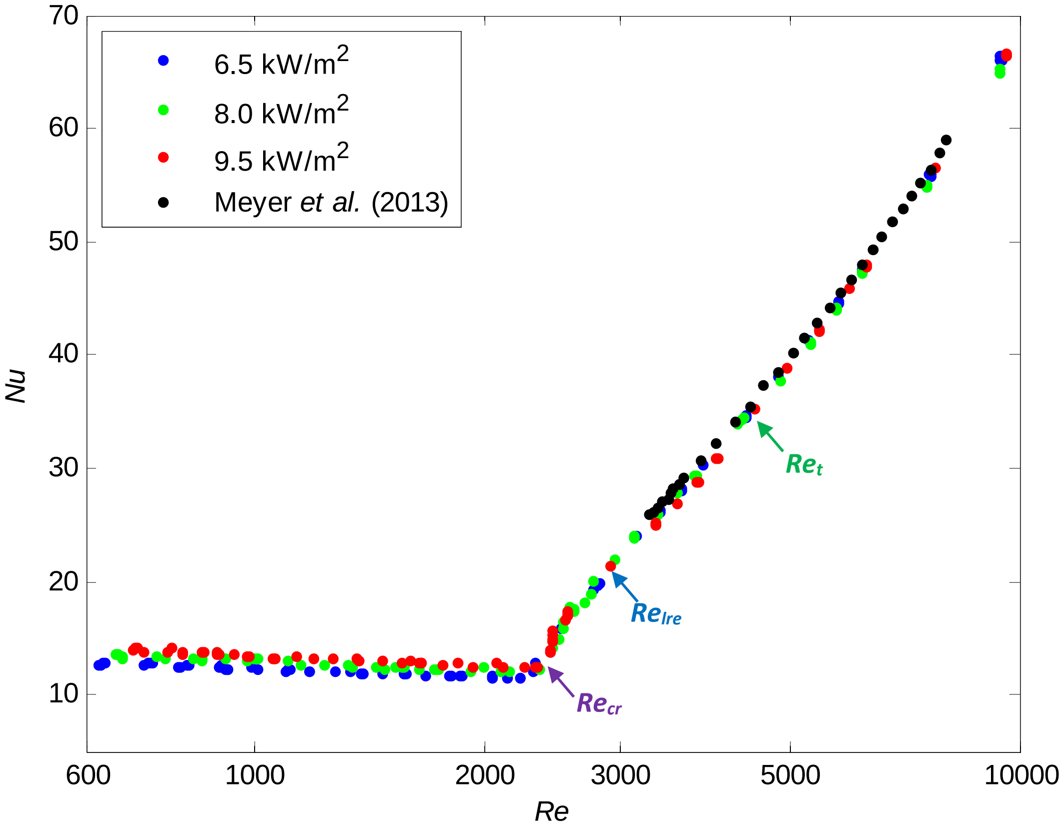

Figure 6.1: Comparison of experimental heat transfer data in terms of the average Nusselt numbers against Reynolds number for different heat fluxes. The results are also compared with literature in the low-Reynolds-number-end and turbulent flow regimes.

6.2.1. Laminar Nusselt numbers

As expected, the laminar Nusselt numbers in Figure 6.1 were significantly higher than the theoretical Nusselt number of 4.36, which is only valid for laminar forced convection flow with a constant heat flux boundary condition. There are two reasons for this. The first reason is the buoyancy-induced secondary flow inside the tube, which was caused by the difference in density of the fluid near the surface and the thermal boundary layer of the tube. The second reason is that developing flow was considered. As demonstrated in Chapter 5 for a constant Reynolds number, the local heat transfer coefficients are a maximum at the inlet of the test section and then decrease gradually along the tube length as the flow approaches fully developed flow. Therefore, the average heat transfer coefficients of developing flow are higher than for fully developed flow.

The Nusselt numbers in the laminar flow regime, at a Reynolds number of approximately 700, increased from 12.74 when the 6.5 kW/m^2 heat flux was applied, to 14.08 when the 9.5 kW/m^2 heat flux was applied. The increasing laminar Nusselt numbers with increasing heat flux is due to the effects of secondary flow. An overall trend is that the Nusselt numbers decreased with approximately 9% between a Reynolds number of 700 and 2 000. As the Reynolds number was increased, the velocity of the fluid increased and the thermal boundary layer thickness decreased which, in turn, decreased the secondary flow effects as well as the Nusselt numbers.

6.2.2. Turbulent Nusselt numbers

The Nusselt numbers in the turbulent flow regime in Figure 6.1 were compared with the experimental data of Meyer *et al*. (2013). The experimental data of the present study are for three different heat fluxes, 6.5 kW/m^2, 8.0 kW/m^2 and 9.5 kW/m^2, while the data of Meyer *et al*. (2013)

are for a heat flux of 13.0 kW/m^2. From Figure 6.1, it follows that there was no significant difference between the heat fluxes in the turbulent flow regime since the secondary flow effects were suppressed by the turbulent fluid motion. The increasing Nusselt numbers with increasing Reynolds number in the turbulent flow regime were caused by the increased mixing as a result of the velocity of the fluid, enhancing heat transfer.

6.2.3. Low-Reynolds-number-end Nusselt numbers

Although the boundaries of the low-Reynolds-number-end regime were not clear, the Colburn *j*-factors in Section 6.3 (Figure 6.3) were used as a guideline to identify them. The low-Reynolds-number-end regime started at a Reynolds number of approximately 3 000 (Re_{lre}) and ended at approximately 4 500 (Re_t). Similar to the turbulent flow regime, there was no significant difference between the Nusselt numbers of the different heat fluxes since the velocity of the fluid was high enough to suppress the secondary effects. Similar to the turbulent flow regime, the increasing Nusselt number with increasing Reynolds number was due to the velocity of the fluid that enhanced heat transfer.

6.2.4. Transitional Nusselt numbers

A detailed view of Figure 6.1 is provided in Figure 6.2 to investigate the influence of heat flux on the average Nusselt numbers in the transitional flow regime. From Figure 6.2, it follows that the start of transition (Re_{cr}) was slightly delayed with increasing heat flux. Transition occurred at a Reynolds number of approximately 2 210 when the 6.5 kW/m^2 heat flux was used, 2 280 when the 8.0 kW/m^2 heat flux was used and 2 330 when the 9.5 kW/m^2 heat flux was used. Although the start of transition was clear, the end of transition (Re_{lre}) could not be easily identified.

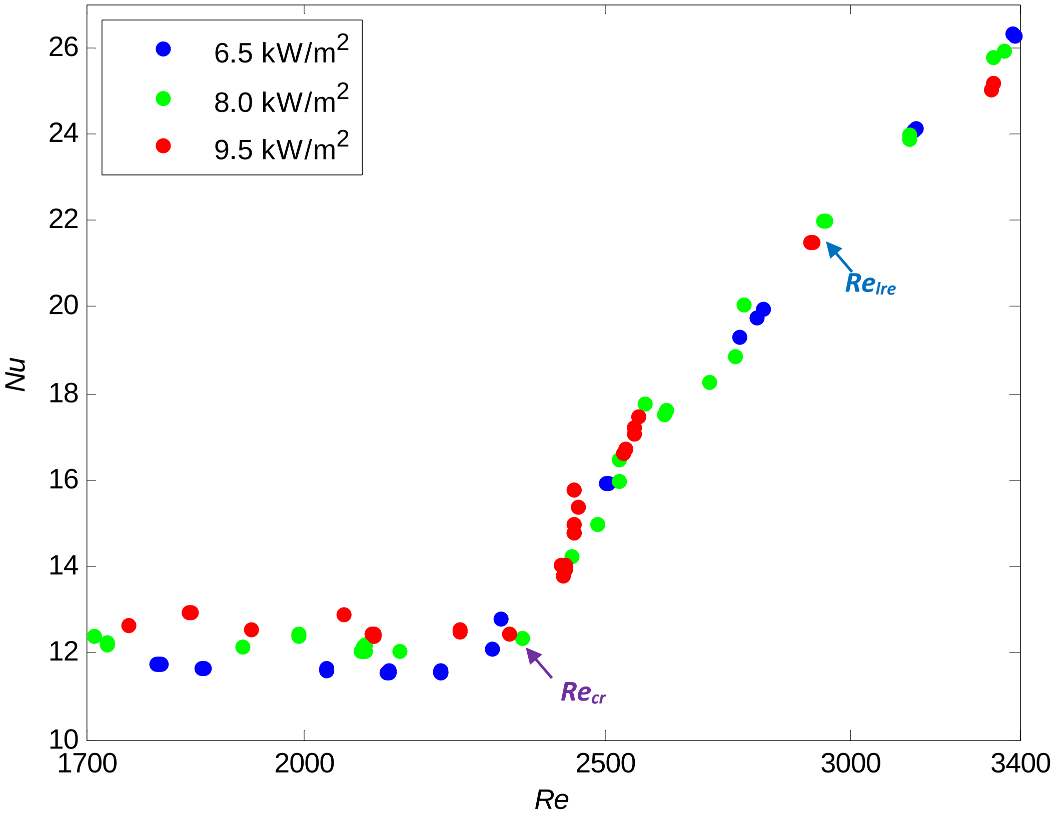

Figure 6.2: Comparison of experimental heat transfer data in the transitional flow regime in terms of the average Nusselt numbers against Reynolds number for different heat fluxes

In order to obtain a better understanding of when transition ends, as well as the effect of heating on the fluid properties (especially the Prandtl number), the heat transfer results are investigated in terms of the Colburn *j*-factor in Section 6.3.

6.3. Colburn *j*-factors

The heat transfer results for different heat fluxes are plotted (Figure 6.3) in terms of the Colburn *j*-factor as a function of Reynolds number to eliminate the effect of changes in the fluid Prandtl number with temperature. For comparison purposes, the fully developed tube flow forced convection heat transfer correlation for laminar flow (Nu = 4.36) is included as the solid blue line in the figure. The forced convection results of Figure 4.2 are also added to compare the influence of forced and mixed convection, as well as developing and fully developed flow, on the Colburn *j*-factor. The Colburn *j*-factor results are discussed in four separate parts: laminar (Section 6.3.1), turbulent (Section 6.3.2), low-Reynolds-number-end (Section 6.3.3) and transitional (Section 6.3.4).

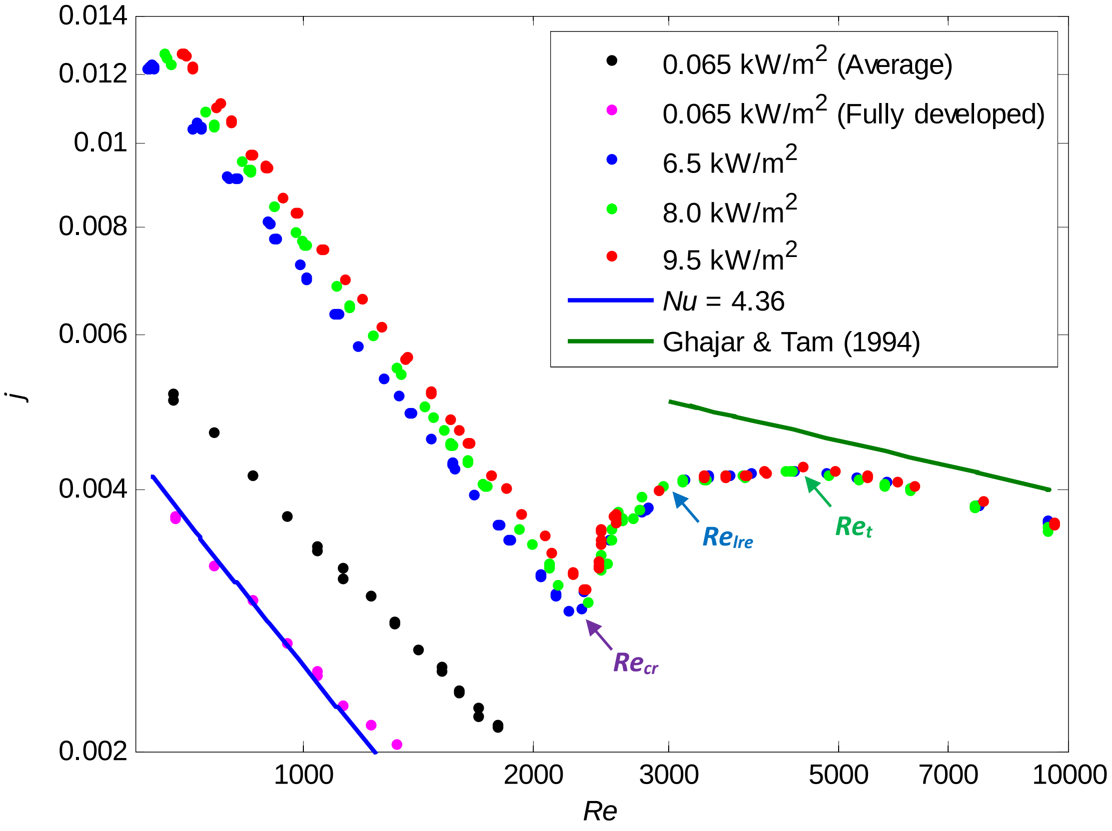

Figure 6.3: Comparison of experimental heat transfer data in terms of the average Colburn *j*-factors against Reynolds number for different heat fluxes. Also included is the line for forced convection (Nu = 4.36) in the laminar flow regime and the Ghajar and Tam (1994) line in the turbulent flow regime.

6.3.1. Laminar Colburn *j*-factors

Similar to the Nusselt numbers in Figure 6.1, the Colburn *j*-factors in the laminar flow regime (Figure 6.3) increased with increasing heat flux due to the secondary flow effects. Furthermore, the data had a pronounced upward parallel shift to the laminar forced convection heat transfer coefficients line (solid blue line in Figure 6.3). This is due to the strong influence of the buoyancy effects that gave rise to secondary flow. As shown in Figure 4.4, the laminar heat transfer coefficients for mixed convection were significantly higher than for forced convection, which therefore led to increased Colburn *j*-factors in the laminar flow regime. When the experimental data were plotted on a flow regime map in Figure 5.6, it was concluded that the flow in the turbulent flow regime and the flow in the upper part of the transitional flow regime (Region C) were dominated by forced convection, while the flow in the laminar flow regime (Region A) and the flow in the lower part of the transitional flow regime (Region B) were dominated by mixed convection. This confirms that the secondary flow effects were significant in the laminar flow regime and explains the presence of an upward parallel shift to the laminar fully developed flow forced convection heat transfer coefficients.

The average Colburn *j*-factors obtained at a heat flux of 65 W/m^2 were also greater than those for fully developed forced convection (indicated by the blue line). A maximum deviation of 71% occurred with the forced convection results at a Reynolds number of 1 800, while the deviation at a Reynolds number of 300 was 39%. Thus the deviation decreased with decreasing Reynolds number. These higher Colburn *j*-factors were therefore not due to the effect of mixed convection, but rather due to the effect of developing flow.

From Figure 5.3, it follows that the heat transfer coefficients and Nusselt numbers near the inlet of the test section were significantly higher than at the outlet of the test section. The high local Nusselt numbers near the inlet led to increased average Nusselt numbers and therefore increased average Colburn *j*-factors. From Figure 5.1, it follows that the thermal entrance length decreased with decreasing Reynolds number, which implies that the developing section of the tube decreased. This led to lower average Nusselt numbers and Colburn *j*-factors. This is confirmed when the fully developed Colburn *j*-factors at x/D =157.6 (indicated by the magenta markers) were added to the graph. The data correlated very well with the fully developed forced convection data (indicated by the blue line). It can therefore be concluded that the increased laminar Colburn *j*-factors of the 6.5 kW/m^2, 8.0 kW/m^2 and 9.5 kW/m^2 heat fluxes were not only due to secondary flow effects, but also due to developing flow effects because the average heat transfer coefficients along the tube length were used.

6.3.2. Turbulent Colburn *j*-factors

Although the turbulent Nusselt numbers in Figure 6.1 increased with increasing Reynolds number, the Colburn *j*-factors in the turbulent flow regime (Figure 6.3) decreased with increasing Reynolds number. From Equation 3.14, it follows that the Colburn *j*-factor is proportional to the Nusselt number, but inversely proportional to the Reynolds number and Prandtl number. The increase in Reynolds number was more than the increase in Nusselt number, which led to a decrease in the Colburn *j*-factors. Furthermore, the Prandtl number also increased with increasing Reynolds number (due to the decreased temperature of the fluid), which contributed to the decreasing Colburn *j*-factors. Similar to the Nusselt number results in Figure 6.1, there was no significant difference between the different heat fluxes since the secondary flow effects were suppressed by the turbulent motion of the fluid. When the turbulent Nusselt numbers were validated in Section 4.5, it was found that the correlation of Ghajar and Tam (1994) overpredicted the experimental data by approximately 7.4% between Reynolds numbers of 4 000 and 10 000. This explains why the Colburn *j*-factors predicted by the correlation of Ghajar and Tam (1994) were higher than the experimental data.

6.3.3. Low-Reynolds-number-end Colburn *j*-factors

From Figure 6.3, it follows that the low-Reynolds-number-end regime started at a Reynolds number of approximately 3 000 (Re_{lre}) and ended at approximately 4 500 (Re_t). The Colburn *j*-factors increased slightly with increasing Reynolds number due to increasing heat transfer coefficients. Similar to the Nusselt number results, there was no significant difference between the Colburn *j*-factors of the different heat fluxes in the low-Reynolds-number-end region, since the velocity of the fluid was able to suppress the secondary flow effects.

6.3.4. Transitional Colburn *j*-factors

From Figure 6.3, it follows that transition (Re_{cr}) was delayed from 2 290 when the 6.5 W/m^2 heat flux was used to 2 330 when the 9.5 W/m^2 heat flux was used. However, heating had no significant influence on the end of transition (Re_{lre}). The Colburn *j*-factors increased significantly with increasing Reynolds number due to the enhanced mixing caused by the velocity of the fluid. There was no significant difference between the Colburn *j*-factors of the 8.0 W/m^2 and 9.5 W/m^2 heat fluxes. However, the Colburn *j*-factors of the 6.5 W/m^2 heat flux were slightly lower between Reynolds numbers of 2 500 and 2 800.

6.4. Isothermal pressure drop

Since the pressure drop experiments were conducted across the entire test section length (2.03 m), the friction factors contained both developing (laminar and transitional flow regimes) and fully developed (low-Reynolds-number-end and turbulent flow regimes) flow. Figure 6.4 contains the isothermal friction factors for Reynolds numbers between 500 and 15 000.

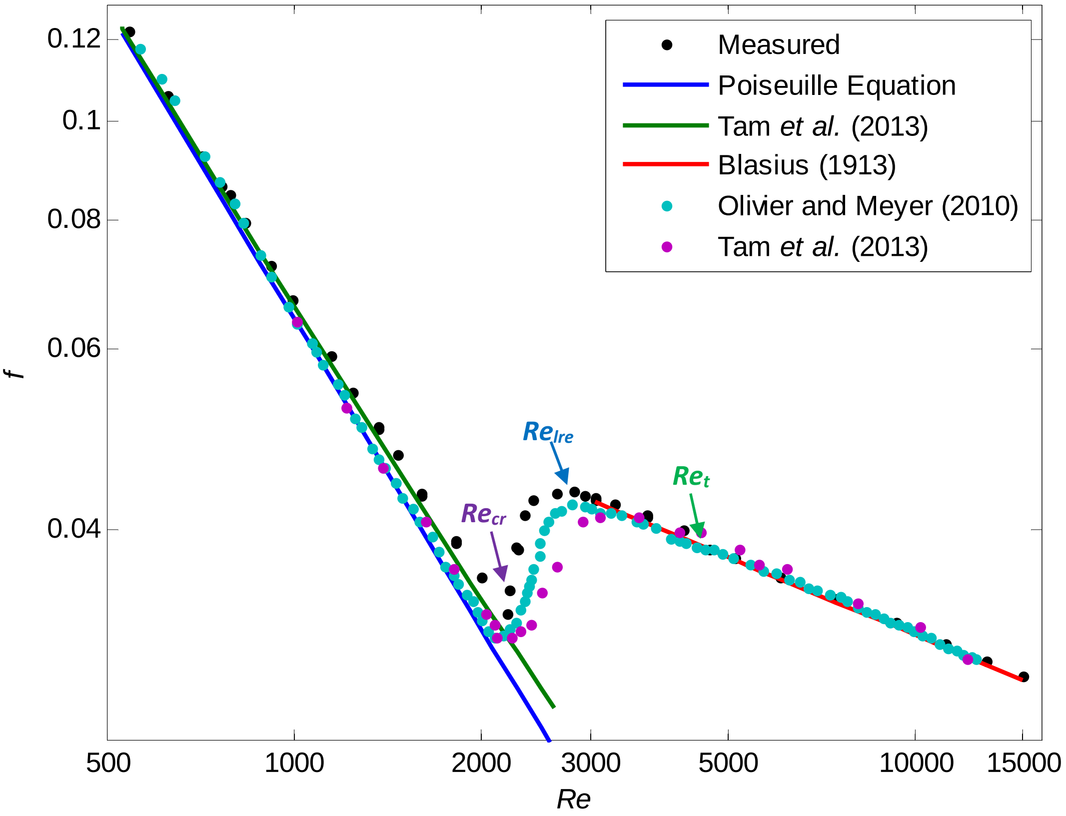

Figure 6.4: Isothermal friction factors as a function of Reynolds number between Reynolds numbers of 500 and 15 000. Also included are the experimental data of previous studies as well as existing correlations in the laminar and turbulent flow regimes.

The friction factors are compared with the Poiseuille (1840) equation, the correlation of Tam *et al.* (2013) for developing laminar flow and the Blasius (1913) equation for fully developed turbulent flow. Furthermore, the experimental data of Olivier and Meyer (2010) and Tam *et al.* (2013) were also included for comparison purposes. The isothermal friction factor results are discussed in three separate parts: laminar (Section 6.3.1), turbulent and low-Reynolds-number-end (Section 6.3.2) and transitional (Section 6.3.3).

6.4.1. Laminar isothermal friction factors

In the laminar flow regime, the friction factors decreased with increasing Reynolds number. Although the pressure drop increased with increasing fluid velocity, the friction factor was inversely proportional to the velocity squared (Equation 3.15). This explains why the friction factor decreased with increasing Reynolds number.

The laminar friction factor results correlated very well with the correlation of Tam *et al.* (2013) for developing flow. The average deviation between Reynolds numbers of 1 000 and 2 000 was 3% and the maximum deviation of 4.6% was obtained at a Reynolds number of 2 000. As mentioned in Section 4.6, the isothermal friction factors predicted by the correlation of Tam *et al*. (2013) were slightly higher (8.3% at a Reynolds number of 2 300) than the friction factors predicted by the Poiseuille (1840) equation. The Poiseuille (1840) equation was developed for fully developed flow and thus underpredicted the developing friction factors of this study. The experimental data of Olivier and Meyer (2010) and Tam et al. (2013) correlated better with the Poiseuille (1840) equation since the flow in these studies was closer to fully developed flow.

6.4.2. Turbulent and low-Reynolds-number-end isothermal friction factors

The thermal entrance length in the low-Reynolds-number-end and turbulent flow regimes was approximately 5% of the length of the test section (Section 5.5) and the flow was therefore considered as fully developed. This explains why the experimental data of all three studies were approximately the same in the turbulent flow regime. As mentioned in Section 4.6, the experimental data correlated very well with the Blasius (1913) equation and the average deviation between Reynolds numbers of 3 500 and 15 000 was 1%. Although there is no clear distinction between the low-Reynolds-number-end and turbulent flow regimes in Figure 6.4, the boundary (Re_t) between these two regimes occurred at a Reynolds number of approximately 4 700. At Reynolds numbers greater than 4 700, the isothermal friction factors fell on the turbulent friction factors predicted by the Blasius (1913) equation.

6.4.3. Transitional isothermal friction factors

The friction factors in the transitional flow regime were compared with the experimental data of Tam *et al.* (2013) and Olivier and Meyer (2010) in Figure 6.5. Although the shape of the transition friction factor curves of all three studies was approximately the same, transition did not start or end at the same Reynolds numbers. Transition occurred first in the results of Olivier and Meyer (2010) and last in the results of Tam *et al.* (2013). The transition gradient (TG line) was obtained by plotting a trend line through the transitional friction factors. The Reynolds numbers at which transition started and ended, as well as the transition gradients, are summarised in Table 6.1.

The transition gradient was the largest in the present study ($4.4642\text{x}10^{-5}$) and the smallest in the results of Tam *et al.* (2013). The flow in the present study was developing, while the flow in the study of Olivier and Meyer (2010) was developing in the first part of the test section and fully developed in the last part, and Tam *et al.* (2013) considered fully developed flow only. It can therefore be concluded that the transition region became wider as the flow approached fully developed flow.

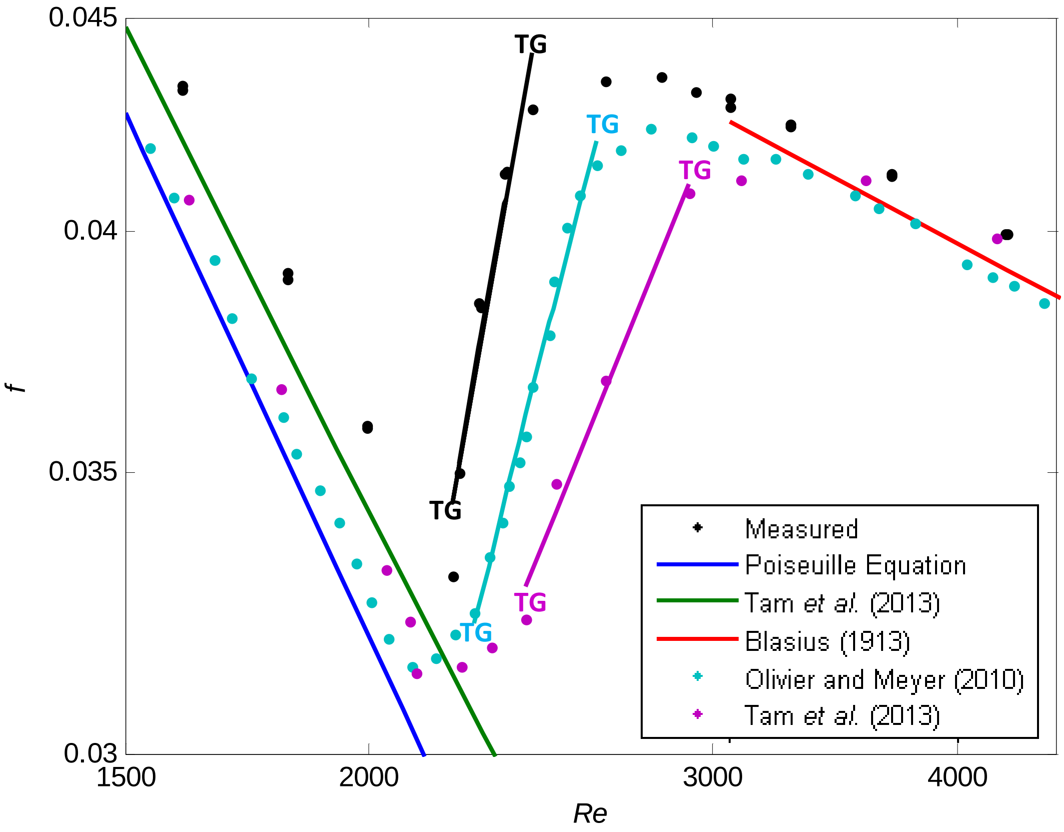

Figure 6.5: Comparison of isothermal friction factors in the transitional flow regime

Table 6.1: Comparison of Reynolds numbers at which transition starts and ends, as well as transition gradients

	Transition start	Transition end	TG	TRG
Present Study	$Re \approx 2\,208$	$Re \approx 2\,822$	$4.4642\text{x}10^{-5}$	$1.7052\text{x}10^{-5}$
Olivier and Meyer (2010)	$Re \approx 2\,101$	$Re \approx 2\,923$	$2.8113\text{x}10^{-5}$	$1.2968\text{x}10^{-5}$
Tam *et al.* (2013)	$Re \approx 2\,227$	$Re \approx 3\,587$	$1.5910\text{x}10^{-5}$	$7.1103\text{x}10^{-6}$

6.5. Diabatic pressure drop

Figure 6.6 contains the experimental friction factors against Reynolds number. The graph consists of 57 data points for the isothermal case (0 kW/m^2), 111 data points for the 6.5 kW/m^2 heat flux, 103 data points for the 8.0 kW/m^2 heat flux and 104 data points for the 9.5 kW/m^2 heat flux. For comparison purposes, the theoretical predictions of Poiseuille (1840), Tam *et al.* (2013), Blasius (1913) and Allen and Eckert (1964) are also shown. The Reynolds number was varied between 1 000 and 10 000 to ensure that the whole transitional flow regime, as well as sufficient parts of the laminar and turbulent flow regimes, was covered. The Reynolds number was not decreased below 1 000 as the pressure drop became too small and the uncertainty too high to take accurate measurements. The results are discussed in four separate parts: laminar (Section 6.5.1), turbulent (Section 6.5.2), low-Reynolds-number-end (Section 6.5.3) and transitional (Section 6.5.4).

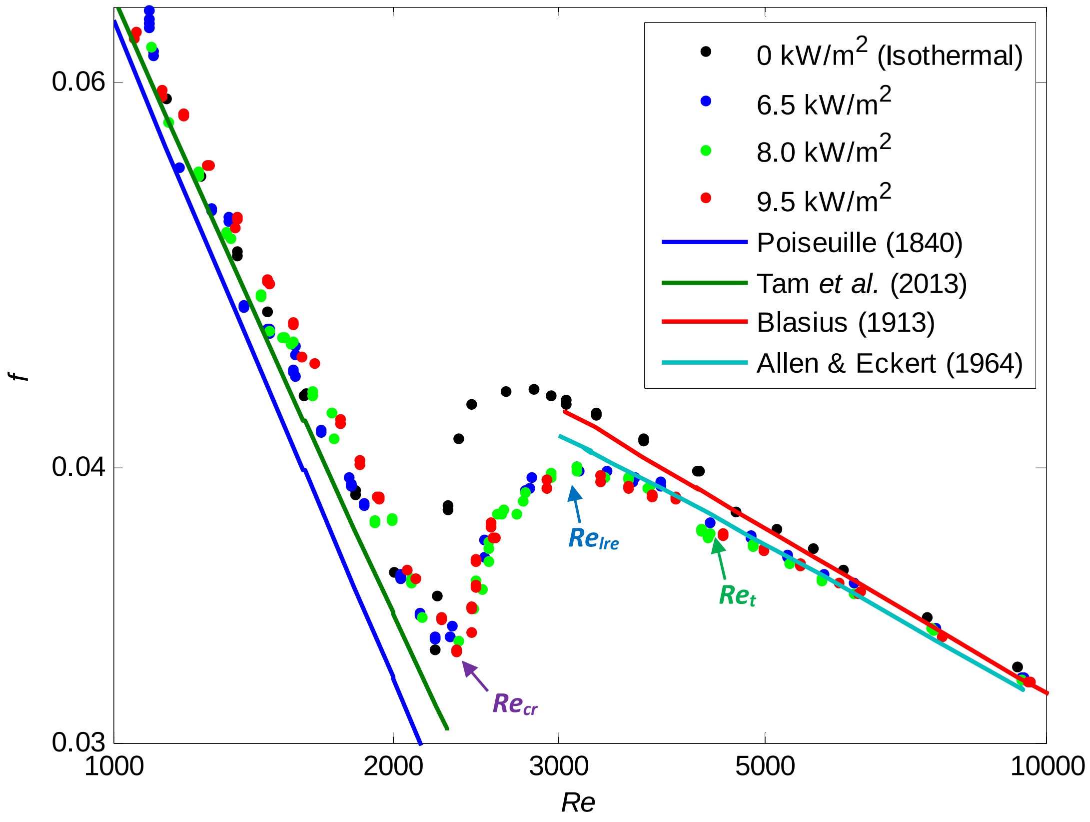

Figure 6.6: Comparison of the experimental friction factors as a function of Reynolds number for different heat fluxes. The results are also compared with literature in the laminar and turbulent flow regimes.

6.5.1. Laminar friction factors

The laminar diabatic friction factors (Figure 6.6) increased slightly with increasing heat flux due to the effects of secondary flow. The fluid near the surface has a higher temperature and lower density and therefore circulates upwards, while the fluid near the thermal boundary layer of the tube has a lower temperature and higher density and therefore circulates downwards. Tam and Ghajar (1997) explain that when mixed convection exists, the velocity profile of the flow changes in such a way that the shear stress and density are changed. Therefore, the friction factor changes as well. When the heat flux is increased, the shear stress due to the change in velocity profile increases while the density decreases, which leads to increasing friction factors.

Figure 6.7 contains the measured pressure drops across the entire test section for different Reynolds numbers and heat fluxes. The pressure drop increased approximately linearly (on a semi-log plot) in the laminar flow regime, as expected, because the friction factor and thus pressure drop are directly proportional to the velocity of the fluid and thus Reynolds number (Equations 2.2 and 3.15). However, the gradient of the pressure drop increased significantly when the flow became transitional and then gradually increased further as the flow became turbulent. It can also be concluded that the pressure drop decreased slightly when heating was applied since the density of the fluid decreased with increasing temperature, as shown in Figure 6.8. Furthermore, the oxygen solubility decreased with increasing temperature, which implies that more oxygen was released. The compressibility of the test fluid was therefore increased due to very small air bubbles inside the test fluid which, in turn, led to decreased pressure drops.

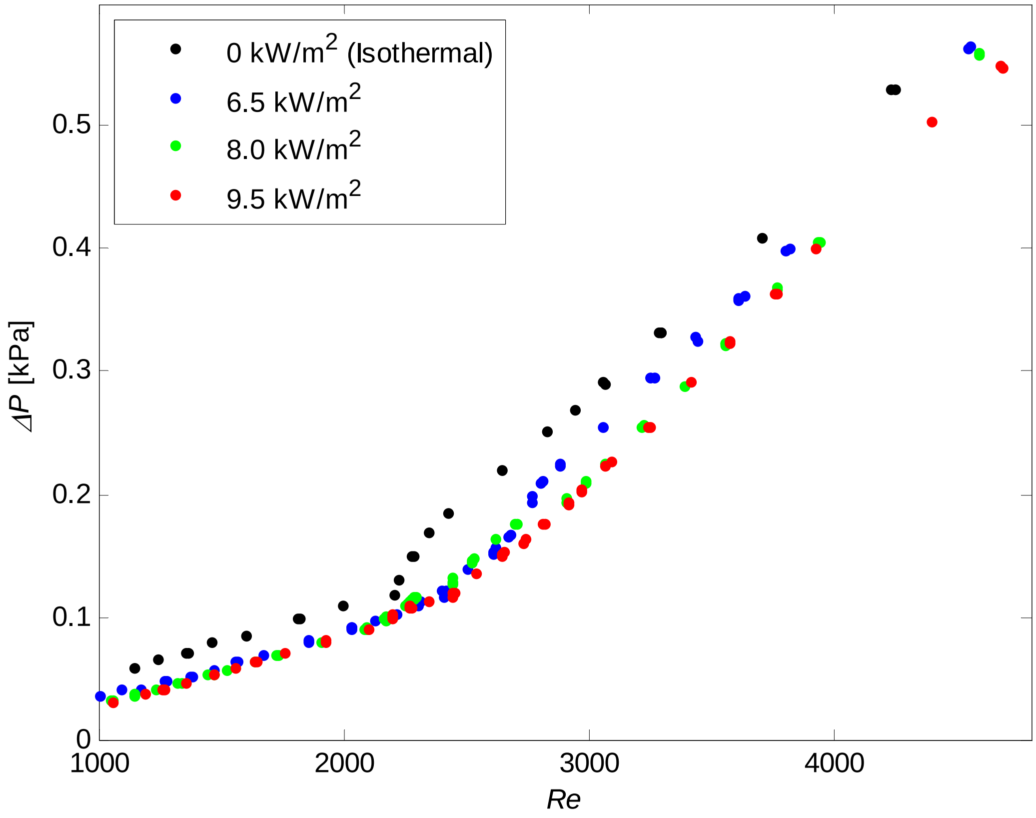

Figure 6.7: Measured pressure drop as a function of Reynolds number for different heat fluxes

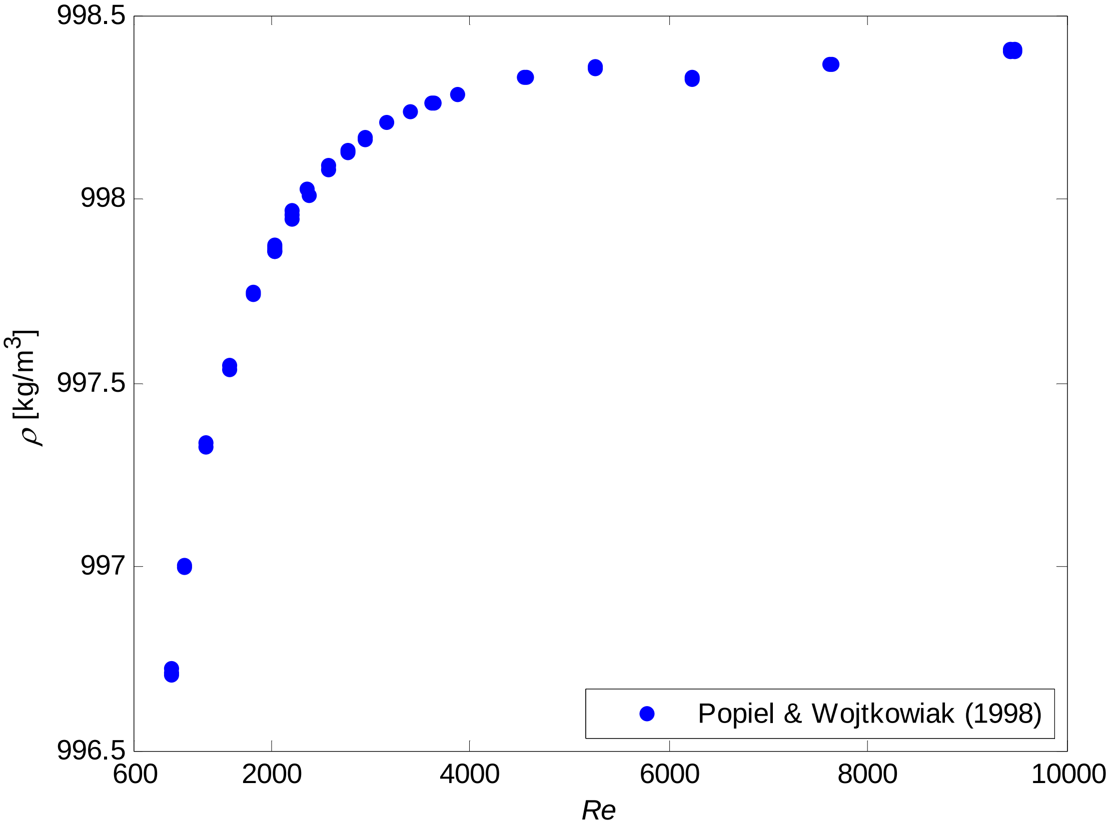

Figure 6.8: Density as a function of Reynolds number at a 6.5 kW/m² heat flux. The density was obtained using the thermophysical correlations for liquid water (Popiel and Wojtkowiak, 1998) evaluated at the bulk fluid temperatures.

The bulk fluid temperatures obtained at a heat flux of 6.5 kW/m^2 were substituted in the thermophysical correlations for liquid water (Popiel and Wojtkowiak, 1998) to obtain the density of the fluid. From Figure 6.8, it follows that the density of the fluid increased significantly with increasing Reynolds number in the laminar flow regime due to the decreasing fluid temperatures with increasing velocity. This increase was less in the transitional flow regime and the density in the turbulent flow regime remained approximately constant.

6.5.2. Turbulent friction factors

As mentioned in Section 6.4.2, the isothermal friction factors (Figure 6.4) in the turbulent flow regime correlated well with the Blasius (1913) equation. Allen and Eckert (1964) added a viscosity correction factor to the Blasius (1913) equation to account for the difference in temperature between the surface and fluid. From Figure 6.6, it follows that the diabatic friction factors correlated very well with the friction factors predicted by the correlation of Allen and Eckert (1964). The diabatic friction factors in the turbulent flow regime were slightly lower than the isothermal friction factors; however, there was no significant difference between the heat fluxes.

6.5.3. Low-Reynolds-number-end friction factors

From Figure 6.6, it is confirmed that the low-Reynolds-number-end regime started at a Reynolds number of approximately 3 000 and ended at approximately 4 500. Similar to the turbulent flow regime, the diabatic friction factors were lower than the isothermal friction factors. However, the diabatic friction factors in the low-Reynolds-number-end regime decreased slightly with increasing heat flux.

6.5.4. Transitional friction factors

In the transitional flow regime, the diabatic friction factors were also significantly lower than the isothermal friction factors. This was due to the decreased pressure drop when heat was applied to the test section, as shown in Figure 6.7. Similar to the heat transfer results, transition was slightly delayed for increasing fluxes. Furthermore, it can be concluded that the transition gradient increased with increasing heat flux. The transition gradients and transition region gradients of the diabatic friction factors (Figure 6.6) are summarised in Table 6.2.

Table 6.2: Diabatic friction factor transition gradients and transition region gradients

Heat flux [kW/m^2]	TG	TRG
6.5	1.1573x10^{-5}	7.7725x10^{-6}
8.0	1.3560x10^{-5}	8.4741x10^{-6}
9.5	2.9727x10^{-5}	8.7239x10^{-6}

6.6. Simultaneous heat transfer and pressure drop analysis

Since the heat transfer and pressure drop data was measured simultaneously during the experiments, the Colburn *j*-factors and friction factors of the different heat fluxes were plotted on the same graph. The boundaries of the different flow regimes, as discussed in Sections 6.3 and 6.4, are also included in Figure 6.9 and it can be concluded that the shape of the Colburn *j*-factors and friction factors was similar.

In the laminar flow regime, both Colburn *j*-factors and friction factors decreased with increasing Reynolds number. At a Reynolds number of approximately 2 300 (Re_{cr}), the transition region started and both Colburn *j*-factors and friction factors increased with increasing Reynolds number. The transition region ended at a Reynolds number of approximately 3 000 (Re_{lre}). In the low-Reynolds-number-end region, the Colburn *j*-factors and friction factors behaved differently. The Colburn *j*-factors continued to increase with increasing Reynolds number, however, this increase was less than in the transitional flow regime. On the other hand, the friction factors began to decrease and it seemed as if the flow was turbulent. It was concluded from Figure 6.6 that the experimental data in this region did not fall exactly on the turbulent friction factors predicted by the correlation of Allen and Eckert (1964). Therefore, although the flow was close to turbulent, it was not fully turbulent yet. The flow only became fully turbulent at a Reynolds number of approximately 4 500 (Re_t) and in this regime, both Colburn *j*-factors and friction factors decreased with increasing Reynolds number.

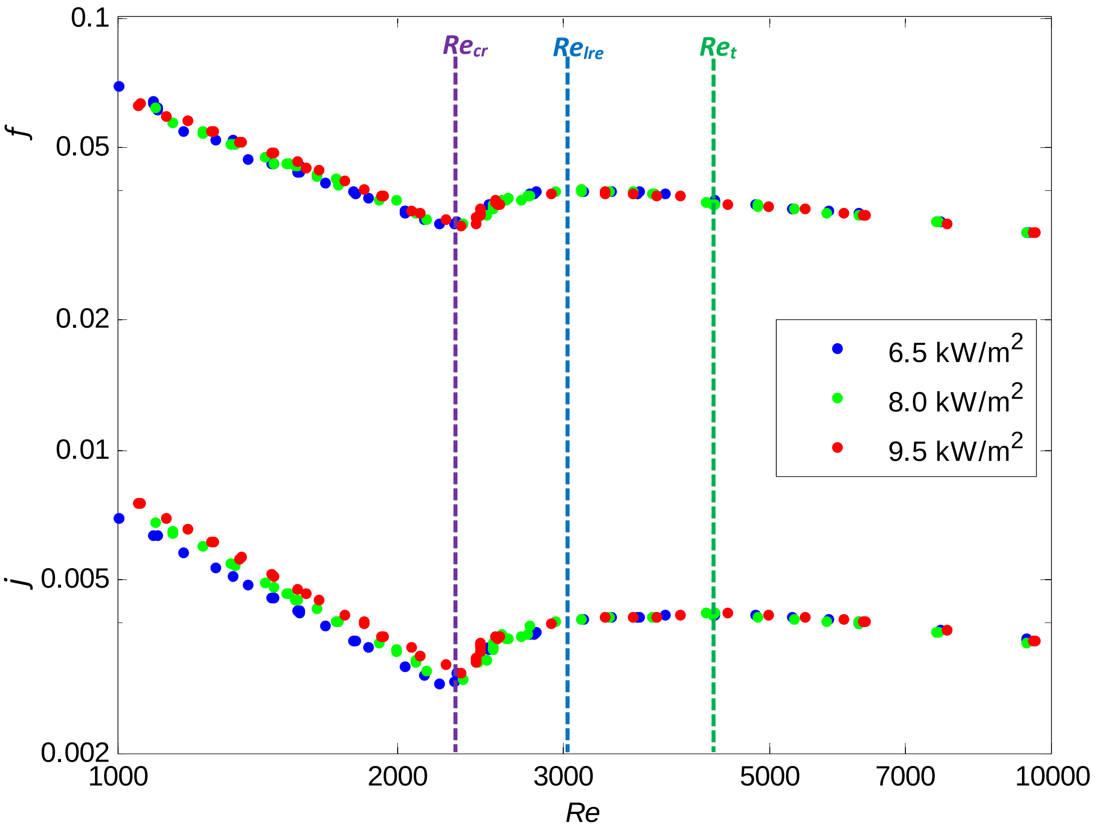

Figure 6.9: Comparison of experimental heat transfer and pressure drop data in terms of the average Colburn *j*-factors and average friction factors against Reynolds number for different heat fluxes

Overall, it can be concluded that the boundaries of the different flow regimes were the same for heat transfer and pressure drop. This is in contrast with the results obtained by Tam *et al.* (2013) since the authors found that the transition region of heat transfer was wider than for pressure drop. A possible explanation for this is that the authors treated the low-Reynolds-number-end region as part of the transitional flow regime when the Colburn *j*-factors were investigated. Furthermore, when the authors investigated the pressure drop results, it seemed as if the low-Reynolds-number-end region was treated as part of the turbulent flow regime. The nomenclature for the flow regime boundaries which were developed in this study (Figure 5.28) can be used as a guideline to identify the different flow regimes in future studies. This will ensure a better understanding of the heat transfer and pressure drop characteristics of the different flow regimes.

As mentioned earlier, the trend of the Colburn *j*-factors and friction factors was similar in Figure 6.9. To investigate the relationship between these two parameters, *f/j*-factors were obtained by dividing the friction factors by the Colburn *j*-factors. The results are summarised in Figure 6.10 and Table 6.3. The *f/j*-factors in the laminar flow regime increased linearly with increasing Reynolds number. There was a significant difference between the *f/j*-factors of the three heat fluxes in the laminar flow regime due to the effects of secondary flow. Thus, a curve fit was done through the laminar data points of each heat flux.

In the transitional flow regime, the *f/j*-factors decreased with increasing Reynolds number. Secondary flow effects were still significant in the transitional flow regime and the *f/j*-factors decreased slightly with increasing heat flux. A second order polynomial curve fit was done through the data points of the 6.5 kW/m^2 and 8.0 kW/m^2 heat fluxes while a third order polynomial function was fitted through the 9.5 kW/m^2 heat flux.

The secondary flow effects in the low-Reynolds-number-end regime were suppressed by the fluid motion, which explains why there was no significant difference between the *f/j*-factors in this regime. The *f/j*-factors decreased with increasing Reynolds number and therefore a linear curve fit was done through the data points.

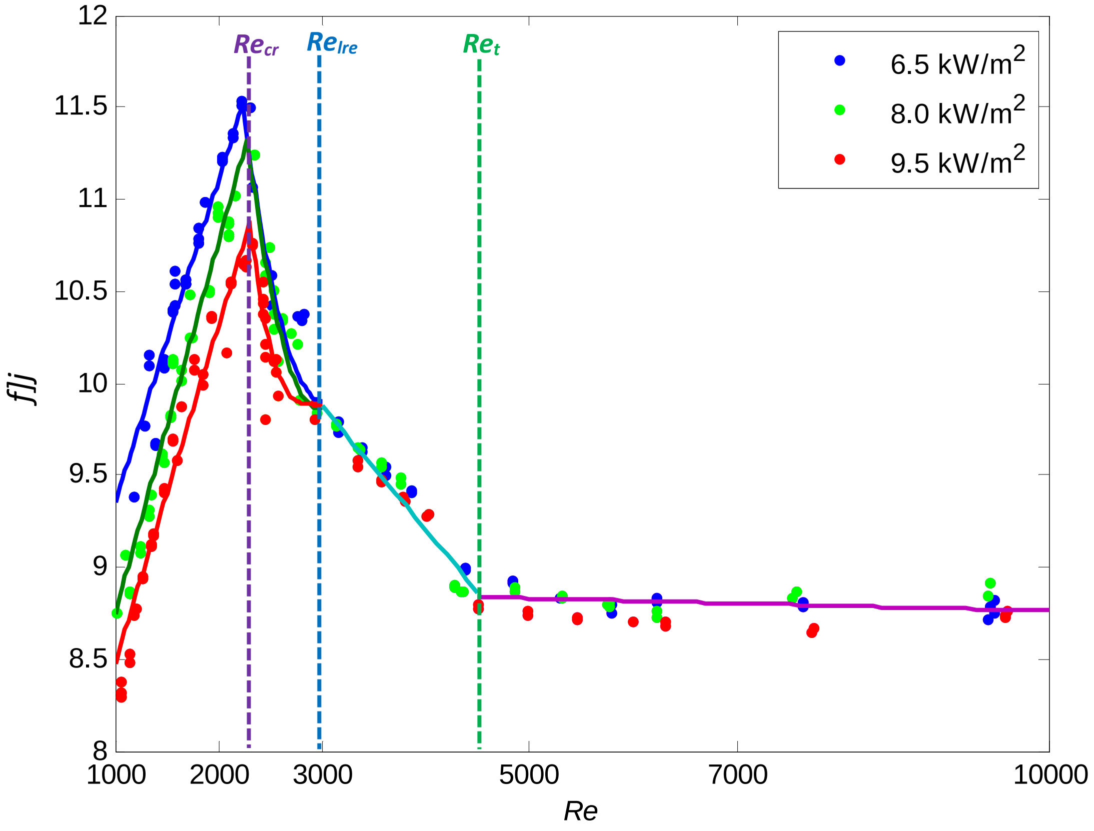

Figure 6.10: Comparison of the friction factor divided by the Colburn *j*-factor as a function of Reynolds number for different heat fluxes. Curve fit lines through the data points in the different flow regimes are also included.

Although it seems from Figure 6.10 as if the *f/j*-factors in the turbulent flow regime remained approximately constant, it did not. A linear curve fit was done through the data points of the three heat fluxes and it was found that the *f/j*-factors decreased with increasing Reynolds number. Similar to the low-Reynolds-number-end regime, the secondary flow effects were suppressed by the fluid motion, which explains why there was no significant difference between the *f/j*-factors of the different heat fluxes.

Table 6.3: Curve fit equations through the *f/j*-factors in the different flow regimes

	Curve fit equation
Laminar	
6.5 kW/m^2	$f/j = 0.0017537 * Re + 7.6001$
8.0 kW/m^2	$f/j = 0.0020224 * Re + 6.7252$
9.5 kW/m^2	$f/j = 0.0018384 * Re + 6.6384$
Transitional	
6.5 kW/m^2	$f/j = 2.74x10^{-6} * Re^2 - 0.0164176 * Re + 34.495087$
8.0 kW/m^2	$f/j = 3.17x10^{-6} * Re^2 - 0.018729 * Re + 37.5277351$
9.5 kW/m^2	$f/j = -4.38437x10^{-9} * Re^3 + 3.823x10^{-5} * Re^2 - 0.1111527 * Re + 117.641866$
Low-Re-end	$f/j = -0.00067155 * Re + 11.886$
Turbulent	$f/j = -0.000013761 * Re + 8.8986$

Table 6.4: Correlations to determine the Nusselt number as a function of friction factor for the different flow regimes

	Correlation
Laminar	
6.5 kW/m^2	$Nu = f\ Re\ Pr^{1/3}/(0.0017537\ Re + 7.6001)$ 1 000 ≤ Re ≤ 2 300; 5.3 ≤ Pr ≤ 5.9; 4.5x10^6 ≤ Ra ≤ 5.5x10^6 Maximum percentage deviation: ± 6.0% Average percentage deviation: ± 1.9%
8.0 kW/m^2	$Nu = f\ Re\ Pr^{1/3}/(0.0020224\ Re + 6.7252)$ 1 000 ≤ Re ≤ 2 300; 5.1 ≤ Pr ≤ 5.9; 4.5x10^6 ≤ Ra ≤ 6.4x10^6 Maximum percentage deviation: ± 2.9% Average percentage deviation: ± 1.1%
9.5 kW/m^2	$Nu = f\ Re\ Pr^{1/3}/(0.0018384\ Re + 6.6384)$ 1 000 ≤ Re ≤ 2 300; 4.6 ≤ Pr ≤ 5.3; 6.8x10^6 ≤ Ra ≤ 9.0x10^6 Maximum percentage deviation: ± 2.8% Average percentage deviation: ± 1.3%
Transitional	
6.5 kW/m^2	$Nu = f\ Re\ Pr^{1/3}/2.74x10^{-6}Re^2 - 0.0164176\ Re + 34.495087$ 2 300 ≤ Re ≤ 3 000; 5.9 ≤ Pr ≤ 6.5; 2.5x10^6 ≤ Ra ≤ 4.5x10^6 Maximum percentage deviation: ± 3.7% Average percentage deviation: ± 2.1%
8.0 kW/m^2	$Nu = f\ Re\ Pr^{1/3}/(3.17x10^{-6} * Re^2 - 0.018729 * Re + 37.5277351)$ 2 300 ≤ Re ≤ 3 000; 5.5 ≤ Pr ≤ 6.4; 2.6x10^6 ≤ Ra ≤ 5.5x10^6 Maximum percentage deviation: ± 2.1% Average percentage deviation: ± 1.1%
9.5 kW/m^2	$Nu = f\ Re\ Pr^{1/3}/(-4.384x10^{-9}Re^3 + 3.823x10^{-5}Re^2 - 0.1111527\ Re + 117.641866)$ 2 300 ≤ Re ≤ 3 000; 5.2 ≤ Pr ≤ 6.3; 3.1x10^6 ≤ Ra ≤ 6.7x10^6 Maximum percentage deviation: ± 5.5% Average percentage deviation: ± 0.8%
Low-Re-end	$Nu = f\ Re\ Pr^{1/3}/(-0.00067155\ Re + 11.886)$ 3 000 ≤ Re ≤ 4 500; 6 ≤ Pr ≤ 6.7; 1.4x10^6 ≤ Ra ≤ 3.1x10^6 Maximum percentage deviation: ± 1.5% Average percentage deviation: ± 0.7%
Turbulent	$Nu = f\ Re\ Pr^{1/3}/(-0.000013761\ Re + 8.8986)$ 4 500 ≤ Re ≤ 10 000; 6.4 ≤ Pr ≤ 7.1; 6.9x10^5 ≤ Ra ≤ 1.9x10^6 Maximum percentage deviation: ± 1.7% Average percentage deviation: ± 0.6%

The curve fit equations (Table 6.3) represents the relationship between the Colburn *j*-factor and friction factor and thus the relationship between heat transfer and pressure drop. Furthermore, the Colburn *j*-factor is a function of the Nusselt number (Equation 3.14), thus the Nusselt number can be calculated from the friction factor using this relationship. Correlations which can be used to determine the Nusselt number from the friction factor, Reynolds number and Prandtl number were developed for the different flow regimes and are summarised in Table 6.4.

The predicted Nusselt numbers using these correlations were compared with the experimental results of this study in Figure 6.11. It can be concluded that the correlations were able to predict the laminar Nusselt numbers within 6%, the transitional Nusselt numbers within 5.5% and the Nusselt numbers in the low-Reynolds-number-end and turbulent flow regimes within 1.5% and 1.7%, respectively. The average deviation between the predicted and experimental Nusselt numbers in the laminar, transitional, low-Reynolds-number-end and turbulent flow regimes was 1.44%, 1.1%, 0.67% and 0.63%, respectively. Although the deviation of the Nusselt numbers were higher in the laminar flow regime than in the other flow regimes, the deviation is still within the friction factor uncertainty which was approximately 6% at a Reynolds number of 1 000 (Figure 3.6).

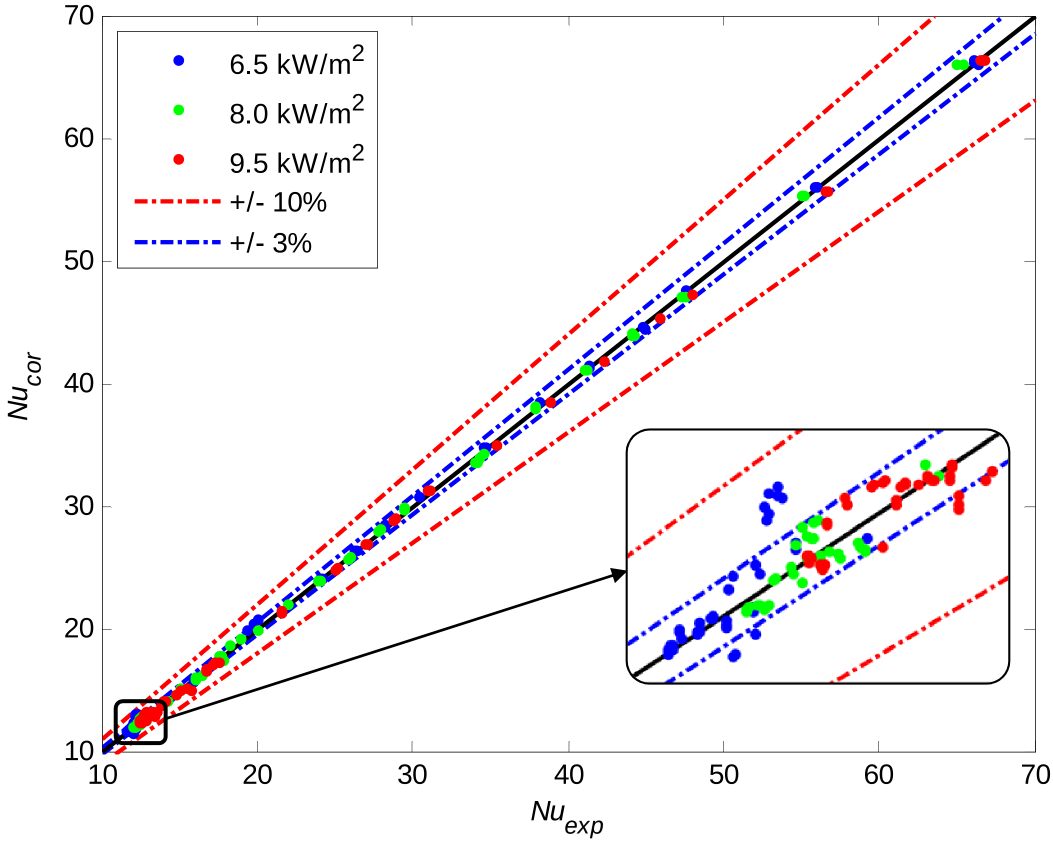

Figure 6.11: Comparison between experimental Nusselt numbers and the Nusselt numbers calculated using the correlations

6.7. Conclusion

The purpose of this chapter was to investigate the influence of heating on the average heat transfer coefficients and friction factors from the experimental measurements. The experiments included the transitional flow regime, as well as sufficient parts of the laminar and turbulent flow regimes. The heat transfer conclusions were presented in terms of the Nusselt numbers and Colburn *j*-factors in the order of laminar, turbulent, low-Reynolds-number-end and transition. The pressure drop conclusions were presented in terms of the isothermal and diabatic friction factors in the same order as the heat transfer conclusions.

From the average Nusselt numbers, it was found that the heat transfer coefficients in the laminar flow regime increased with increasing heat flux due to the buoyancy-induced secondary flow. The same trend was observed when the heat transfer results were plotted in terms of the Colburn *j*-factor, as the data had an almost parallel shift to the laminar forced convection line. However, from the Colburn *j*-factor results, it followed that the increased heat transfer coefficients in the laminar flow regime were not only due to the secondary flow effects, but also due to developing flow. The average heat transfer coefficients of developing flow were higher than for fully developed flow since the heat transfer coefficients decreased along the tube length as the flow approached fully developed flow.

From the Nusselt number and Colburn *j*-factor results, it was concluded that the heat transfer coefficients increased with increasing Reynolds number in the turbulent and low-Reynolds-number-end regimes due to the increased fluid velocity that enhanced mixing inside the tube. Heating had no significant influence on the heat transfer coefficients in these two flow regimes since the secondary flow effects were suppressed by the turbulent motion of the fluid.

Both Nusselt numbers and Colburn *j*-factor results revealed that the start of transition was delayed for increasing heat fluxes. However, heating did not have a significant influence on the end of transition or the magnitude of the heat transfer coefficients in the transitional flow regime.

The isothermal friction factors correlated very well with existing correlations in both laminar and turbulent flow regimes. The friction factors in the transitional flow regime were compared with the experimental data of previous studies. Although the shape of the transition friction factor curves of all three studies was approximately the same, transition did not start or end at the same Reynolds numbers. Furthermore, the gradient of transition differed for each study. The gradient of transition was the largest in the present study and it was concluded that the transition region became wider as the flow approached fully developed flow.

The diabatic friction factors increased slightly in the laminar flow regime due to the effects of secondary flow. When the heat flux was increased, the shear stress due to the change in velocity profile increased, while the density decreased. This led to the increased friction factors. Although the diabatic friction factors in the turbulent flow regime were slightly lower than the isothermal friction factors, there was no significant difference between the turbulent diabatic friction factors of the three heat fluxes. However, in the low-Reynolds-number-end regime, the diabatic friction factors decreased slightly with increasing heat flux. In the transitional flow regime, the diabatic friction factors were also significantly lower than the isothermal friction factors due to the decreased pressure drop when heat was applied. Similar to the heat transfer results, transition was slightly delayed for increasing fluxes. Furthermore, the gradient of transition increased with increasing heat flux.

When heat transfer and pressure drop were investigated simultaneously by plotting the Colburn *j*-factors and friction factors on a single graph, it was concluded that the boundaries of the different flow regimes in terms of heat transfer and pressure drop were the same. Furthermore, the relationship between heat transfer and pressure drop was investigated and correlations were developed to predict the Nusselt number as a function of friction factor, Reynolds number and Prandtl number in all four flow regimes (laminar, transition, low-Reynolds-number end and turbulent). The correlations were able to predict the laminar Nusselt numbers within 6%, the transitional Nusselt numbers within 5.5% and the Nusselt numbers in the low-Reynolds-number-end and turbulent flow regimes within 1.5% and 1.7%, respectively.

7. Summary, Conclusion and Recommendations

7.1. Summary

Heat exchangers have a wide range of applications including heating, ventilation and air-conditioning (HVAC) systems, fossil fuel power, nuclear power and concentrated solar power. Therefore, engineers need accurate design correlations to optimise the design of these heat exchangers. Designers are usually advised to avoid the transitional flow regime since the flow is believed to be unstable and chaotic. However, changes in operating conditions, design constraints, additional equipment, scaling and corrosion can cause heat exchangers to operate in or close to the transitional flow regime.

Flow in tubes has been extensively investigated since as early as 1883 especially focusing on laminar and turbulent flow. Since the 1990s, limited research has been done on tube flow in the transitional flow regime, and these studies considered either fully developed flow or average measurements of developing and fully developed flow across a tube length. No research has been done with the focus on developing flow in smooth tubes in the transitional flow regime. The thermal entrance length is a function of the tube diameter, Reynolds number and Prandtl number and therefore increases with increasing Reynolds number. At a Reynolds number of 2 000, the entrance length inside a 15 mm tube can vary between 9 m and 30 m for Prandtl numbers between 6 (water) and 20 (glycol mixture). This implies that the flow in heat exchangers will most likely be developing and not fully developed. Therefore, in order to optimise the design of heat exchangers, the heat transfer characteristics of developing flow in the transitional flow regime should be properly understood.

An experimental set-up, which can be used to investigate the heat transfer and pressure drop characteristics in the transitional flow regime, was designed, built and validated. The test section consisted of a copper tube with an inner diameter and length of 11.52 mm and 2.03 m, respectively, and a square-edged inlet was used. Thirteen thermocouple stations, each with four thermocouples, were spaced across the test section to measure the surface temperature. To measure the pressure drop across the test section, one pressure tap was located at the inlet of the test section and another at the outlet. Experiments were conducted during which the Reynolds number was varied between 500 and 10 000. This ensured that the whole transitional flow regime, as well as sufficient parts of the laminar and turbulent flow regimes, was covered. Water was used as the test fluid and the Prandtl number varied between 3 and 7. A constant heat flux boundary condition was used and three different heat fluxes were applied to the test section. A total of 398 tests were conducted, which consisted of 398 mass flow rate measurements, 19 158 temperature measurements and 370 pressure drop measurements.

An uncertainty analysis was also conducted and the experimental set-up and data reduction method were validated by comparing the heat transfer and friction factor results with literature. The heat transfer coefficients were validated by comparing local and average Nusselt numbers under both forced and mixed convection conditions. The friction factors were validated using the isothermal pressure drop data. The Nusselt number and Colburn *j*-factor uncertainties varied between 4% and 5% and the friction factor uncertainties varied between 1% and 17% depending on the mass flow rate and heat flux. However, at Reynolds numbers greater than 2 000, the friction factor uncertainties were less than 2.2%.

7.2. Conclusion

In order to gain a better understanding of developing flow, the thermal entrance length was investigated first. In the laminar flow regime, the thermal entrance length increased significantly with increasing Reynolds number, but decreased slightly with increasing heat flux due to the fluid Prandtl number. The thermal entrance length in the turbulent flow regime was independent of Reynolds number and Prandtl number, and was only a function of the tube diameter. When the forced and mixed convection results were compared, the thermal entrance length during forced convection conditions seemed to be shorter. However, due to the small temperature differences compared with the uncertainty of the temperature measurements, no accurate conclusions could be made.

Secondary flow was investigated by plotting the ratios of the heat transfer coefficients at the top and bottom of the test section. Secondary flow effects were suppressed near the inlet of the test section, but became significant as the thermal boundary layer increased along the tube length. As expected, the secondary flow effects increased with increasing heat flux due to increased temperature difference between the surface and fluid. However, the effects of secondary flow at a specific location on the tube decreased with increasing Reynolds number since the thickness of the thermal boundary layer decreased.

The Nusselt numbers and Colburn *j*-factors were calculated at each of the 13 thermocouple stations and then compared with each other to investigate the heat transfer characteristics of developing flow. The maximum heat transfer coefficients were found at the inlet of the test section and the Nusselt numbers at the first thermocouple station increased gradually with increasing Reynolds number. Thus, there were no distinct boundaries between the laminar, transitional and turbulent flow regimes. As the non-dimensional distance from the inlet of the test section (x/D) was increased, the laminar and turbulent regimes could be identified. Between x/D = 1.3 and x/D = 36, there was no significant difference between the heat transfer coefficients of the different heat fluxes in the laminar flow regime and the secondary flow effects only became significant after x/D = 53.4.

Nomenclature was developed to more specifically define the different flow regimes. Five different flow regions (laminar, developing laminar, transitional, low-Reynolds-number-end and turbulent) were identified from the Colburn *j*-factors between x/D = 1.3 and x/D = 36. The developing laminar region was unique to this part of the test section and became narrower with increasing x/D. The start of transition occurred earlier with increasing values of x/D between x/D = 1.3 and approximately x/D = 25.6, but was delayed as x/D was increased further. The end of transition was delayed for increasing values of x/D along the whole tube length. However, although the width of the transition region seemed to be approximately constant (Reynolds number range of approximately 2 100) between x/D = 25.6 and x/D = 174.9, it decreased slightly. Transition occurred earlier with increasing heat flux between x/D = 1.3 and x/D = 25.6, while both the start and end of transition were slightly delayed with increasing heat fluxes for x/D between x/D = 25.6 and x/D = 174.9. Furthermore, secondary flow had no significant influence on the width of the transition region. A previous investigation on fully developed flow found that the transition region became wider along the tube length, which is different from the developing flow results of this study. However, a longer test section is required to make accurate conclusions regarding the transition region of developing flow, since the entire entrance region as well as a sufficient part of the fully developed region should be covered.

The average heat transfer and pressure drop data included both developing (laminar and transitional flow regimes) as well as fully developed (turbulent flow regime) data. From the Nusselt number and Colburn *j*-factor results, it was concluded that the laminar heat transfer coefficients increased with increasing heat flux due to the buoyancy-induced secondary flow. However, from the Colburn *j*-factor results, it followed that the increased heat transfer coefficients in the laminar flow regime were not only due to the secondary flow effects, but also due to developing flow. In the turbulent and low-Reynolds-number-end regimes, the heat transfer coefficients increased with increasing Reynolds number due to the enhanced mixing inside the tube. The turbulent fluid motion also suppressed the secondary flow effects; thus heating had no significant influence on the heat transfer coefficients in these two regimes. Both Nusselt numbers and Colburn *j*-factors revealed that transition was delayed for increasing heat fluxes. However, heating did not have a significant influence on the end of transition. It was also concluded that heating did not have a significant influence of the magnitude of the heat transfer coefficients in the transitional flow regime.

The diabatic friction factors were slightly larger than the isothermal friction factors in the laminar flow regime due to the effects of secondary flow. When the heat flux was increased, the shear stress due to the change in velocity profile increased, while the density decreased, which led to the increased friction factors. Although the diabatic friction factors were slightly lower than the isothermal friction factors, there was no significant difference between the turbulent diabatic friction factors of the three heat fluxes. However, in the low-Reynolds-number-end regime, the diabatic friction factors decreased slightly with increasing heat flux. The diabatic friction factors in the transitional flow regime were also significantly lower than the isothermal friction factors due to the decreased pressure drop when heat was applied. Similar to the heat transfer results, transition was slightly delayed for increasing fluxes. Furthermore, the gradient of transition increased with increasing heat flux.

Heat transfer and pressure drop were investigated simultaneously by plotting the Colburn *j*-factors and friction factors on a single graph and it was concluded that the boundaries of the different flow regimes in terms of heat transfer and pressure drop were the same. Furthermore, the relationship between heat transfer and pressure drop was investigated and correlations were developed to predict the Nusselt number as a function of friction factor, Reynolds number and Prandtl number in the laminar, transitional, low-Reynolds-number-end and turbulent flow regimes. The correlations were able to predict the laminar Nusselt numbers within 6%, the transitional Nusselt numbers within 5.5% and the Nusselt numbers in the low-Reynolds-number-end and turbulent flow regimes within 1.5% and 1.7%, respectively

Overall, it was concluded that the heat transfer characteristics of developing and fully developed flow are significantly different and more work is required in order to fully understand developing flow in the transitional flow regime.

7.3. Recommendations

The following future work is recommended:

- an experimental set-up which can accommodate a test section with the same tube diameter (11.52 mm) as in this study and a length of 10 m to be able to investigate the entire developing flow region, as well as a fully developed region;
- pressure taps at different locations on the test section to investigate the pressure drop characteristics of developing flow;
- different inlet geometries to investigate the influence of inlet disturbances on developing flow;
- three rough test sections with a length of 10 m but different values of relative surface roughness to investigate the influence of surface roughness on developing flow.

References

Allen, R.W. & Eckert, E.R.G., 1964, 'Friction and heat-transfer measurements to turbulent pipe flow of water (Pr = 7 and 8) at uniform wall heat flux', *J. Heat Transfer* 86, 301-310.

ASHRAE 2009, *Fluid Flow, ASHRAE Handbook - Fundamentals,* American Society of Heating, Refrigerating and Air-Conditioning Engineers, Inc., Atlanta.

Bakker, A., LaRoche, R.D. & Marshall, E.M., 2000, *Laminar flow in static mixers with helical elements*, viewed 25 February 2014, from www.bakker.org/cfmbook/lamstat.pdf.

Blasius, P.R.H., 1913, 'Das Aehnlichkeitsgesetz bei Reibungsvorgangen in Flüssigkeiten', *Forschungsheft* 131, 1-41.

Cengel, Y.A., 2006, *Heat and Mass Transfer: A Practical Approach,* 3rd edn., McGraw-Hill, Singapore.

Cengel, Y.A. & Cimbala, J.M., 2006, *Fluid Mechanics: Fundamentals and Applications,* 1st edn., McGrawHill, New York.

Cengel, Y.A. & Ghajar, A.J., 2011, *Heat and Mass Transfer: Fundamentals and Applications,* 4th edn., McGraw-Hill, Singapore.

Dirker, J., Meyer, J.P. & Garach, D.V., 2014, 'Inlet flow effects in micro-channels in the laminar and transitional regimes on single-phase heat transfer coefficients and friction factors', *International Journal of Heat and Mass Transfer* 77, 612-626.

Dunn, P.F., 2010, *Measurement and Data Analysis for Engineering and Science,* 2nd edn., CRC Press, Boca Raton.

Filonenko, G.K., 1954, 'Hydraulischer Widerstand von Rohrleitungen (Org. Russ.) (Hydraulic resistance in pipes)', *Teploenergetika* 1(4), 40-44.

Ghajar, A.J. & Madon, K.F., 1992, 'Pressure drop measurements in the transition region for a circular tube with three different inlet configurations', *Experimental Thermal and Fluid Science* 5(1), 129-135.

Ghajar, A.J. & Tam, L.M., 1991, 'Laminar-transition-turbulent forced and mixed convective heat transfer correlations for pipe flows with different inlet configurations', *Winter Annual Meeting of the American Society of Mechanical Engineers,* Publ by ASME, New York, NY, United States, December 1-6, 1991, pp. 15.

Ghajar, A.J. & Tam, L.M., 1994, 'Heat transfer measurements and correlations in the transition region for a circular tube with three different inlet configurations', *Experimental Thermal and Fluid Science* 8(1), 79-90.

Ghajar, A.J. & Tam, L.M., 1995, 'Flow regime map for a horizontal pipe with uniform wall heat flux and three inlet configurations', *Experimental Thermal and Fluid Science* 10(3), 287-297.

Ghajar, A.J., Tang, C.C. & Cook, W.L., 2010, ‘Experimental investigation of friction factor in the transition region for water flow in minitubes and microtubes’, *Heat Transfer Engineering* 31(8), 646-657.

Ghiaasiaan, S.M., 2011, *Convective Heat and Mass Transfer,* 1st edn., Cambridge University Press, Cambridge.

Gnielinski, V., 1976, ‘New equations for heat and mass transfer in turbulent pipe and channel flow’, *Int. Chem. Eng.* 16(2), 359-368.

Gnielinski, V., 2010, ‘G1 Heat Transfer in Pipe Flow’ in *VDI Heat Atlas*, 2nd edn., Springer-Verlag, Berlin Heidelberg.

Holman, J.P., 1986, *Heat Transfer,* 6th edn., McGraw-Hill, Singapore.

Metais, B. & Eckert, E.R.G., 1964, ‘Forced, mixed and free convection regimes’, *Trans. ASME J. Heat Transfer* 10, 295-296.

Meyer, J.P., 2014, ‘Heat transfer in tubes in the transitional flow regime’, *15th International Heat Transfer Conference, IHTC-15*, Kyoto, Japan, August 10-15, 2014.

Meyer, J.P., McKrell, T.J. & Grote, K., 2013, ‘The influence of multi-walled carbon nanotubes on single-phase heat transfer and pressure drop characteristics in the transitional flow regime of smooth tubes’, *International Journal of Heat and Mass Transfer* 58(1-2), 597-609.

Meyer, J.P. & Olivier, J.A., 2011a, ‘Transitional flow inside enhanced tubes for fully developed and developing flow with different types of inlet disturbances: Part I - Adiabatic pressure drops’, *International Journal of Heat and Mass Transfer* 54(7-8), 1587-1597.

Meyer, J.P. & Olivier, J.A. 2011b, ‘Transitional flow inside enhanced tubes for fully developed and developing flow with different types of inlet disturbances: Part II - heat transfer’, *International Journal of Heat and Mass Transfer* 54(7-8), 1598-1607.

Meyer, J.P. & Olivier, J.A., 2014, ‘Heat transfer and pressure drop characteristics of smooth horizontal tubes in the transitional flow regime’, *Heat Transfer Engineering* 35(14-15), 1246-1253.

Nagendra, H.R., 1973, ‘Interaction of free and forced convection in horizontal tubes in the transitional regime’, *Journal of Fluid Mechanics* 57(2), 269-288.

Oliver, D.R., 1962, ‘The effect of natural convection on viscous-flow heat transfer in horizontal tubes’, *Chemical Engineering Science* 17(5), 335-350.

Olivier, J.A. & Meyer, J.P., 2010, ‘Single-phase heat transfer and pressure drop of the cooling of water inside smooth tubes for transitional flow with different inlet geometries (RP-1280)’, *HVAC and R Research* 16(4), 471-496.

Palen, J.W. & Taborek, J., 1985, ‘An improved heat transfer correlation for laminar flow of high Prandtl number fluids in horizontal tubes’, *AIChE Symposium Series* 81(245), 90-96.

Poiseuille, J.L.M., 1840, ‘Recherches expérimentelles sur le mouvement des liquids dans le tubes de trés petits diamétres’, *Comptes Rendu* 11, 961-967; 1041-1048.

Popiel, C.O. & Wojtkowiak, J., 1998, ‘Simple formulas for thermophysical properties of liquid water for heat transfer calculations [from O°C to 150°C]’, *Heat Transfer Engineering* 19(3), 87-101.

Rayle, R.E., 1959, *Influence of orifice geometry on static pressure measurements*, ASME Paper No. 59-A-234.

Reynolds, O., 1883, ‘An experimental investigation of the circumstances which determine whether the motion of water in parallel channels shall be direct or sinuous and of the law of resistance in parallel channels’, *Philosophical Transactions of the Royal Society of London* 174, 935-982.

Shah, R.K. & London, A.L., 1978, *Laminar Flow Forced Convection in Ducts*, Academic Press, New York.

Shah, R.K. & Seculic, D.P., 2003, *Fundamentals of Heat Exchanger Design,* John Wiley and Sons Inc., New Jersey.

Tam, L.M. & Ghajar, A.J., 1997, ‘Effect of inlet geometry and heating on the fully developed friction factor in the transition region of a horizontal tube’, *Experimental Thermal and Fluid Science* 15(1), 52-64.

Tam, L.M. & Ghajar, A.J., 1998, ‘The unusual behavior of local heat transfer coefficient in a circular tube with a bell-mouth inlet’, *Experimental Thermal and Fluid Science* 16(3), 187-194.

Tam, H.K., Tam, L.M. & Ghajar, A.J., 2013, ‘Effect of inlet geometries and heating on the entrance and fully-developed friction factors in the laminar and transition regions of a horizontal tube’, *Experimental Thermal and Fluid Science* 44, 680-696.

Tam, H.K., Tam, L.M., Ghajar, A.J. & Cheong, C.W., 2010, ‘Development of a unified flow regime map for a horizontal pipe with the support vector machines’, *AIP Conference Proceedings*, pp. 608.

Tam, L.M., Tam, H.K., Ghajar, A.J., Ng, W.S. & Wu, C.K., 2014, "The effect of inner surface roughness and heating on friction factor in horizontal mini-tubes", *15th International Heat Transfer Conference,* Kyoto, Japan, August 10-15, 2014.

Tam, L.M., Ghajar, A.J., Tam, H.K. & Tam, S.C., 2009, ‘Development of a flow regime map for a horizontal pipe with the multi-classification Support Vector Machines’, *2008 ASME Summer Heat Transfer Conference, HT 2008*, August 10-14, 2008, pp. 537.

Tam, H.K., Tam, L.M., Ghajar, A.J., Tam, S.C. & Zhang, T., 2012, ‘Experimental investigation of heat transfer, friction factor, and optimal fin geometries for the internally microfin tubes in the transition and turbulent regions’, *Journal of Enhanced Heat Transfer* 19(5), 457-476.

Ulaby, F.T., Michielssen, E. & Ravaioli, U., 2010, *Fundamentals of Applied Electromagnetics,* 6th edn., Pearson, Boston.

White, F.M., 2009, *Fluid Mechanics,* 6th edn., McGraw-Hill, Singapore.

White, F.M., 2006, *Viscous Fluid Flow,* 3rd edn., McGraw-Hill, Singapore.

Appendix A: Calibration

A.1. Introduction

This appendix describes the calibration process of the thermocouples and the pressure transducers. The calibration factors of the thermocouples, as well as the calibration curve of the pressure transducers are also given.

A.2. Thermocouple calibration

In the past (Olivier and Meyer, 2010; Meyer and Olivier, 2011a, 2011b, 2014; Meyer *et al.*, 2013; Meyer, 2014), the thermocouples were first calibrated using a thermostat bath and then soldered onto the test section. However, the properties of the thermocouple junction are likely to change during the attachment process. To improve the accuracy and reliability of the calibration factors, in situ calibration was used. Once the test section was completely built and inserted into the experimental set-up, the supply and return lines were connected to a thermal bath. To minimise any possible heat losses, the supply and return lines between the test section and thermal bath were made as short as possible and were properly insulated.

The thermocouples were calibrated using a LAUDA ECO RE 1225 thermostat bath with an accuracy of 0.03 °C and three PT-100 probes, which were calibrated to an accuracy of 0.1 °C. One PT-100 was placed at the inlet of the test section, one at the outlet of the test section and another in the thermostat bath. The thermocouples were calibrated between 20 °C and 60 °C at 2.5 °C intervals using the water from the thermostat bath. Therefore, no heating was applied to the tubes using the heating wire. Once the thermostat bath reached the desired temperature and all three PT-100 probes measured approximately the same temperature, a measurement, consisting of 200 measuring points, was taken. The process was also repeated for decreasing temperatures (from 60 °C to 20 °C) to ensure that a constant curve was obtained as well as to investigate the effect of hysteresis.

The 200 measuring points of each measurement for each thermocouple were averaged and a plot of the measured temperature against the average PT-100 temperature (Figure A.1(a)) was generated for each thermocouple and the results are summarised in Table A.1. A linear curve fit was done through the data points to obtain the calibration factors of each thermocouple. The calibrated temperatures were obtained using the following equation:

$$T_{cal} = \frac{(T_{uncal} - c)}{m} \tag{A.1}$$

Figure A.1(b) contains the temperatures profiles of the thermocouple inside the calming section after calibration. When comparing Figures A.1(a) and (b), it can be concluded that the calibration was successful since the calibrated temperatures were very close to the PT-100 measurements. Figure A.2 contains the uncalibrated and calibrated temperature measurements of all the thermocouples along the tube length at temperatures of 19.9 °C, 44.9 °C, 49.9 °C and 59.9 °C. From this figure, it follows that the calibration was successful and the average standard deviation of the calibrated temperature measurements along the test section for temperatures between 20 °C and

60 °C was 0.037 °C. Furthermore, the maximum thermocouple uncertainty was calculated to be 0.11 °C.

Table A.1: Thermocouple calibration factors. The thermocouple stations are shown in Figure 3.4.

	m	*c*		*m*	*c*		*m*	*c*
Ti1	0.9955	1.1300	E3	0.9973	0.9963	J1	0.9975	0.7488
A2	0.9956	0.8281	E4	0.9996	0.9224	J2	0.9986	0.7933
A3	0.9941	1.0130	F1	0.9985	1.0879	J3	0.9961	0.8253
A4	0.9955	0.9187	F2	0.9951	1.0687	J4	0.9940	0.8426
B1	0.9935	0.8904	F3	0.9958	0.7145	K2	0.9916	0.9629
B2	0.9969	0.9078	F4	0.9961	0.8549	K3	0.9973	0.8120
B3	0.9966	0.9944	G1	0.9968	0.7791	K4	0.9975	0.7333
B4	0.9928	1.2611	G2	0.9953	0.8583	L1	0.9975	0.9021
C1	0.9967	1.1695	G3	0.9983	0.6419	L3	0.9984	0.7928
C2	0.9966	1.0386	G4	0.9972	0.8790	L4	0.9974	0.9825
C3	0.9971	0.9847	H1	0.9952	0.8804	M1	0.9983	0.7001
C4	0.9955	0.8373	H2	0.9992	0.3943	M2	0.9999	0.8345
D1	0.9960	1.2913	H3	0.9946	0.7913	M3	1.0012	0.7600
D2	0.9975	0.7046	H4	0.9923	0.7984	M4	1.0016	0.7876
D3	0.9975	0.9512	I1	0.9943	0.5666	Te1	0.9923	0.4684
D4	0.9969	1.0302	I2	0.9943	0.7342	Te2	0.9937	0.6284
E1	0.9969	1.1098	I3	0.9934	0.6643	Te3	0.9930	0.7042
E2	0.9986	0.8349	I4	0.9931	0.7586	Te4	0.9944	0.4983

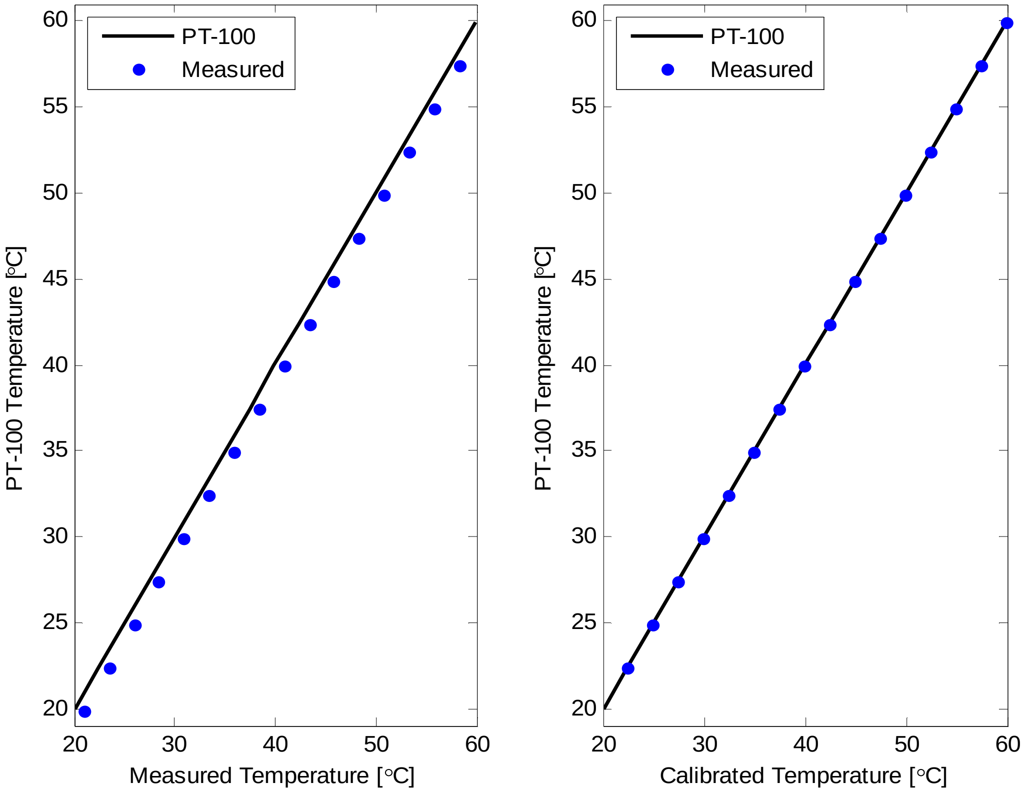

(a) (b)

Figure A.1: Temperature profile of temperatures measured by the thermocouple inside the calming section (a) before calibration and (b) after calibration

Table A.1: Thermocouple calibration factors. The thermocouple stations are shown in Figure 3.4.

	m	*c*		*m*	*c*		*m*	*c*
Ti1	0.9955	1.1300	E3	0.9973	0.9963	J1	0.9975	0.7488
A2	0.9956	0.8281	E4	0.9996	0.9224	J2	0.9986	0.7933
A3	0.9941	1.0130	F1	0.9985	1.0879	J3	0.9961	0.8253
A4	0.9955	0.9187	F2	0.9951	1.0687	J4	0.9940	0.8426
B1	0.9935	0.8904	F3	0.9958	0.7145	K2	0.9916	0.9629
B2	0.9969	0.9078	F4	0.9961	0.8549	K3	0.9973	0.8120
B3	0.9966	0.9944	G1	0.9968	0.7791	K4	0.9975	0.7333
B4	0.9928	1.2611	G2	0.9953	0.8583	L1	0.9975	0.9021
C1	0.9967	1.1695	G3	0.9983	0.6419	L3	0.9984	0.7928
C2	0.9966	1.0386	G4	0.9972	0.8790	L4	0.9974	0.9825
C3	0.9971	0.9847	H1	0.9952	0.8804	M1	0.9983	0.7001
C4	0.9955	0.8373	H2	0.9992	0.3943	M2	0.9999	0.8345
D1	0.9960	1.2913	H3	0.9946	0.7913	M3	1.0012	0.7600
D2	0.9975	0.7046	H4	0.9923	0.7984	M4	1.0016	0.7876
D3	0.9975	0.9512	I1	0.9943	0.5666	Te1	0.9923	0.4684
D4	0.9969	1.0302	I2	0.9943	0.7342	Te2	0.9937	0.6284
E1	0.9969	1.1098	I3	0.9934	0.6643	Te3	0.9930	0.7042
E2	0.9986	0.8349	I4	0.9931	0.7586	Te4	0.9944	0.4983

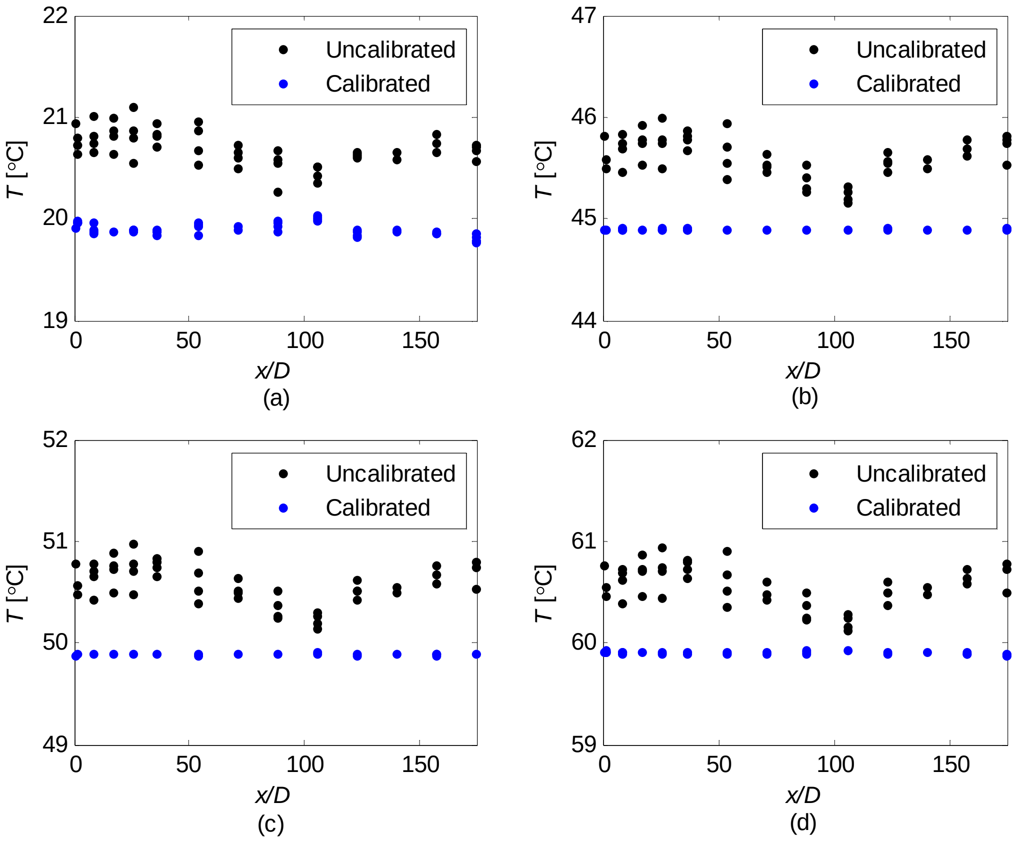

(a)
(b)
(c)
(d)

Figure A.2: Local calibrated and uncalibrated temperatures as a function of axial position at a temperature of (a) 19.9 °C, (b) 44.9 °C, (c) 49.9 °C and (d) 59.9 °C

A.3. Pressure transducer calibration

Differential pressure transducers with interchangeable diaphragms were used to measure the pressure drop across the test section. A 0.86 kPa diaphragm was used for Reynolds number measurements between 500 and 1 700, while a 5.5 kPa diaphragm was used for Reynolds numbers greater than 1 700. The 0.86 kPa diaphragm was calibrated using a Betz manometer with an accuracy of 2.5 Pa, while the 5.5 kPa diaphragm was calibrated using a low pressure controlled air manometer with an accuracy of 10 Pa.

The amplifier was adjusted such that the zero of the manometer corresponded to 4 mA in the Labview program and the full scale corresponded to 20 mA. The current signal obtained from the Labview program was converted to a pressure reading in MATLAB via interpolation. The relationship between the pressure and current readings of each transducer was obtained by doing a linear curve fit through the manometer readings and the current signals. The plots of the two pressure transducers are shown in Figures A.3 and A.4.

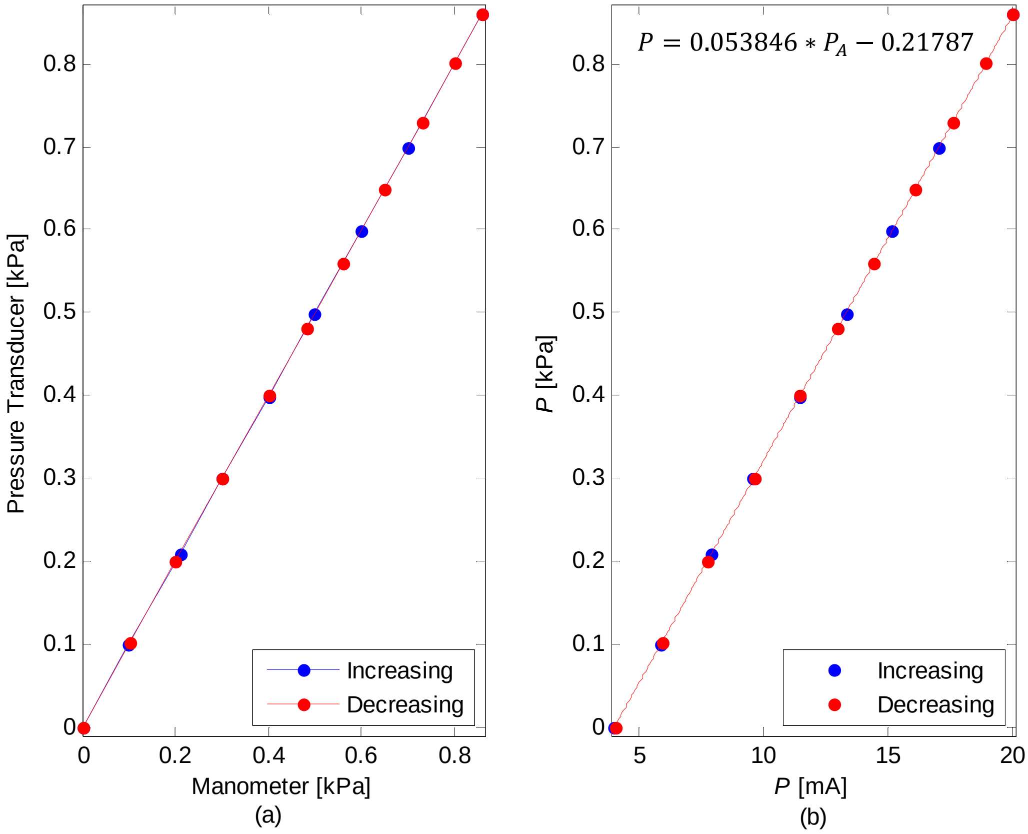

(a)

(b)

Figure A.3: Graph of pressure drop against (a) the manometer and (b) the current signal for the 0.86 kPa diaphragm

The equation of the line was determined for each pressure transducer and used during the data reduction of the actual tests. However, after each start of the pump, the pressure taps and pressure transducers were bled to ensure that there was no air in the system. A pressure reading was then taken during no-flow conditions and was used as the offset. The no-flow condition was obtained by opening the bypass valve and closing the supply valve to ensure that there was water supply for the pump, but not through the test section. One reading consisting of 200 measuring points was taken and the average reading was used as the offset value. The final pressure equations used in the MATLAB code were therefore:

$$P_{0.86\,kPa} = 0.053846 * P_A - 0.21787 - \text{offset} \tag{A.2}$$

$$P_{5.5\,kPa} = 0.34378 * P_A - 1.3744 - \text{offset} \tag{A.3}$$

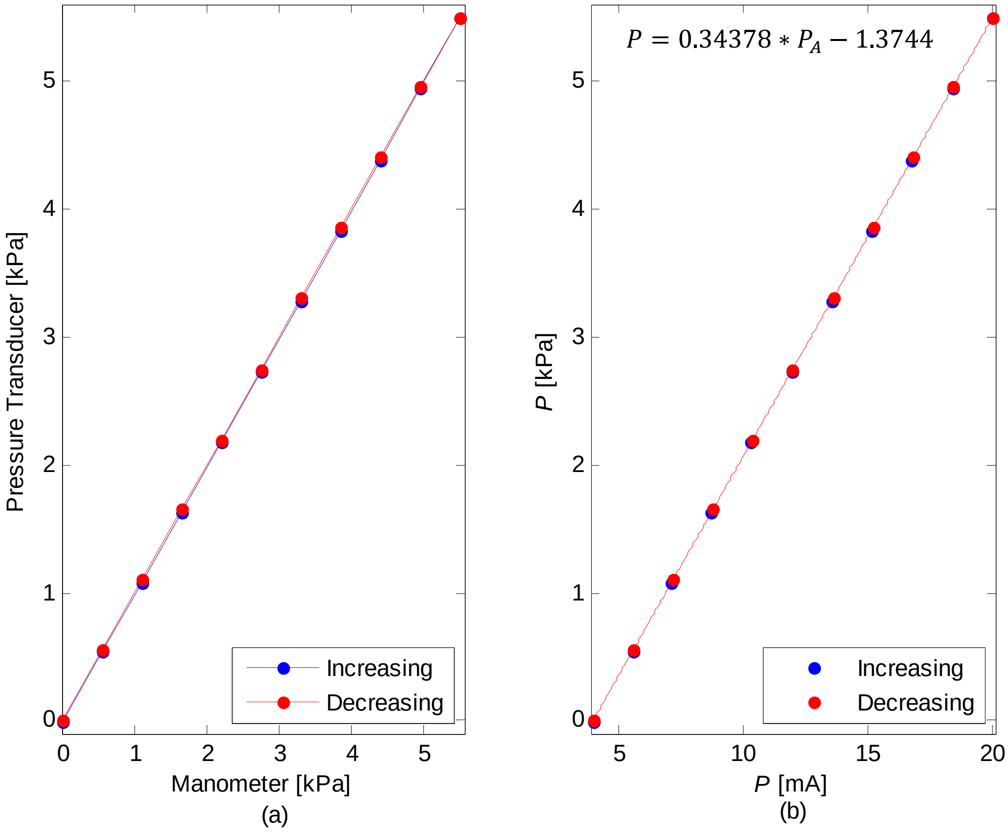

Figure A.4: Graph of pressure drop against (a) the manometer and (b) the current signal for the 5.5 kPa diaphragm

According to the manufacturer's specifications, the diaphragms have an accuracy of 0.25% of the full-scale value. From the linear regression analysis and uncertainty analysis, it was concluded that a maximum uncertainty of 0.239% was obtained at the full scale of the 0.86 kPa diaphragm and 0.254% was obtained at the full scale of the 5.5 kPa diaphragm. The average uncertainties of the 0.86 kPa diaphragm and 5.5 kPa diaphragm were 0.236% and 0.224%, respectively. Therefore, it can be concluded that the pressure transducer calibration was successful.

A.4. Conclusion

This appendix contained the calibration procedure and results of the thermocouples and pressure transducers. In situ calibration was used for the thermocouples since the properties of the thermocouple junction were likely to change when the thermocouple was soldered to the test section. The thermocouples were calibrated using a thermostat bath with an accuracy of 0.03 °C and three PT-100 probes with accuracies of 0.1 °C. The average standard deviation of the calibrated temperature measurements along the test section for temperatures between 20 °C and 60 °C was 0.037 °C. Furthermore, the maximum thermocouple uncertainty was calculated to be 0.11 °C.

To improve the accuracy of the pressure measurements, two different manometers were used to calibrate the two diaphragms. The 0.86 kPa diaphragm was calibrated using a Betz manometer with an accuracy of 2.5 Pa, while the 5.5 kPa diaphragm was calibrated using a low pressure controlled air manometer with an accuracy of 10 Pa. A linear curve fit through the manometer readings and current signals was done to obtain the relationship between the pressure and current readings of each diaphragm. The average uncertainties of the 0.86 kPa diaphragm and 5.5 kPa diaphragm were 0.236% and 0.224%, respectively.

A.5. Nomenclature

c	y-intercept	
cal	Calibrated value	
D	Inner diameter	m
m	Slope	
P	Pressure	Pa
P_A	Pressure	A
T	Temperature	°C or K
$uncal$	Uncalibrated value	
x	Distance from inlet	m

Appendix B: Heating Wire

B.1. Introduction

Single strand constantan heating wire was coiled around the test section to apply a constant heat flux. However, if the heating wire is coiled too close to the thermocouples, the temperature measurements will be affected. On the other hand, if the gap between the heating wire and the thermocouple is too big, the heat flux will not be constant in an axial direction along the test section. Therefore, it is important to find a suitable coil spacing to ensure a constant heat flux and accurate surface temperature readings.

B.2. Test section

A copper tube with an inside diameter of 11.52 mm and length of 3 m was used for this experiment. Twelve thermocouple stations were spaced 15 cm apart between $x = 1.2$ m and $x = 2.9$ m. A schematic representation of the test section is shown in Figure B.1. There were four types of thermocouple stations and each coiling type was repeated three times. Figure B.2 is a schematic representation of the different types. In Figure B.1, a small gap implies that the heating wire nearly touches the thermocouple junction, while a medium gap implies a 1 mm gap between the thermocouple and the heating wire. After the thermocouples are soldered to the tube, care must be taken to avoid the thermocouple breaking off. Therefore, it would be desirable to coil the heating wire once or twice over the thermocouple wire to secure it and minimise damages. However, it is important to ensure that the heating wire across the thermocouple wire does not affect the thermocouple readings. To investigate this effect, the heating wire was either coiled twice across the thermocouple wire or not at all.

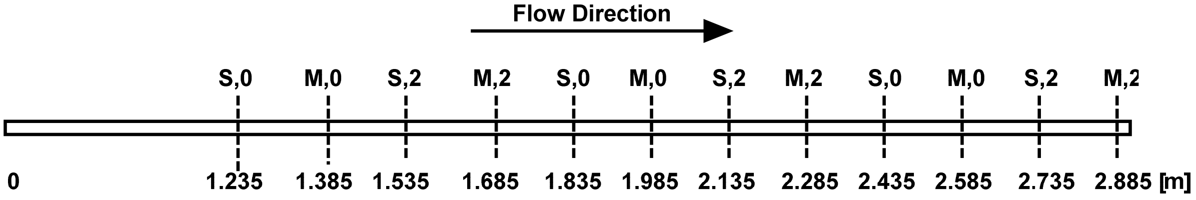

Figure B.1: Schematic representation of test section used to investigate the heating wire coiling techniques

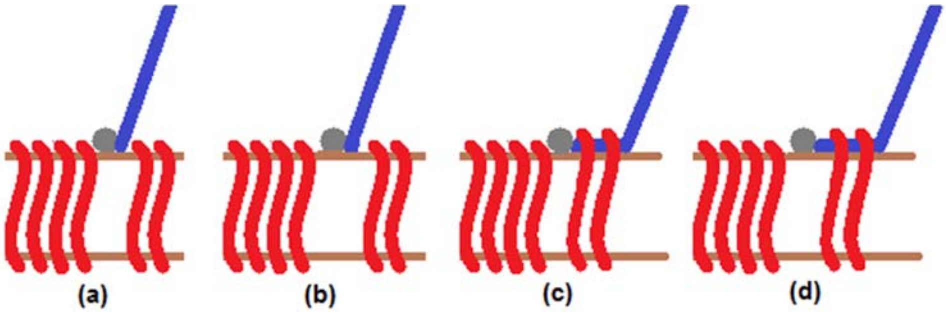

Figure B.2: Schematic representation of different heating wire coiling techniques: (a) small gap with no coils (S,0), (b) medium gap with no coils (M,0), (c) small gap with two coils (S,2) and (d) medium gap with two coils (M,2)

Figure B.3 contains the local Nusselt number results for four different Reynolds numbers at a heat flux of 65 W/m^2. Figure B.3(a) contains the results of the thermocouple station with a small gap and no coils while Figure B.3(b) contains the results of the thermocouple station with a medium gap and no coils. The Nusselt numbers in Figure B.3(b) were slightly higher than in Figure B.3(a). A possible reason for this is that the heating wire influenced the temperature measurements when the gap was too small and a higher temperature was measured. The increased surface temperature led to a decreased heat transfer coefficient and therefore decreased Nusselt number. Figure B.3(d) contains the Nusselt number results of the thermocouple stations with a medium gap and two coils. When comparing Figure B.3(d) with Figures B.3(a) to (c), it can be concluded that this technique gave the best results since the local Nusselt numbers were more consistent than with the other techniques.

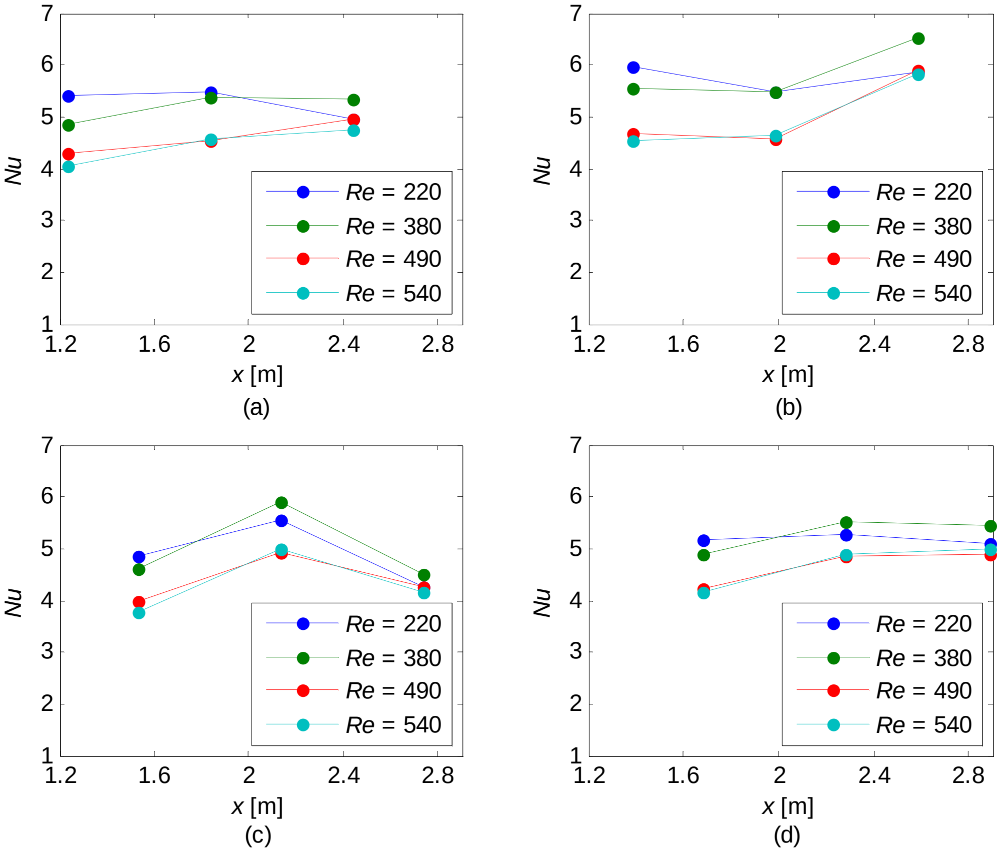

(a) (b) (c) (d)

Figure B.3: Local Nusselt number results as a function of axial position for different Reynolds numbers at a heat flux of 65 W/m^2 for (a) small gap with no coils, (b) medium gap with no coils, (c) small gap with two coils and (d) medium gap with two coils

B.3. Conclusion

An experiment was conducted to obtain a suitable technique to coil the heating wire close to the thermocouple junctions. From the local Nusselt number results, it was concluded that consistent results were obtained when the gap between the thermocouple junction and the heating wire was approximately 1 mm. It was found that when the heating wire was coiled twice over the thermocouple wire, the thermocouple was secured without affecting the temperature measurements.

B.4. Nomenclature

Nu	Nusselt number	
x	Distance from inlet	m

Appendix C: Uncertainty Analysis

C.1. Introduction

An uncertainty analysis was conducted to determine the uncertainty of the parameters that were relevant to this study, such as Nusselt number, Colburn *j*-factor, friction factor and Reynolds number. This section gives the details of the uncertainty analysis as well as the results of the Reynolds number, friction factor, Nusselt number and Colburn *j*-factor uncertainties.

C.2. Theory

Two types of errors, bias and precision, arise during measurement processes. The bias determines the accuracy of the measurement and is normally specified by the manufacturer of the instrument. The bias errors result from calibration, imperfections in measuring equipment, etc. The precision relates to the scatter in the data, which determines the precision of the data. The precision errors are always present and are due to variations in the measurement process, electrical noise, etc. The magnitudes of the bias and precision errors correspond to the 95% probability that the actual error will not be more than the estimate. The uncertainty in a single measurement is based on the bias and precision and is calculated as follows (Dunn, 2010):

$$\delta x_i = \left(b_i^2 + p_i^2\right)^{1/2} \tag{C.1}$$

x_i is a single observation and δx_i represents the standard deviation multiplied with Student's *t* variable (Dunn, 2010). The result *R* of a measurement is a function of several variables and is calculated from a group of equations.

$$R = R(x_1, x_2, x_3, \dots, x_n) \tag{C.2}$$

Once the uncertainties of x_i are known, the uncertainty in *R* can be determined as follows:

$$\delta R = \frac{\partial R}{\partial x_i} \delta x_i \tag{C.3}$$

The sensitivity coefficient, δR, is used to determine the effect that x_i has on the overall uncertainty. The root sum square method can be used to determine the uncertainty *R* for several independent variables:

$$\delta R = \left[\left(\frac{\partial R}{\partial x_1}\right)^2 \delta x_1 + \left(\frac{\partial R}{\partial x_2}\right)^2 \delta x_2 + \dots + \left(\frac{\partial R}{\partial x_n}\right)^2 \delta x_n\right]^{1/2} \tag{C.4}$$

Linear regression analysis was used to determine the bias of the thermocouples and pressure transducers. Regression analysis determines a mathematical relation between two or more variables (Dunn, 2010). The value of *x* is usually known, while the value of *y* is obtained from measurements. This implies that the uncertainty results from the *y* variable (Dunn, 2010). The uncertainty in the *y* variable is determined using Equation C.5:

$$\delta y = \pm\, t\, S_{yx}\sqrt{\frac{1}{N}+\frac{1}{M}+\frac{(x_i-\bar{x})^2}{S_{xx}}} \tag{C.5}$$

where S_{xx} is defined as follows:

$$S_{xx} = \sum_{i=1}^{N}(x_i-\bar{x})^2 \tag{C.6}$$

S_{yx} is obtained by first calculating the parameters *a* and *b*:

$$S_{xy} = \sum_{i=1}^{N}(x_i-\bar{x})(y_i-\bar{y}) \tag{C.7}$$

$$b = \frac{S_{xy}}{S_{xx}} \tag{C.8}$$

$$a = \bar{y} - b\bar{x} \tag{C.9}$$

$$S_{yx} = \sqrt{\frac{\sum_{i=1}^{N}(y_i-y_{ci})^2}{N-2}} \tag{C.10}$$

To obtain the uncertainty in the *x* variable, the uncertainty in *y* is divided by the slope of the regression line.

$$\delta x = \frac{\delta y}{m} \tag{C.11}$$

C.3. Instruments

For all instruments, the bias was considered as the accuracy specified by the manufacturer. The precision was obtained from the standard deviation of 200 measuring points, which was then multiplied by Student's *t* variable to fall within the 95% confidence region.

C.3.1. Thermocouples

A PT-100 probe with an accuracy of 0.1°C and a thermostat bath with an accuracy of 0.03°C were used to calibrate the thermocouples. Eighteen data points, consisting of 200 measuring points, were taken between 20 °C and 60 °C. The readings of each thermocouple were then plotted against the measurements of the PT-100. Since a linear relationship between the thermocouples and PT-100 exists, a linear line was used to obtain the calibration curve.

Using this calibration curve, the calibrated thermocouple readings were compared with those of the PT-100. The accuracy of the PT-100 was used as the bias of the thermocouples and the precision of the thermocouples was calculated using Equations C.5 to C.11. The overall uncertainty of each thermocouple was then calculated using Equation C.1 and the uncertainties of the different thermocouples varied between 0.1 °C and 0.11 °C.

C.3.2. Coriolis flow meters

Two Coriolis flow meters with different capacities were used to measure the mass flow rate. The bias of the flow meters was 0.05% of the full scale. Thus the accuracy was 0.054 ℓ/h for the flow meter with a capacity of 108 ℓ/h and 1.09 ℓ/h for the flow meter with a capacity of 2 180 ℓ/h.

C.3.3. Pressure transducer

Two differential pressure transducers with interchangeable diaphragms were used to measure the pressure drop across the test section. A Betz manometer with an accuracy of 2.5 Pa was used to calibrate the 0.86 kPa diaphragm, while a low pressure controller air manometer with an accuracy of 10 Pa was used to calibrate the 5.5 kPa diaphragm. The accuracies of the manometers were used as the bias of each pressure transducer. During the pressure transducer calibration, 21 data points, each consisting of 200 measuring points, were taken between zero and the maximum of each diaphragm. A linear relationship between the pressure transducer and the manometer exists; therefore, a linear line was fitted through the calibration points.

Similar to the thermocouple calibration, the precision of the pressure transducers was calculated using Equations C.5 to C.11. The overall uncertainty of pressure transducers was then calculated using Equation C.1. The uncertainty of the 0.86 kPa diaphragm varied between 0.234% and 0.239%, while the uncertainty of the 5.5 kPa diaphragm varied between 0.205% and 0.254%.

C.3.4. Power supply

Two PS 8360-30 2U power supplies were used for heating. The voltage and current accuracies were both 0.2% of the nominal value.

C.3.5. Diameter

A split-ball instrument was used to obtain the exact inner diameter of the test section and a vernier calliper with an accuracy of 20 µm was used to measure the inner diameter of the test section.

C.3.6. Length

A measuring tape with an accuracy of 1 mm was used to measure the length of the test section.

C.4. Fluid properties

The properties of water were calculated using the thermophysical equations of Popiel and Wojtkowiak (1998). The uncertainties associated with these equations were specified by the authors and are summarised in Table C.1.

Table C.1: Uncertainties of fluid properties (Popiel and Wojtkowiak, 1998)

Property	ρ [kg/m^3]	C_p [J/kg.K]	k [W/m.K]	μ [kg/m.s]	Pr [-]
Uncertainty (%)	0.004	0.04	2	1	2.3

C.5. Calculated parameters

C.5.1. Temperatures

The test section contained 13 thermocouple stations, each with four thermocouples. A representative temperature at the thermocouple station was obtained by taking the average of the four thermocouples:

$$\bar{T} = \frac{T_1+T_2+T_3+T_4}{4} \tag{C.12}$$

The uncertainty of this temperature was calculated as follows:

$$\delta\bar{T} = \left[\left(\frac{\delta T_1}{4}\right)^2 + \left(\frac{\delta T_2}{4}\right)^2 + \left(\frac{\delta T_3}{4}\right)^2 + \left(\frac{\delta T_4}{4}\right)^2\right]^{1/2} \tag{C.13}$$

C.5.2. Heat transfer area

The uncertainty of the heat transfer area is:

$$A = \pi D l \tag{C.14}$$

$$\delta A = \left[\left(\frac{\partial A}{\partial D}\delta D\right)^2 + \left(\frac{\partial A}{\partial L}\delta L\right)^2\right]^{1/2}$$

$$\delta A = \left[(\pi\, L\, \delta D)^2 + (\pi\, D\, \delta L)^2\right]^{1/2} \tag{C.15}$$

C.5.3. Heat input

The uncertainty of the heat input using two power supplies was determined using the following equation:

$$\dot{Q} = V_1 * I_1 + V_2 * I_2 \tag{C.16}$$

$$\delta\dot{Q} = \left[\left(\frac{\partial\dot{Q}}{\partial V_1}\delta V_1\right)^2 + \left(\frac{\partial I_1}{\partial I_1}\delta I_1\right)^2 + \left(\frac{\partial\dot{Q}}{\partial V_2}\delta V_2\right)^2 + \left(\frac{\partial\dot{Q}}{\partial I_2}\delta I_2\right)^2\right]^{1/2}$$

$$\delta\dot{Q} = \left[(I_1\delta V_1)^2 + (V_1\delta I_1)^2 + (I_2\delta V_2)^2 + (V_2\delta I_2)^2\right]^{1/2} \tag{C.17}$$

C.5.4. Heat flux

The uncertainty of the heat flux was calculated as follows:

$$q = \frac{Q}{A} \tag{C.18}$$

$$\delta q = \left[\left(\frac{\partial q}{\partial Q}\delta Q\right)^2 + \left(\frac{\partial q}{\partial A}\delta A\right)^2\right]^{1/2}$$

$$\delta q = \left[\left(\frac{1}{A}\delta Q\right)^2 + \left(-\frac{Q}{A^2}\delta A\right)^2\right]^{1/2} \tag{C.19}$$

C.5.5. Heat transfer coefficient

The uncertainty of the heat transfer coefficient is:

$$h = \frac{q}{(T_s - T_b)} \tag{C.20}$$

$$\delta h = \left[\left(\frac{\partial h}{\partial q}\delta q\right)^2 + \left(\frac{\partial h}{\partial T_s}\delta T_s\right)^2 + \left(\frac{\partial h}{\partial T_b}\delta T_b\right)^2\right]^{1/2}$$

$$\delta h = \left[\left(\frac{1}{T_s - T_b}\delta q\right)^2 + \left(\frac{-q}{(T_s - T_b)^2}\delta T_s\right)^2 + \left(\frac{q}{(T_s - T_b)^2}\delta T_b\right)^2\right]^{1/2} \tag{C.21}$$

C.5.6. Nusselt number

The uncertainty of the Nusselt number was determined as follows:

$$Nu = \frac{hD}{k} \tag{C.22}$$

$$\delta Nu = \left[\left(\frac{\partial Nu}{\partial h}\delta h\right)^2 + \left(\frac{\partial Nu}{\partial D}\delta D\right)^2 + \left(\frac{\partial Nu}{\partial k}\delta k\right)^2\right]^{1/2}$$

$$\delta Nu = \left[\left(\frac{D}{k}\delta h\right)^2 + \left(\frac{h}{k}\delta D\right)^2 + \left(-\frac{hD}{k^2}\delta k\right)^2\right]^{1/2} \tag{C.23}$$

C.5.7. Cross-sectional area

The uncertainty of the cross-sectional area was calculated as follows:

$$A_c = \frac{\pi}{4}D^2 \tag{C.24}$$

$$\delta A_c = \left[\left(\frac{\partial A_c}{\partial D}\delta D\right)^2\right]^{1/2}$$

$$\delta A_c = \frac{\pi D}{2}\delta D \tag{C.25}$$

C.5.8. Reynolds number

The uncertainty of the Reynolds number was determined as:

$$Re = \frac{\dot{m}D}{\mu A_c} \tag{C.26}$$

$$\delta Re = \left[\left(\frac{\partial Re}{\partial \dot{m}}\delta \dot{m}\right)^2 + \left(\frac{\partial Re}{\partial D}\delta D\right)^2 + \left(\frac{\partial Re}{\partial \mu}\delta \mu\right)^2 + \left(\frac{\partial Re}{\partial A_c}\delta A_c\right)^2\right]^{1/2}$$

$$\delta Re = \left[\left(\frac{D}{\mu A_c}\delta \dot{m}\right)^2 + \left(\frac{\dot{m}}{\mu A_c}\delta D\right)^2 + \left(-\frac{\dot{m}D}{\mu^2 A_c}\delta \mu\right)^2 + \left(-\frac{\dot{m}D}{\mu A^2}\delta A_c\right)^2\right]^{1/2} \tag{C.27}$$

C.5.9. Colburn *j*-factor

The uncertainty of the Colburn *j*-factor was determined as follows:

$$j = \frac{Nu}{RePr^{1/3}} \tag{C.28}$$

$$\delta j = \left[\left(\frac{\partial j}{\partial Nu}\delta Nu\right)^2 + \left(\frac{\partial j}{\partial Re}\delta Re\right)^2 + \left(\frac{\partial j}{\partial Pr}\delta Pr\right)^2\right]^{1/2}$$

$$\delta j = \left[\left(\frac{1}{RePr^{1/3}}\delta Nu\right)^2 + \left(-\frac{Nu}{Re^2 Pr^{1/3}}\delta Re\right)^2 + \left(-\frac{1}{3}\frac{Nu}{RePr^{4/3}}\delta Pr\right)^2\right]^{1/2} \tag{C.29}$$

C.5.10. Flow velocity

The uncertainty of the flow velocity is:

$$u = \frac{\dot{m}}{\rho A} \tag{C.30}$$

$$\delta u = \left[\left(\frac{\partial u}{\partial \dot{m}}\delta \dot{m}\right)^2 + \left(\frac{\partial u}{\partial \rho}\delta \rho\right)^2 + \left(\frac{\partial u}{\partial A}\delta A\right)^2\right]^{1/2}$$

$$\delta u = \left[\left(\frac{1}{\rho A}\delta \dot{m}\right)^2 + \left(-\frac{\dot{m}}{\rho^2 A}\delta \rho\right)^2 + \left(-\frac{\dot{m}}{\rho A^2}\delta A\right)^2\right]^{1/2} \tag{C.31}$$

C.5.11. Friction factor

The uncertainty of the friction factor can be determined as follows:

$$f = \frac{\Delta P\ \rho\ D^5 \pi^2}{8\ \dot{m}^2 L} \tag{C.32}$$

$$f = \frac{2\Delta P\ D}{\rho u^2 L}$$

$$\delta f = \left[\left(\frac{\partial f}{\partial \Delta P}\delta \Delta P\right)^2 + \left(\frac{\partial f}{\partial D}\delta D\right)^2 + \left(\frac{\partial f}{\partial \rho}\delta \rho\right)^2 + \left(\frac{\partial f}{\partial u}\delta u\right)^2 + \left(\frac{\partial f}{\partial L}\delta L\right)^2\right]^{1/2}$$

$$\delta f = \left[\left(\frac{2D}{\rho u^2 L}\delta \Delta P\right)^2 + \left(\frac{2\Delta P}{\rho u^2 L}\delta D\right)^2 + \left(-\frac{2\Delta P\ D}{\rho^2 u^2 L}\delta \rho\right)^2 + \left(-\frac{4\Delta P\ D}{\rho u^3 L}\delta u\right)^2 + \left(-\frac{2\Delta P\ D}{\rho u^2 L^2}\delta L\right)^2\right]^{1/2} \tag{C.33}$$

C.6. Example calculation

Example calculations are given to illustrate the linear regression analysis as well as the uncertainty analysis method.

C.6.1. Linear regression analysis

Linear regression analysis was used to determine the uncertainties of the thermocouples and pressure transducers during the calibration process.

C.6.1.1 Temperature

The uncertainty of the thermocouple inside the calming section is used as an example. Using Equation C.6, S_{xx} was determined as follows:

$$S_{xx} = \sum_{i=1}^{N}(x_i - \bar{x})^2$$

$$\begin{aligned} S_{xx} = {} & (19.9-39.9)^2 + (22.4-39.9)^2 + (24.9-39.9)^2 + (27.4-39.9)^2 + (29.9-39.9)^2 \\ & + (32.4-39.9)^2 + (34.9-39.9)^2 + (37.4-39.9)^2 + (39.9-39.9)^2 \\ & + (42.4-39.9)^2 + (44.9-39.9)^2 + (47.4-39.9)^2 + (49.9-39.9)^2 \\ & + (52.4-39.9)^2 + (54.9-39.9)^2 + (57.4-39.9)^2 + (59.9-39.9)^2 \\ S_{xx} = {} & 2550 \end{aligned}$$

S_{xy} was determined using Equation C.7:

$$S_{xy} = \sum_{i=1}^{N} (x_i - \bar{x})(y_i - \bar{y})$$

$$\begin{aligned} S_{xx} = \; & (19.9 - 39.9)(19.9000 - 39.8898) + (22.4 - 39.9)(22.3929 - 39.8898) \\ & + (24.9 - 39.9)(24.9045 - 39.8898) + (27.4 - 39.9)(27.3836 - 39.8898) \\ & + (29.9 - 39.9)(29.8664 - 39.8898) + (32.4 - 39.9)(32.3957 - 39.8898) \\ & + (34.9 - 39.9)(34.8833 - 39.8898) + (37.4 - 39.9)(37.3921 - 39.8898) \\ & + (39.9 - 39.9)(39.8953 - 39.8898) + (42.4 - 39.9)(42.3919 - 39.8898) \\ & + (44.9 - 39.9)(44.8900 - 39.8898) + (47.4 - 39.9)(47.3817 - 39.8898) \\ & + (49.9 - 39.9)(49.8743 - 39.8898) + (52.4 - 39.9)(52.3706 - 39.8898) \\ & + (54.9 - 39.9)(54.8959 - 39.8898) + (57.4 - 39.9)(57.4088 - 39.8898) \\ & + (59.9 - 39.9)(59.9000 - 39.8898) \end{aligned}$$

$$S_{xy} = 2550$$

The parameters *a* and *b* were then determined using Equations C.8 and C.9:

$$b = \frac{S_{xy}}{S_{xx}}$$

$$b = \frac{2550}{2550}$$

$$b = 1$$

$$a = \bar{y} - b\bar{x}$$

$$a = 39.8898 - 39.9$$

$$a = -0.0101$$

With both *a* and *b* known, y_{ci} was calculated using Equation C.9. Next, S_{yx} was determined as follows:

$$S_{yx} = \sqrt{\frac{\sum_{i=1}^{N} (y_i - y_{ci})^2}{N - 2}}$$

$$sum1 = \sum_{i=1}^{N} (y_i - y_{ci})^2$$

$$\begin{aligned} sum1 = \; & (19.9000 - 19.8899)^2 + (22.3929 - 22.3899)^2 + (24.9045 - 24.8899)^2 \\ & + (27.3836 - 27.3899)^2 + (29.8664 - 29.8899)^2 + (32.3957 - 32.3899)^2 \\ & + (34.8833 - 34.8899)^2 + (37.3921 - 37.3899)^2 + (39.8953 - 39.8899)^2 \\ & + (42.3919 - 42.3899)^2 + (44.8900 - 44.8899)^2 + (47.3817 - 47.3899)^2 \\ & + (49.8743 - 49.8899)^2 + (52.37060 - 52.38899)^2 + (54.8959 - 54.8899)^2 \\ & + (57.4088 - 57.3899)^2 + (59.9000 - 59.8899)^2 \end{aligned}$$

$$S_{yx} = \sqrt{\frac{sum1}{15}}$$

$$S_{yx} = 0.0121$$

The precision component of the thermocouple uncertainty at 20 °C was then calculated by combining Equations C.5 and C.6:

$$p = \pm \frac{t * S_{yx}}{m} \sqrt{\frac{1}{N} + \frac{1}{M} + \frac{(x_i - \bar{x})^2}{S_{xx}}}$$

$$p = \pm \frac{2.11 * 0.0121}{0.9955} \sqrt{\frac{1}{200} + \frac{1}{17} + \frac{(19.9 - 39.9)^2}{2550}}$$

$$p = \pm 0.0122$$

The accuracy of the PT-100 probes, which were used during the calibration, was 0.1 °C and was used as the bias component of the thermocouple uncertainty. The overall uncertainty of the thermocouple inside the calming section at 20 °C was then calculated using Equation C.1:

$$\delta x_i = \left(b_i^2 + p_i^2\right)^{1/2}$$

$$\delta T = (0.1^2 + 0.0122^2)^{1/2}$$

$$\delta x_i = 0.1007\ ^\circ\mathrm{C}$$

The uncertainty of the temperature measurements of this thermocouple decreased to 0.1002 °C at 40 °C and then increased again to 0.1007 °C at 60 °C.

C.6.1.2 Pressure

The uncertainty of the 0.86 kPa diaphragm is used as an example. Using Equation C.6, S_{xx} was determined as follows:

$$S_{xx} = \sum_{i=1}^{N} (x_i - \bar{x})^2$$

$$\begin{aligned} S_{xx} = {} & (0 - 0.4155)^2 + (0.1 - 0.4155)^2 + (0.21 - 0.4155)^2 + (0.3 - 0.4155)^2 \\ & + (0.4 - 0.4155)^2 + (0.5 - 0.4155)^2 + (0.6 - 0.4155)^2 + (0.7 - 0.4155)^2 \\ & + (0.86 - 0.4155)^2 + (0.8 - 0.4155)^2 + (0.73 - 0.4155)^2 + (0.65 - 0.4155)^2 \\ & + (0.56 - 0.4155)^2 + (0.481 - 0.4155)^2 + (0.401 - 0.4155)^2 \\ & + (0.301 - 0.4155)^2 + (0.201 - 0.4155)^2 + (0.101 - 0.4155)^2 + (0 - 0.4155)^2 \end{aligned}$$

$$S_{xx} = 1.3055$$

S_{xy} was determined using Equation C.7:

$$S_{xy} = \sum_{i=1}^{N} (x_i - \bar{x})(y_i - \bar{y})$$

$$\begin{aligned}S_{xy} = {} & (0-0.4155)(0-0.4154)+(0.1-0.4155)(0.1-0.4154)\\ & +(0.21-0.4155)(0.2093-0.4154)+(0.3-0.4155)(0.2996-0.4154)\\ & +(0.4-0.4155)(0.3988-0.4154)+(0.5-0.4155)(0.4993-0.4154)\\ & +(0.6-0.4155)(0.599-0.4154)+(0.7-0.4155)(0.6993-0.4154)\\ & +(0.86-0.4155)(0.86-0.4154)+(0.8-0.4155)(0.8005-0.4154)\\ & +(0.73-0.4155)(0.7302-0.4154)+(0.65-0.4155)(0.65-0.4154)\\ & +(0.56-0.4155)(0.5604-0.4154)+(0.481-0.4155)(0.4811-0.4154)\\ & +(0.401-0.4155)(0.4010-0.4154)+(0.301-0.4155)(0.3011-0.4154)\\ & +(0.201-0.4155)(0.2012-0.4154)+(0.101-0.4155)(0.1012-0.4154)\\ & +(0-0.4155)(0-0.4154)\end{aligned}$$

$$S_{xy} = 1.3055$$

The parameters *a* and *b* were then determined using Equations C.8 and C.9:

$$b = \frac{S_{xy}}{S_{xx}}$$

$$b = \frac{1.3055}{1.3055}$$

$$b = 1$$

$$a = \bar{y} - b\bar{x}$$

$$a = 0.4154 - 0.4155$$

$$a = -1x10^{-4}$$

With both *a* and *b* known, y_{ci} was calculated using Equation C.9. Next, S_{yx} was determined as follows:

$$S_{yx} = \sqrt{\frac{\sum_{i=1}^{N}(y_i - y_{ci})^2}{N-2}}$$

$$sum1 = \sum_{i=1}^{N}(y_i - y_{ci})^2$$

$$\begin{aligned}sum1 = {} & (0-0)^2+(0.1-0.0998)^2+(0.2093-0.2098)^2+(0.2996-0.2998)^2\\ & +(0.3988-0.3998)^2+(0.4993-0.4998)^2+(0.599-0.5998)^2\\ & +(0.6993-0.6998)^2+(0.86-0.8598)^2+(0.8005-0.7998)^2\\ & +(0.7302-0.7298)^2+(0.65-0.6498)^2+(0.5604-0.5598)^2\\ & +(0.4811-0.4808)^2+(0.401-0.4008)^2+(0.3011-0.3008)^2\\ & +(0.2012-0.2008)^2+(0.1012-0.1008)^2+(0-0)^2\end{aligned}$$

$$S_{yx} = \sqrt{\frac{sum1}{19}}$$

$$S_{yx} = 5.0572x10^{-4}$$

The precision component of the pressure uncertainty at 0.65 kPa was then calculated by combining Equations C.5 and C.6:

$$p = \pm \frac{t * S_{yx}}{m} \sqrt{\frac{1}{N} + \frac{1}{M} + \frac{(x_i - \bar{x})^2}{S_{xx}}}$$

$$p = \pm \frac{2.021 * 5.0572x10^{-4}}{1} \sqrt{\frac{1}{200} + \frac{1}{19} + \frac{(0.65 - 0.4155)^2}{1.3055}}$$

$$p = \pm 3.3079x10^{-4} \text{ kPa}$$

The accuracy of the manometer, which was used during the calibration of the 0.86 kPa diaphragm, was 2 Pa and was used as the bias component of the pressure uncertainty. The overall uncertainty of the 0.86 kPa pressure transducer at 0.68 kPa was then calculated using Equation C.1:

$$\delta x_i = \left(b_i^2 + p_i^2\right)^{1/2}$$

$$\delta T = (0.002^2 + (3.3079x10^{-4})\ ^2)^{1/2}$$

$$\delta x_i = 0.002 \text{ kPa}$$

C.6.2. Uncertainty analysis

Example calculations of the Nusselt number, Reynolds number, Colburn *j*-factor and friction factor uncertainties are given in this section. A Reynolds number of 4 943 at a heat flux of 9.5 W/m^2 was used for the sample calculations.

C.6.2.1 Nusselt number

In order to calculate the Nusselt number uncertainty, the uncertainty of the surface temperature, bulk temperature, heat flux, heat transfer coefficient, inner diameter and thermal conductivity must first be known.

A total of 43 thermocouples were used to measure the surface temperature, thus the uncertainty of the surface temperature was approximated as follows:

$$\delta T_s = \left[\left(\frac{\delta T_1}{43}\right)^2 + \left(\frac{\delta T_2}{43}\right)^2 + \cdots + \left(\frac{\delta T_{43}}{43}\right)^2\right]^{1/2}$$

$$\delta T_s = 0.0189°\text{C}$$

Only one thermocouple was used to measure the inlet water temperature, thus the uncertainty of the inlet water temperature was 0.1025 °C. Four thermocouples were used to measure the outlet temperature of the water inside the calming section and the uncertainty of the outlet water temperature was calculated similar to the uncertainty of the surface temperature:

$$\delta T_o = \left[\left(\frac{\delta T_1}{4}\right)^2 + \left(\frac{\delta T_2}{4}\right)^2 + \left(\frac{\delta T_3}{4}\right)^2 + \left(\frac{\delta T_4}{4}\right)^2\right]^{1/2}$$

$$\delta T_o = \left[\left(\frac{0.1247}{4}\right)^2 + \left(\frac{0.1311}{4}\right)^2 + \left(\frac{0.1334}{4}\right)^2 + \left(\frac{0.1211}{4}\right)^2\right]^{1/2}$$

$$\delta T_o = 0.0638\ °\text{C}$$

With both the uncertainties of the inlet and outlet temperatures known, the uncertainty of the bulk fluid temperature was calculated next:

$$\delta T_b = \left[\left(\frac{\delta T_i}{2}\right)^2 + \left(\frac{\delta T_o}{2}\right)^2\right]^{1/2}$$

$$\delta T_b = \left[\left(\frac{0.1025}{2}\right)^2 + \left(\frac{0.0638}{2}\right)^2\right]^{1/2}$$

$$\delta T_b = 0.0604°\text{C}$$

Equation C.15 was used to calculate the uncertainty of the heat transfer area:

$$\delta A = \left[(\pi\ L\ \delta D)^2 + (\pi\ D\ \delta L)^2\right]^{1/2}$$

$$\delta A = \left[(\pi * 2.06 * \ 2x10^{-5})^2 + (\pi * 0.01152 * 0.001)^2\right]^{1/2}$$

$$\delta A = \ 1.344x10^{-4}\ \text{m}^2$$

The uncertainty of the heat input was calculated using Equation C.17:

$$\delta\dot{Q} = \left[(I_1\delta V_1)^2 + (V_1\delta I_1)^2 + (I_2\delta V_2)^2 + (V_2\delta I_2)^2\right]^{1/2}$$

$$\delta\dot{Q} = \left[(1.33 * 0.5386)^2 + (269.3 * 0.00266)^2 + (1.31 * 0.5322)^2 + (266.1 * 0.002662)^2\right]^{1/2}$$

$$\delta\dot{Q} = \ 1.4136\ W$$

Once the uncertainties of the heat transfer area and heat input were known, the heat flux uncertainty was calculated using Equation C.19:

$$\delta q = \left[\left(\frac{1}{A}\delta Q\right)^2 + \left(-\frac{Q}{A^2}\delta A\right)^2\right]^{1/2}$$

$$\delta q = \left[\left(\frac{1}{0.0746} * 1.4136\right)^2 + \left(-\frac{706.76}{0.0746^2} * 1.344x10^{-4}\right)^2\right]^{1/2}$$

$$\delta q = \ 25.5262\ W/\text{m}^2$$

The uncertainty of the heat transfer coefficient was then calculated using Equation C.21:

$$\delta h = \left[\left(\frac{1}{T_s - T_b}\delta q\right)^2 + \left(\frac{-q}{(T_s - T_b)^2}\delta T_s\right)^2 + \left(\frac{q}{(T_s - T_b)^2}\delta T_b\right)^2\right]^{1/2}$$

$$\delta h = \left[\left(\frac{1}{24.8932 - 20.11095} * 25.5262\right)^2 + \left(\frac{-9\,479.9}{(24.8932 - 20.11095)^2} * 0.0189\right)^2 + \left(\frac{9\,479.9}{(24.8932 - 20.11095)^2} * 0.0604\right)^2\right]^{1/2}$$

$$\delta h = 26.7556 \text{ W/m}^2$$

Once the uncertainty of the heat transfer coefficient, inner diameter and thermal conductivity was known, the Nusselt number uncertainty was calculated using Equation C.23:

$$\delta Nu = \left[\left(\frac{D}{k}\delta h\right)^2 + \left(\frac{h}{k}\delta D\right)^2 + \left(-\frac{hD}{k^2}\delta k\right)^2\right]^{1/2}$$

$$\delta Nu = \left[\left(\frac{0.01152}{0.6019} * 26.7556\right)^2 + \left(\frac{1\,982.3}{0.6019} * 2x10^{-5}\right)^2 + \left(-\frac{1\,982.3 * 0.01152}{0.6019^2} * 0.012\right)^2\right]^{1/2}$$

$$\delta Nu = 0.9178$$

The Nusselt number at a Reynolds number of 4 943.4 and heat flux of 9.5 kW/m^2 was 37.9385, thus the uncertainty of the Nusselt number was 2.42%.

C.6.2.2 Reynolds number

In order to calculate the uncertainty of the Reynolds number, the uncertainties of the mass flow rate, inner diameter, dynamic viscosity and cross-sectional area must be known. The uncertainty of the cross-sectional area was calculated using Equation C.24:

$$\delta A_c = \frac{\pi D}{2}\delta D$$

$$\delta A_c = \frac{\pi * 0.01152}{2} * 2x10^{-5}$$

$$\delta A_c = 3.6191x10^{-7} \text{ m}^2$$

Equation C.1 was used to determine the uncertainty of the mass flow rate. The precision was obtained by multiplying the standard deviation across 200 measuring points with Student's *t* variable (Dunn, 2010), while the bias was obtained from the manufacturer's specifications.

$$\delta \dot{m} = \left(b_i^2 + p_i^2\right)^{1/2}$$

$$\delta \dot{m} = ((3.0221x10^{-5})^2 + (1.981 * 4.249x10^{-5})^2)^{1/2}$$

$$\delta \dot{m} = 8.9433x10^{-5} \text{ kg/s}$$

The Reynolds number uncertainty was then calculated using Equation C.27:

$$\delta Re = \left[\left(\frac{D}{\mu A_c}\delta \dot{m}\right)^2 + \left(\frac{\dot{m}}{\mu A_c}\delta D\right)^2 + \left(-\frac{\dot{m}D}{\mu^2 A_c}\delta\mu\right)^2 + \left(-\frac{\dot{m}D}{\mu A_c^2}\delta A\right)^2\right]^{1/2}$$

$$\begin{aligned}\delta Re = \Bigg[&\left(\frac{0.01152}{9.9936x10^{-4} * 1.0423x10^{-4}} * 8.9433x10^{-5}\right)^2 \\ &+ \left(\frac{0.0447}{9.9936x10^{-4} * 1.0423x10^{-4}} * 2x10^{-5}\right)^2 \\ &+ \left(-\frac{0.0447 * 0.01152}{(9.9936x10^{-4})^2 * 1.0423x10^{-4}} * 9.9936x10^{-6}\right)^2 \\ &+ \left(-\frac{0.0447 * 0.01152}{9.9936x10^{-4} * (1.0423x10^{-4})^2} * 3.6191x10^{-7}\right)^2\Bigg]^{1/2}\end{aligned}$$

$$\delta Re = 53.94$$

A Reynolds number of 4 943.4 was used, thus the uncertainty of the Reynolds number was 1.0911%.

C.6.2.3 Colburn *j*-factor

The uncertainties of the Nusselt number, Reynolds number and Prandtl number are required to calculate the uncertainty of the Colburn *j*-factor. The uncertainty of the Nusselt number and Reynolds number was calculated to be 0.9178 (Section C.6.2.1) and 53.94 (Section C.6.2.2), respectively. From Table C.1 it follows that the uncertainty of the Prandtl number is 2.3%. At a Reynolds number of 4 943 and heat flux of 9.5 W/m^2, the Prandtl number was found to be 6.5094, therefore the Prandtl number uncertainty was 0.1497. The Colburn j-factor uncertainty can then be calculated using Equation C.29:

$$\delta j = \left[\left(\frac{1}{RePr^{1/3}}\delta Nu\right)^2 + \left(-\frac{Nu}{Re^2 Pr^{1/3}}\delta Re\right)^2 + \left(-\frac{1}{3}\frac{Nu}{RePr^{4/3}}\delta Pr\right)^2\right]^{1/2}$$

$$\begin{aligned}\delta j = \Bigg[&\left(\frac{1}{4\,943.4 * 6.5094^{1/3}} * 0.9178\right)^2 + \left(-\frac{37.9385}{4\,943.4^2 * 6.5094^{1/3}} * 53.9423\right)^2 \\ &+ \left(-\frac{1}{3} * \frac{37.9385}{4\,943.4 * 6.5094^{4/3}} * 0.1497\right)^2\Bigg]^{1/2}\end{aligned}$$

$$\delta j = 1.1354x10^{-4}$$

The Colburn *j*-factor at a Reynolds number of 4 943.4 and heat flux of 9.5 kW/m^2 was 0.0041, thus the uncertainty of the Colburn *j*-factor was 2.76%.

C.6.2.4 Friction factor

From Equation C.33, it follows that the uncertainty of the pressure drop, inner diameter, density, flow velocity and test section length is required to calculate the friction factor uncertainty. The uncertainty of the pressure drop measurements was calculated using Equation C.1. The bias was obtained using linear regression analysis (Section C.6.1.2), while the precision was obtained by multiplying the standard deviation of 200 measuring points with Student's *t* variable (Dunn, 2010).

$$\delta \Delta P = \left(b_i^2 + p_i^2\right)^{1/2}$$

$$\delta \Delta P = (0.002^2 + (1.981 * 0.0096)^2)^{1/2}$$

$$\delta \Delta P = 0.0191 \text{ kPa}$$

Equation C.31 was used to calculate the uncertainty of the flow velocity:

$$\delta u = \left[\left(\frac{1}{\rho A}\delta \dot{m}\right)^2 + \left(-\frac{\dot{m}}{\rho^2 A}\delta \rho\right)^2 + \left(-\frac{\dot{m}}{\rho A^2}\delta A\right)^2\right]^{1/2}$$

$$\delta u = \left[\left(\frac{1}{998.1294 * 1.0423x10^{-4}} * 8.9433x10^{-5}\right)^2 + \left(-\frac{0.0447}{998.1294^2 * 1.0423x10^{-4}} * 0.004\right)^2 + \left(-\frac{0.0447}{998.1294 * (1.0423x10^{-4})^2} * 3.6191x10^{-7}\right)^2\right]^{1/2}$$

$$\delta u = 1.7219x10^{-3} \text{ m/s}$$

The friction factor uncertainty was calculated using Equation C.33:

$$\delta f = \left[\left(\frac{2D}{\rho u^2 L}\delta \Delta P\right)^2 + \left(\frac{2\Delta P}{\rho u^2 L}\delta D\right)^2 + \left(-\frac{2\Delta P\, D}{\rho^2 u^2 L}\delta \rho\right)^2 + \left(-\frac{4\Delta P\, D}{\rho u^3 L}\delta u\right)^2 + \left(-\frac{2\Delta P\, D}{\rho u^2 L^2}\delta L\right)^2\right]^{1/2}$$

$$\delta f = \left[\left(\frac{2 * 0.01152}{998.1294 * 0.4296^2 * 2.03} * 0.0191\right)^2 + \left(\frac{2 * 632.6}{998.1294 * 0.4296^2 * 2.03} * 2x10^{-5}\right)^2 + \left(-\frac{2 * 632.6 * 0.01152}{998.1294^2 * 0.4296^2 * 2.03} * 0.004\right)^2 + \left(-\frac{4 * 632.6 * 0.01152}{998.1294 * 0.4296^3 * 2.03} * 1.7219x10^{-3}\right)^2 + \left(-\frac{2 * 632.6 * 0.01152}{998.1294 * 0.4296^2 * 2.03^2} * 0.001\right)^2\right]^{1/2}$$

$$\delta f = 3.2027x10^{-4}$$

The friction factor at a Reynolds number of 4 943.4 and heat flux of 9.5 kW/m^2 was 0.039, thus the friction factor uncertainty was 0.82%.

C.7. Results

The uncertainties of the Reynolds number, friction factor, Nusselt number and Colburn *j*-factor at different heat fluxes are summarised in Table C.2:

Table C.2: Uncertainties of Reynolds number, friction factor, Nusselt number and Colburn *j*-factor at different heat fluxes

	0 kW/m^2	6.5 kW/m^2	8.0 kW/m^2	9.5 kW/m^2
Reynolds number	1.08% - 1.2%	1.08% - 1.12%	1.08% - 1.12%	1.07% - 1.13%
Friction factor	0.51% - 7.52%	0.48% - 8.41%	0.48% - 14.79%	0.48% - 17.02%
Nusselt number	-	4.39% - 5.14%	4.08% - 5.03%	3.85% - 4.55%
Colburn *j*-factor	-	4.59% - 5.31%	4.29% - 5.2%	4.04% - 4.47%

C.8. Conclusion

This appendix contained the uncertainty analysis method, sample calculations of linear regression analysis and the uncertainty method, as well as the uncertainties of the Reynolds numbers, friction factors, Nusselt numbers and Colburn *j*-factors. Linear regression analysis was used to determine the bias of the thermocouples and pressure transducers. For all the other instruments, the bias was considered as the accuracy of the instrument (specified by the manufacturer). The precision was obtained from the standard deviation of 200 measuring points, which was then multiplied by Student's *t* variable to fall within the 95% confidence region. The Reynolds number uncertainties were approximately 1%, while the friction factor uncertainties varied between 0.5% and 17%. Both Nusselt number and Colburn *j*-factor uncertainties varied between 4% and 5%.

C.9. References

Dunn, P.F., 2010, *Measurement and Data Analysis for Engineering and Science,* 2nd edn., CRC Press, Boca Raton.

Popiel, C.O. & Wojtkowiak, J., 1998, 'Simple formulas for thermophysical properties of liquid water for heat transfer calculations [from O°C to 150°C]', *Heat Transfer Engineering* 19(3), 87-101.

C.10. Nomenclature

A	Area	m^2
a	Best-fit intercept	
b	Bias Best-fit slope	
c_p	Constant pressure specific heat	J/kg.K
D	Diameter	m
f	Friction factor	
h	Heat transfer coefficient	W/m^2
I	Current	A
j	Colburn *j*-factor	
k	Thermal conductivity	W/m.K
L	Length	m
M	Number of measuring points	
m	Slope of regression line	
$\dot{m}$	Mass flow rate	kg/s
N	Number of data points	
Nu	Nusselt number	
Pr	Prandtl number	
p	Precision	
ΔP	Pressure drop	Pa
Q	Heat input	W
$\dot{q}$	Heat flux	W/m^2
R	Result	
Re	Reynolds number	
S_{XX}	Sum of the squares of *x*	
S_{Xy}	Sum of the squares of *x* and *y*	
S_{yx}	Standard error of best-fit	
S_{yy}	Sum of the squares of *y*	
T	Temperature	°C
t	Student's *t* variable	

u	Velocity	m/s
V	Voltage	V
x	x-axis variable	
y	y-axis variable	

C.10.1 Superscripts

-	Average

C.10.2 Subscripts

ci	Calculated value
i	Index
b	Bulk
s	Surface
1	Power supply 1
2	Power supply 2

C.10.3 Greek letters

δ	Uncertainty	
ρ	Density	kg/m^3
μ	Dynamic viscosity	kg/m

Appendix D: Temperature Fluctuations

D.1. Introduction

During experiments, it was found that the temperatures fluctuated in the transitional flow regime and these fluctuations had a significant effect on the temperature uncertainties and the time required to reach steady-state conditions. To investigate the temperature fluctuations, measurements were taken between Reynolds numbers of 1 700 and 3 300 using three different heat fluxes.

D.2. Heat flux at 8.0 kW/m²

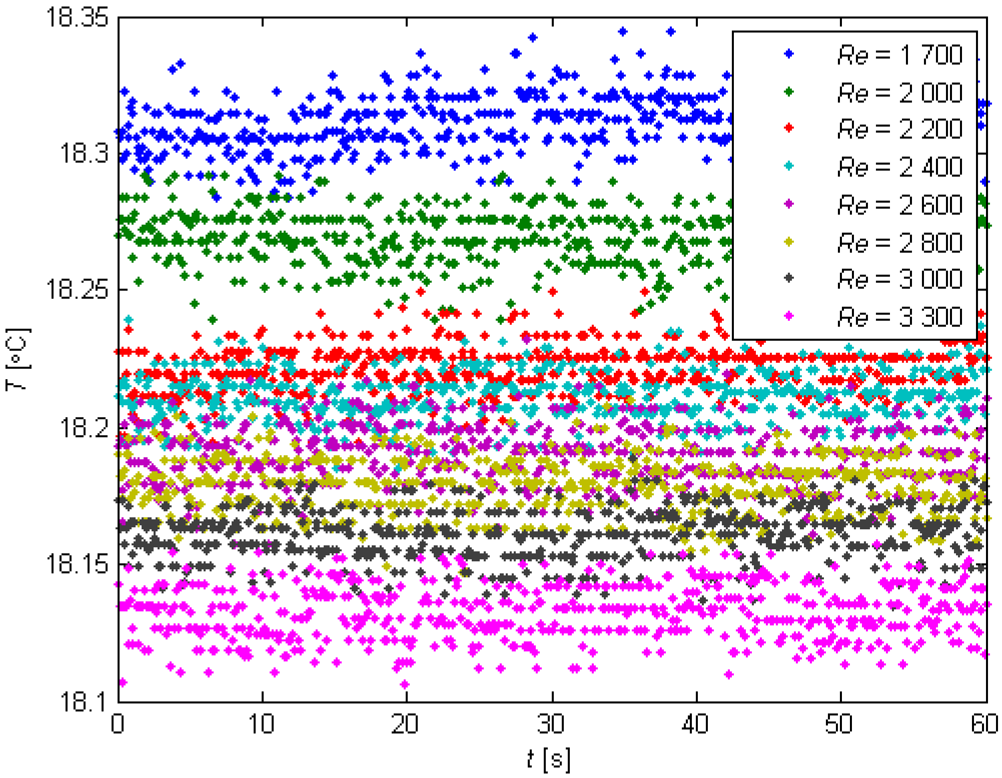

Figure D.1: Temperature fluctuations in the calming section for different Reynolds numbers and a heat flux of 8.0 kW/m^2

Figure D.1 contains the temperature measurements of the thermocouple inside the calming section. As expected, the temperatures remained approximately constant throughout the measurements and the average standard deviation across the 60-second period was approximately 0.01 °C. The inlet temperature decreased slightly with increasing Reynolds number since the inlet temperature depended on the chiller, which went through its own operating cycles. However, throughout the measurements at this heat flux, the inlet water temperature varied with 0.2 °C only.

Figure D.2 contains the data of the thermocouples at $x/D = 1.3$. Only three thermocouples were used at this station since the thermocouple at the top of the tube got damaged during the assembly process. At Reynolds numbers between 1 700 and 2 600, the average standard deviation was less than 0.02 °C and it can be concluded that the temperatures remained approximately constant. When the Reynolds number was increased further, slight fluctuations occurred and the average standard deviation between Reynolds numbers of 2 800 and 3 300 was 0.03 °C, which is still very small.

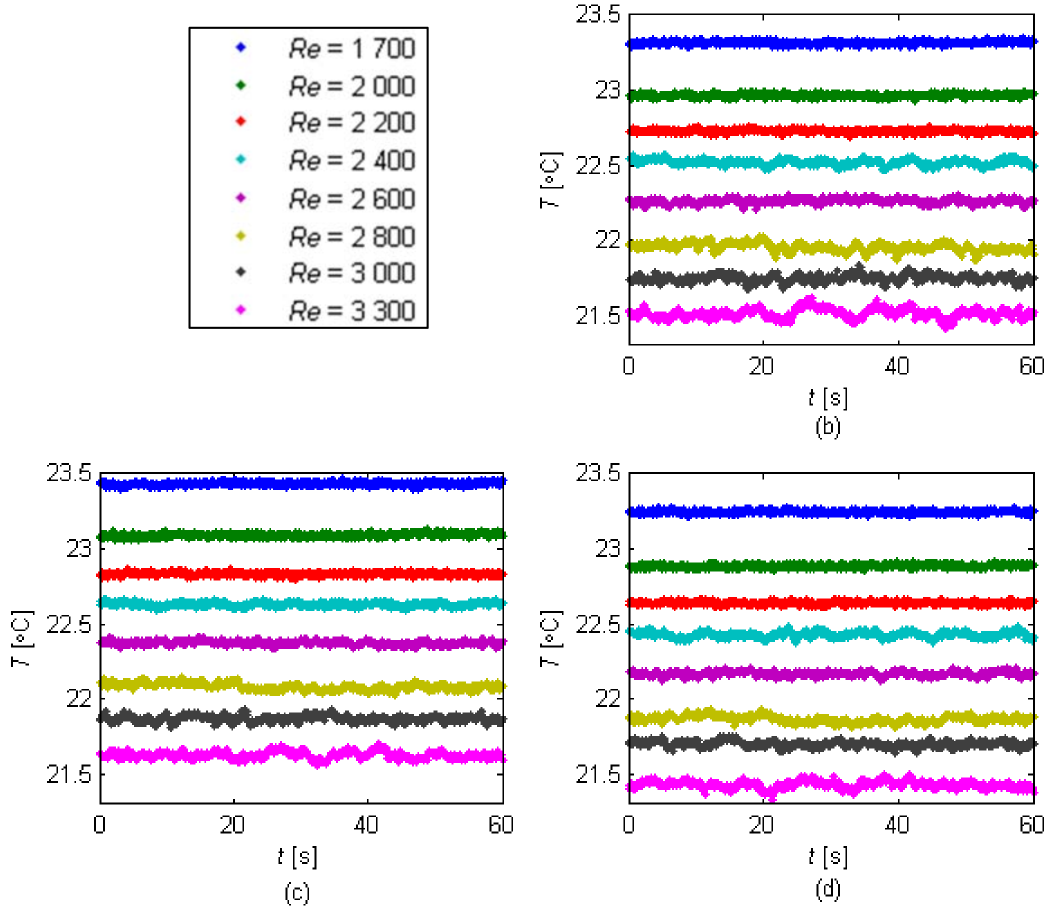

Figure D.2: Temperature fluctuations at the (b) left, (c) bottom and (d) right of the tube at *x/D* = 1.3 (Station A in Figure 3.4) for different Reynolds numbers and a heat flux of 8.0 kW/m^2

Figure D.3 contains the data of the thermocouples at *x/D* = 8.2. At Reynolds numbers between 1 700 and 2 200, the standard deviation was less than 0.02 °C and it can be concluded that the temperatures remained approximately constant. At Reynolds numbers between 2 400 and 2 600, the average standard deviation was 0.035°C. Slight fluctuations occurred when the Reynolds number was increased further and the average standard deviation between Reynolds numbers of 2 800 and 3 300 was 0.085 °C.

At *x/D* = 16.9 (Figure D.4) and *x/D* = 25.6 (Figure D.5), the temperatures remained approximately constant at Reynolds numbers between 1 700 and 2 200 and the standard deviation was less than 0.02 °C. As the Reynolds number was increased, the fluctuations increased and the maximum standard deviation of 0.2 °C occurred at a Reynolds number of 2 800 at *x/D* = 16.9. However, when the Reynolds number was increased further, the fluctuations decreased slightly and the standard deviation at a Reynolds number of 3 300 was 0.13 °C. When comparing Figures D.4 and D.5, it follows that the fluctuations increased slightly along the tube length.

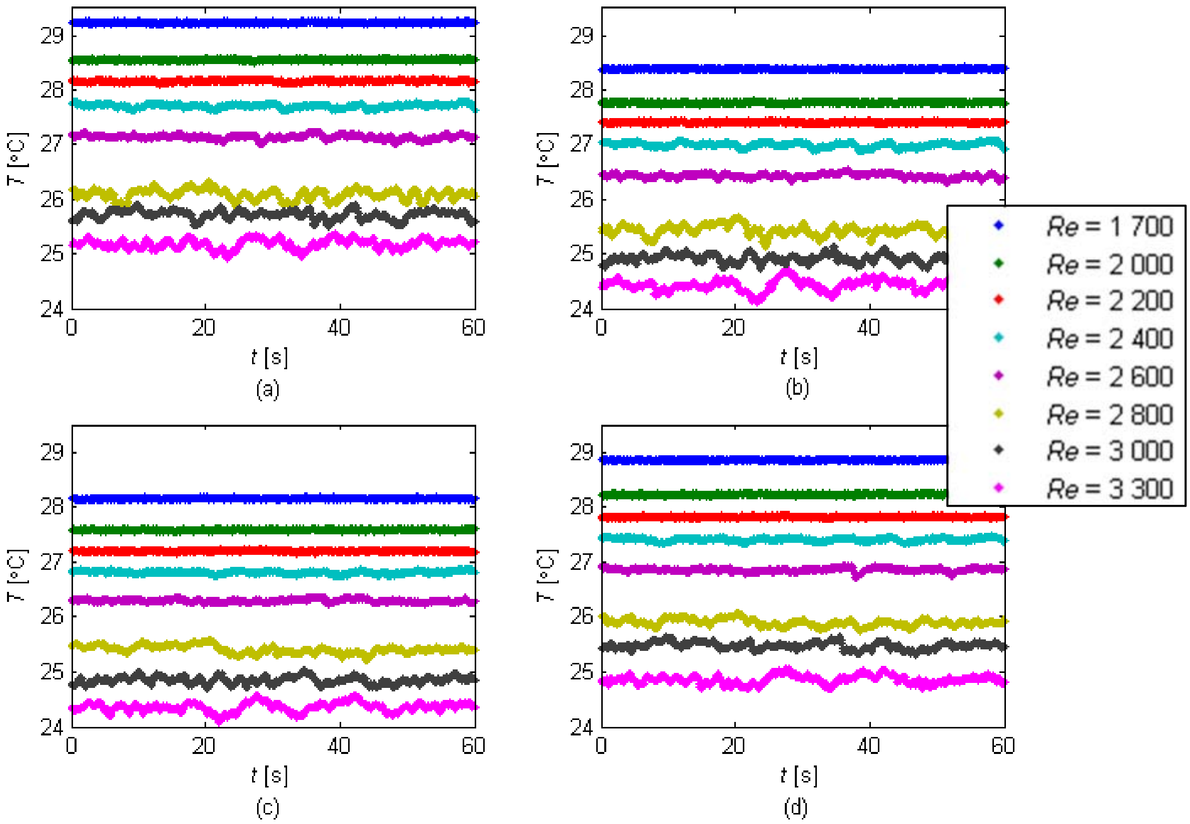

Figure D.3: Temperature fluctuations at the (a) top, (b) left, (c) bottom and (d) right of the tube at *x/D* = 8.2 (Station B in Figure 3.4) for different Reynolds numbers and a heat flux of 8.0 kW/m^2

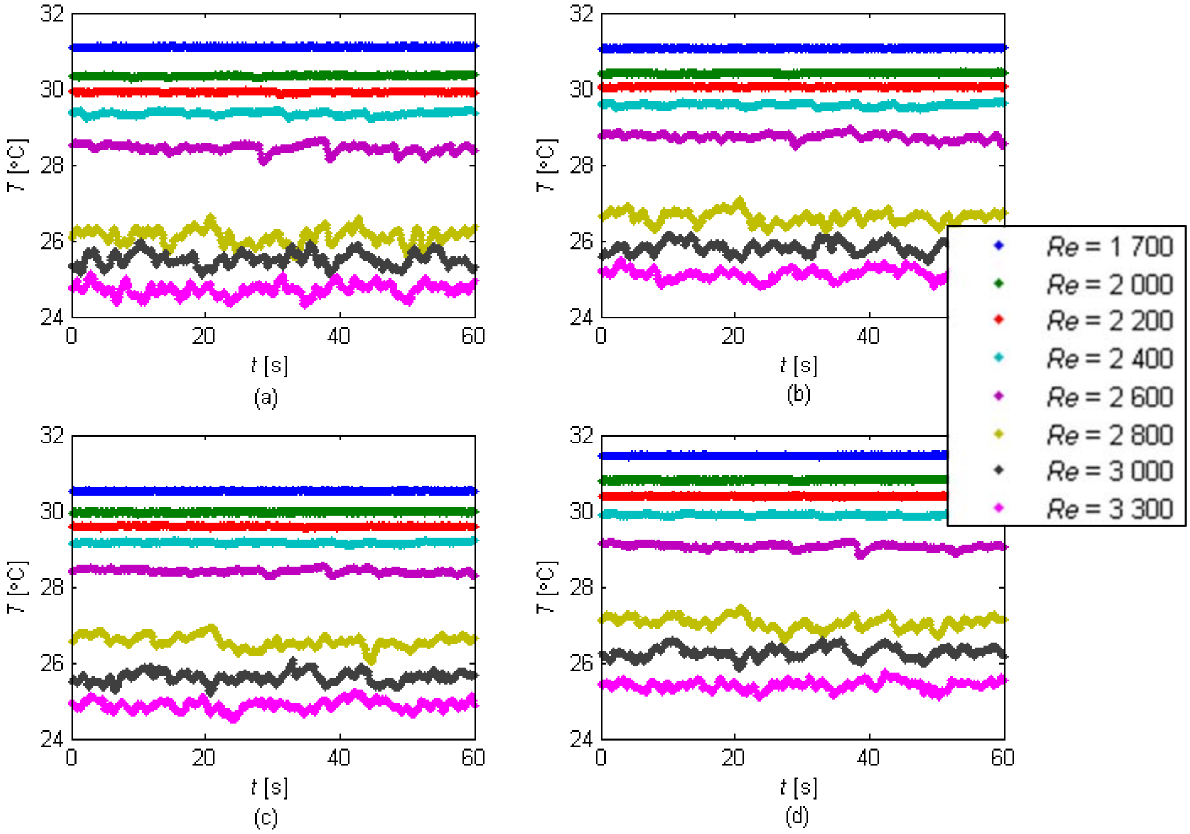

Figure D.4: Temperature fluctuations at the (a) top, (b) left, (c) bottom and (d) right of the tube at *x/D* = 16.9 (Station C in Figure 3.4) for different Reynolds numbers and a heat flux of 8.0 kW/m^2

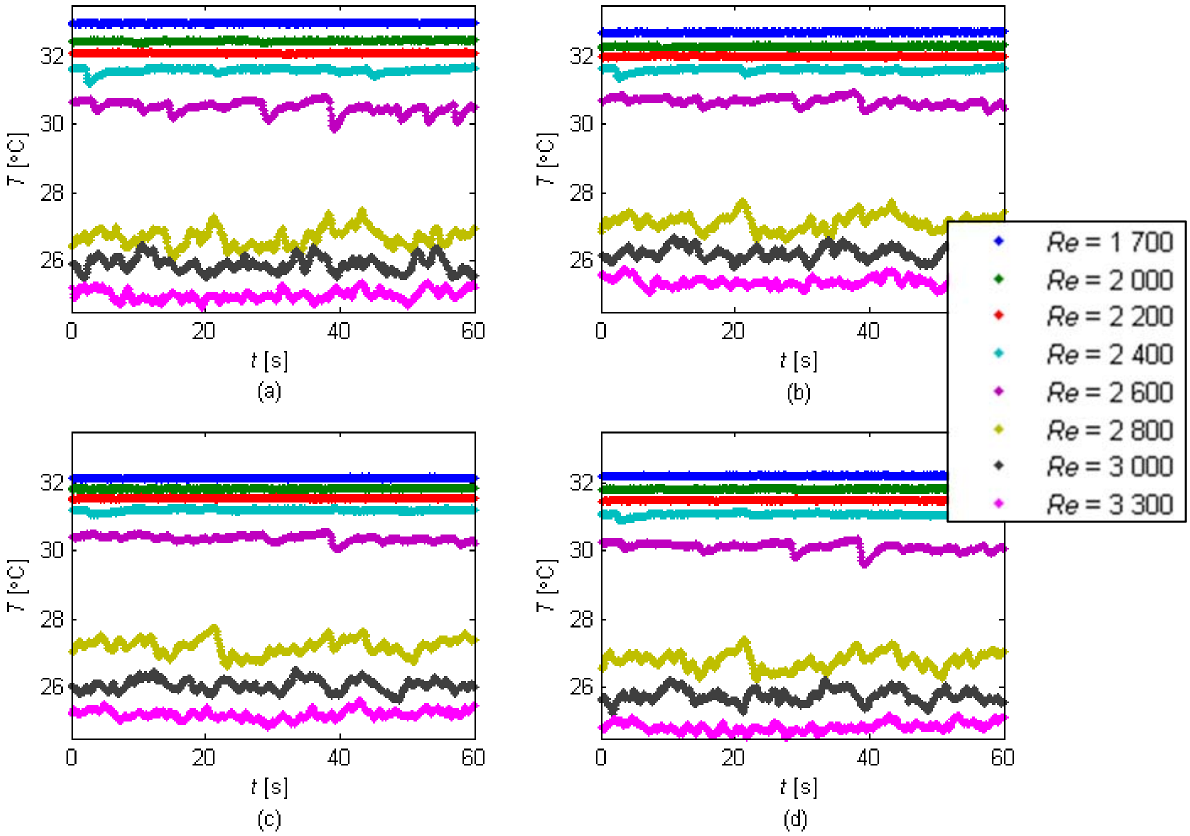

Figure D.5: Temperature fluctuations at the (a) top, (b) left, (c) bottom and (d) right of the tube at *x/D* = 25.6 (Station D in Figure 3.4) for different Reynolds numbers and a heat flux of 8.0 kW/m^2

From Figure D.6, it follows that at *x/D* = 36, the fluctuations at Reynolds numbers of 2 400 and 2 600 formed a pattern. Although the pattern was approximately the same for all four thermocouples, the amplitudes of the peaks were greater at the top of the tube than at the bottom. Therefore, the buoyancy-induced secondary flow might be a reason for these flow patterns.

As *x/D* was increased to 53.4 and 70.7 in Figures D.7 and D.8, respectively, the magnitude of the amplitudes increased significantly. Similar to Figure D.6, the amplitudes at the top of the tube were higher than at the bottom. The temperatures measured by the thermocouples at the top of the tube at *x/D* = 53.4 and *x/D* = 70.7 were also significantly higher due to the secondary flow effects inside the tube. There was no distinct pattern in the temperature fluctuations at Reynolds numbers between 2 800 and 3 300, however, the standard deviation increased with increasing *x/D* as well.

From Figure D.9, it follows that at *x/D* = 88.1, the temperature profiles at the top and bottom of the tube began to differ at Reynolds numbers of 2 400 and 2 600. As *x/D* was increased to 105.5 and 122.8 in Figures D.10 and D.11, respectively, the difference between the temperature patterns at the top and bottom of the tube increased. The patterns obtained from the thermocouples at the top of the tube were smoother compared with those obtained from the thermocouples at the bottom of the tube. Distinct peaks were visible in the patterns obtained from the thermocouples at the bottom of the tube. The patterns obtained from the thermocouples at the sides of the tube were similar. Furthermore, the temperatures were a maximum at the top of the tube, a minimum at the bottom of the tube and the temperature at the sides of the tube was approximately the same. These temperature distributions were due to the secondary flow effects inside the tube.

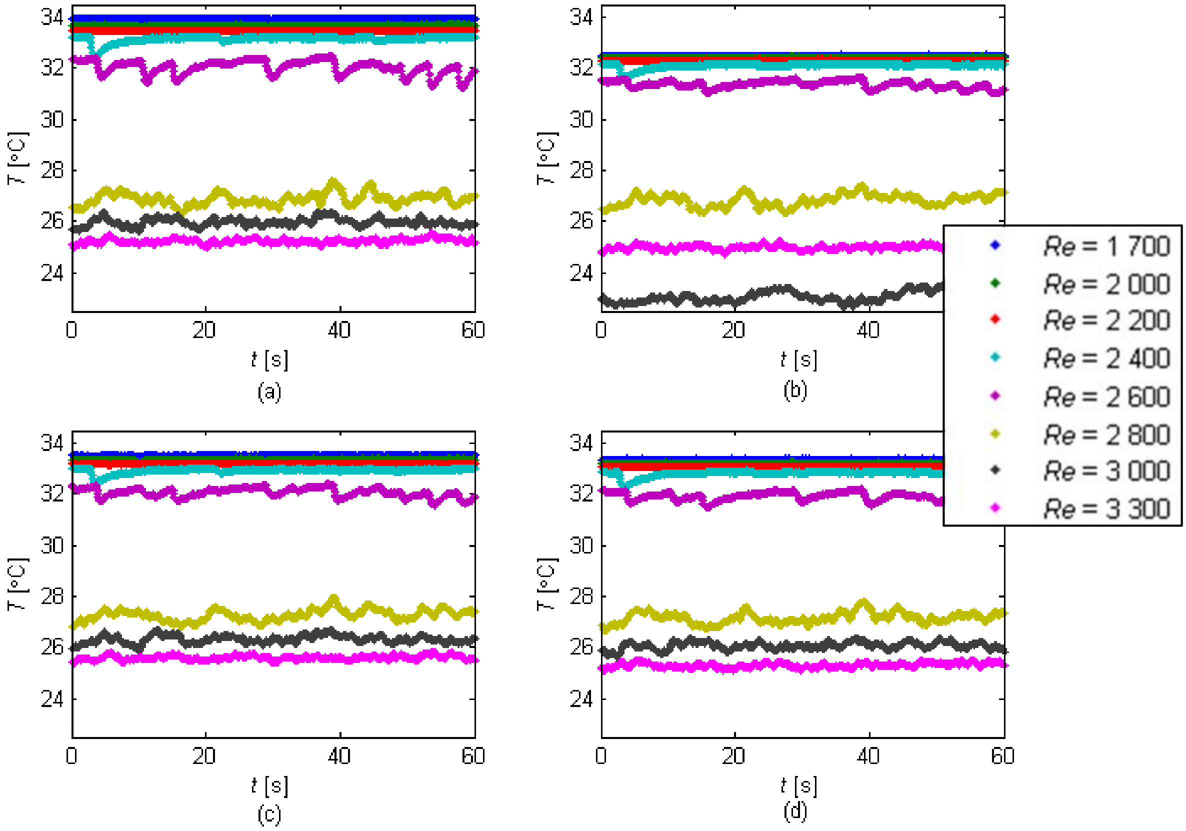

Figure D.6: Temperature fluctuations at the (a) top, (b) left, (c) bottom and (d) right of the tube at *x/D* = 36 (Station E in Figure 3.4) for different Reynolds numbers and a heat flux of 8.0 kW/m^2

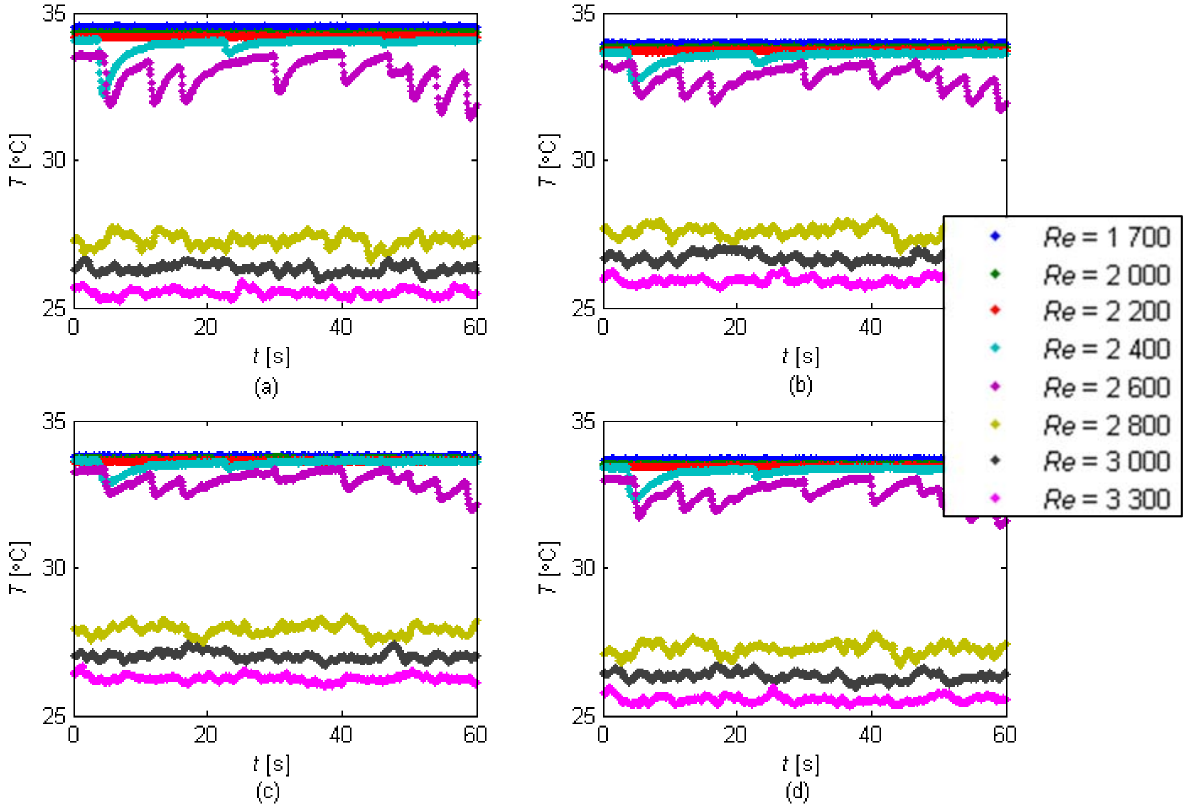

Figure D.7: Temperature fluctuations at the (a) top, (b) left, (c) bottom and (d) right of the tube at *x/D* = 53.4 (Station F in Figure 3.4) for different Reynolds numbers and a heat flux of 8.0 kW/m^2

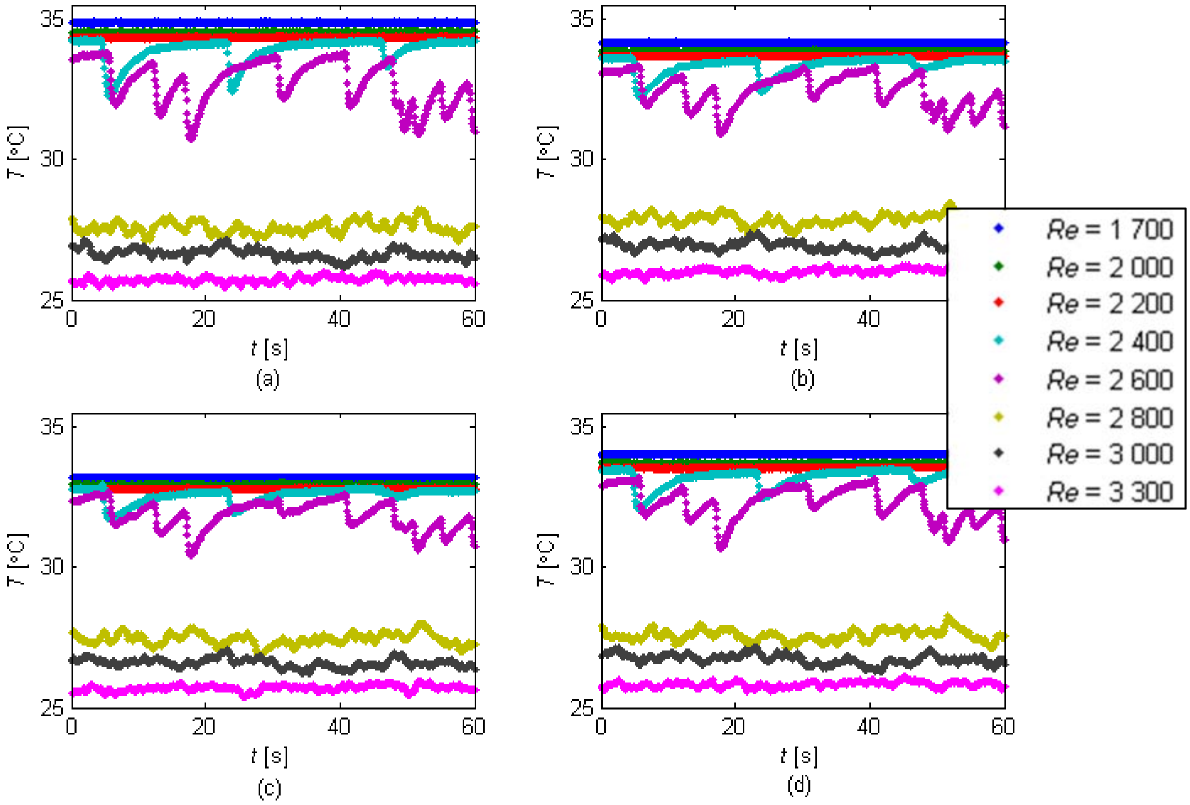

Figure D.8: Temperature fluctuations at the (a) top, (b) left, (c) bottom and (d) right of the tube at x/D = 70.7 (Station G in Figure 3.4) for different Reynolds numbers and a heat flux of 8.0 kW/m^2

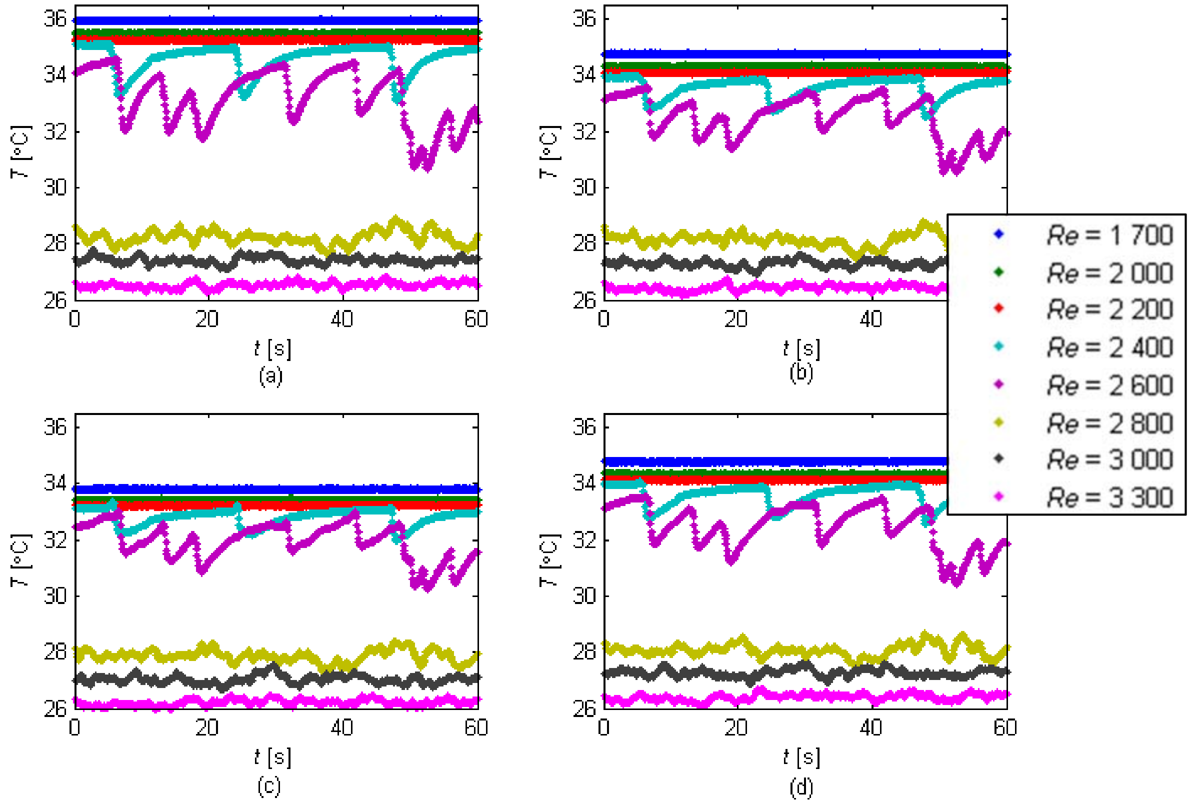

Figure D.9: Temperature fluctuations at the (a) top, (b) left, (c) bottom and (d) right of the tube at x/D = 88.1 (Station H in Figure 3.4) for different Reynolds numbers and a heat flux of 8.0 kW/m^2

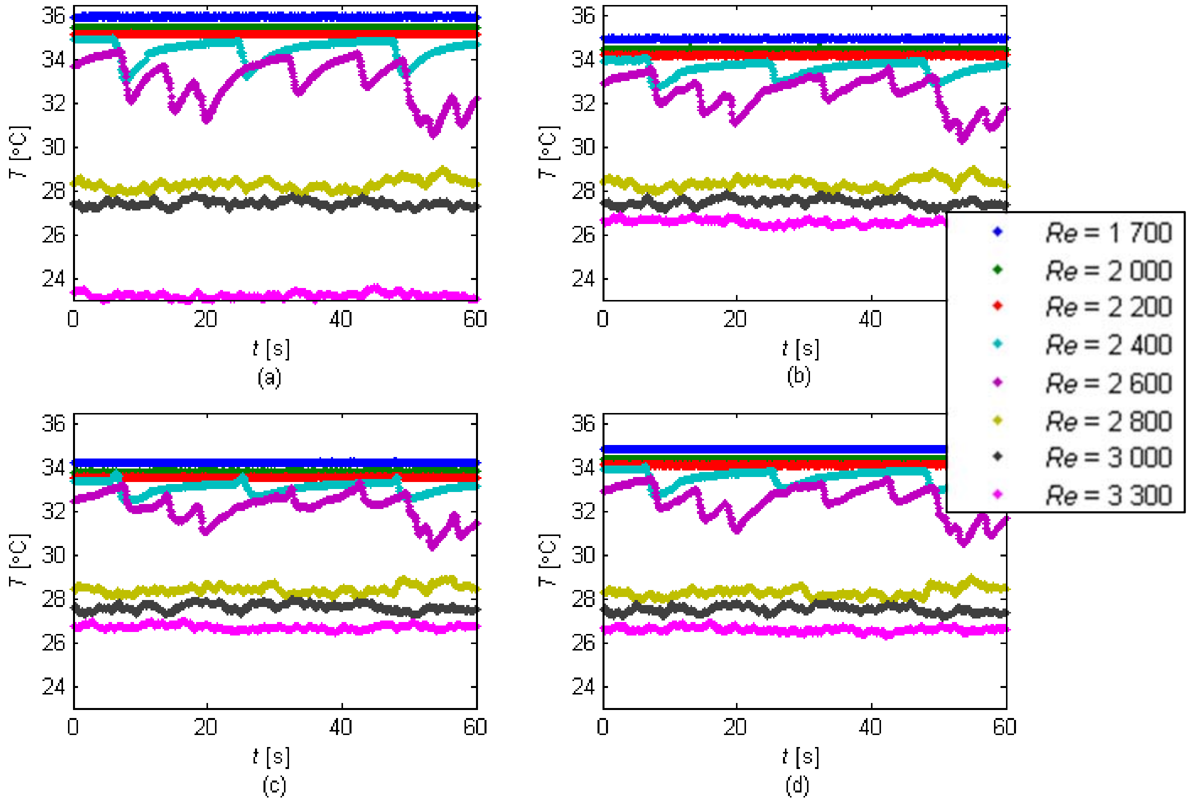

Figure D.10: Temperature fluctuations at the (a) top, (b) left, (c) bottom and (d) right of the tube at *x/D* = 105.5 (Station I in Figure 3.4) for different Reynolds numbers and a heat flux of 8.0 kW/m^2

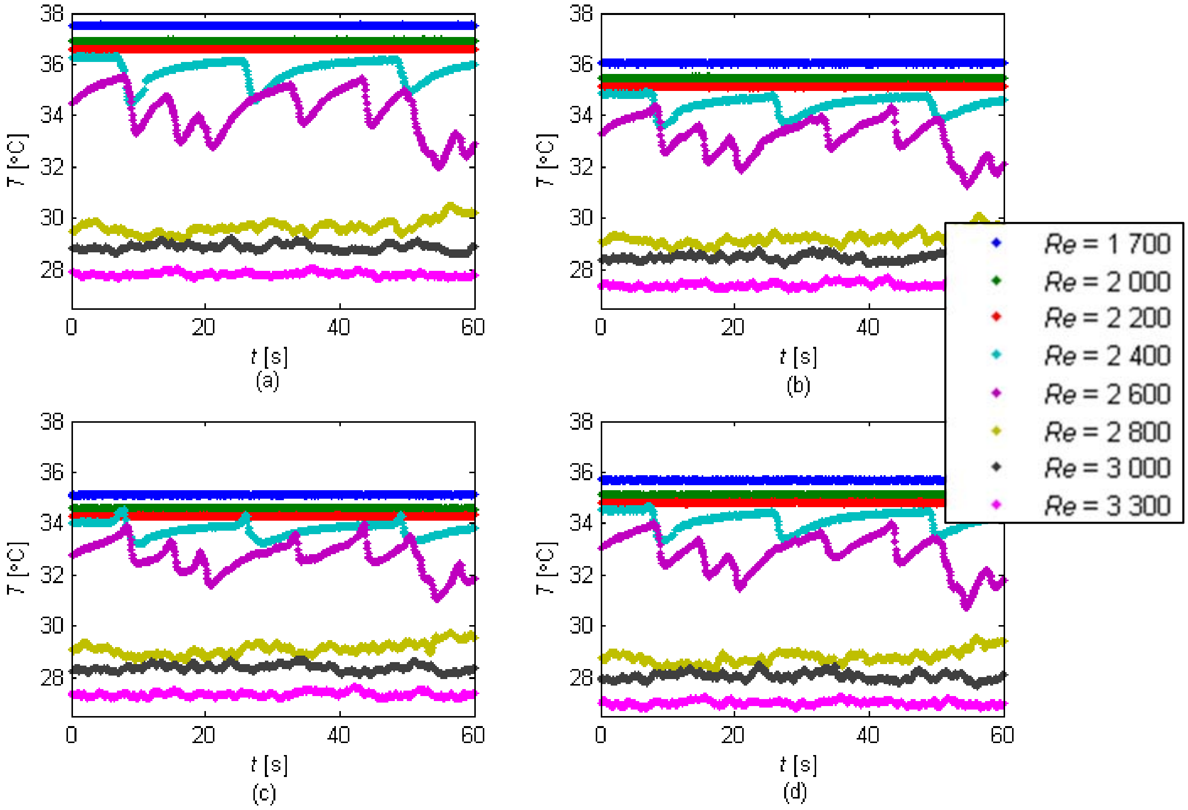

Figure D.11: Temperature fluctuations at the (a) top, (b) left, (c) bottom and (d) right of the tube at *x/D* = 122.8 (Station J in Figure 3.4) for different Reynolds numbers and a heat flux of 8.0 kW/m^2

The thermocouple at the top of the tube at *x/D* = 140.2 got damaged during the assembly process and was therefore not taken into account during the experiments. Figure D.13 contains the temperature profiles at *x/D* = 157.6. The left thermocouple was excluded during the measurements since it got damaged as well. Once again there was a significant difference between the patterns and temperatures obtained by the thermocouples at the top and bottom of the tube.

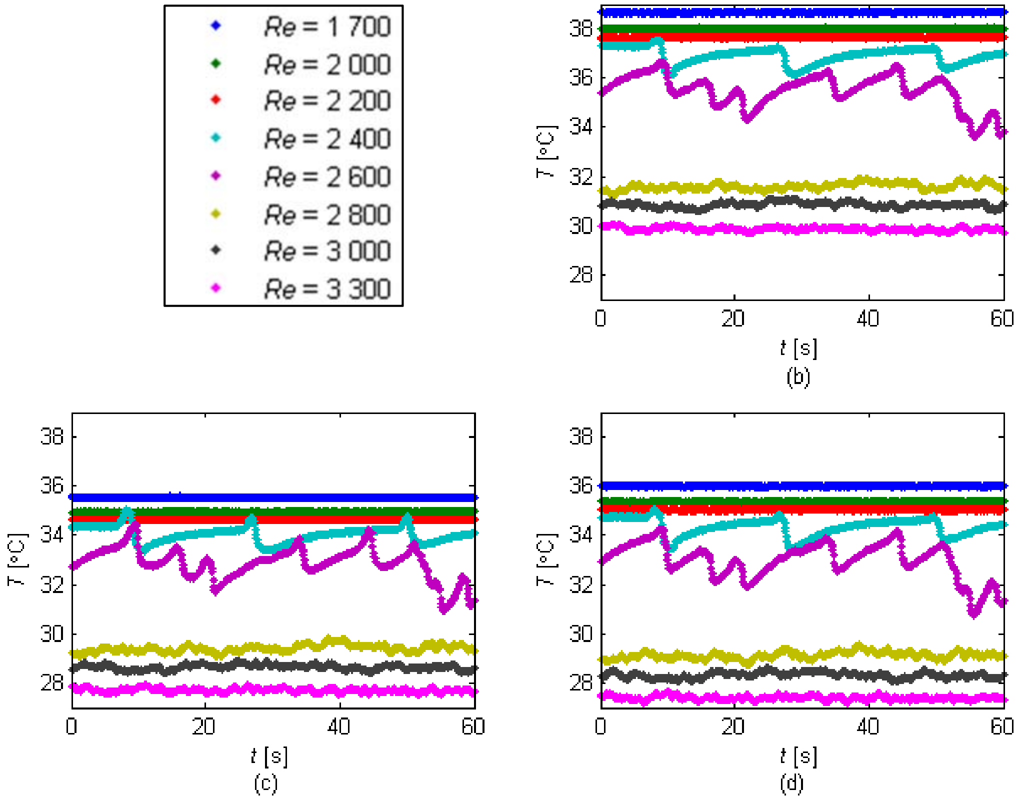

Figure D.12: Temperature fluctuations at the (a) top, (b) left, (c) bottom and (d) right of the tube at *x/D* = 140.2 (Station K in Figure 3.4) for different Reynolds numbers and a heat flux of 8.0 kW/m²

Figure D.14 contains the temperature fluctuations at the last thermocouple station (*x/D* = 174.9). Similar to Figures D.9 to D.13, the patterns at the top and bottom of the tube were different. When comparing these figures, it can be concluded that the difference between the patterns at the top and bottom of the tube increased with increasing *x/D*, and the difference only became significant after *x/D* = 88.1. The different patterns were caused by the secondary flow effects, which were caused by the difference in temperature and density between the fluid near the surface and near the thermal boundary layer of the tube. Therefore, it was confirmed that secondary flow effects required a certain length along the tube to develop and become significant.

The temperature fluctuations obtained from the thermocouples inside the mixing section were summarised in Figure D.15. Although the patterns of all four thermocouples were approximately the same, the temperatures measured by the thermocouples at the top and right of the mixing section were slightly different from those measured at the left and bottom of the tube. When comparing Figures D.14 and D.15, it follows that the patterns of the temperature profiles differed significantly. Figure D.14 contains the results of the last thermocouple station on the tube (constant heat flux applied), while Figure D.15 contains the results of the thermocouples inside the mixing section (no heat applied).

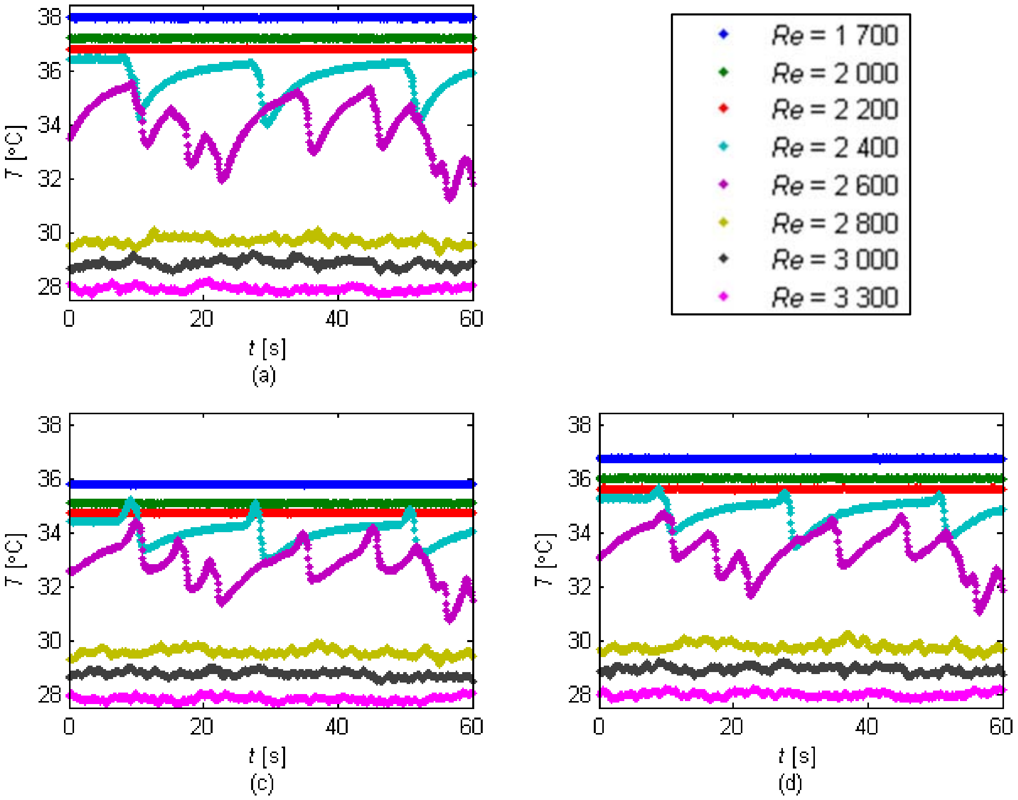

Figure D.13: Temperature fluctuations at the (a) top, (b) left, (c) bottom and (d) right of the tube at x/D = 157.6 (Station L in Figure 3.4) for different Reynolds numbers and a heat flux of 8.0 kW/m^2

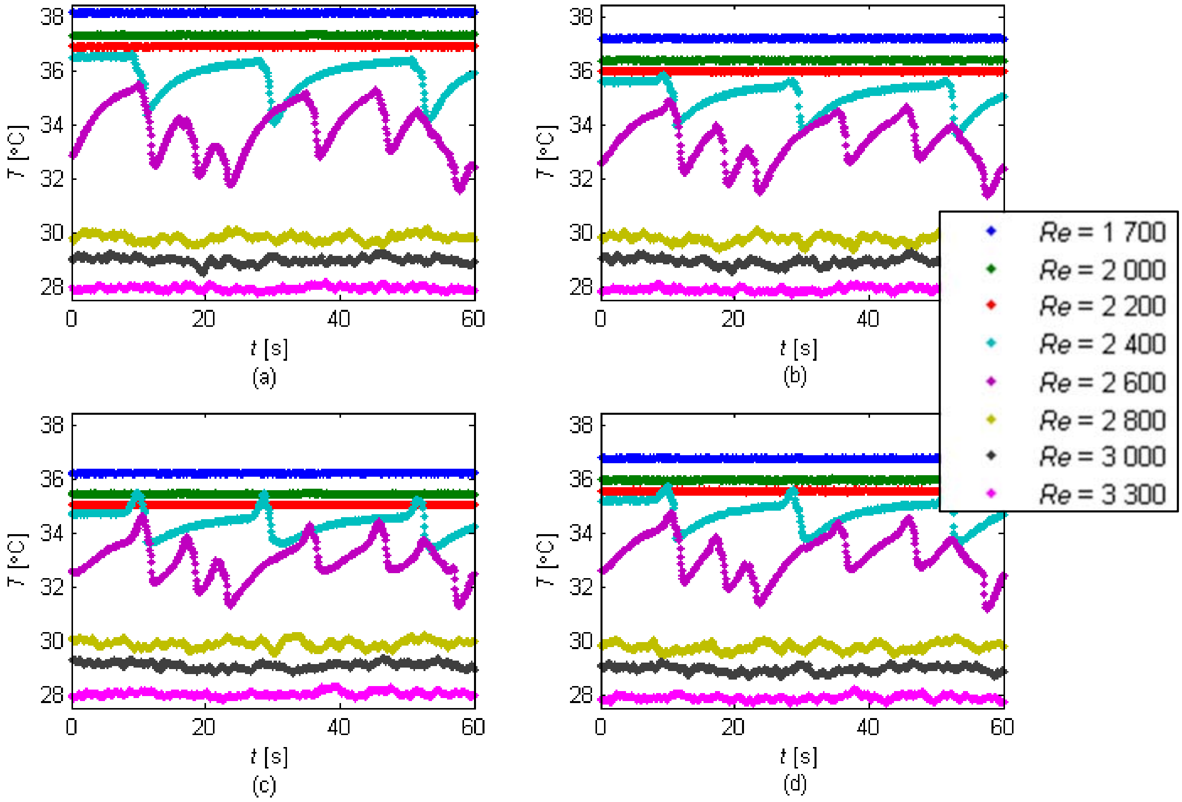

Figure D.14: Temperature fluctuations at the (a) top, (b) left, (c) bottom and (d) right of the tube at x/D = 174.9 (Station M in Figure 3.4) for different Reynolds numbers and a heat flux of 8.0 kW/m^2

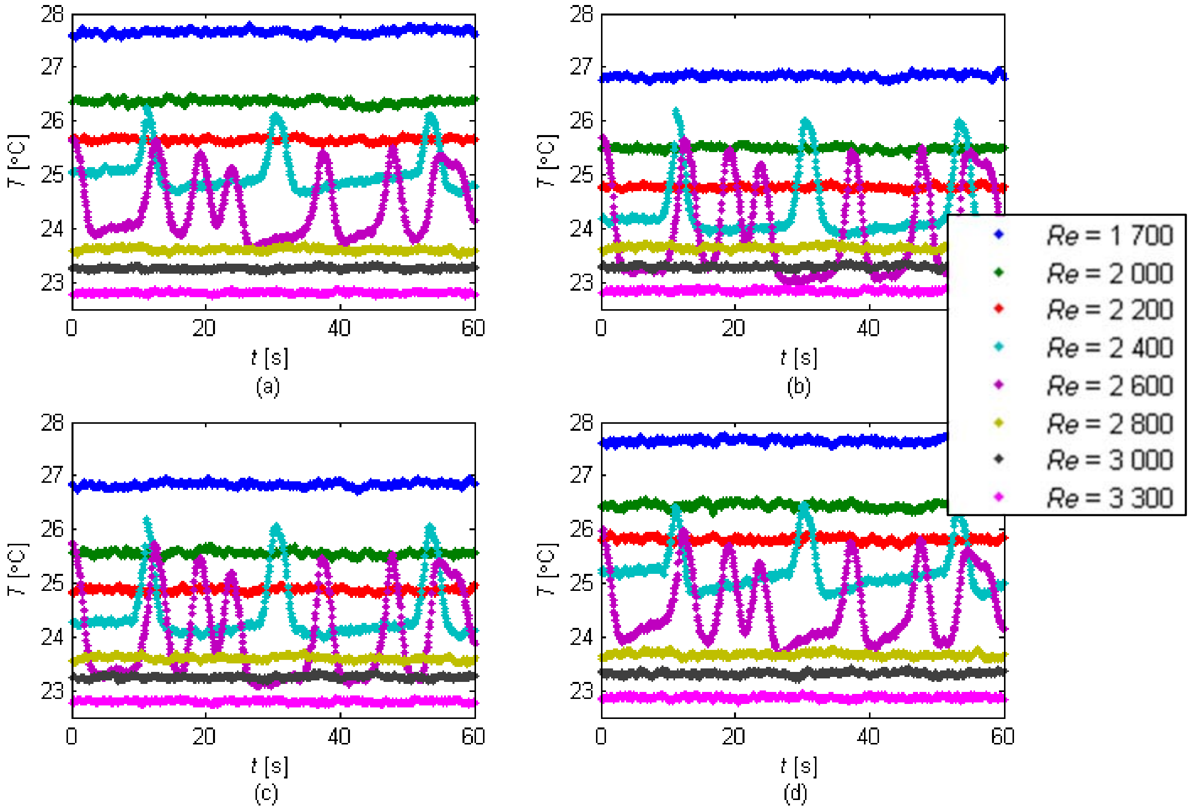

Figure D.15: Temperature fluctuations at the (a) top, (b) left, (c) bottom and (d) right of the mixing section for different Reynolds numbers and a heat flux of 8.0 kW/m^2

Overall, it can be concluded that these temperature fluctuation patterns are unique to the start of the transitional flow regime because it was only observed at Reynolds numbers of 2 400 and 2 600. Although slight temperature fluctuations occurred at higher Reynolds numbers, which were also part of the transitional flow regime, no distinct patterns were observed.

Figure D.16 contains the temperature measurements at the top and bottom of the tube for different values of *x/D* at a Reynolds number of 1 700. From both Figures D.16(a) and (b), it follows that the temperatures remained constant throughout the 60-second period. The temperatures measured at the top of the tube were higher than at the bottom of the tube due to the effects of secondary flow.

Figure D.17 contains the temperature measurements at the top and bottom of the tube at a Reynolds number of 2 600 for different locations along the tube length. From Figure D.16(a), it follows that the temperature fluctuations increased with increasing *x/D*, as expected, because the secondary flow effects required a certain length to develop and become significant. As *x/D* was increased, the temperature difference between the surface and fluid increased, which then led to increased secondary flow effects. When comparing Figures D.17(a) and (b), it follows that the temperatures at the bottom of the tube were not only less than at the top of the tube, but the patterns of the temperature fluctuations differed significantly. However, the temperature difference between the top and bottom of the tube was less than at a Reynolds number of 1 700 (Figure D.16).

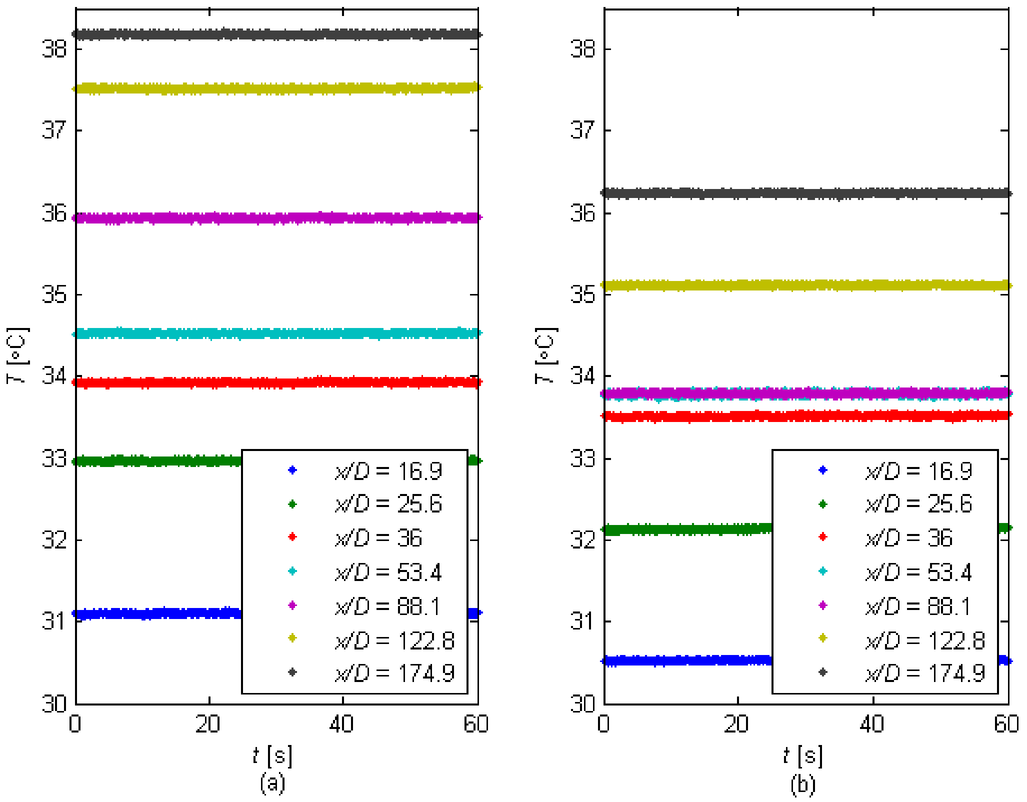

Figure D.16: Temperature fluctuations at the (a) top and (b) bottom of the tube for different values of x/D, a Reynolds number of 1 700 and a heat flux of 8.0 kW/m²

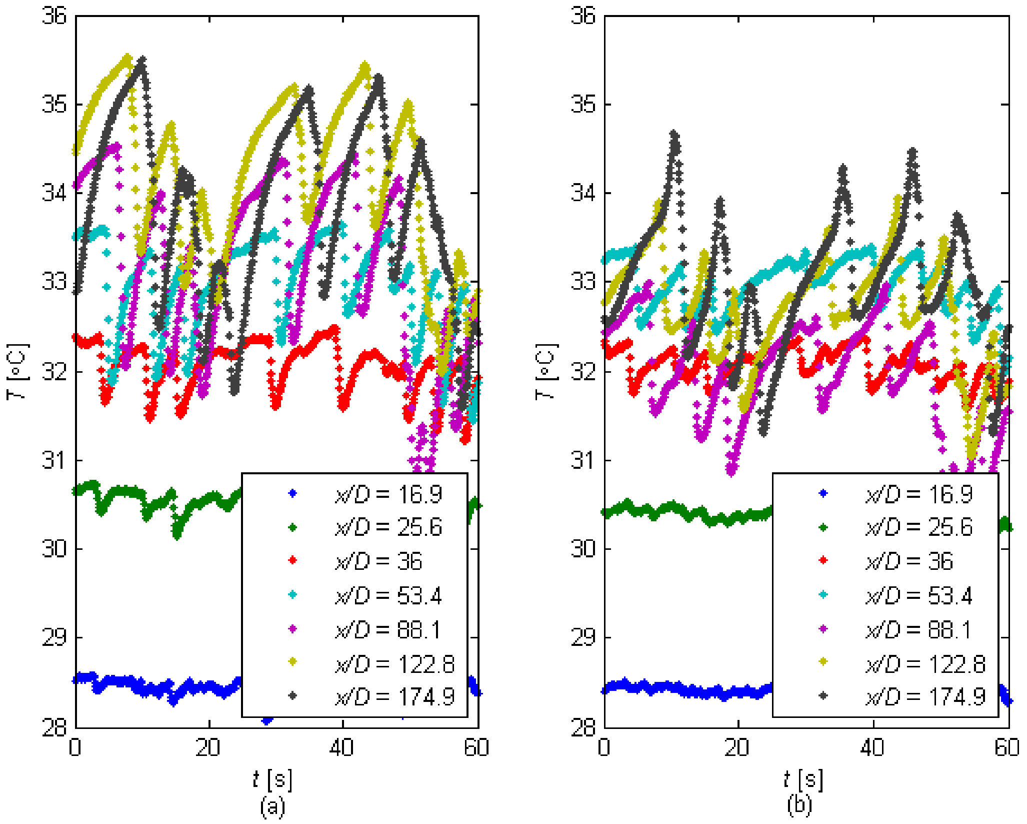

Figure D.17: Temperature fluctuations at the (a) top and (b) bottom of the tube for different values of *x/D*, a Reynolds number of 2 600 and a heat flux of 8.0 kW/m²

Figure D.18 contains the temperature measurements at the top and bottom of the tube for different values of *x/D* at a Reynolds number of 3 300. From this figure, it follows that temperature fluctuations occurred along the whole tube length, but decreased with increasing *x/D.* The temperature difference between the thermocouples at the top and bottom of the tube was negligible near the inlet of the test section. However, as *x/D* increased, a slight difference between the temperature measurements at the top and bottom of the tube was found and the secondary flow effects became significant.

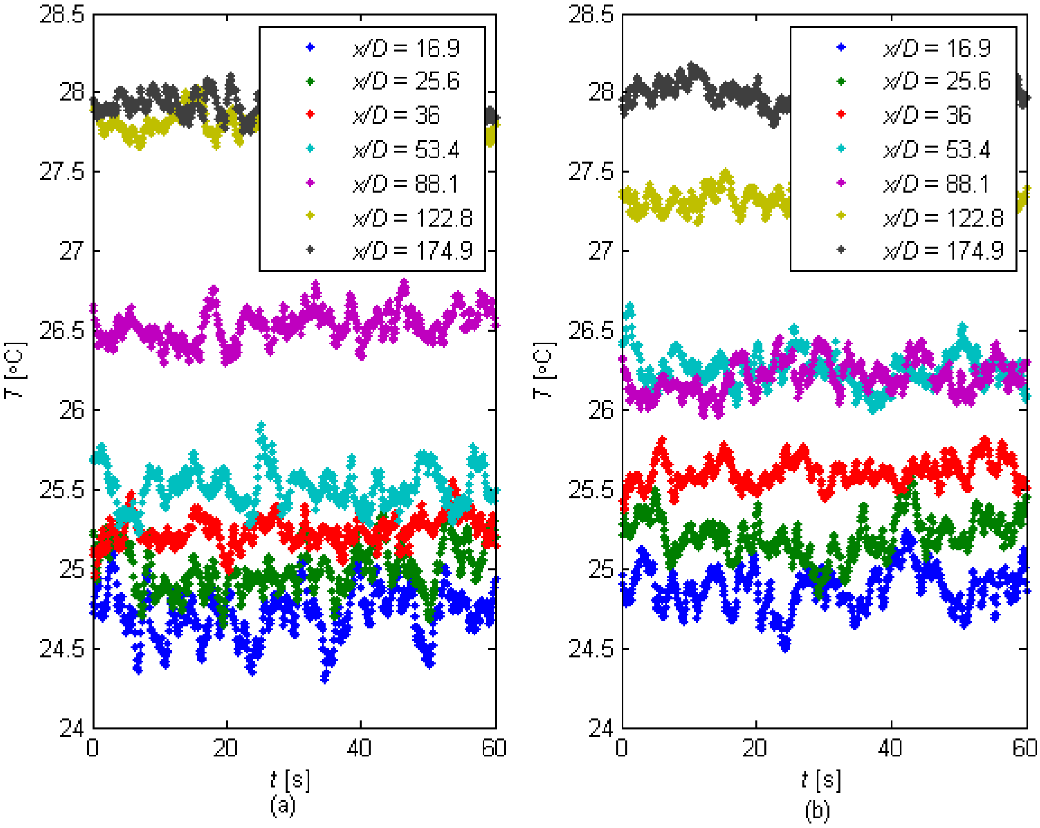

Figure D.18: Temperature fluctuations at the (a) top and (b) bottom of the tube for different values of x/D, a Reynolds number of 3 300 and a heat flux of 8.0 kW/m^2

The same experiments were repeated at a heat flux of 6.5 kW/m^2 and 9.5 kW/m^2 and the results are summarised in Sections D.3 and D.4. However, the graphs are not discussed again since the trends were similar to those of the 8.0 kW/m^2 heat flux.

D.3. Heat flux at 6.5 kW/m^2

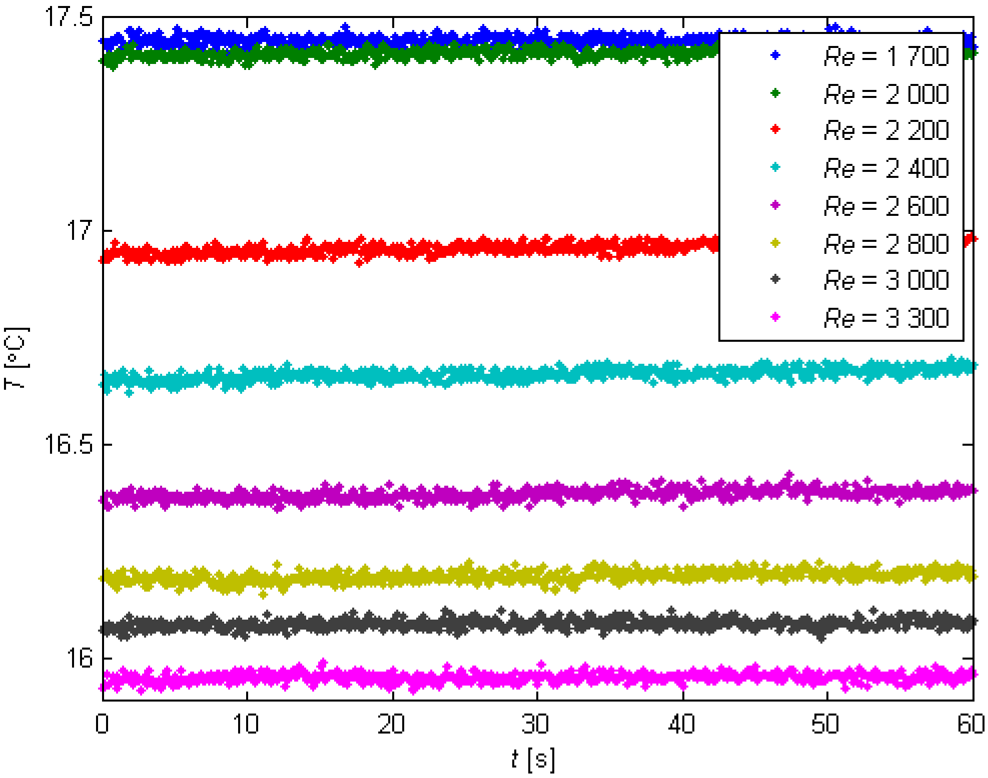

Figure D.19: Temperature fluctuations in the calming section for different Reynolds numbers and a heat flux of 6.5 kW/m^2

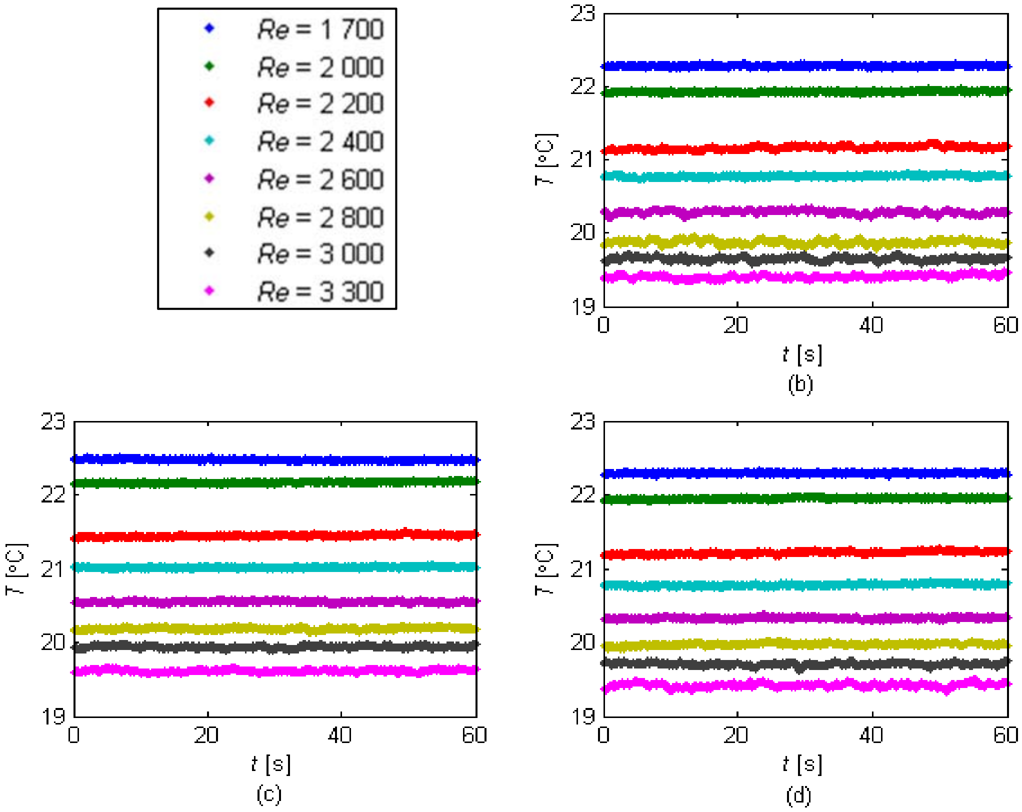

Figure D.20: Temperature fluctuations at the (a) top, (b) left, (c) bottom and (d) right of the tube at x/D = 1.3 (Station A in Figure 3.4) for different Reynolds numbers and a heat flux of 6.5 kW/m^2

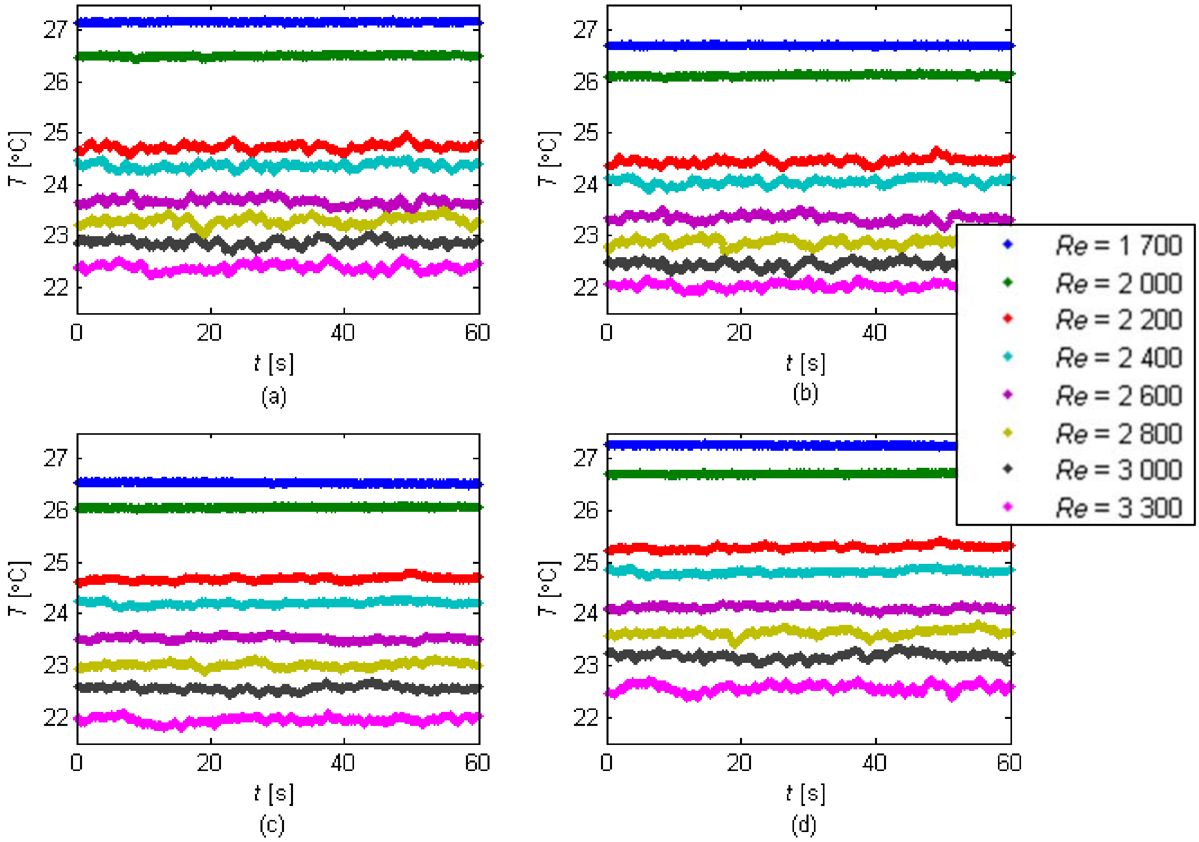

Figure D.21: Temperature fluctuations at the (a) top, (b) left, (c) bottom and (d) right of the tube at *x/D* = 8.2 (Station B in Figure 3.4) for different Reynolds numbers and a heat flux of 6.5 kW/m²

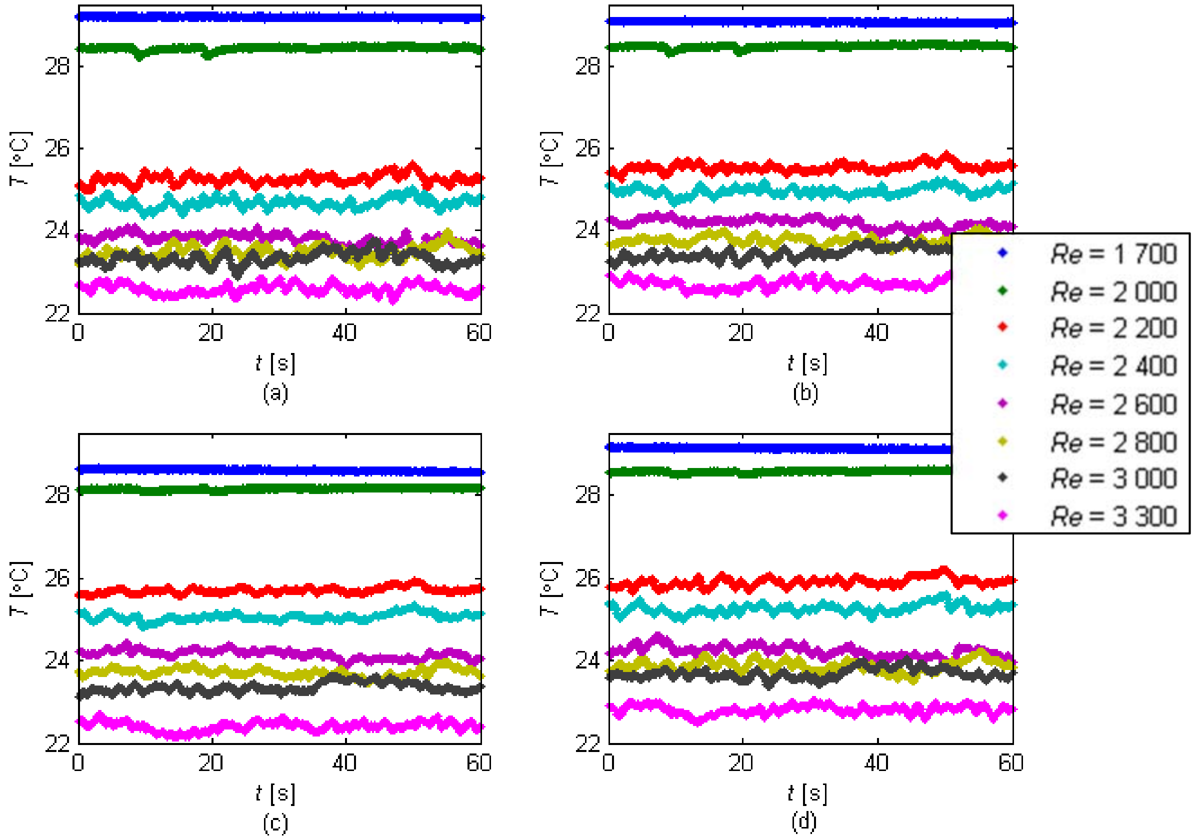

Figure D.22:Temperature fluctuations at the (a) top, (b) left, (c) bottom and (d) right of the tube at *x/D* = 16.9 (Station C in Figure 3.4) for different Reynolds numbers and a heat flux of 6.5 kW/m²

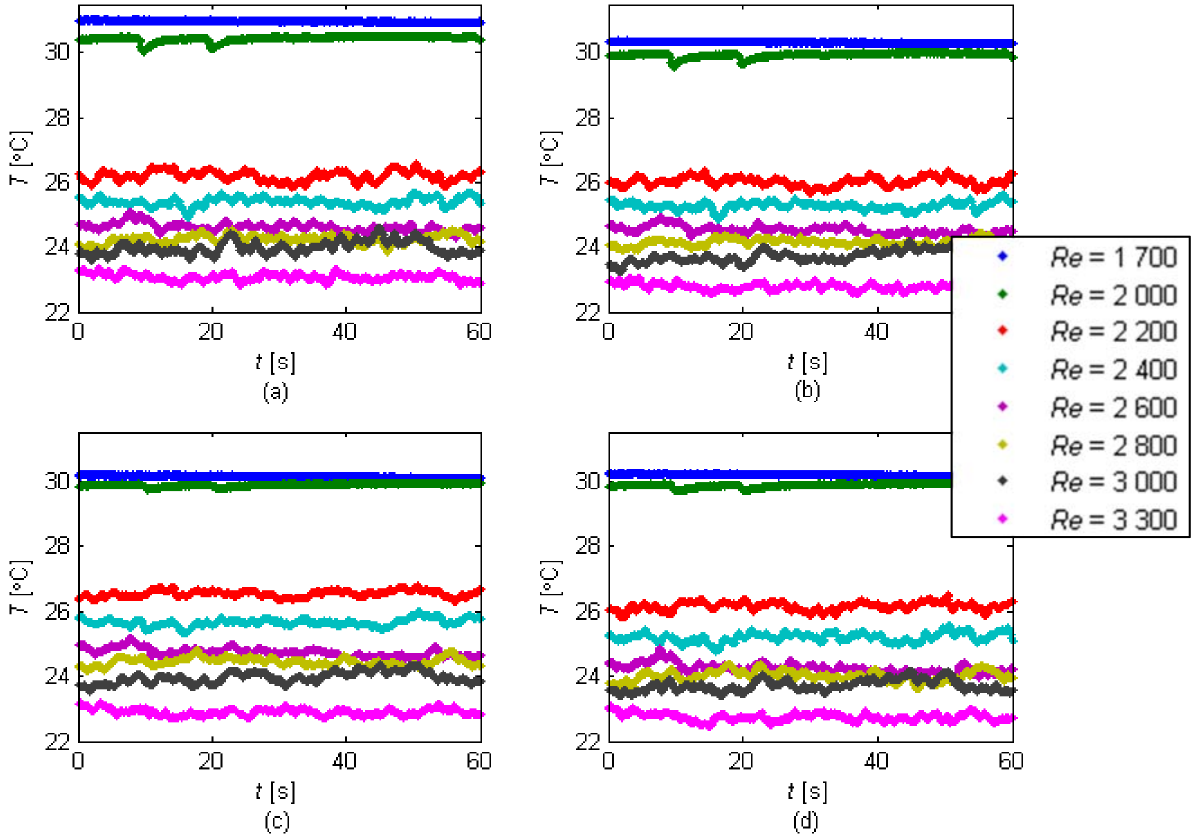

Figure D.23: Temperature fluctuations at the (a) top, (b) left, (c) bottom and (d) right of the tube at *x/D* = 25.6 (Station D in Figure 3.4) for different Reynolds numbers and a heat flux of 6.5 kW/m^2

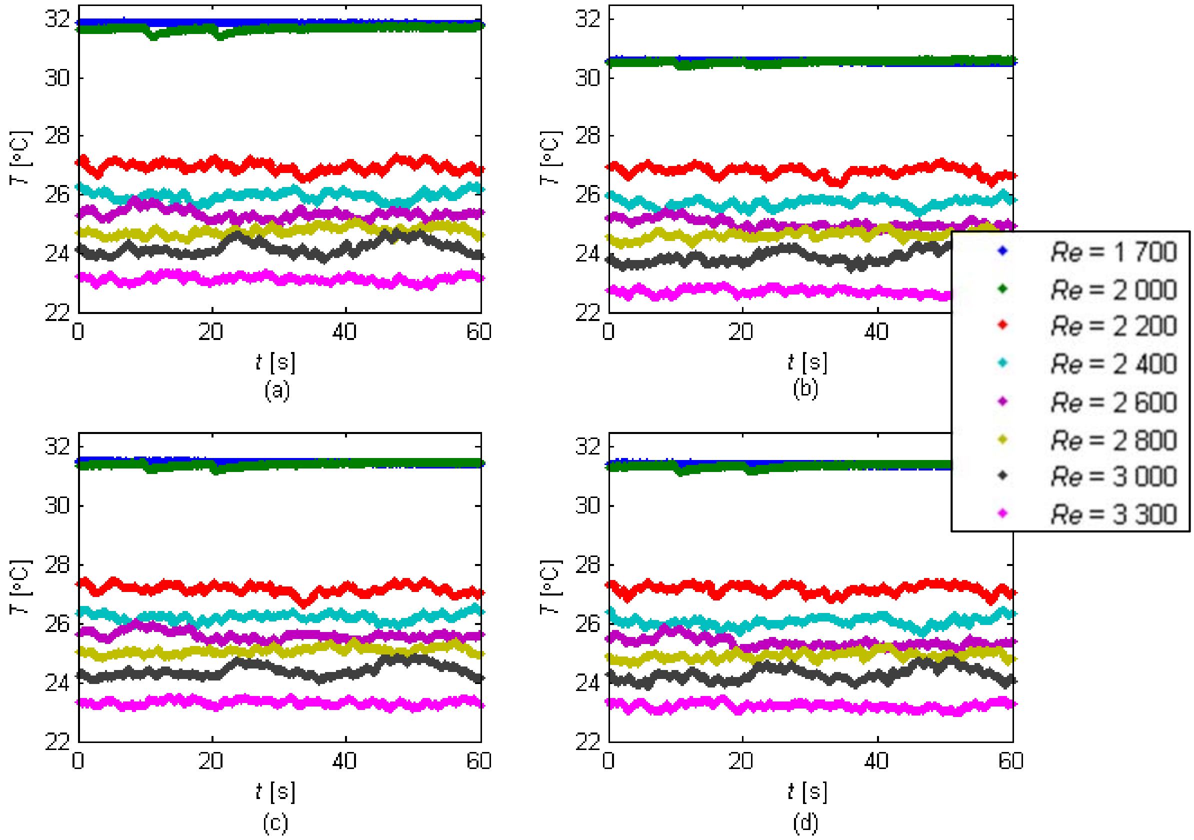

Figure D.24: Temperature fluctuations at the (a) top, (b) left, (c) bottom and (d) right of the tube at *x/D* = 36 (Station E in Figure 3.4) for different Reynolds numbers and a heat flux of 6.5 kW/m^2

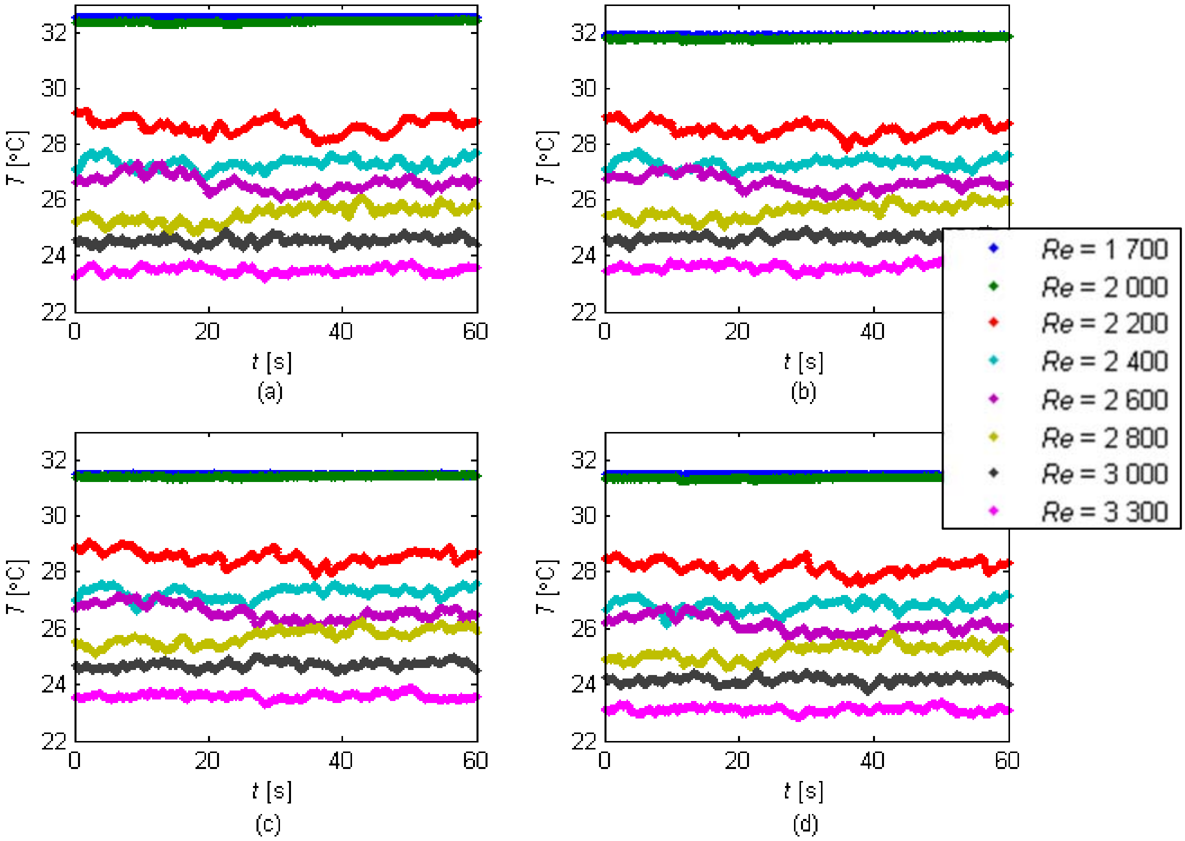

Figure D.25: Temperature fluctuations at the (a) top, (b) left, (c) bottom and (d) right of the tube at *x/D* = 53.4 (Station F in Figure 3.4) for different Reynolds numbers and a heat flux of 6.5 kW/m^2

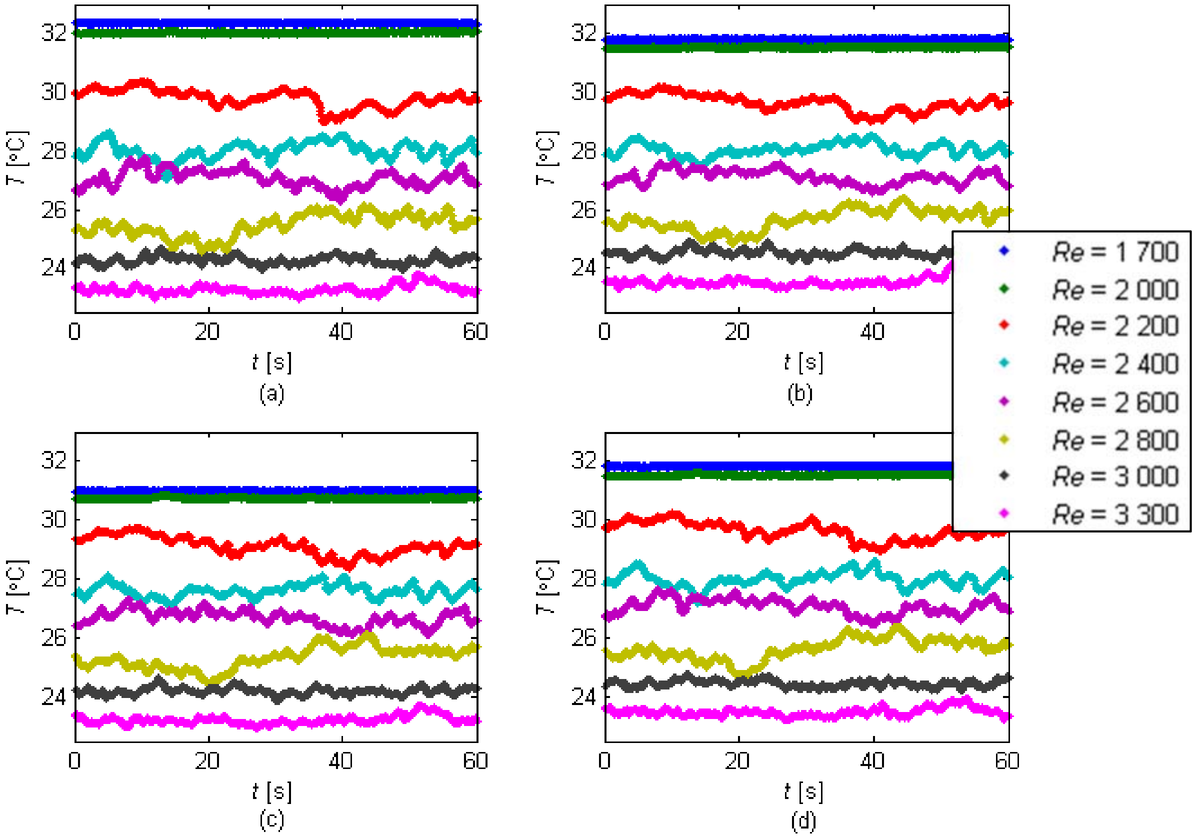

Figure D.26: Temperature fluctuations at the (a) top, (b) left, (c) bottom and (d) right of the tube at *x/D* = 70.7 (Station G in Figure 3.4) for different Reynolds numbers and a heat flux of 6.5 kW/m^2

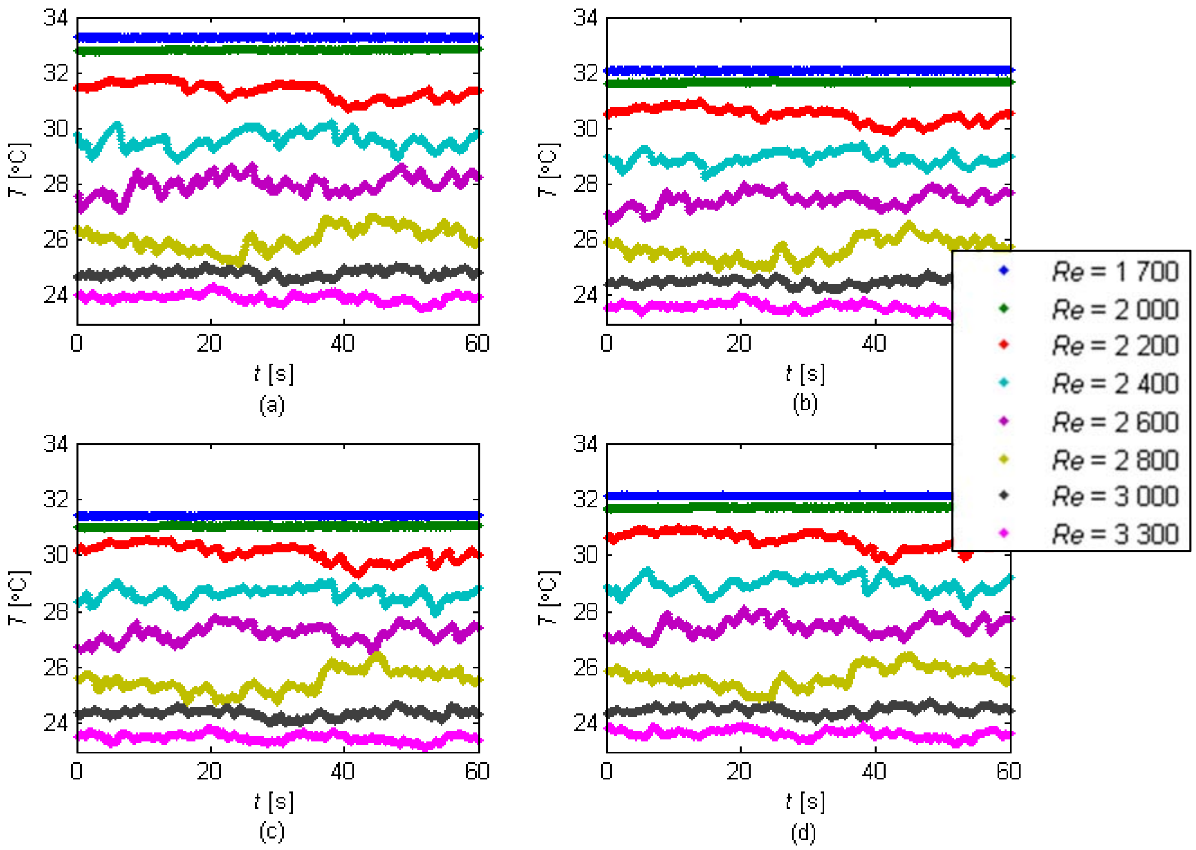

Figure D.27: Temperature fluctuations at the (a) top, (b) left, (c) bottom and (d) right of the tube at *x/D* = 88.1 (Station H in Figure 3.4) for different Reynolds numbers and a heat flux of 6.5 kW/m^2

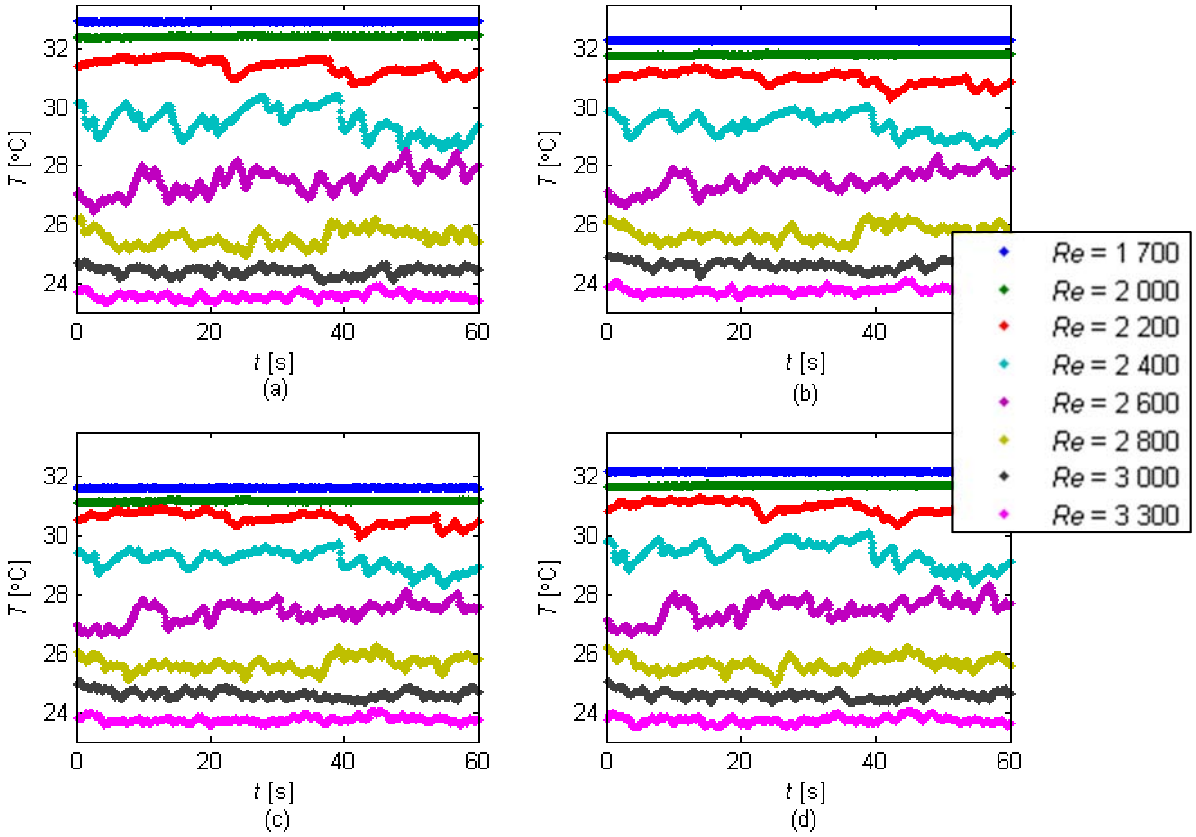

Figure D.28: Temperature fluctuations at the (a) top, (b) left, (c) bottom and (d) right of the tube at *x/D* = 105.5 (Station I in Figure 3.4) for different Reynolds numbers and a heat flux of 6.5 kW/m^2

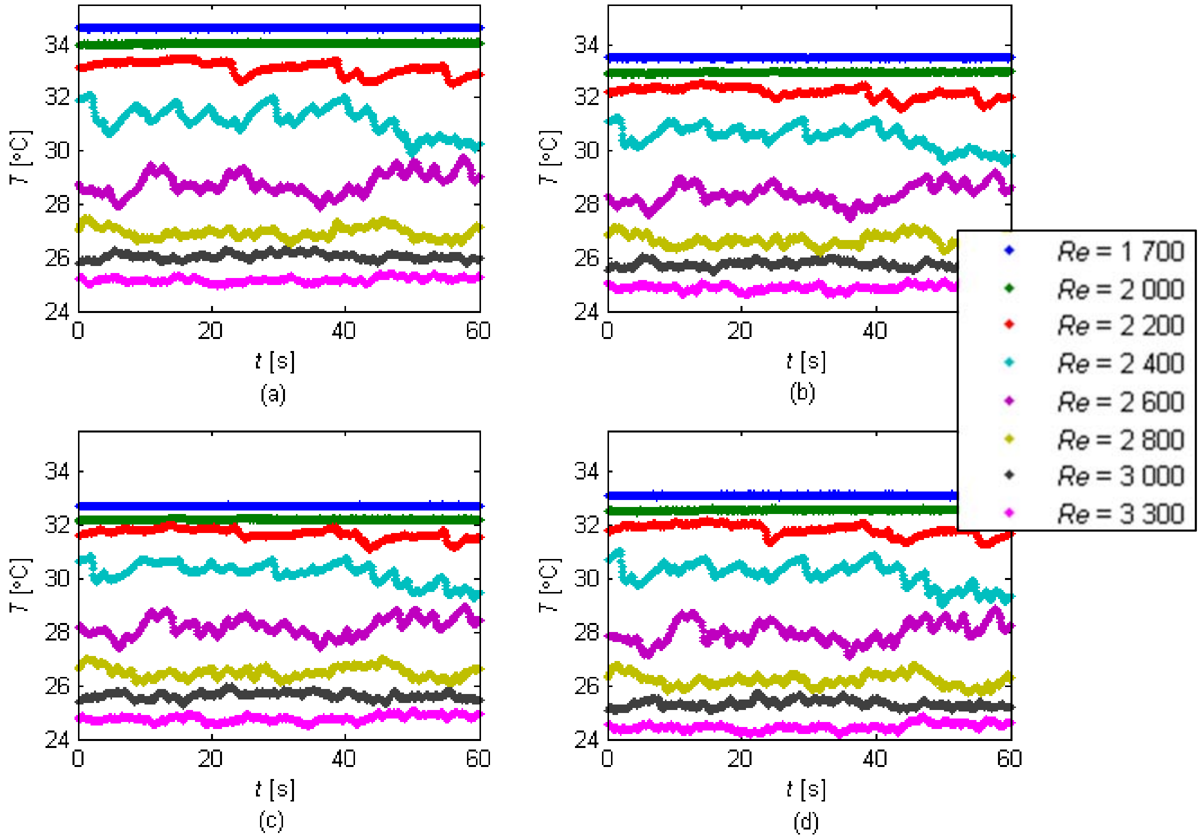

Figure D.29: Temperature fluctuations at the (a) top, (b) left, (c) bottom and (d) right of the tube at *x/D* = 122.8 (Station J in Figure 3.4) for different Reynolds numbers and a heat flux of 6.5 kW/m^2

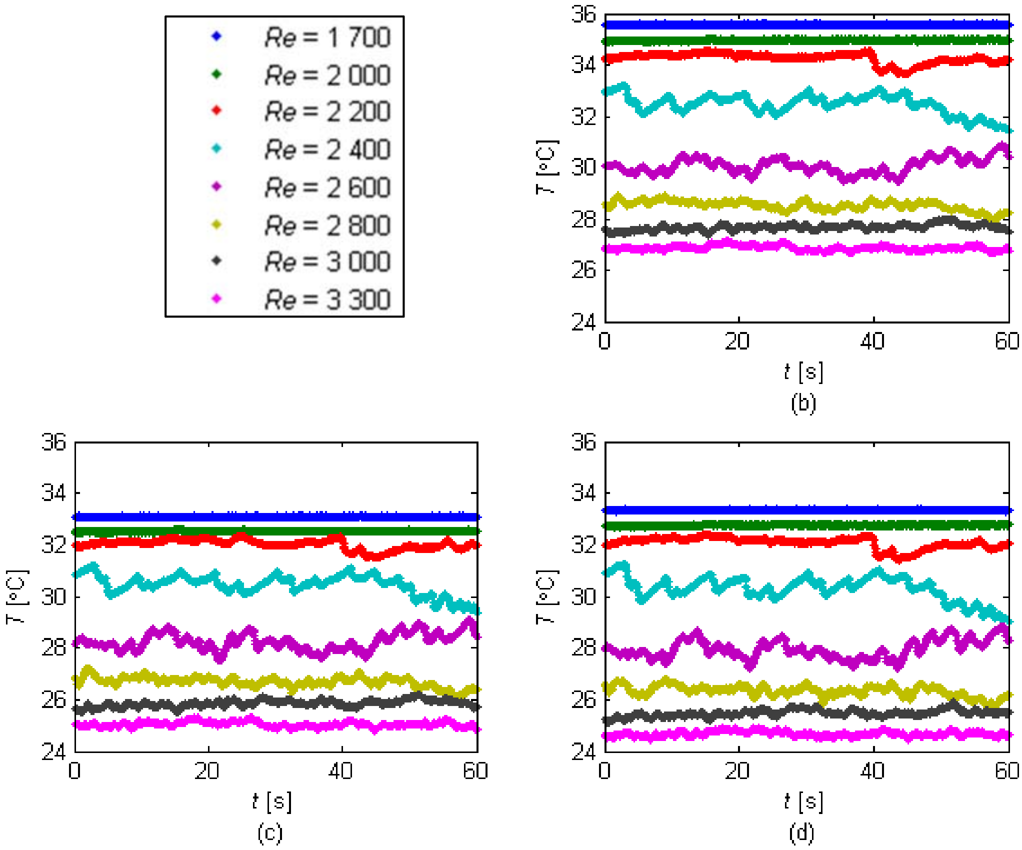

Figure D.30: Temperature fluctuations at the (a) top, (b) left, (c) bottom and (d) right of the tube at *x/D* = 140.2 (Station K in Figure 3.4) for different Reynolds numbers and a heat flux of 6.5 kW/m^2

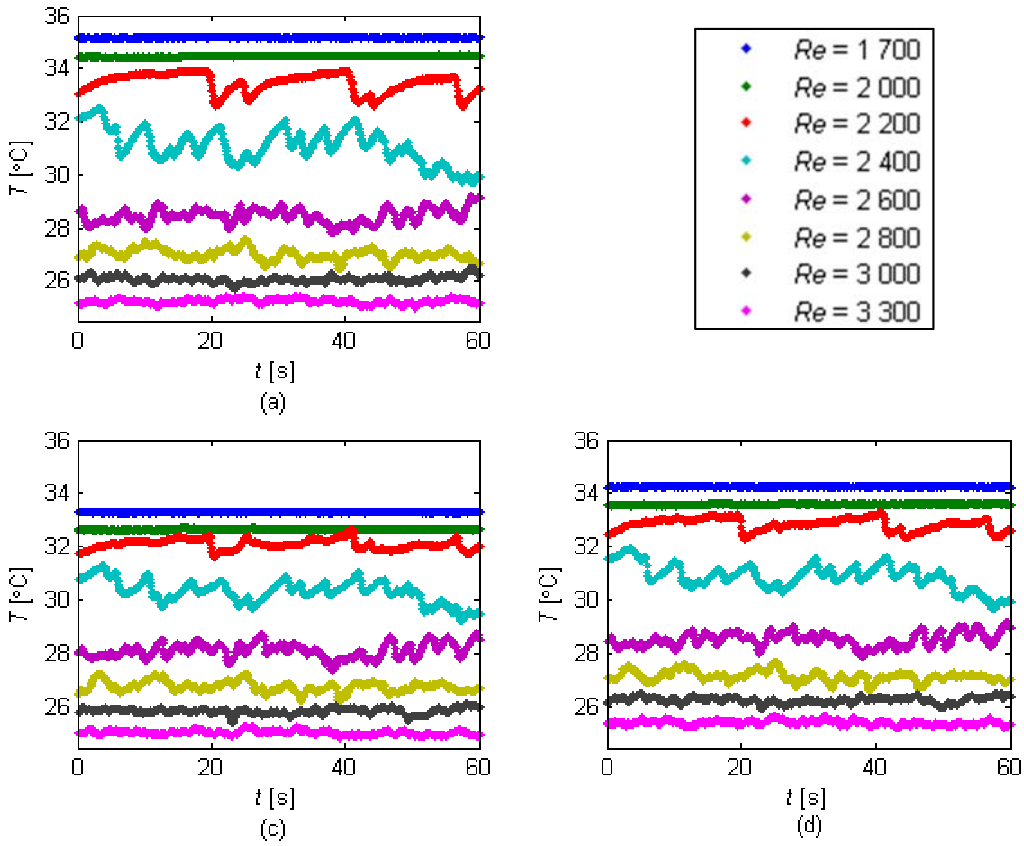

Figure D.31: Temperature fluctuations at the (a) top, (b) left, (c) bottom and (d) right of the tube at *x/D* = 157.6 (Station L in Figure 3.4) for different Reynolds numbers and a heat flux of 6.5 kW/m^2

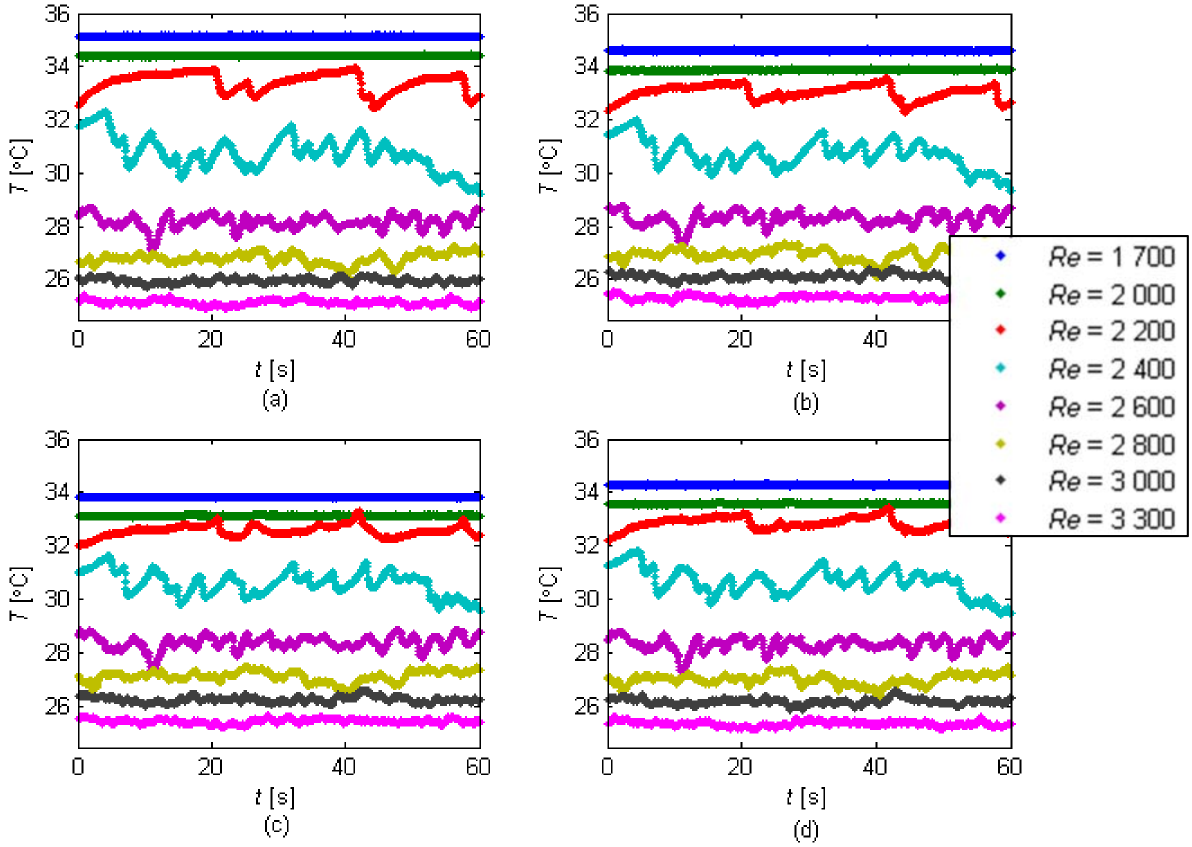

Figure D.32: Temperature fluctuations at the (a) top, (b) left, (c) bottom and (d) right of the tube at *x/D* = 174.9 (Station M in Figure 3.4) for different Reynolds numbers and a heat flux of 6.5 kW/m^2

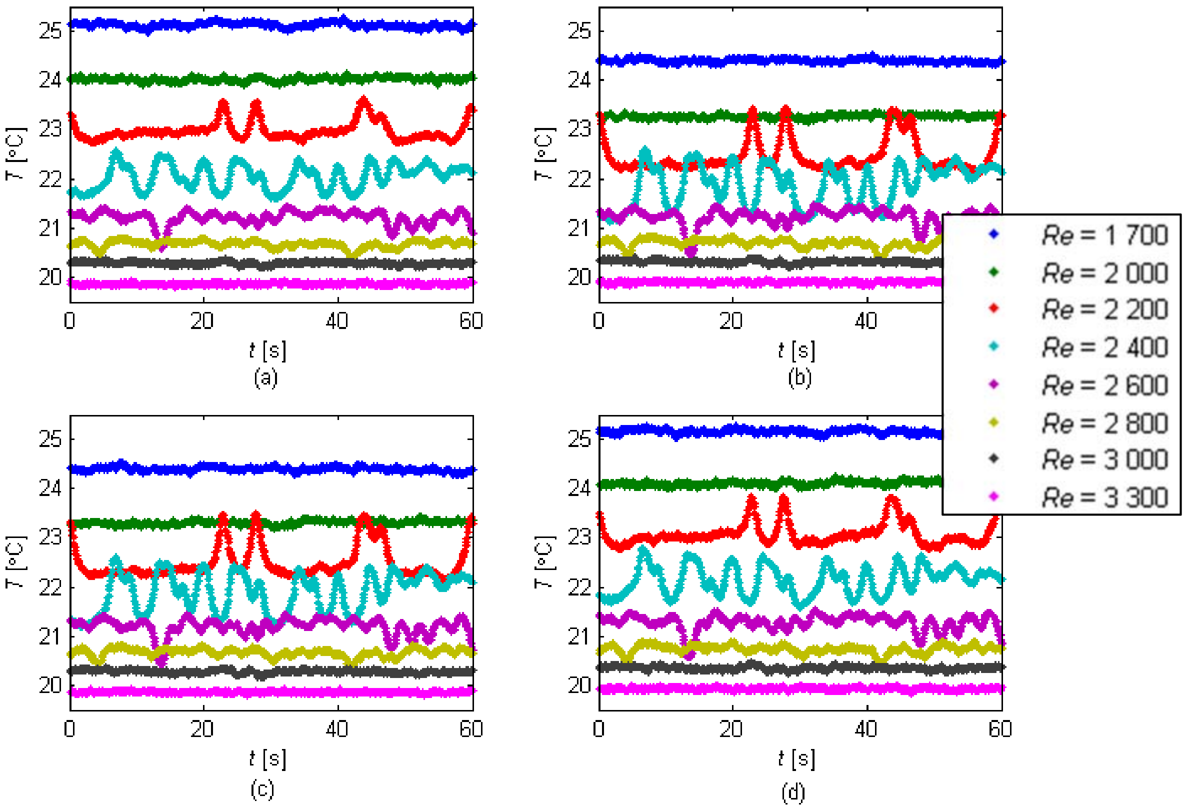

Figure D.33: Temperature fluctuations at the (a) top, (b) left, (c) bottom and (d) right in the mixing section for different Reynolds numbers and a heat flux of 6.5 kW/m²

D.4. Heat flux at 9.5 kW/m²

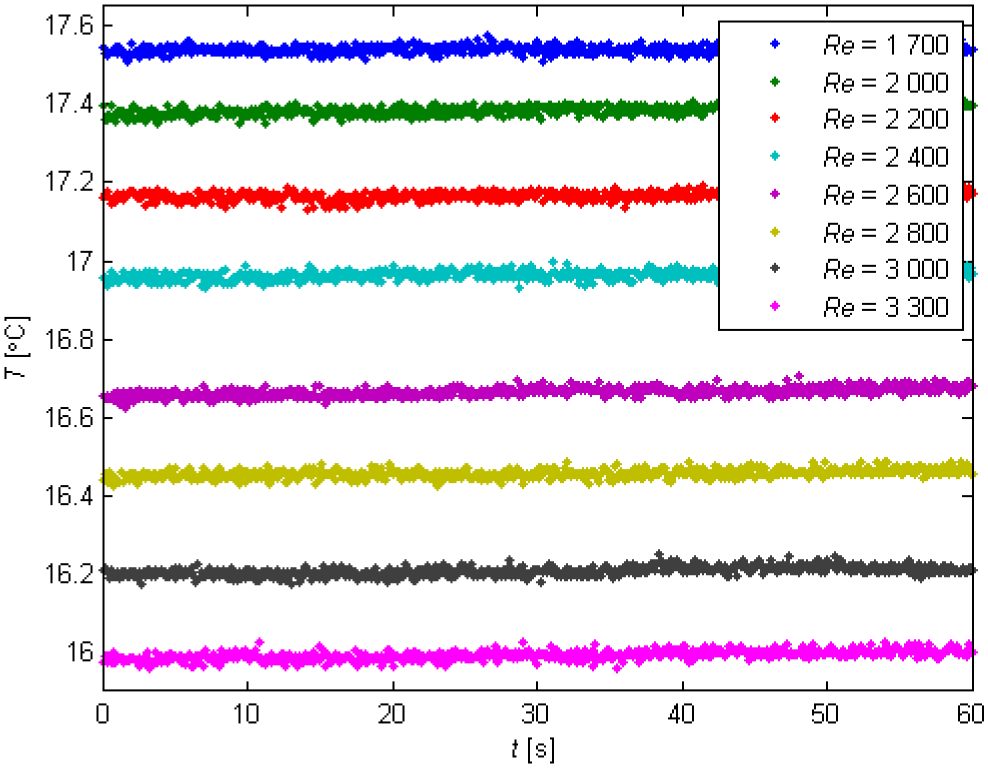

Figure D.34: Temperature fluctuations in the calming section for different Reynolds numbers and a heat flux of 9.5 kW/m²

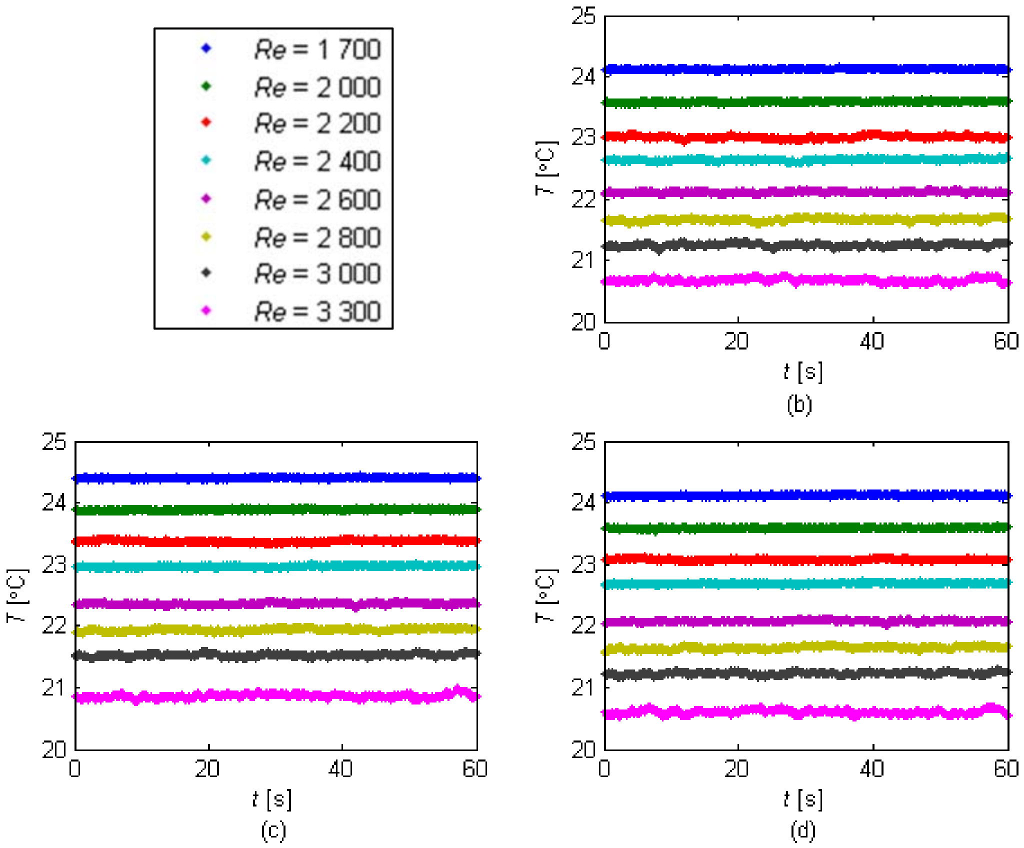

Figure D.35: Temperature fluctuations at the (a) top, (b) left, (c) bottom and (d) right of the tube at *x/D* = 1.3 (Station A in Figure 3.4) for different Reynolds numbers and a heat flux of 9.5 kW/m^2

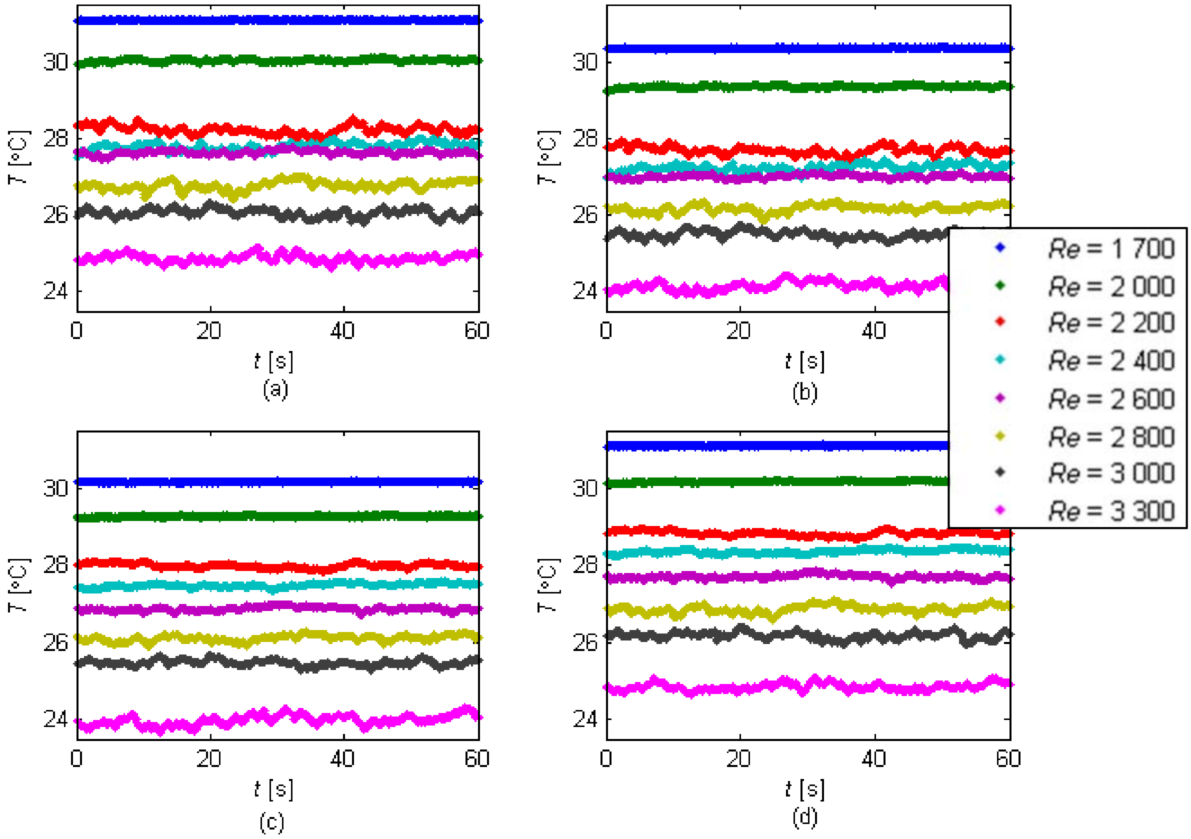

Figure D.36: Temperature fluctuations at the (a) top, (b) left, (c) bottom and (d) right of the tube at *x/D* = 8.2 (Station B in Figure 3.4) for different Reynolds numbers and a heat flux of 9.5 kW/m^2

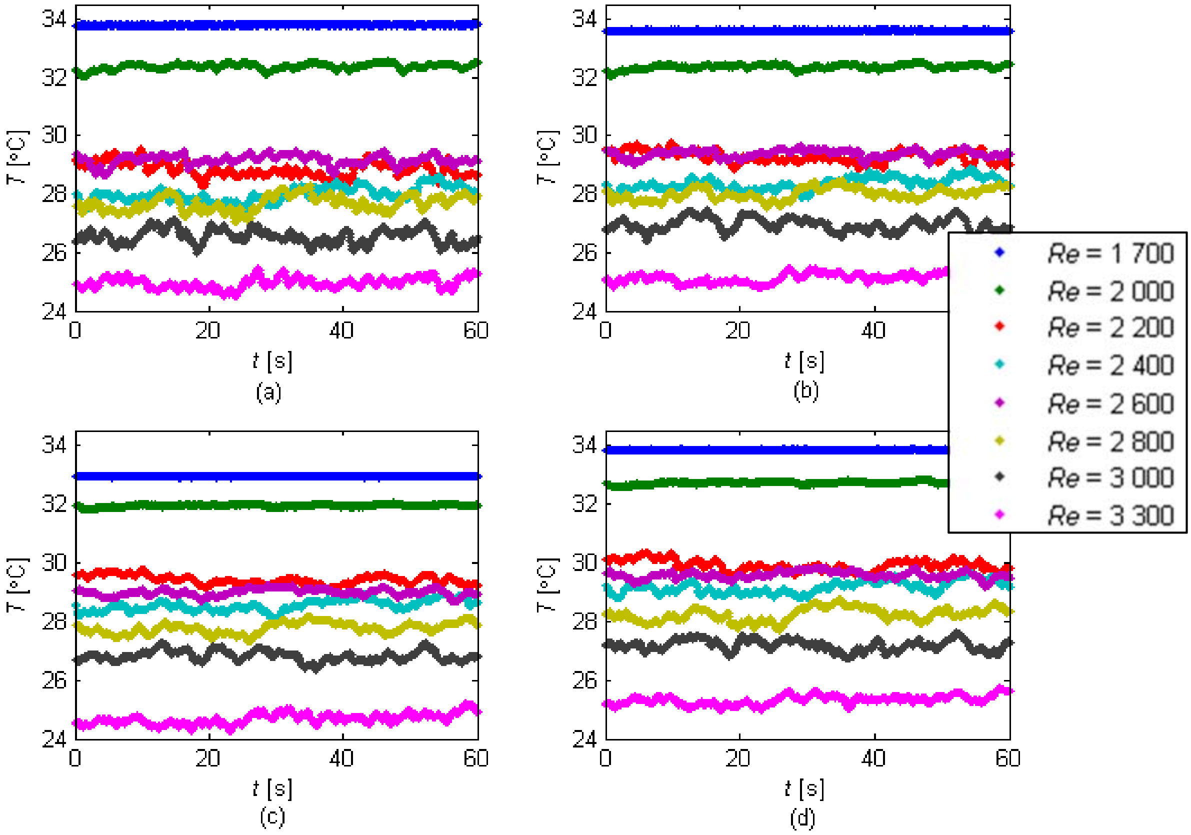

Figure D.37: Temperature fluctuations at the (a) top, (b) left, (c) bottom and (d) right of the tube at *x/D* = 16.9 (Station C in Figure 3.4) for different Reynolds numbers and a heat flux of 9.5 kW/m²

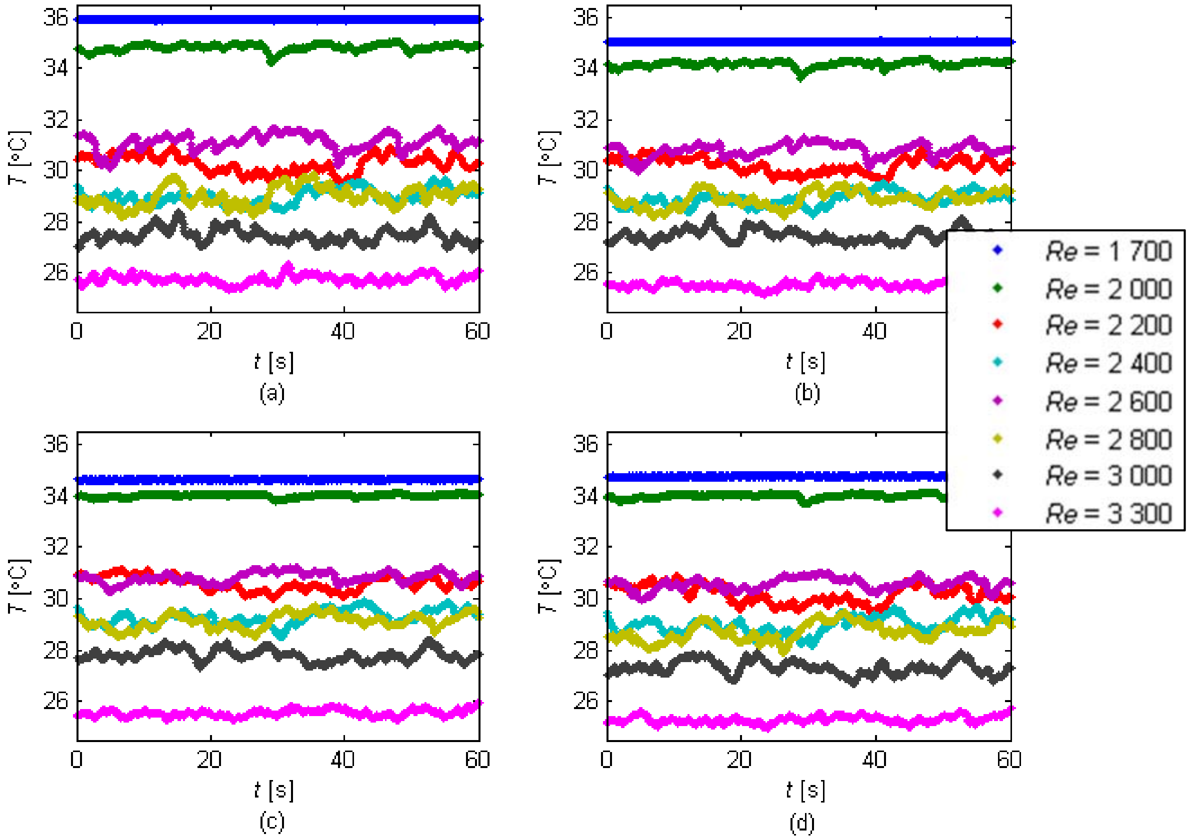

Figure D.38: Temperature fluctuations at the (a) top, (b) left, (c) bottom and (d) right of the tube at *x/D* = 25.6 (Station D in Figure 3.4) for different Reynolds numbers and a heat flux of 9.5 kW/m²

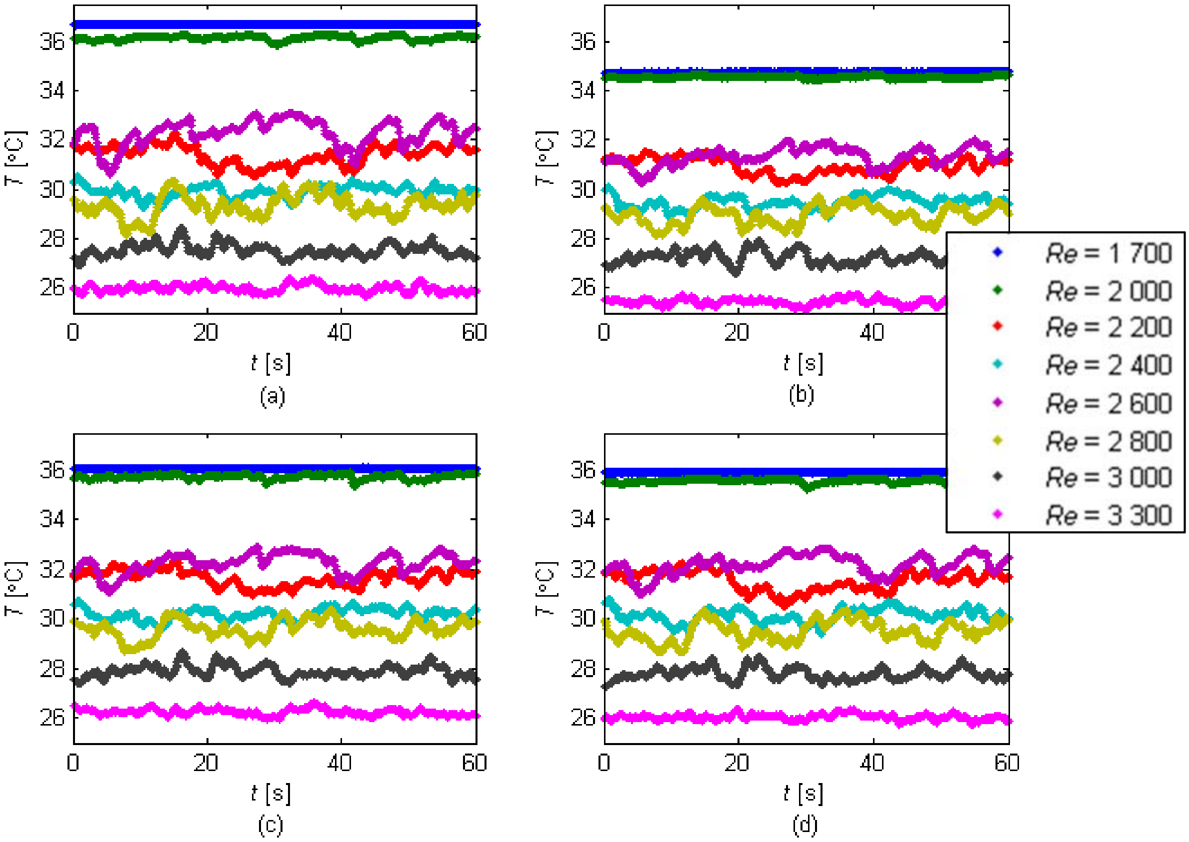

Figure D.39: Temperature fluctuations at the (a) top, (b) left, (c) bottom and (d) right of the tube at *x/D* = 36 (Station E in Figure 3.4) for different Reynolds numbers and a heat flux of 9.5 kW/m^2

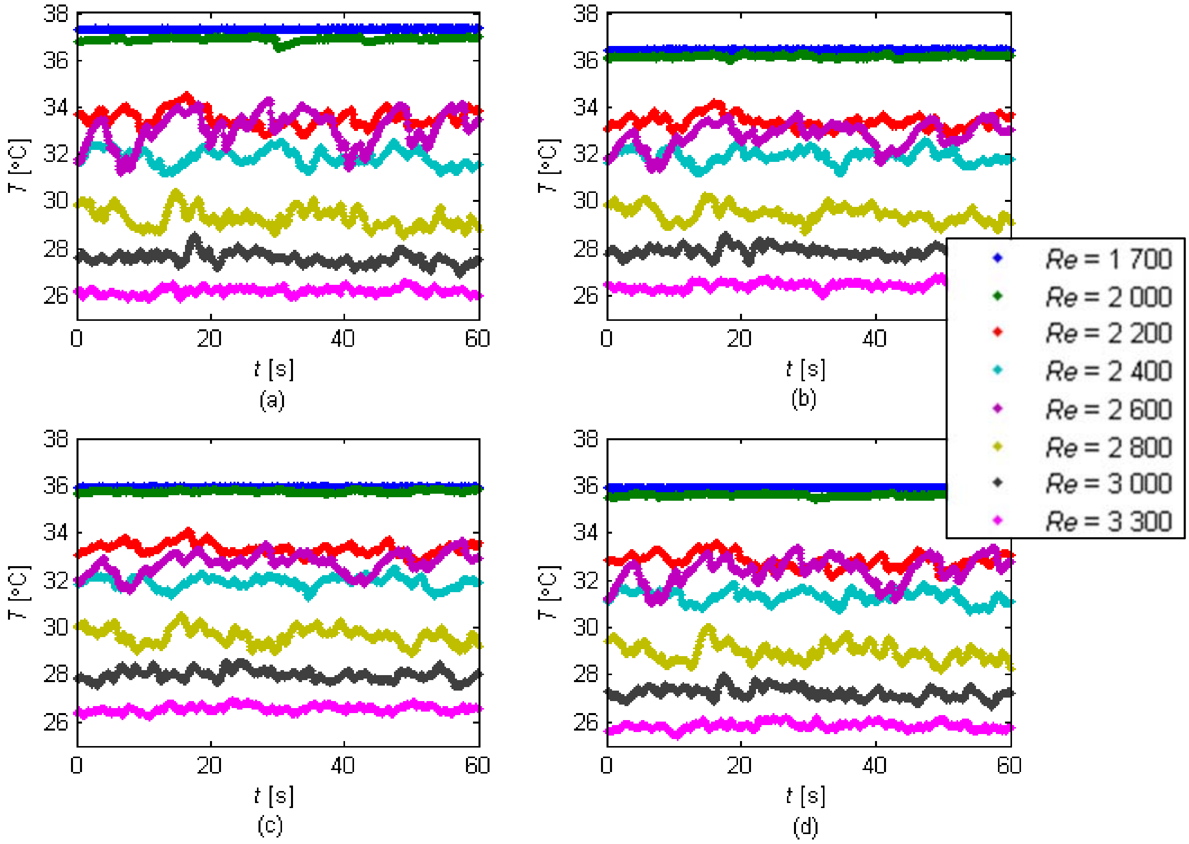

Figure D.40: Temperature fluctuations at the (a) top, (b) left, (c) bottom and (d) right of the tube at *x/D* = 53.4 (Station F in Figure 3.4) for different Reynolds numbers and a heat flux of 9.5 kW/m^2

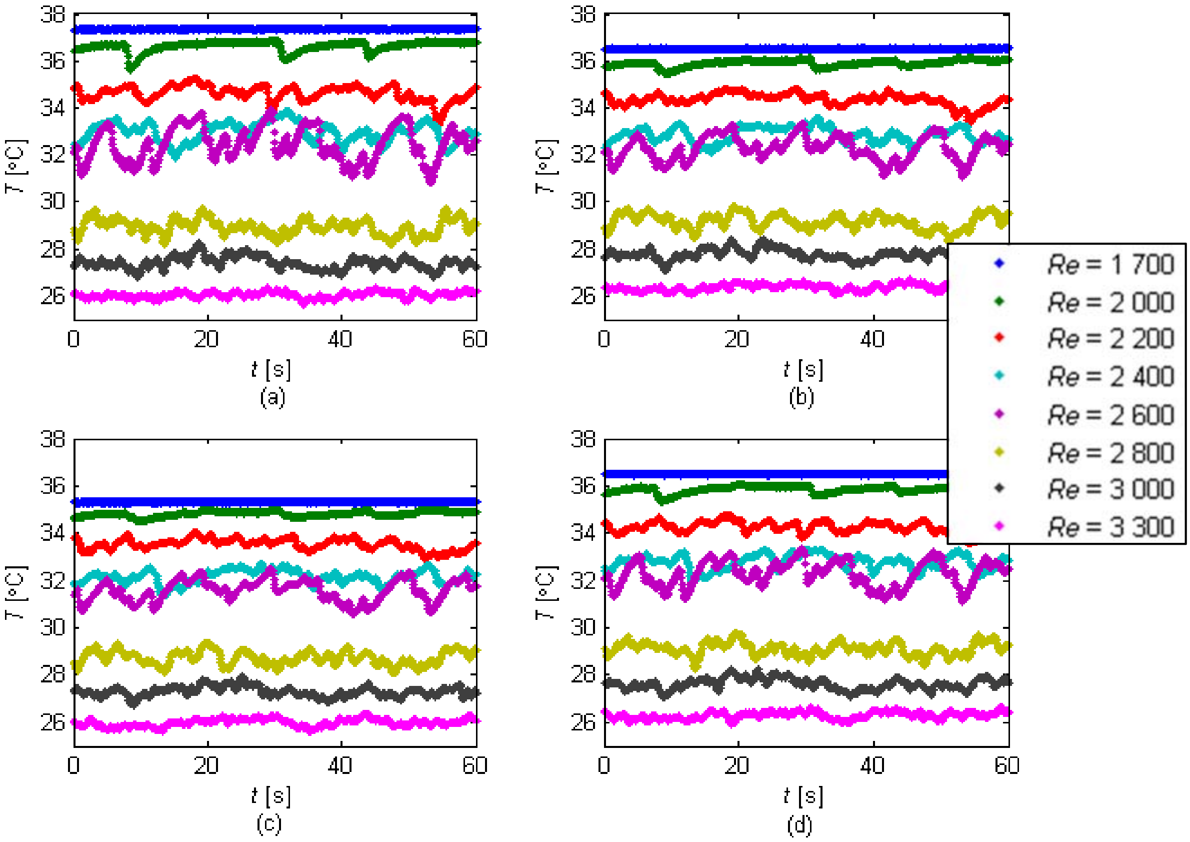

Figure D.41: Temperature fluctuations at the (a) top, (b) left, (c) bottom and (d) right of the tube at *x/D* = 70.7 (Station G in Figure 3.4) for different Reynolds numbers and a heat flux of 9.5 kW/m²

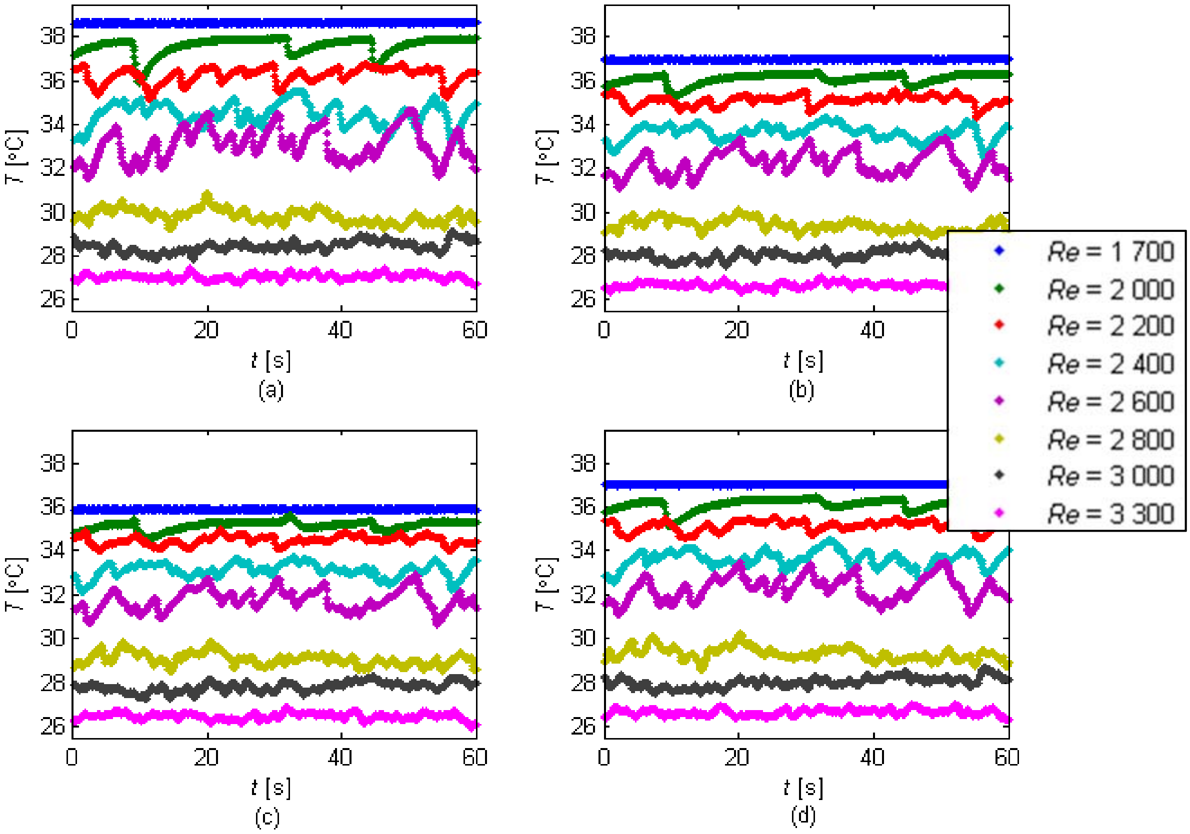

Figure D.42: Temperature fluctuations at the (a) top, (b) left, (c) bottom and (d) right of the tube at *x/D* = 88.1 (Station H in Figure 3.4) for different Reynolds numbers and a heat flux of 9.5 kW/m²

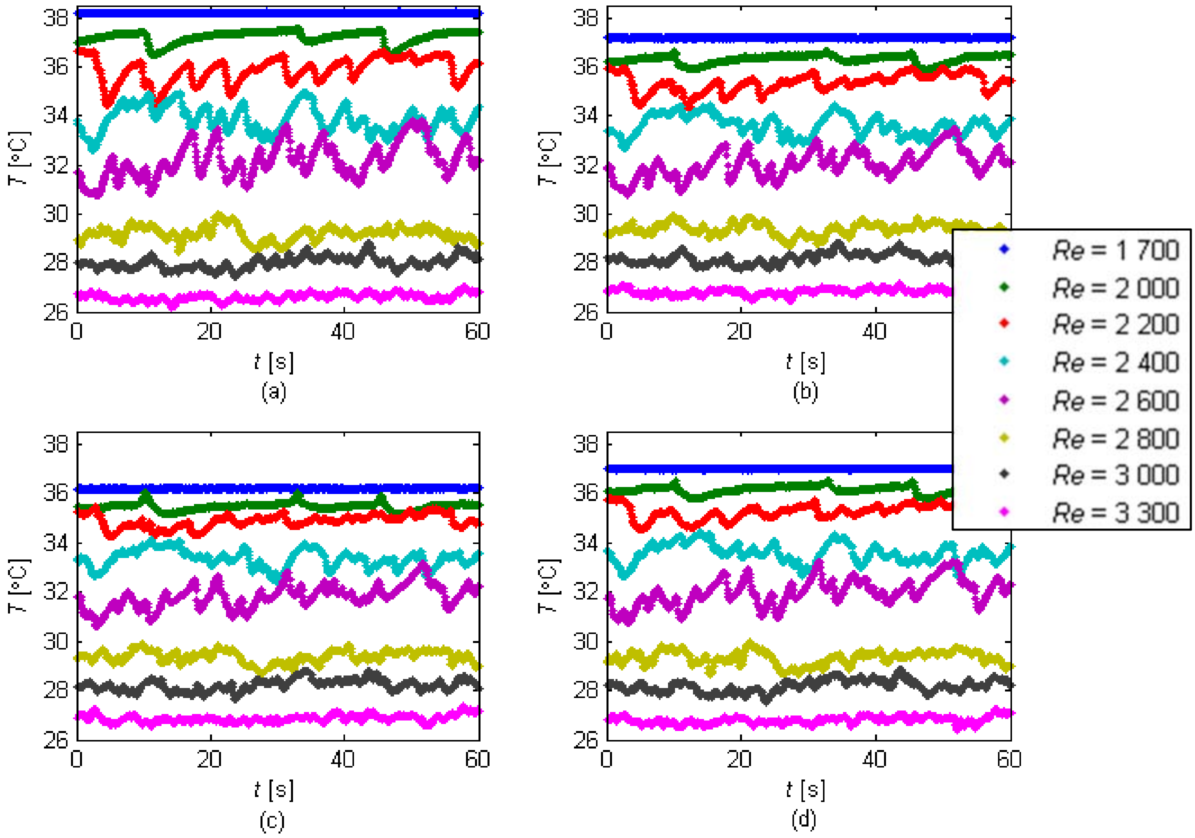

Figure D.43: Temperature fluctuations at the (a) top, (b) left, (c) bottom and (d) right of the tube at *x/D* = 105.5 (Station I in Figure 3.4) for different Reynolds numbers and a heat flux of 9.5 kW/m^2

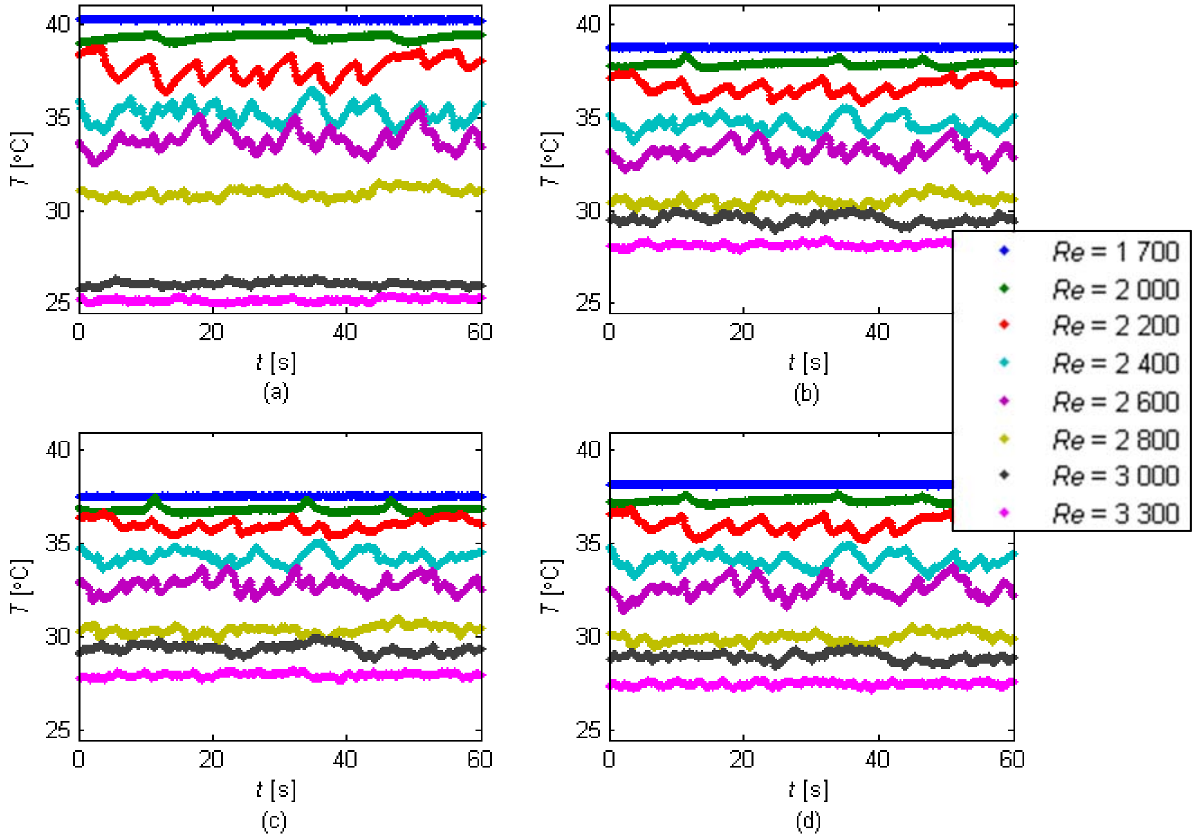

Figure D.44: Temperature fluctuations at the (a) top, (b) left, (c) bottom and (d) right of the tube at *x/D* = 122.8 (Station J in Figure 3.4) for different Reynolds numbers and a heat flux of 9.5 kW/m^2

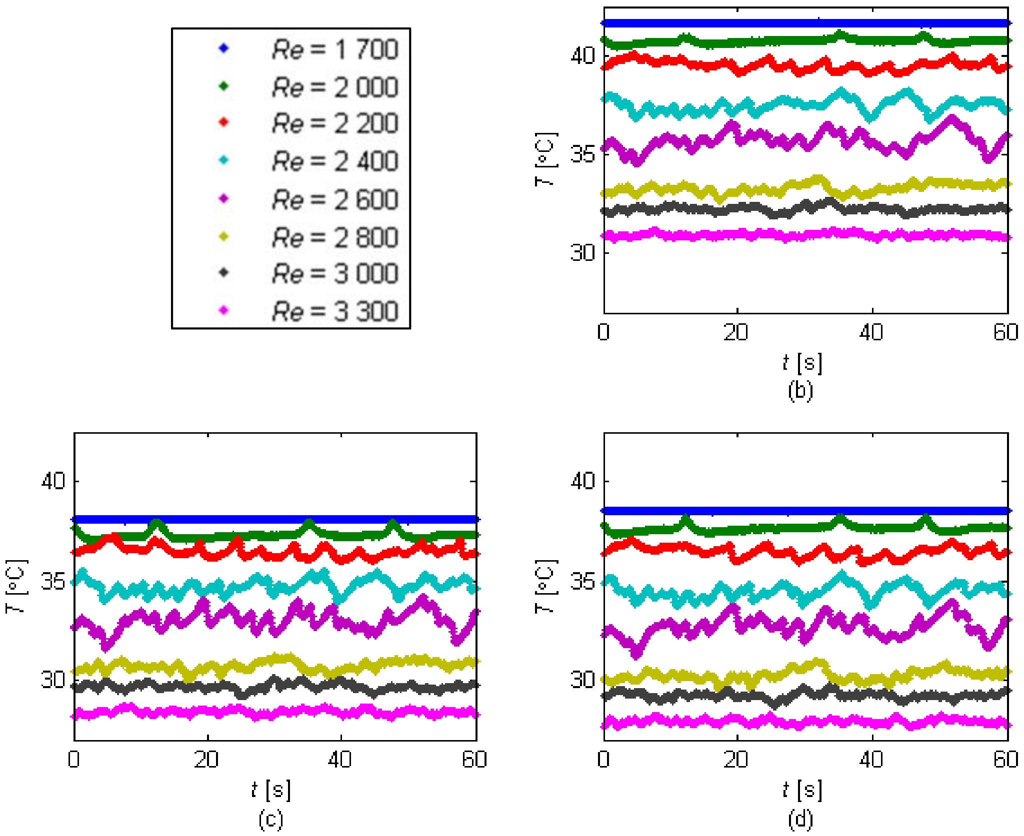

Figure D.45: Temperature fluctuations at the (a) top, (b) left, (c) bottom and (d) right of the tube at *x/D* = 140.2 (Station K in Figure 3.4) for different Reynolds numbers and a heat flux of 9.5 kW/m^2

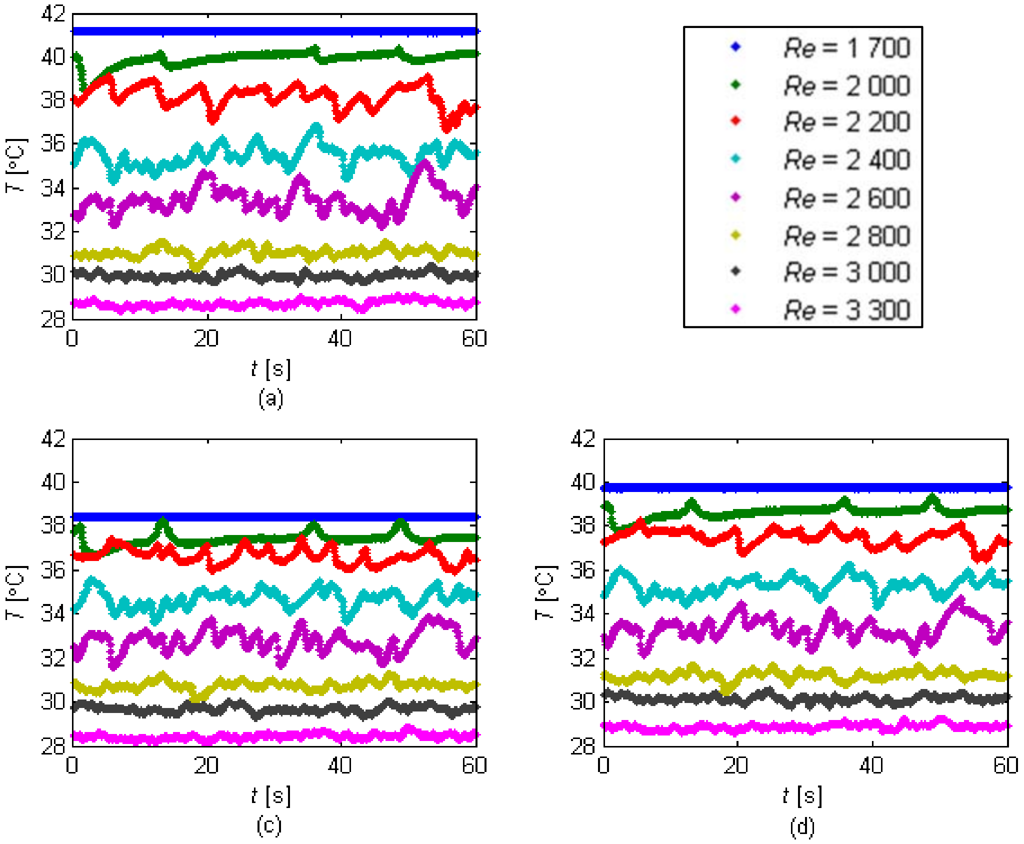

Figure D.46: Temperature fluctuations at the (a) top, (b) left, (c) bottom and (d) right of the tube at *x/D* = 157.6 (Station L in Figure 3.4) for different Reynolds numbers and a heat flux of 9.5 kW/m^2

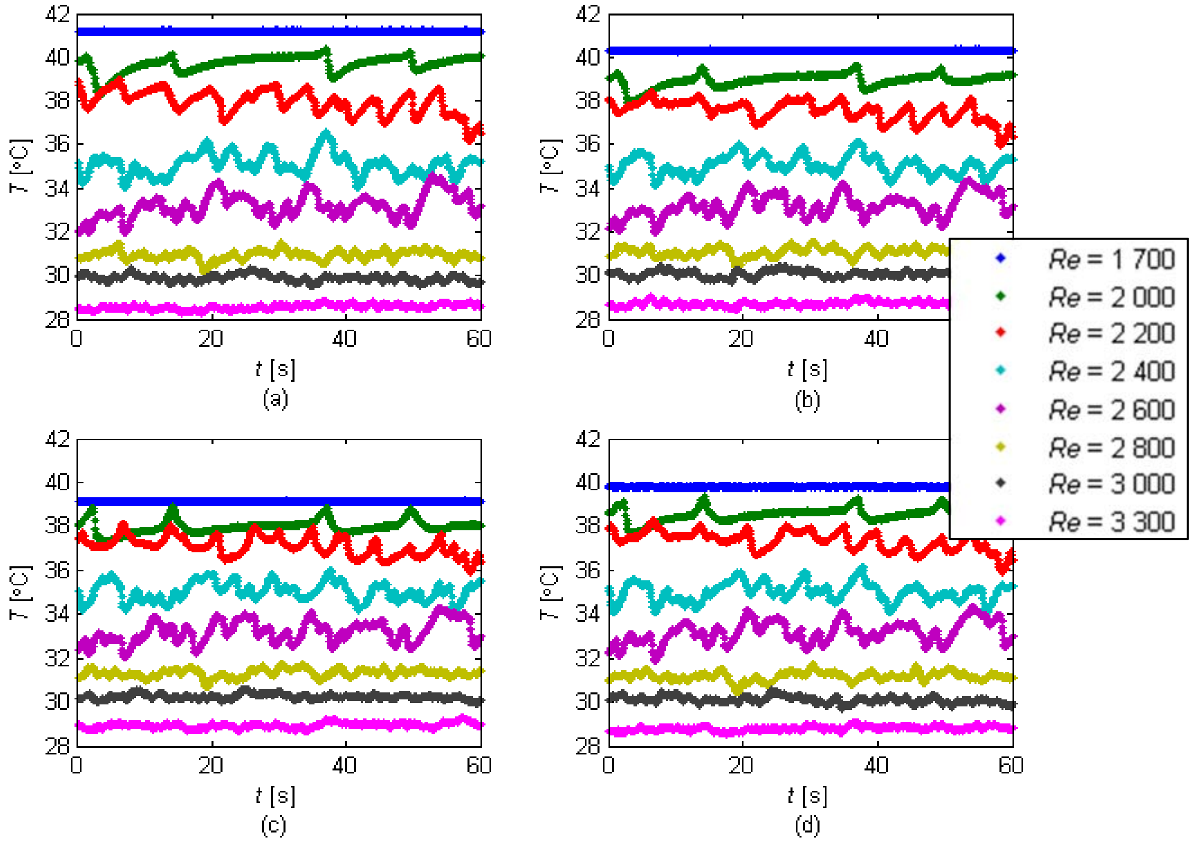

Figure D.47: Temperature fluctuations at the (a) top, (b) left, (c) bottom and (d) right of the tube at *x/D* = 174.9 (Station M in Figure 3.4) for different Reynolds numbers and a heat flux of 9.5 kW/m^2

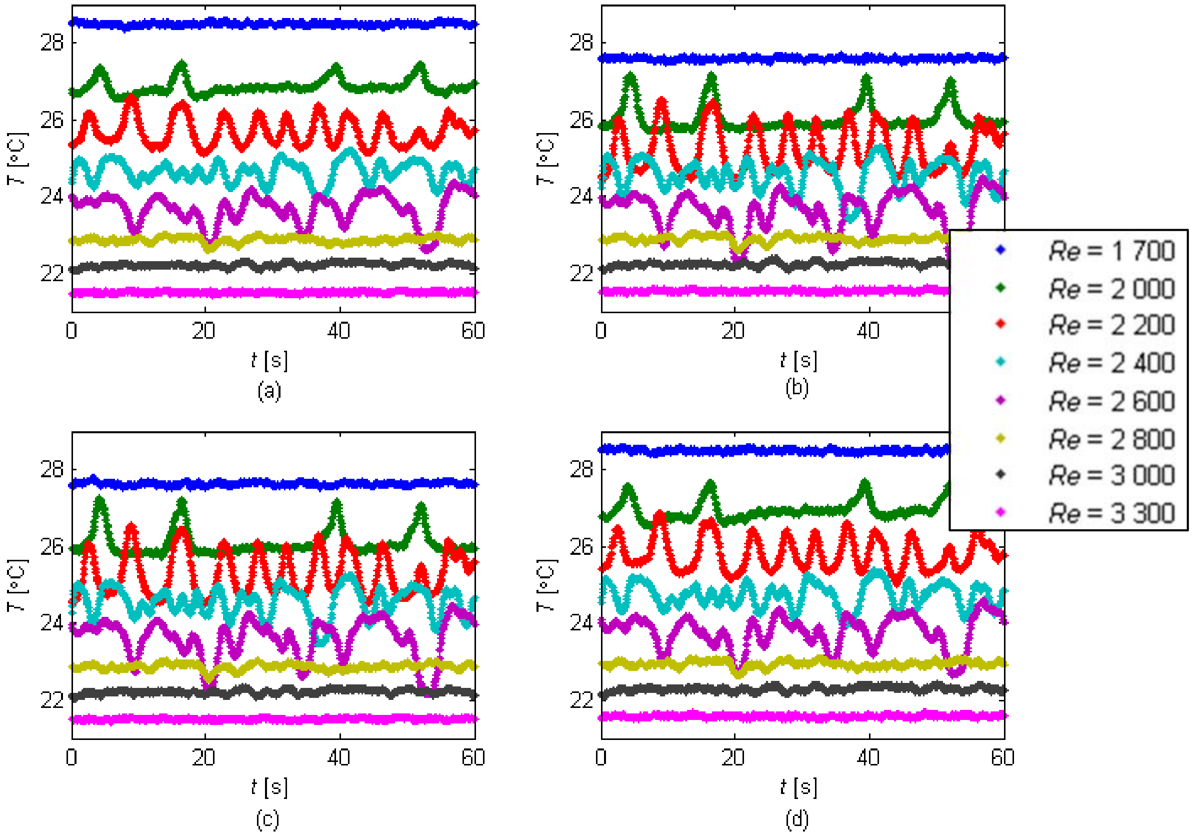

Figure D.48: Temperature fluctuations at the (a) top, (b) left, (c) bottom and (d) right in the mixing section for different Reynolds numbers and a heat flux of 9.5 kW/m^2

D.5. Conclusion

The temperature fluctuations measured along the test section were summarised in this appendix. The temperature fluctuations increased with increasing Reynolds number up to the point where transition started ($Re \approx 2\,400 - 2\,600$). Once transition started, the temperature fluctuations began to decrease. The temperature fluctuations also increased with increasing x/D along the tube length. Near the inlet of the test section, the fluctuations were negligible for all Reynolds numbers and heat fluxes, however, after $x/D = 53.4$, distinct patterns in the temperature fluctuations were observed. The patterns obtained from the temperature measurements at the top and bottom of the tube differed, while the patterns obtained from the temperature measurements on the side of the tube were similar. Furthermore, the temperatures measured at the top of the tube were higher than at the bottom of the tube due to the effects of secondary flow. Overall, it was concluded that these fluctuations were due to the buoyancy-induced secondary flow and were unique to the start of transition since it did not occur in the entire transitional flow regime.

D.6. Nomenclature

T	Temperature	°C
t	Time	s

Appendix E: Investigation of the Turbulent Temperature Measurements and Heat Transfer Coefficients

E.1. Introduction

From the local heat transfer coefficient ratios in Section 5.4, it was found that significant peaks occurred at *x/D* = 36 and *x/D* = 53.4 before it decreased along the test section. Furthermore, the magnitude of these peaks increased with increasing Reynolds number, although it was expected to decrease and approach unity. To investigate the cause of this, the temperatures along the test section were investigated for laminar and turbulent flow.

E.2. Local surface temperatures

Figure E.1 contains the local surface temperatures along the test section at Reynolds numbers of 600 and 9 500 at a heat flux of 6.5 kW/m^2. From Figure E.1(a), it follows that the temperature increased gradually between the inlet and outlet of the test section in the laminar flow regime and no distinct peaks were found. Unlike in Figure E.1(a), several peaks were found in the local temperature measurements in the turbulent flow regime (Figure E.1(b)). However, it is important to note that the temperature scales were different. The temperatures in Figure E.1(a) varied between 25 °C and 50 °C, while the temperatures in Figure E.1(b) varied between 19.6 °C and 21.6 °C. A small temperature difference might thus be negligible in the laminar flow regime, but significant in the turbulent flow regime.

Figure E.2 contains the same data as Figure E.1, however, the same temperature scale was used for both laminar and turbulent temperatures. Although the profile of the temperature measurements in the turbulent flow regime (Figure E.2(b)) seems to be significantly smoother, there were radial temperature differences between *x/D* = 30 and *x/D* = 60. However, it is important to note that in order to see the temperature gradients in Figure E.2(b), different colour legends were used for the two graphs. Figure E.2(b) was thus more sensitive to temperature variations.

To obtain a better understanding of the radial temperature distributions, the temperatures measured by the thermocouples at the top, left, bottom and right of the test section at a heat flux of 6.5 kW/m^2 are summarised in Figure E.3. Figure E.3(a) contains the data at a Reynolds number of 600 while Figure E.3(b) contains the data at a Reynolds number of 9 500. Figure E.3(b) confirms that the temperature measured by the bottom thermocouples at *x/D* = 36 and *x/D* = 53.4 was higher than expected since it measured a higher temperature than the thermocouple at the top of the test section. The temperature difference between the temperatures at the top and bottom of the test section was higher in the laminar flow regime (Figure E.3(a)) than in the turbulent flow regime

(Figure E.3(b)). This explains why a small temperature increase in the turbulent flow regime can have a significant effect on the results.

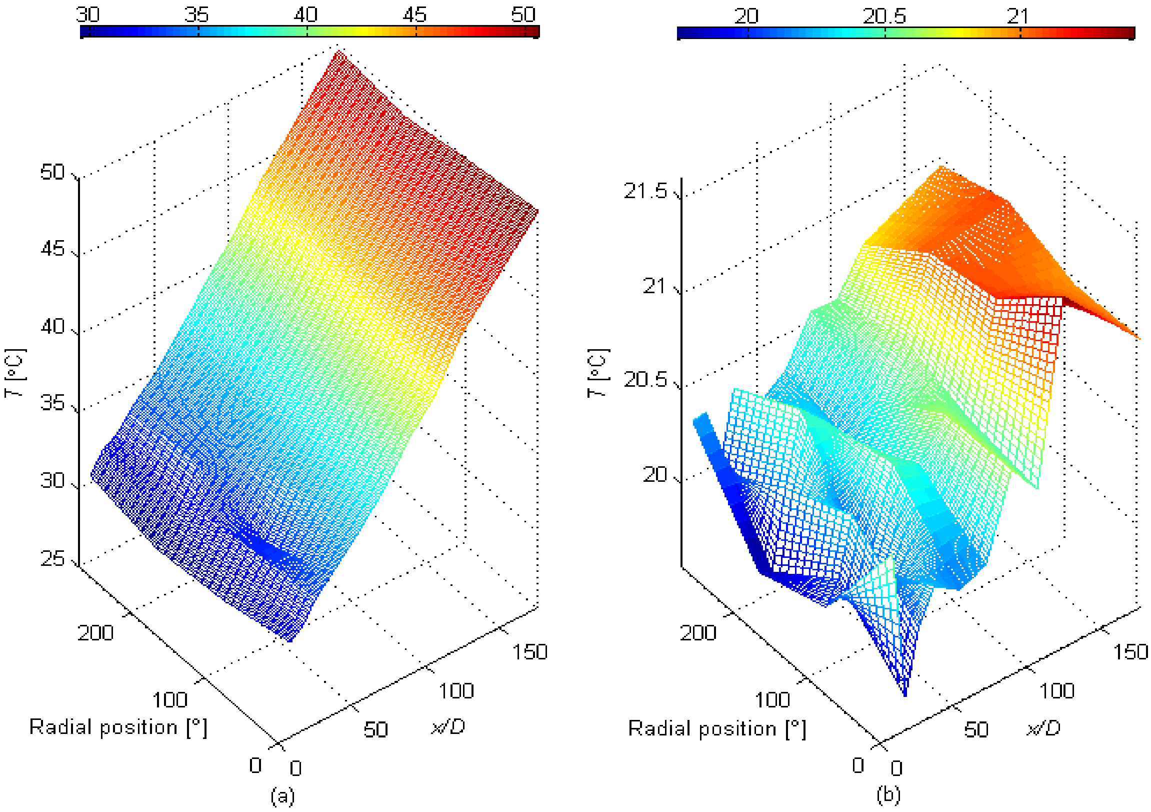

Figure E.1: Local radial and axial surface temperatures along the test section at a heat flux of 6.5 kW/m^2 and a Reynolds number of (a) 600 and (b) 9 500

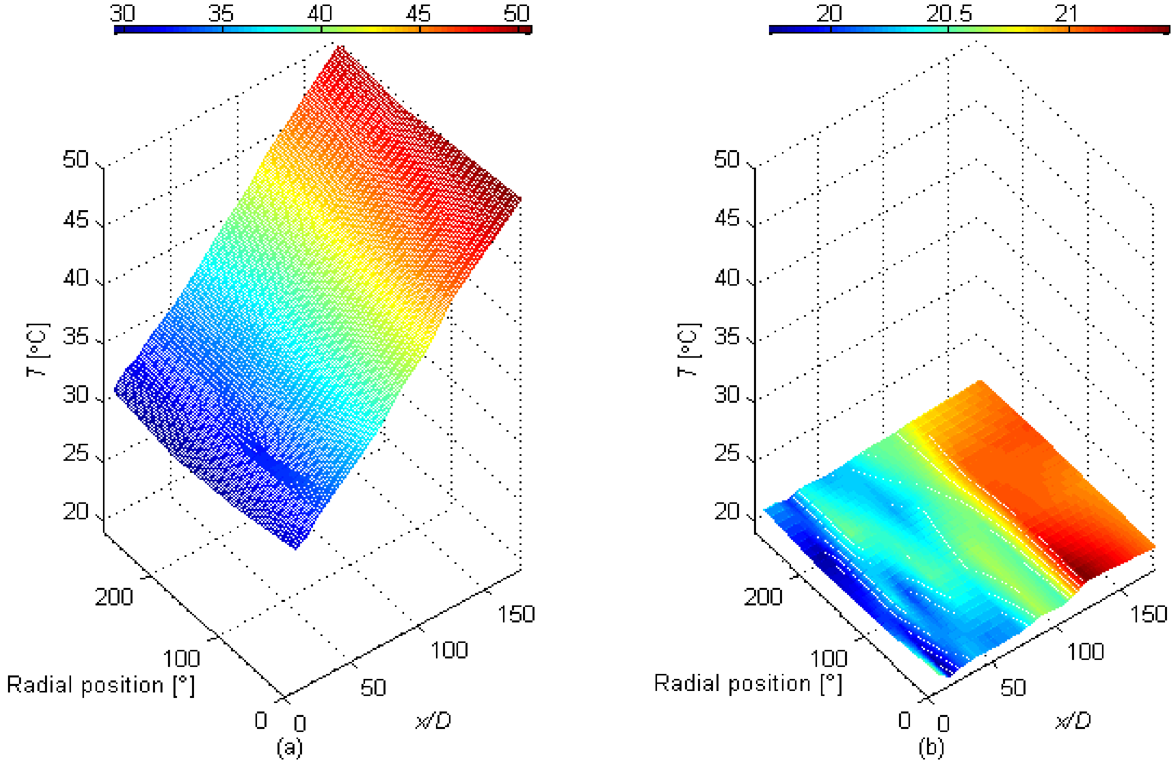

Figure E.2: Local radial and axial surface temperatures along the test section at a heat flux of 6.5 kW/m^2 and a Reynolds number of (a) 600 and (b) 9 500, using the same temperature scale but different colour legends

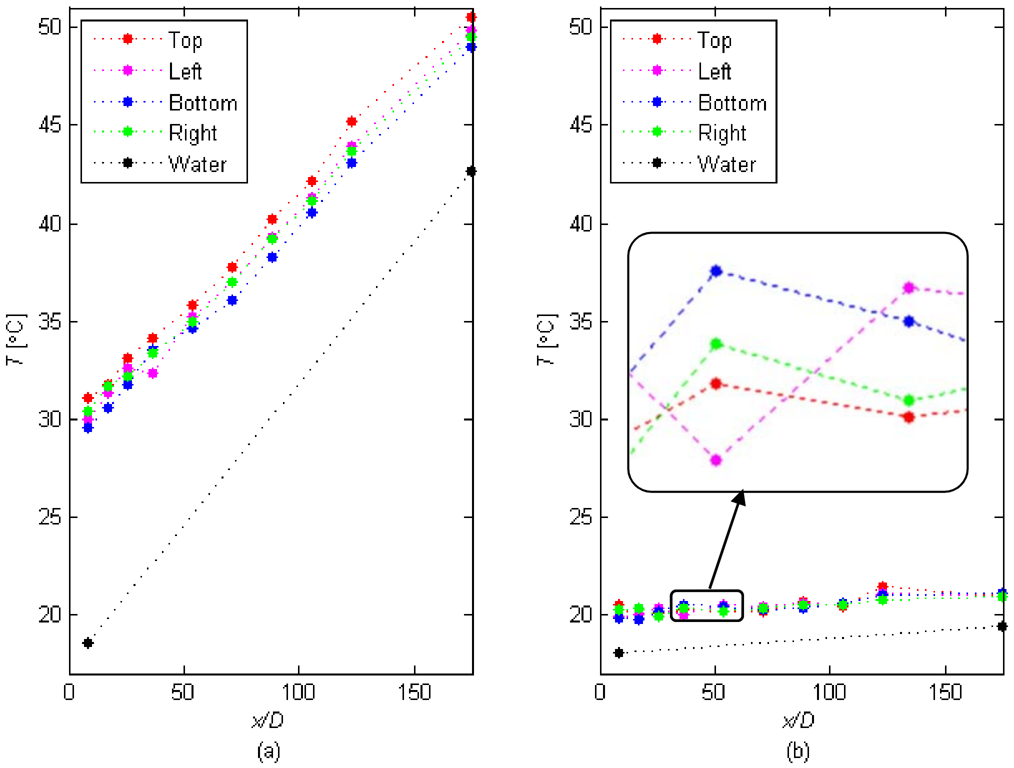

Figure E.3: Temperatures measured by the thermocouples at the top, left, bottom and right of the test section as a function of axial position for Reynolds numbers of (a) 600 and (b) 9 500 at a heat flux of 6.5 kW/m^2

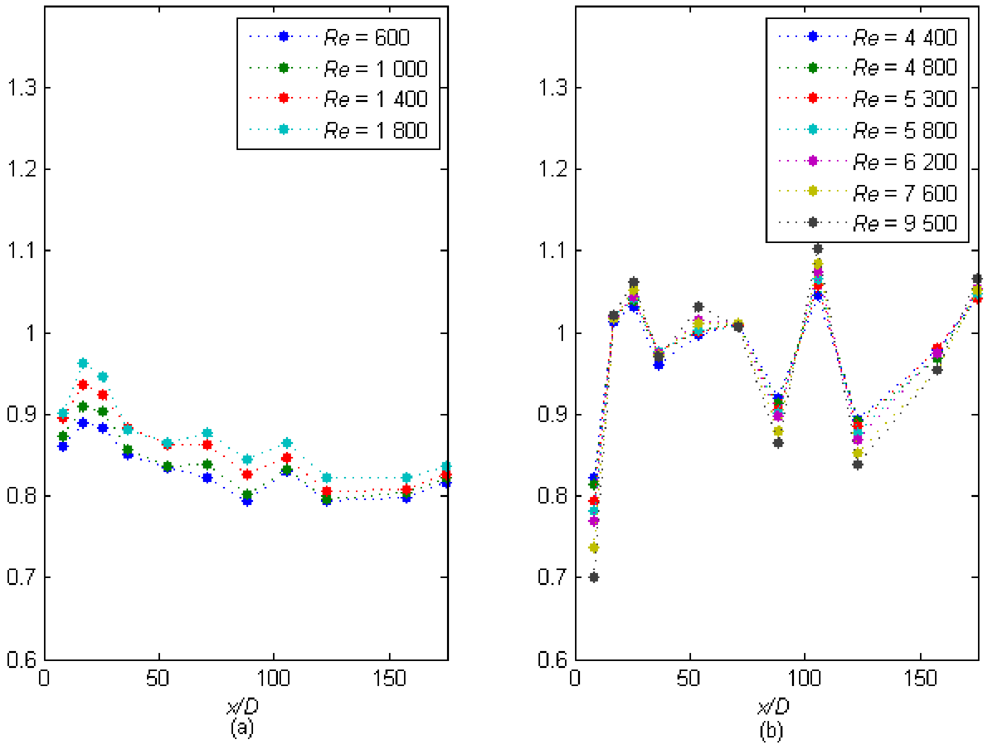

Figure E.4: Comparison of the local heat transfer coefficient ratio as a function of axial position at a Reynolds number of (a) 600 and (b) 9 500 at a heat flux of 6.5 kW/m^2

To verify this, the thermocouples at the bottom of the test section at x/D = 36 and x/D = 53.4 were removed during the processing of the results of Figure E.4. A new representative temperature was obtained by interpolating between the thermocouples at the bottom of the test section at x/D = 25.61 and x/D = 70.75. The ratio of the local heat transfer coefficients at the top and bottom of the test section using the interpolated temperature at x/D = 36 and x/D = 53.4 is shown in Figure E.4. From Figure E.4(a), it follows that forced convection dominated near the inlet of the test section, but as x/D was increased, the thickness of the thermal boundary layer increased and mixed convection began to dominate.

The heat transfer coefficient ratios in the turbulent flow regime (Figure E.4(b)) were approximately unity across the whole test section. This confirms that secondary flow effects were suppressed by the fluid motion and that flow was dominated by forced convection.

Although the interpolated temperatures were used to generate the graphs in Figure E.4, these temperatures were not used during the processing of all the other results of this study. Because the average temperature at each station was used during the data processing, the slightly higher temperatures at x/D = 36 and x/D = 53.4 did not have a significant effect on the results.

E.3. Conclusion

The local surface temperature measurements along the test section for a laminar and turbulent case were investigated in detail to gain a better understanding of why peaks occurred in the results of the local heat transfer coefficient ratios. It was found that the temperatures measured by two thermocouples at the bottom of the tube were slightly higher and since the temperature differences in the turbulent flow regime were very small, these higher temperatures became significant. However, the average of the four thermocouples at each thermocouple station was used during the data processing of this study, thus these slightly higher temperatures did not have a significant effect on the results.

Appendix F: Data and Publications Repository

F.1. Introduction

All the experimental data of this study, as well as the journal articles and conference papers that were consulted during this study, are summarised in an Excel file on a CD, which is attached at the end of this appendix.

F.2. Nomenclature

Table F.1 contains an example of the data at a Reynolds number of 622 when a heat flux of 6.5 kW/m^2 is applied to the test section. The first column contains the symbol, the middle column contains the description and the last column contains the value. "-_*A*" refers to the local value at Station A in Figure 3.4. Thus the values of *T_A*, *Nu_A*, *DT_A*, etc., refer to the first thermocouple station. Thus, in the Excel file, *T_B*, *Nu_B*, *DT_B*, etc., refer to Station B in Figure 3.4. Although an example of the other stations is not given in Table F.1, the data are given on the CD.

Table F.1: Symbols, description and example values of experimental data in data repository

	Description	Units	Value
Re	Reynolds number		622
Nu	Nusselt number		12.74
u_Nu	Nusselt number uncertainty		0.56
j	Colburn *j*-factor		0.01220
u_j	Colburn *j*-factor uncertainty		0.00056
f	Friction factor		1.23839
u_f	Friction factor uncertainty		0.01311
u_Re%	% uncertainty of Reynolds number		1.09
u_f%	% uncertainty of friction factor		1.06
u_Nu%	% uncertainty of Nusselt number		4.39
u_j%	% uncertainty of Colburn *j*-factor		4.59
P	Pressure drop	Pa	0.19
Tin	Inlet temperature	°C	18.17
Tout	Outlet temperature	°C	44.00
Tb	Bulk fluid temperature	°C	31.08
Ts	Surface temperature	°C	40.61
T_A	Surface temperature at Station A	°C	25.48
Lt	Theoretical thermal entrance length	m	1.69
Nu_A	Local Nusselt number at Station A		17.60
ρ	Density	kg/m^3	995.28
V	Velocity	m/s	0.04
m	Mass flow rate	kg/s	0.00439
Ra	Rayleigh number		7.27E+06

Table F.1 (Continued): Symbols, description and example values of experimental data in data repository

	Description	Units	Value
DT_A	Temperature difference at Station A	°C	7.12
h_A	Heat transfer coefficient at Station A	W/m^2	915.07
k_A	Thermal conductivity at Station A	W/m.K	0.60
Re_A	Reynolds number at Station A		466
LtP_A	% Fully developed flow at Station A		0.63
jl_A	Colburn *j*-factor at Station A		0.02011
Pr_A	Prandtl number at Station A		6.61
Gr_A	Grashof number at Station A		3.79E+05
Ra_A	Rayleigh number at Station A		2.50E+06